# BRANCHED POLYMER ELECTROLYTES: RESPONSIVE NANOMATERIALS FOR CONTROLLED ION MOBILITY

A Dissertation
Presented to
The Academic Faculty

by

Andrew J. Erwin

In Partial Fulfillment
of the Requirements for the Degree
Doctor of Philosophy in the
School of Materials Science and Engineering

Georgia Institute of Technology

May 2021

# BRANCHED POLYMER ELECTROLYTES: RESPONSIVE NANOMATERIALS FOR CONTROLLED ION MOBILITY

Approved by:


Dr. Vladimir V. Tsukruk, Advisor
School of Materials Science and Engineering
*Georgia Institute of Technology*

Dr. Alexei P. Sokolov
School of Chemistry and Physics
*University of Tennessee*

Dr. Blair K. Brettman
School of Materials Science and Engineering
*Georgia Institute of Technology*

Dr. Alberto Fernandez-Nieves
School of Physics
*Georgia Institute of Technology*

Dr. Zhiqun Lin
School of Materials Science and Engineering
*Georgia Institute of Technology*

Dr. Paul S. Russo
School of Materials Science and Engineering
*Georgia Institute of Technology*


Date Approved: February 24, 2021

*Dedicated to my family*

# ACKNOWLEDGEMENTS

I would like to start by thanking my academic advisor Prof. Vladimir V. Tsukruk for providing me with the opportunity to pursue my PhD under his supervision. His guidance, patience, and encouragement have all served as an invaluable source of motivation in moving me forward in both my academic and personal pursuits. He has consistently shown confidence in my abilities even when I would doubt myself, and for this I cannot express enough appreciation. I likewise thank Prof. Alexei P. Sokolov for supporting me during my time at ORNL. Throughout the challenges encountered in my graduate career, I have been fortunate enough to receive instruction and insight from two incredibly inspirational advisors. Furthermore, I thank Prof. Blair K. Brettmann, Prof. Zhiqun Lin, Alberto Fernandez-Nieves, and Prof. Paul S. Russo for agreeing to serve on my committee, offering their support, sharing their expertise and suggestions, and for sticking with me on this long journey.

I would also like to acknowledge our collaborators in this project: Prof. Constantinos Tsitsilianis (University of Patras, Greece), Prof. V. Shevchenko (National Academy of Science of Ukraine, Ukraine), and Prof. Krzysztof Matyjaszewski (Caranegie Mellon University) and their respective research groups for providing us with the fascinating polymer materials which have motivated this research. In addition, I thank Dr. John Ankner from ORNL for his guidance in conducting the neutron reflectivity measurements and for his invaluable assistance in analyzing the results. It has been a humbling experience and a pleasure to work with these excellent scientists who were generous in sharing their expertise.

I thank all my peers and mentors both in SEMA Lab at Georgia Tech and from the Chemical Sciences Division at ORNL. In particular, I extent special thanks to Dr. Weinan Xu, Dr. Volodymyr F. Korolovych, Dr. Vera Bocharova, Dr. Pengfei Cao, Hansol Lee, Michelle Krecker, Sheng Zhao, and Sirui Ge for all of their instruction, helpful discussion,

and technical assistance. I have learned much from studying and working alongside so many talented and knowledgeable individuals.

The research in this dissertation was made possible due to financial support from the Division of Materials Research of the National Science Foundation in addition to the Materials Sciences and Engineering Division of the U.S. Department of Energy. Neutron scattering measurements were performed at the Spallation Neutron Source at ORNL and I appreciate the Neutron Scattering Directorate for providing us the beam time for these experiments. I want to also thank the Georgia Tech staff working within the MSE graduate office for their extensive support and guidance.

Finally, I am infinitely grateful for the boundless support and love I receive from my parents. They have been there for me through all my accomplishments and struggles, always showing an active interest in my life with more care than I could ever ask for.

# TABLE OF CONTENTS

# LIST OF TABLES

# LIST OF FIGURES AND SCHEMES

# LIST OF SYMBOLS AND ABBREVIATIONS

| | |
|---|---|
| $a_T$ | Horizontal Shift Factor |
| $B$ | Pseudoactivation Energy |
| b | Statistical Monomer Length |
| $c$ | Concentration of Free Charge Carriers |
| $C^*$ | Complex Capacitance |
| $C_0$ | Vacuum Capacitance |
| $C_p$ | Specific Heat Capacity |
| $D$ | Diffusion Coefficient, Strength Parameter |
| $\delta$ | Phase Angle Shift |
| $\varepsilon^*$ | Permittivity |
| $\varepsilon_\infty$ | Permittivity at the High-Frequency Limit |
| $\Delta\varepsilon$ | Dielectric Relaxation Strength |
| $E_a$ | Activation Energy |
| f | Number of Star Polymer Arms |
| $f$ | Frequency |
| $G^*$ | Shear Modulus |
| $\Gamma$ | Surface Coverage |
| $h$ | Film Thickness |
| $i$ | Current |
| $J_{eq}$ | Steady-State Compliance |
| $k_i$ | Incident Neutron Propagation Vector |
| $k_0$ | Reflected Neutron Propagation Vector |
| $\lambda$ | Wavelength |
| $l_B$ | Bjerrum Length |

| | |
|---|---|
| $M^*$ | Electric Modulus |
| $m$ | Fragility Index |
| $N$ | Degree of Polymerization |
| $N_{arm}$ | Star Polymer Arm Degree of Polymerization |
| $N_{span}$ | Star Polymer Span Degree of Polymerization |
| $\mu$ | Ionic Mobility |
| $\eta$ | Viscosity |
| $\omega$ | Angular Frequency |
| $\phi$ | Volume Fraction |
| $\pi$ | Surface Pressure |
| $q$ | Charge |
| $R$ | Reflectivity |
| $R_F$ | Fresnel Reflectivity |
| $R_g$ | Radius of Gyration |
| $R_e$ | Polymer Chain End-to-End Distance |
| $R_\tau$ | Decoupling Ratio |
| $R_q$ | Surface Roughness |
| $\rho$ | Scattering Length Density |
| $P$ | Mass Density |
| $\sigma$ | Interfacial Width |
| $\sigma^*$ | Complex Conductivity |
| $\sigma_{dc}$ | Direct Current Conductivity |
| $\sigma_0$ | Conductivity at Infinite Temperature |
| $T$ | Temperature |
| $T_g$ | Glass Transition Temperature |
| $T_0$ | Vogel Temperature |

| | |
|---|---|
| $T_r$ | Reference Temperature |
| $T_x$ | Dynamic Crossover Temperature |
| $\theta$ | Incident Scattering Angle |
| $\tau$ | Time Constant |
| $\tau_\alpha$ | Alpha Relaxation Time |
| $\tau_\beta$ | Beta Relaxation Time |
| $\tau_{\sigma,dc,ion}$ | Conductivity Relaxation Time |
| $\tau_0$ | High-Temperature Time Constant |
| $\tau_r$ | Terminal Relaxation Time |
| $\tau_s$ | Segmental Relaxation Time |
| $t_+$ | Transference Number |
| $Q$ | Wave Vector Transfer |
| $Q_c$ | Critical Reflection Wave Vector Transfer |
| $Z^*$ | Impedance |
| AFM | Atomic Force Microscopy |
| ATRP | Atom Transfer Radical Polymerization |
| BCD | β-cyclodextrin-14Br |
| BDS | Broadband Dielectric Spectroscopy |
| BNN | Barton, Nakajima, and Namikawa (Relation) |
| CC | Cole-Cole (Function) |
| CD | Cole-Davidson (Function) |
| CVFF | Consistent-Valence Force-Field |
| DP | Degree of Polymerization |
| DSC | Differential Scanning Calorimetry |
| FFT | Fast Fourier Transform |
| GPC | Gel Permeation Chromatography |

| | |
|---|---|
| HBP | Hyperbranched Polyester |
| HN | Havriliak-Negami (Function) |
| Im | Imidazolium |
| FTIR | Fourier Transform Infrared Spectroscopy |
| LB | Langmuir-Blodgette |
| LBL | Layer-by-Layer |
| LCST | Lower Critical Solution Temperature |
| LVE | Linear Viscoelastic |
| MMA | Mean Molecular Area |
| MW | Molecular Weight |
| NR | Neutron Reflectivity |
| P2VP | Poly(2-Vinylpyridine) |
| PAA | Poly(Acrylic Acid) |
| PDI | Polydispersity |
| PEI | Poly(Ethyleneimine) |
| PEM | Polyelectrolyte Multilayer |
| PNIPAM | Poly(N-Isopropylacrylamide) |
| PolyIL or PIL | Polymerized/Polymeric Ionic Liquid or Poly(Ionic Liquid) |
| POSS | Polyhedral Oligomeric Silsesquioxane |
| PS | Polystyrene |
| PSD | Power Spectral Density |
| PSS | Poly(Styrenesulfonate) |
| RBM | Random Barrier Model |
| SA-LbL | Spin-Assisted Layer-by-Layer |
| SANS | Small Angle Neutron Scattering |
| SAOS | Small Angle Oscillatory Shear |

| | |
|---|---|
| SE | Spectroscopic Ellipsometry |
| SGQP | Star-Graft Quarterpolymer |
| SLD | Scattering Length Density |
| TA | Tannic Acid |
| TFSI or $TF_2N$ | Bis(trifluoromethane)sulfonimide |
| TGA | Thermogravimetric Analysis |
| tTS | Time-Temperature Superposition |
| UCST | Upper Critical Solution Temperature |
| VBBI | 1-(4-Vinylbenzyl)-3-Butylimidazolium |
| VFT | Vogel-Fulcher-Tammann (Equation) |
| vGP | Van Gurp-Palmen (Plot) |
| WLF | Williams-Landel-Ferry (Equation) |
| XRD | X-Ray Diffraction |

# SUMMARY

Polymers containing ionic groups such as polyelectrolytes and polymerized ionic liquids are promising candidates for the design of organized ionically conductive media due to their controlled morphology, robust chemical and thermal stability, and single-ion conductivity. However, while polymerization of ionic groups affords electrolytes a greater degree of dimensional control, the effect of nonlinear chain architecture remains mostly an unexplored consideration, despite the unique functional group densities, chain conformations, counterion condensation, and dynamics of branched polymers.

First, the stimuli-responsive interfacial assembly and tunable morphologies of star-shaped polyelectrolyte block-copolymers and polymerized ionic liquids in monolayers and multicomponent systems are examined. In the former case, a dual-responsive star-graft block-quarterpolymer with variable arm number, arm length, and grafting density are integrated into hydrogen-bonded multilayer films and their morphologies were evaluated in different environments using surface probe microscopy and neutron reflectivity. The results point toward the amphiphilicity endowed by the star-graft architecture as the chief factor controlling the temperature and pH-induced conformational changes which lead to the diverse star-like clustering at the molecular scale. Likewise, the surface organization of linear and star-shaped polymerized ionic liquids in monolayers and multilayers is compared under variable adsorption conditions for polymers with the different branching architectures. Both studies demonstrate how polyelectrolytes and polymerized ionic liquids with branched architecture assemble into multilayer films with variable porosity, thickness, and textured morphologies featuring compartmentalized internal structure that are remarkably distinct from traditional multilayer systems.

The second part of this work focuses on the ion transport in polyelectrolytes comprised of star and hyperbranched polymerized ionic liquids. Long-chain arms were found to exhibit more sluggish and elastic dynamics at longer timescales while the glass transition temperature, rates of segmental relaxation, ion disassociation, and dc conductivity were similar regardless of the polymer architecture and arm length. But when polymerized ionic liquids are branched on a smaller scale, such as in the ionic liquid tethered macromolecules

consisting of both POSS and hyperbranched polyester cores, considerable shifts in the glass transition temperatures and conductivities were observed.

This ability to control the ion mobility in polymerized ionic liquids near the $T_g$ is critical for the development of solid-state electrolytes in which it is desirable to have high conductivities in the glassy state. Overall, this dissertation provides an initial view of branched polymer electrolytes as uniquely versatile nanomaterials in the assembly of multifunctional polymer electrolytes with tunable morphologies and controlled ion transport properties.

# CHAPTER 1. INTRODUCTION

## 1.1 Motivation

The growing demand for clean, affordable, and sustainable electrochemical energy storage and harvesting technologies has spurred great interest in new electrolyte materials with tunable properties and multifaceted functionality.[1] Development of such materials is critical to meeting the requirements for new energy sources and storage devices with high energy density, long and stable cycle life, and low maintenance to be safely used not only in portable electronics, wearable devices, sensors, medical implants, and electric vehicles, but also in large-scale grid-energy storage systems and load-levelling for energy produced from intermittent renewable sources (e.g., wind and solar energy harvesting).[2,3,4,5,6] Current electrolyte media are often based on organic liquids which have high conductivity ($10^{-1}$ to $10^{-3}$ S $cm^{-1}$) but are toxic and flammable, possess a limited electrochemical stability window, are difficult to process and package, and are susceptible to leakage, degradation, and thermal runaway at high temperatures.[7]

As a result, solid-state electrolytes have emerged as a promising alternative to the traditional fluid-based electrolytes. Inorganic solid electrolytes, for example, include amorphous glasses and crystalline ceramics such as the oxide-type, sulfide-type, and sodium superionic conductor materials.[2] They are generally metal-based and tend to be brittle and expensive.[5] These ionic conductors excel due to their large elastic moduli and good electrochemical stabilities which are necessary for preventing parasitic reactions (e.g., the growth of metallic dendrites) that lead to short-circuiting, rapid discharge, and other catastrophic failures.[8,9] Moreover, these ceramic materials boast high conductivities comparable to those of organic liquid electrolytes. However, their inflexibility, hypersensitivity to moisture/oxygen, and issues concerning large volume changes and charge-transfer resistances at the rigid separator/electrode interfaces have precluded their wide-spread adoption in electrochemical devices.[2,3]

In contrast, soft, viscoelastic electrolytes are light-weight, flexible, and more adaptable as electrode contacts; their compliant nature allows them to accommodate the large stresses

produced by the cyclic swelling and deswelling throughout electrochemical processes or during mechanical actuation.[5,10] These solid-state electrolytes are composed of macromolecular or nanoparticle 'building blocks' whose interactions and correlations can be tailored synthetically, thereby allowing for the modular assembly of intricate microstructures with unique emergent properties. Polyelectrolytes are particularly interesting components in this regard due to the variability of their charged monomer chemistry, molecular weight, and chain architecture; adjusting these parameters enables the tuning of shear modulus, water retention, gas permeability, glass transition temperature, dielectric constant, and so on. Hence, polymer electrolytes have garnered considerable interest due to their convincing advantages as a light-weight, non-volatile, non-toxic, non-flammable, flexible, and safer alternative to liquid electrolytes.[11] But because ion dynamics are generally linked to the slow structural relaxation rates of covalently linked chains, the ion mobility and conductivity are greatly depressed in these materials (~$10^{-6}$ S $cm^{-1}$ for dry, single-ion conductors).

A distinguishing feature of polymer materials, in contrast to traditional condensed matter, is that the characteristic length scales of polymer microstructures is quite large, giving rise to substantial response functions with multiple relevant timescales.[12,13] The complexity of these novel soft materials requires extensive collaboration between synthetic chemistry, materials assembly and fabrication, and physical characterization in order to elucidate the connection between molecular structure, responsive assembly, morphology, dynamics, and phase states. A central objective is to understand how these relationships can be controlled to program the multifunctional properties of these emerging materials. Achieving this, a comprehensive approach to engineering polymer electrolytes can be understood in order to expedite the upcoming revolution in energy storage materials.

## 1.2 Polymer Electrolytes: Physical Properties and Responsive Morphologies

### *1.2.1 Polyelectrolytes*

Polyelectrolytes are polymers composed of ionizable repeat units (Figure 1.1).[14,15,16] The unique properties exhibited by polyelectrolytes are due to the electrostatic effects of the ionic groups, which may exist in associated or dissociated states. As a result, the chain

conformations and properties of polyelectrolytes depend significantly on the ionization of repeat units, molecular charge, osmotic pressure, and the entropy of free counterions (or conversely, their association into ion pairs and larger aggregates)—in addition to the standard interactions governing the behavior of neutral polymers in solutions and melts, such as excluded volume and hydrogen-bonding interactions.[15,17,18,19,20,21]

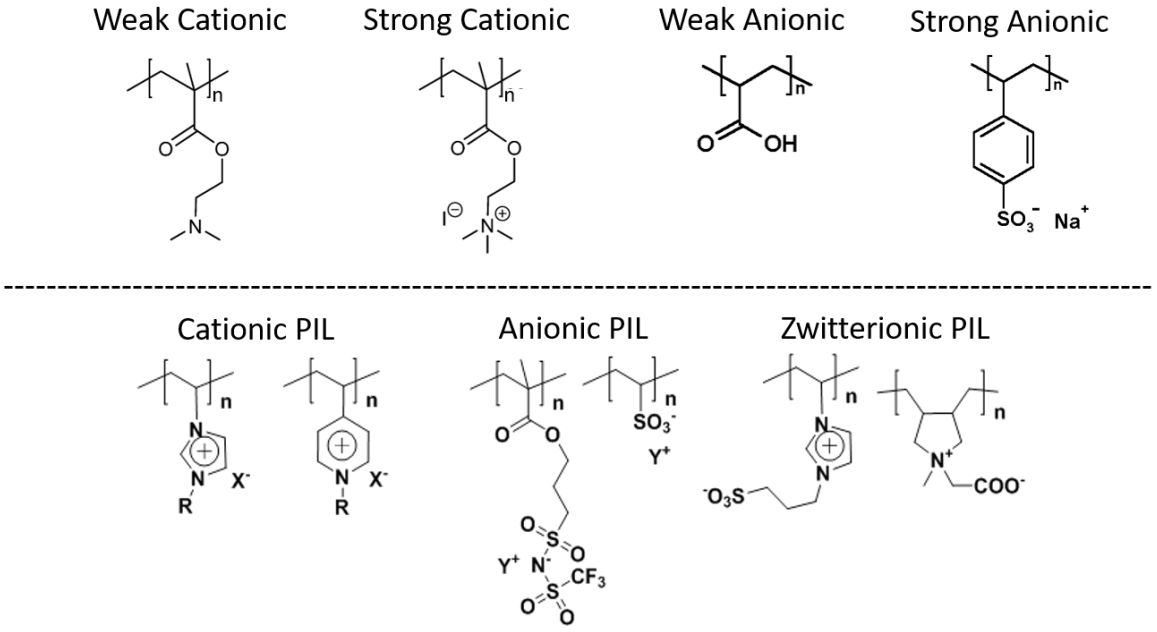


**Figure 1.1.** Molecular structures of several example polyelectrolytes (top) and poly(ionic liquid)s (bottom).

The extent to which the ions are dissociated in polyelectrolytes depends on both the ionic chemistry in addition to the polarity of the polymer medium.[22] The Bjerrum length $l_B$ specifies the separation at which the electrostatic interaction between two ions is comparable to the thermal energy $kT$ of the electrolyte. If the charge density is high enough such that the separation between ionizable groups is smaller than $l_B$, counterions condense onto the polymer chain, thereby lowering the electrostatic energy of the polyelectrolyte at the cost of a smaller translational entropy of the counterions.[23] The charge density can be varied, for example, by synthetically introducing neutral blocks or strongly dissociated polyelectrolyte groups in copolymers, or alternatively by adjusting the pH of polyelectrolytes consisting of weak acids and bases (Figure 1.1).

Polyelectrolytes with low ion content are generally known as ionomers and possess characteristics typically found in thermoplastic elastomers wherein the association and dissociation of ionic groups form the basis of thermally reversible networks.[24,25,26] As the ionic density increases, strongly associated ions can exist in a variety of condensed states, including ion pairs, quadrupoles, or larger ion aggregates. This can result in the segregation of a polar ion-rich or ionophilic phase from the nonpolar polymer phase.[27]

The organization of these two phases can have a substantial impact on the physical properties of the polyelectrolyte. Intermolecular dipole-dipole associations and the presence of ion-rich aggregates reinforces the thermomechanical properties, for example, by increasing the melt viscosity, the elastic modulus, and/or the glass transition temperature $T_g$ of the polyelectrolytes.[22] Moreover, the overlapping of polarizability volumes associated with ionic groups causes the electrostatic interactions and ion mobility to be more correlated to the segmental motions of the polymer chain while broadening the relaxation mode distribution.[27,28] The charge density, ionic dissociation, and resulting morphologies thus have a significant impact on the viscoelasticity, glass transition, phase behavior, and ion transport in polyelectrolyte materials.[24]

### *1.2.2 Polymerized Ionic Liquids*

Whereas typical molecular electrolytes consist of smaller ion salts that need to be dissolved in aqueous or organic solutions, ionic liquids (ILs) are organic/inorganic salts which are unique in that their large bulky ions tend to have delocalized charge and thus exhibit much weaker, non-directional coulombic interactions. As a result, ILs have lower energies of association and generally exist as disordered, concentrated electrolyte fluids at room temperature.[6,29] Originally used as nonvolatile solvents in green chemistry due to their high polarity and solvating characteristics, ILs are now finding widespread use towards electrochemical applications as a result of their enhanced chemical and thermal stability, low flammability, low vapor pressure, high ionic charge density and conductivity, high catalytic activity, and diverse set of accessible chemical compositions with tunable basicity/acidity and polarity.[30,31]

Polymerized/polymeric ionic liquids or Poly(ionic liquid)s are an important subclass of ionic polymers that exploit IL chemistry in the repeat unit along the polymer chain, thereby leveraging the advantageous functional properties of ILs with the synthetic tunability, versatile and facile processability, and viscoelasticity of polymers.[32,33,34,35] For example, polymerization of ILs produces a sharp increase in electroresponsivity of rheological fluids[36], enhances the mechanical stability of gas separation membranes[37], improves the anti-wear properties of lubricating greases[38], and increases ionic dissociation and molar conductivity[39]. Furthermore, while most polyelectrolytes exist as glassy solids at room temperature, many PolyILs are distinct in that their weak, relatively non-directional coulombic attractions between the bulky ion-pairs typically depresses their glass transition temperature.[32,35]

Due to the fact that one of the ions in the IL pair is tethered to the polymer chain, PolyILs are distinct from their molecular counterparts in that the mobility of one ion is promoted over that of its oppositely charged counterpart. This effect has profound consequences towards the polarization and flow of charge within the electrolyte medium. For example, immobilization of one of the charged species within a PolyIL results in a high transference number, uniform electric fields at electrode interfaces, and an enhanced electrochemical stability against metal electrodes thereby improving the cycling stability in batteries (Figure 1.2).[40,41] In addition, when there is a large size disparity between each ion in the pair, the motion of the free counterion in response to an electric potential can generate internal stresses of a PolyIL film for actuation.[42] In ionic thermoelectric materials, the sign and magnitude of the Seebeck coefficient is determined by which ion is free to respond to the applied thermal gradient.[43]

### *1.2.3 Structure and Stimuli-Responsive Organization*

The structural complexity of the relatively large ions in ILs renders them amenable to a variety of intermolecular attractions ranging from the nondirectional, nonspecific van der Waals and solvophobic interactions to the stronger and more directional Coulombic, hydrogen bonding, and dipole-dipole forces.[44] Together, these interactions promote the segregation of polar and nonpolar components as well as local arrangements into

supramolecular clusters, hydrogen bonded networks, and micellar or bicontinuous morphologies.

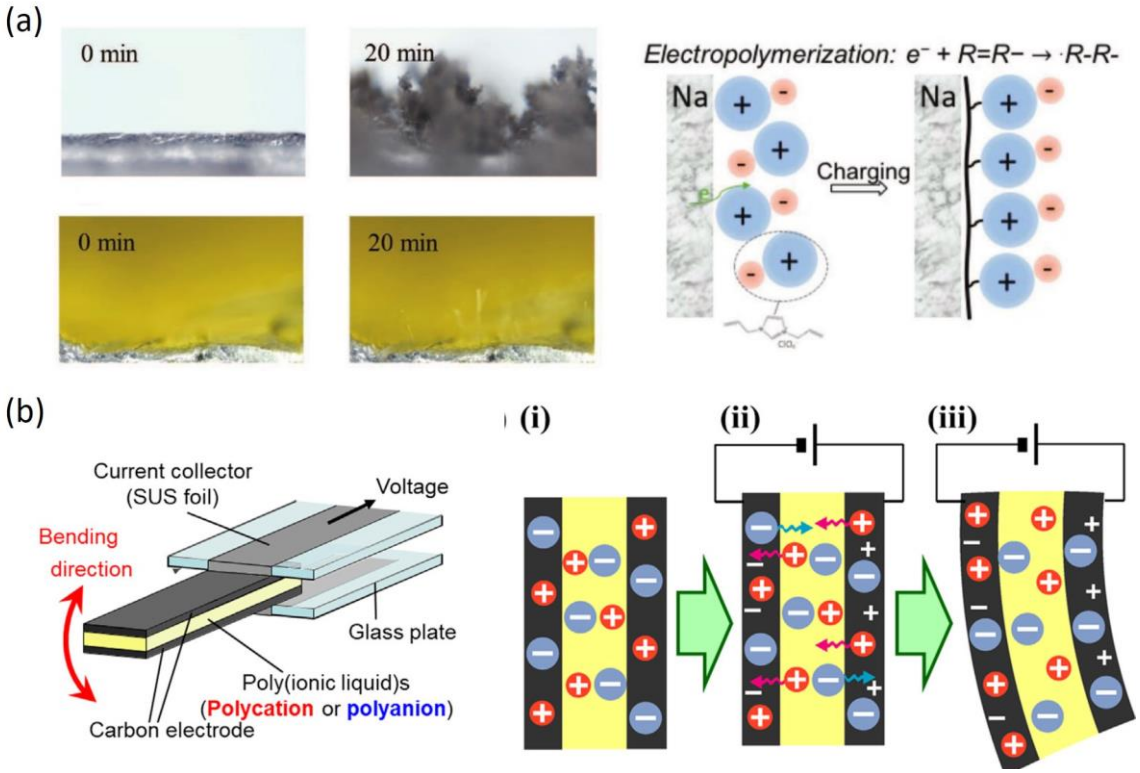


**Figure 1.2.** Advantages of single-ion conductivity. (a) The electrochemical sodium deposition in a traditional electrolyte results in pronounced metallic dendrites (top left) whereas the in-situ polymerization of ionic liquids at the electrode interface stabilizes the electrode interface (bottom left). A schematic drawing illustrates formation of the PolyIL film throughout the charging process (right).[40] (b) The disparity in ion size and mobility in PolyILs produces mechanical actuation during the charging of the electric double layer.[42]

In some cases, polymerization can simply improve the mechanical properties while preserving the original IL morphology. Liquid crystal mesogens that contain IL moieties, for example, can first be assembled and then subsequently photopolymerized to produce stable anisotropic films with 1-D ion conductive channels.[45,46] Alternatively, the covalent connectivity can add another layer of complexity to the association and morphology of hierarchical PolyIL assemblies. Yuan et al. reported PolyIL nanoparticles which not only possessed a highly ordered inner structure that could be tuned by the length of alkyl chains in the cationic pendant group, but also exhibited superstructural assembly into nanoworm mesostructures.[47]

When the functional properties of ILs are integrated into PolyILs via polymerization, the resulting polymer chain can exhibit dramatic changes in conformation in response to external stimuli.[29] In particular, the compositional diversity of ILs allows for a wide range of stimuli-responsive changes to PolyIL assemblies via counterion exchange. For example, exchanging a small water-soluble bromide in PolyILs with the large, organic bis(trifluoromethane)sulfonimide (TFSI) counteranion corresponds to a shift from hydrophilic to hydrophobic character and the formation of vesicles and micelles in aqueous solution.[48] Exchanging the Br anions in achiral PolyILs with chiral amino acids triggers the transformation into double-helix bundles with chiroptical properties.[49] Conversely, exposing PolyILs with fixed ions to different solvents can also facilitate the restructuring of their assembled morphologies.[48] Block copolymers subjected to solvent exchange can yield even more complex microstructures, such as bicontinuous cubosomes (Figure 1.3).[50]

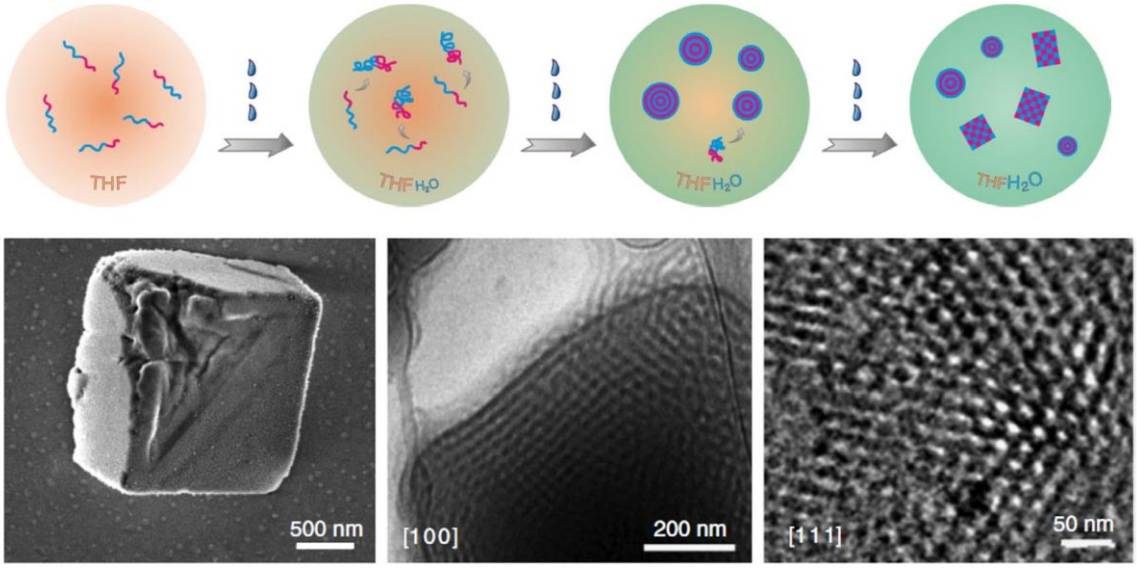


**Figure 1.3.** (a) Schematic illustration of the self-assembly of cubosomes from a PolyIL block copolymer upon the solvent exchange to aqueous solution. (b) Electron microscopy of the bicontinuous morphology.[50]

Furthermore, application of an external field such as an electric potential to PolyIL films can result in mechanical actuation and/or unique electrowetting effects wherein the hydrophobicity of the surface is reversibly tuned.[42,51] Of course, PolyILs can be responsive to more than one stimuli at once: hydrogels composed of PolyILs with alternating ferrocene units and tetraalkylphosphonium sulfonate pendants are redox-active and possess a lower critical solution temperature (LCST) with unusual hysteretic volume-phase transitions that

are potentially useful towards thermal memory applications.[52] In addition to solvent[53] and temperature[54], materials based on PolyIL are also known to be responsive to pH[55,56,57], light[58] , and $CO_2$[59].

### *1.2.4 Viscoelasticity and Ion Transport*

Ion transport is not only relevant towards the operation of batteries and other energy storage and harvesting devices, but also governs the behavior of electrolyte materials in sensors, actuators, and others. When a static electric field is applied to a polymer electrolyte, the free ions will migrate and contribute to the direct current conductivity $\sigma_{dc}$:

$$\sigma_{dc} = \sum_{i=1}^{n} c_i \mu_i |q_i| \qquad (1.1)$$

where $c_i$, $\mu_i$, and $|q_i|$ are the effective concentration of free charge carriers, ionic mobility, and magnitude of charge for each conducting species *i*. For diffusion-controlled conductivity, the mobility is

$$\mu_i = \frac{q_i D_i}{T} \qquad (1.2)$$

where $T$ is the absolute temperature and $D_i$ is the diffusion coefficient. In Equation 1.1, the transport of both positive and negative charges contributes to the conductivity. In most practical applications, only the motions of one charge carrier are of interest. To distinguish the contribution of the charge carrier of interest, the ratio of the current carried by this particular species (in this case the cation) to the total measured current is quantified as the transference number:

$$t_+ = \frac{i_+}{(i_+ + i_-)} = \frac{i_+}{i} \qquad (1.3)$$

Because structural relaxations "freeze" when polymers melts are cooled to their $T_g$, there has been considerable interest in understanding the coupling—or lack thereof—between structural/segmental and ion conductivity relaxation times ($\tau_\alpha$ and $\tau_{dc}$, respectively) in polyelectrolytes and PolyILs (Figure 1.4).[7,12,60,61,62,63,64,65,66,67] This question has important implications on transport: the conductivity will drop dramatically at lower temperatures in coupled systems because the segmental motions governing ionic mobility are frozen-out in

the glassy solid. In contrast, the mobility of ions surpasses the structural motion of the polymer matrix in decoupled systems, potentially allowing for fast transport in room temperature solid-state electrolytes.

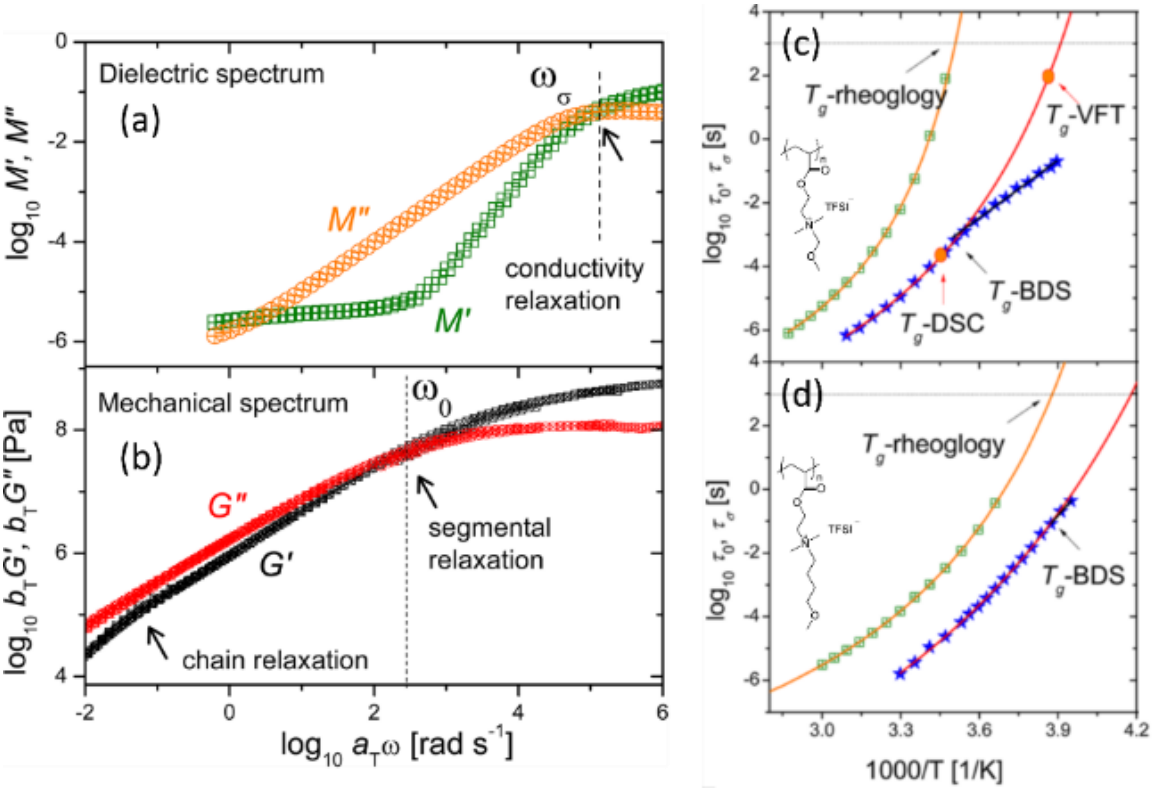


**Figure 1.4.** The conductivity and structural relaxation times $\tau_{dc}$ and $\tau_{\alpha}$ are obtained from dielectric (a) and mechanical (b) measurements, respectively. In dynamically decoupled systems (c), there is a transition in $\tau_{dc}$ from VFT to Arrhenius $T$-dependence at $T_g$. For coupled electrolytes (d), the $T$-dependencies of $\tau_{dc}$ and $\tau_{\alpha}$ both follow similar behavior.[72]

The ion transport in many traditional polymer-based electrolytes is coupled to the structural motions of the conducting media.[68] In such cases, the time corresponding to the onset of long-range ion diffusion will increase ($\sigma_{dc}$ decreases) exponentially as the system temperature approaches some finite $T_0$, known as the Vogel temperature. $\sigma_{dc}$ and $\tau_{dc}$ are usually related to $T$ by the Vogel-Fulcher-Tammann (VFT) equations:

$$\tau_{dc} = \tau_0 \exp\left(\frac{DT_0}{T-T_0}\right) \qquad (1.4)$$

$$\sigma_{dc} = \sigma_0 \exp\left(\frac{-DT_0}{T-T_0}\right) \qquad (1.5)$$

where $\tau_0$ and $\sigma_0$ are the time constant and conductivity in the high temperature limit, and $D$ is a material-specific strength parameter inversely related to the dynamic fragility.[69] Note that Equation 1.5 predicts a divergence in the conductivity at $T = T_0$, which is not representative of the behavior of real electrolytes. Alternatively, in ion motions exhibiting a temperature "activated" transport mechanism that is decoupled from the structural relaxation of the electrolyte, $\tau_{dc}$ and $\sigma_{dc}$ are given by their respective Arrhenius equations:

$$\tau_{\mathrm{dc}} = \tau_o \exp\frac{E_{\mathrm{a}}}{T} \qquad (1.6)$$

$$\sigma_{\mathrm{dc}} = \sigma_o \exp\frac{-E_{\mathrm{a}}}{T} \qquad (1.7)$$

where $E_a$ is the activation energy of the process.

Flexible, 'strong' glass-formers such as $Li^+$ conducting poly(ethylene oxide) (PEO) are good examples of coupled systems.[68] Additionally, most aprotic ILs are coupled at high temperatures[61,70] and show a weak decoupling of self-diffusion from structural dynamics at lower temperatures closer to the glass transition.[71] On the other hand, systems possessing a conductivity which is strongly decoupled from the structural relaxation of the molecular framework include rigid/fragile polyelectrolytes, some protic ILs, and PolyILs. Ion transport in such cases tends to be described by an ion dissociation/rearrangement and intra-/intermolecular hopping mechanism.[63] These electrolytes are typified by a pronounced transition in their temperature-dependent conductivity from VFT (super-Arrhenius) to Arrhenius character (Figure 1.4).[61,72,73,74]

The significance of the latter group of electrolytes is in their potential to demonstrate high conductivities at low temperatures. This is emphasized in a double logarithmic plot of the molar conductivity vs. the rate of segmental motion (the modified Walden plot, Figure 1.5a).[72,73] In the so-called superionic regime, the ion diffusion is considerably faster than the rate of segmental relaxation, especially at lower temperatures. Subtle changes in the polymer structures, such as increasing the flexible pendant groups, molecular weight, or multivalent ion concentration are enough to transform the system dynamics from coupled to decoupled.[65,72,73] The advantage of designing electrolytes with decoupled dynamics is

the possibility of improving $\sigma_{dc}$ while simultaneously reinforcing the mechanical properties (Figure 1.5b).

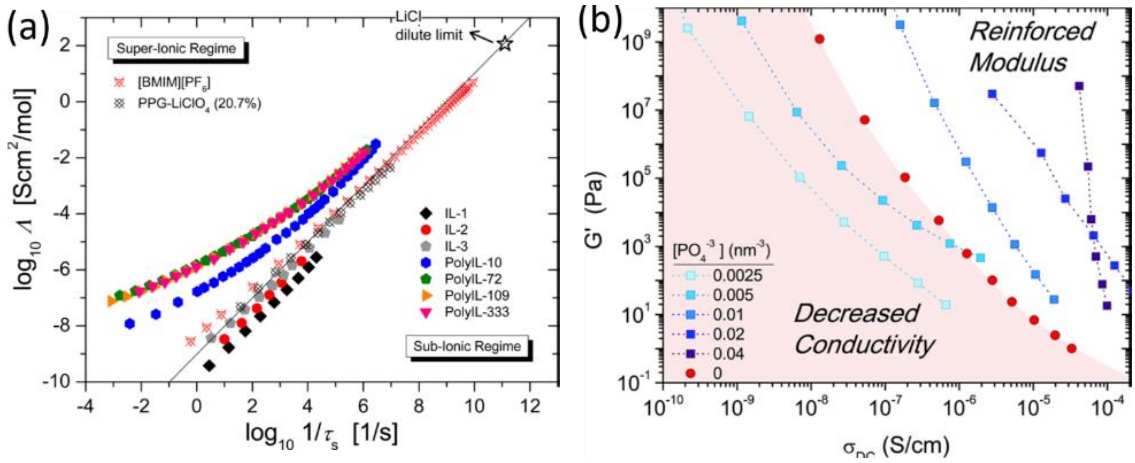


**Figure 1.5.** Aspects of decoupled single-ion conducting PolyILs. (a) A modified Walden plot for ILs and PILs with different molecular weights. PolyILs show positive deviations in the superionic regime.[73] (b) Incorporation of trivalent counterions promote decoupled ion conduction with a simultaneously "reinforced modulus".[65]

## 1.3 Branched Multifunctional Polymers

### *1.3.1 Nonlinear Polymer Architectures*

Polymerization covalently connects monomers into long chains and imparts viscoelasticity and other emerging properties in the melt. To further tune these properties, synthetic chemists have explored polymer backbone configurations beyond that of linear chains. Given the importance of free ion concentrations and the coupling/decoupling of conductivity and structural relaxations, nonlinear polymer topologies are interesting due to their anomalous packing, free volume, tunable glass transition, and ion confinement.[75,76,77,78,79,80] Hierarchical control is established by integrating charged monomers into complex architectures in which different branches, arms, blocks within arms, grafts, and terminal groups can express different functionalities.[14,81,82,83] As recent advances in polymer chemistry have led to the synthesis of both homogenous and heterogeneous hyperbranched[84,85,86], star[87,88,89,90,91], dendritic[92], tadpole and barbell-shaped cyclic[93], pearl-necklace[94], and other multiblock compartmentalized comb/graft brush polymers[14,95,96,97,98], precise control over the configuration, composition, and architecture

of polymers is now a feasible and promising approach to optimizing structure-property relationships of these materials (Figure 1.6).[14,99,100]

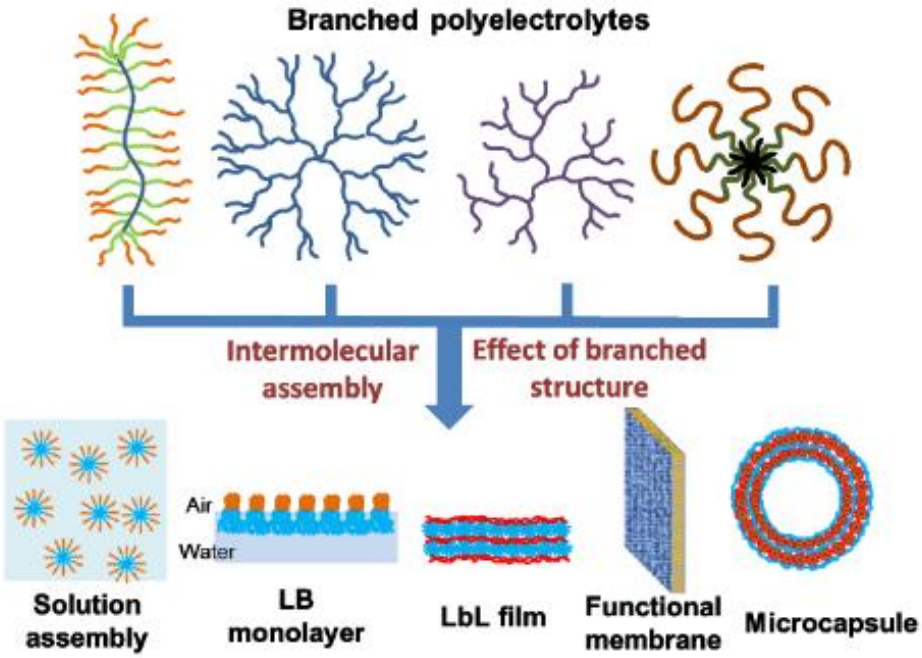


**Figure 1.6.** Examples of branched polyelectrolytes and their self-organization into nanostructures.[14]

As the ratio of arm number to arm molecular weight $f/MW_{arm}$ increases, a branched macromolecule behaves less like a tenuous coil or rod and more like a soft, deformable particle.[82,101,102,103,104,105] Moreover, highly branched macromolecules exhibit distinct packing and chemical properties due to the high concentration of functional terminal groups confined within their compact shape combined with a low level of entanglements.[106,107] In particular, the density of functional groups, chain tension, and excluded volume are amplified near branch points.[76,108,109] In addition, branching introduces intramolecular dynamic heterogeneity in the form of strong segmental confinement at the branch point (nodes).[110,111,112] A high degree of branching imparts a three-dimensional architecture which can result in a lower viscosity in solution or in the molten state. [92]

The crowded monomer packing increases the energy gain upon adsorption to non-repulsive interfaces whereas the inherently stretched arm conformations minimize the associated entropic penalty. These features are responsible for promoting the migration of branched

polymers to external interfaces—even in the case of repulsive monomer-surface interactions—thereby locally altering the morphology, phase separation, and aging behavior.[75,113,114,115] This can lead to a decrease in the free volume at interfaces and hence slower dynamics—the opposite effect of what would be expected for linear chains (Figure 1.7).[104,110] Nonlinear architectures therefore promote surface confinement effects in addition to accommodating efficient packing densities.

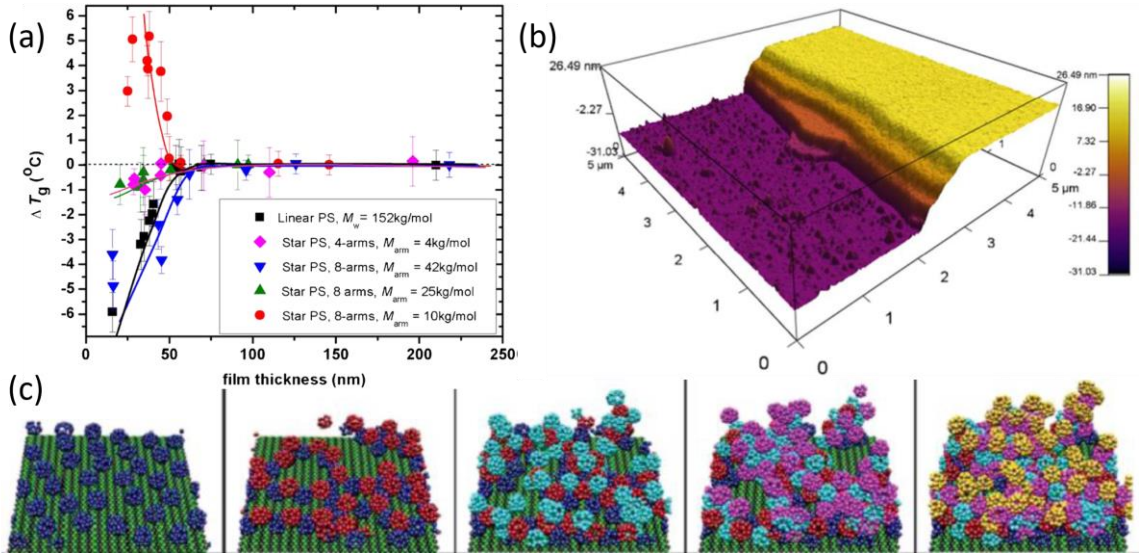


**Figure 1.7.** (a) Star polymers in thin films exhibit an increase in $T_g$ relative to the bulk state.[78] (b) Excluded volume repulsions guide the self-organization of stars into highly stratified layers across the film.[79] (d) The colloidal assembly of highly branched stars as functional nanoparticles generates compartmentalized microstructures.[80]

In the case of star polyelectrolytes, electrostatic forces introduce a strong counterion confinement (i.e. counterion condensation) effect that increases the osmotic pressure of the swollen molecular interior.[76,101,102] An entropic repulsion develops which limits the aggregation behavior as the molecules pack into more concentrated environments. Accordingly, substituting the counterions with multivalent ions can reduce the osmotic pressure and collapse the charged arms.[116,117] In block copolymer electrolytes, this manifests in block-specific swelling and the compartmentalization of hydrophilic and hydrophobic regions in the self-assembled structures which mimic the complexity of self-ordered systems in nature.[95] Among the notable assembled morphologies are nanoscale soft, patchy particles and unimolecular micelles in addition to their hierarchical microscale

and macroscale cylinders, vesicles, and interconnected, dendritic worm-like micellar morphologies.[118,119,120]

Furthermore, the peculiar assembly behavior of branched polymers are known to result in a wide range of unique properties. For instance, the supramolecular assembly of hyperbranched polytriphenylmethanols into micelles and compound micelles results in the restricted intramolecular rotation of phenyl groups, thereby allowing for unique aggregation-induced emission with tunable intensity and emission colors beyond that achieved from the linear triphenylmethanol polymer.[85] Dendronized wedge polymers which adopt cylindrical conformations have been reported to phase separate, producing two distinct glass transition temperatures.[121] These examples demonstrate how intra- and intermolecular density, configurational entropy, chain rigidity, etc. can be tuned in order to control the conformation, association, vitrification, and dynamics of branched polymer electrolytes in the melt and at interfaces—without changing the monomer or substrate chemistries.

### 1.4 Emerging Broader Applications

Traditional molecular electrolytes face challenging hurdles in their integration into multifunctional materials due to complications associated with processing, packaging, and operation in the liquid state.[29] On the other hand, ionic polymers with nonlinear molecular architectures such as branched PolyILs are promising materials for the fabrication of ion-conductive membranes and solid-state electrolytes since they combine tunable viscoelastic properties with the intrinsic functional advantages of ionic liquids such as high chemical stability, low vapor pressure, nonflammability, and fast ion transport. Branched polymer electrolytes are not only anticipated to be able to assemble into a distinct, responsive morphologies, but the corresponding effect of nonlinear topologies on ionic conductivity in traditional salt-in-polymer electrolytes can be dramatic.[122,123] Hence, tuning the balance of interactions in branched polymer electrolytes is a viable route to achieving solid-state, nanostructured electrolytes with appreciable conductivity. As discussed above, this has immediate applications towards the ion-conducting media for more stable batteries, dye-sensitized solar cells, fuel cells, and thermoelectrics.[7,124,125]

However, tuning the ionic interactions and aggregated morphologies of PolyIL has other far-reaching implications beyond ion transport. For instance, tuning the alkyl spacer length within imidazolium-based PolyILs was demonstrated to influence the organization of nanoscale structural heterogeneity arising from the arrangement of ion clusters, which can be controlled to mitigate shockwave energy for impact-absorbing materials.[126] An example of how polymerization of ILs increases their processability and functionality is demonstrated in their implementation as 4D printing materials wherein PolyILs are 3D printed into smart materials whose shape can be further augmented in the presence of external stimuli.[127] Other responsive behavior of branched polymer electrolytes can find use in programmable dispersants for nanoparticles[128], stabilizing agents in nanoinks for scalable 3D printing[129], and switchable antifouling surfaces[130].

The catalytic activity and chemical affinity of the IL groups and controlled morphology of their polymerized forms have a myriad of important uses. For example, the synergistic effects of catalytic activity and the salting-out effect (phase separation) of PolyILs has been successfully exploited to accelerate the crystallization of open organic materials such as covalent organic frameworks[131]. Similarly, IL functionality in polymers has also found use in metal-free membranes for the capture and conversion of $CO_2$ emissions[132], recyclable materials for absorbing toxic heavy metal ions[133], gas separation membranes[134], heterogeneous nanocatalysts capable of realizing selective reactions in response to temperature change[135], biocompatible membranes with antimicrobial activities[136], and photothermal desalination materials[137]. Other applications arising from the extensive processing, shaping, and morphology control PolyILs have been demonstrated in electrosopun fibers and mats for carbonaceous frameworks[138], supramolecular photosensitive films[139], the stabilization of high-capacity supercapacitors[140], environmentally friendly agricultural additives[141], and many others.[32, 33, 34, 142, 143]

# CHAPTER 2. RESEARCH GOALS AND OVERVIEW

While branched polymers have exhibited intriguing thermomechanical properties and some architectural control over ion transport, little has been reported regarding star PolyILs with controlled arm length and the effects of the associated counterion confinement and entropic repulsions on electrolyte properties. Moreover, systematic approaches focused on unraveling the influence of branched polymer architecture on the molecular assembly and phase separation as well as on the mechanics and ion conductivity unique to dendrimer and hyperbranched polymers is still lacking. This highlights the need for a more integrative approach that starts at the architectural and functional design of the polymer building blocks and guides their self-organization into high-performance electrolytes by systematically tailoring their interactions to control charge transport.

## 2.1 Primary Objectives

The overarching goals of the work in this dissertation is twofold. **First**, it aims to unravel the role of molecular architecture and functional composition on the molecular interactions and interfacial organization of star-shaped polyelectrolytes and polymerized ionic liquids as mediated by external stimuli and spatial confinement. In particular, special attention is given to the effects of arm composition and length, arm number, and type of branching architecture of the multicomponent branched macromolecules on their global and local conformations and configurations, microphase state and molecular/ionic aggregation. These results are used to understand the self-assembly of branched macromolecules to higher-order nanomaterials by way of electrostatic and hydrophobic interactions, hydrogen bonding, osmotic pressure, microphase separation, and terminal group anchoring on uniform and heterogeneous surfaces. Then, morphology and stimuli-responsive behavior for the hydrophilic, hydrophobic, and amphiphilic branched polymers (e.g., to pH, temperature, and ion exchange) and the corresponding phase transitions at different interfaces, in unimolecular and aggregated micellar/vesicle states, and in hierarchical compartmentalized structures for highly functional membranes are investigated. Studies will differentiate the conformations, phase states, and responsive microstructures

assembled from the nonlinear polyelectrolytes and PolyILs from those of traditional linear polymers.

**Secondly**, the research evaluates the dynamic properties of branched ionic polymers as the active building blocks in polymer electrolytes, analyzing the mechanical and dielectric behavior in order to draw conclusions regarding the free volume, local/percolating mobility, and ion association in branched polymer electrolytes. Linear, star, and hyperbranched compounds are investigated in conjunction to arm length, branching generation, terminal group density, and ion chemistry with the aim of reconciling molecular architectures/functionality and tunable physical properties for controlling the coupling/decoupling of ion motions from structural relaxations and understanding the associated molecular-level transport mechanisms.

In short, this study evaluates global material properties by ascertaining the behavior of individual macromolecules and their "specialized" blocks, the same macromolecules in limited aggregated state and under influence of different interfacial factors, and finally, in their condensed state in the form of electrolyte films. The results are used to make conclusions on how polymer electrolytes can be synthetically tuned to achieve particular morphologies and dynamic properties. In this regard, the principles of organization for multifunctional branched polyelectrolyte and polymeric ionic liquids are developed in order to outline a new approach to engineering prospective electrolyte materials tailored for energy harvesting and storage, controlled delivery materials, chemical microreactors, smart surfaces, actuators, sensors, ion-exchange membranes, and so on.

## 2.2 Organization and Composition of Dissertation

**Chapter 1** provides a critical review of polymer electrolytes, emphasizing first the issues and pressing demands of the field which motivate the research constituting this PhD work. In this overview, traditional electrolyte chemistries are compared to the emerging class of polymerized ionic liquids, with special attention given to their guided molecular assembly, stimuli-responsive morphologies, viscoelasticity, and ion transport. Branched polymer architectures are then introduced as a route to modifying these important properties. Lastly,

a wide range of emerging applications for branched polymer electrolytes is discussed, linking back to the motivation of the work in this dissertation.

**Chapter 2** outlines the principal objectives of this dissertation in conjunction to the tasks undertaken to address these points. In addition, the content and general organization of the dissertation is briefly described in the context of two main parts: (1) the stimuli-responsive assembly of star-graft polyelectrolytes and star PolyILs and (2) the viscoelasticity and ion transport of star and hyperbranched PolyILs.

**Chapter 3** introduces the synthesis, molecular structure, and other related characteristics of the branched polymer electrolytes that are used throughout this work. This chapter then summarizes the general polymer processing and assembly techniques used in sample preparation, as well as the main characterization tools that are employed in examining the structural, thermomechanical, and dynamic properties of the samples.

**Chapter 4** reports the integration of heteroarm star-graft block-quarterpolymers with pH-sensitive weak polycationic/polyanionic arms and grafted thermo-responsive outer chains into hydrogen-bonded multilayers whose morphologies are distinct from those in traditional layer-by-layer assemblies. *In-situ* neutron reflectivity demonstrates how the block-specific swelling promotes heterogeneous partitioning of hydrophobic and hydrophilic reservoirs within the interior of the swollen multilayers. The discussion highlights the importance of molecular architecture and amphiphilicity balance in governing the aggregation of these functional “soft nanoparticles” into star clusters and how this internal reorganization and film swelling is regulated via solution pH and temperature. These hierarchically-structured dual-responsive films possessing tunable charge, porosity, and localized water retention/swelling expand the prospective capabilities of responsive hydrogen-bonded multilayers for targeted separations, programmable encapsulation/release, and ion transport.

**Chapter 5** presents the surface organization of a PolyIL comprised of the imidazolium/bis(trifluoromethane)sulfonimide ionic liquid pair polymerized into distinct architectures and different molecular weights. Due to the mixed polar and hydrophobic interactions of the PolyIL, its assembly at the air-water and air-solid interfaces is first

investigated via the formation of Langmuir monolayers and their subsequent Langmuir-Blodgett deposition. Secondly, the PolyIL is alternatively and sequentially co-assembled with poly(styrene sulfonate) via layer-by-layer assembly into unconventional multilayer films. The stimuli-responsive surface morphologies are evaluated in conjunction to macromolecular structure, adsorption conditions, and post-assembly treatment of the monolayers and multilayers. The discussion emphasizes the importance of both the ionic liquid counterion and branching architectures in guiding the assembly of films with variable porosity, thickness, and textured morphologies. The PolyIL assemblies explored in this study are relevant to the design of sophisticated coatings and nanostructured membranes with dynamically controllable permeability, encapsulation, and transport properties.

**Chapter 6** reports the viscoelastic and dielectric response of the linear and star-shaped PolyILs examined in Chapter 5 over a broad range of frequencies and temperatures and the results are evaluated in connection to the polymer architecture and morphology. At longer timescales, the arm dynamics of star PolyILs are demonstrated to be more sluggish and elastic relative to linear chains of comparable size. Yet at shorter timescales, long-chain branching is shown to have only secondary, more nuanced effects on the segmental and ion motions. Even so, all PolyILs ultimately exhibit nearly identical rates of segmental relaxation, ion disassociation, and dc conductivity over the investigated temperature range, regardless of polymer architecture. This study thus demonstrates how the disparity between chain, segmental, and ion dynamics in branched PolyILs can be exploited in the assembly of functional polymer electrolyte materials with divergent morphologies and controlled viscoelasticity properties, both of which can be tuned independently of ion transport.

**Chapter 7** expands upon chapter 6 by investigating a series of relatively smaller IL-based macromolecules with greater degrees of branching in regards to their dynamic properties and ion transport characteristics. Linear poly(ethylene oxide), hyperbranched polyester, and polyhedral oligomeric silsesquioxane core structures are functionalized with a variety of protic and aprotic IL chemistries and are examined to discern the influence of chain topology, core rigidity, and ion-pair interaction on the functional properties in the molten and glassy states. PolyILs with rigid, inorganic cores possess the highest glass transition

temperatures and lowest conductivities whereas those with the more flexible polyester cores have lower $T_g$s and faster ion transport. The decoupling of ion dynamics from the segmental process is evaluated based on the conductivity at the glass transition temperature $\sigma_{dc}(T_g)$, which shows the general significance of ion-pair interactions: functional groups comprised of ILs with highly directional electrostatic or hydrogen-bonding attractions exhibit ion transport that is more correlated to the segmental motions while pairs exhibiting weaker attractions resulted in more decoupled ion-segmental dynamics. Furthermore, the PolyIL branching and core structure had considerable effects on the dynamic behavior depending on the IL chemistry. Compounds with aprotic counterions show an increasing $\sigma_{dc}(T_g)$ with decreasing degree of architectural branching whereas the opposite trend is observed in the protic counterparts. It is concluded that nonlinear molecular architectures have a significant effect on ion-pair interactions and charge transport, which has implications towards tuning the dynamic properties of polymeric/oligomeric ILs in solid polymer electrolytes for advanced electrochemical applications.

**Chapter 8** summarizes the major results and conclusions from the studies performed in this dissertation and describes the broader significance and generality of these findings in relationship to the larger research community. Finally, suggested areas of research for further studies on branched polymer electrolytes are proposed for maximizing their potential in emerging applications. A number of unresolved issues and open questions which are of wider relevance to the soft matter community are highlighted in motivating future investigations.

# CHAPTER 3. MATERIALS AND EXPERIMENTAL METHODS

## 3.1 Materials: Chemical Composition and Molecular Architecture

### 3.1.1 Star Block Quarterpolymers

Heteroarm star-graft block-copolymers with polyampholyte character were synthesized by Prof. Constantinos Tsitsilianis et al. (University of Patras, Greece) via a multi-step, sequential anionic living polymerization procedure (Scheme 3.1).[96] In short, $PS_n(P2VP\text{-}b\text{-}PAA)_n$ star precursors were synthesized first *via* a multistep living anionic polymerization of $PS_n(P2VP\text{-}b\text{-}PtBA)_n$, comprising a tightly crosslinked poly(divinylbenzene) core in the first pot, followed by the acid hydrolysis of the tert-butyl acrylate blocks in a second pot.[144]

**Scheme 3.1.** $[PS_n(P2VP\text{-}b\text{-}PAA\text{-}g\text{-}PNIPAM)_n]$ star graft topologies corresponding to the SG2 (a), SG3 (b), and SG4 (c) polymers with the responsive blocks.

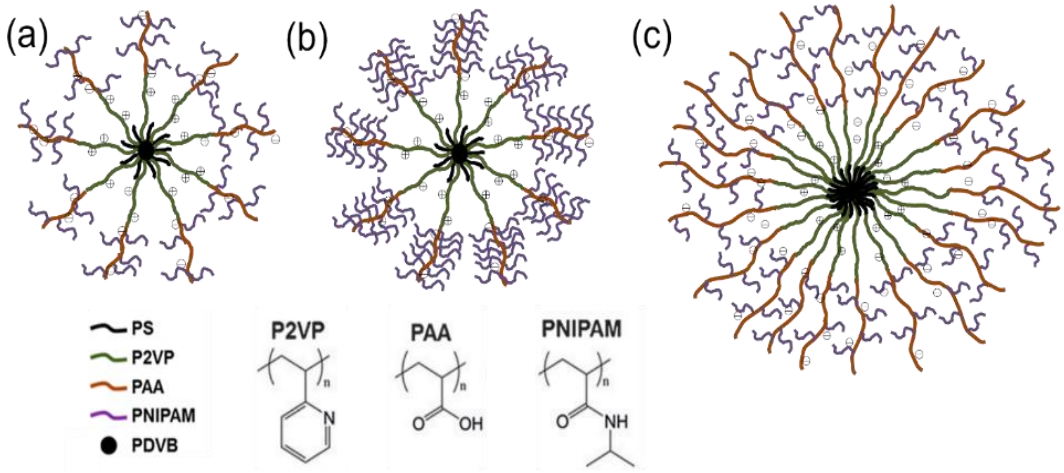


In the final pot, PNIPAM-$NH_2$ chains were then grafted in basic conditions to the neutralized PAA blocks and the final product was recovered from freeze drying after dialysis to remove ungrafted PNIPAM chains. Samples were extracted for characterization at every step of the synthetic procedure to ensure that polymers exhibited well-defined molecular characteristics. Three different topologies include: SG2, SG3, and SG4 (Scheme 3.1, Table 3.1).

**Table 3.1** Molecular Characteristics of the $PS_n$(P2VP-*b*-PAA-*g*-PNIPAM)$_n$ Star Polymers

[a] S: PS, V: P2VP, A: PAA, (in parenthesis the degree of polymerization of each block) and N: PNIPAM, $DP_n$=48, [b] by light scattering of $PS_n$ star precursor, [c] by light scattering of heteroarm star $PS_n(P2VP\text{-}PtBA)_n$ and assuming quantitative deprotection of tBA moities, [d] calculated from $M_w$ of $PS_n(P2VP\text{-}PAA)_n$ precursor and PNIPAM weight fraction, [e] by $^1$H-NMR.

| name | topology[a] | no. of arms[b] | $M_w$ star prec.[c] | $M_w$ star prec.[d] | PNIPAM chains per arm[e] | PNIPAM weight fraction[e] |
|---|---|---|---|---|---|---|
| SG2 | $S(33)_9(V(126)\text{-}b\text{-}A(69)\text{-}g\text{-}N_{4.5})_9$ | 9.2 | 199000 | 426194 | 4.49 | 0.53 |
| SG3 | $S(33)_9(V(126)\text{-}b\text{-}A(69)\text{-}g\text{-}N_{11})_9$ | 9.2 | 199000 | 759648 | 11.08 | 0.74 |
| SG4 | $S(34)_{22}(V(136)\text{-}b\text{-}A(119)\text{-}g\text{-}N_4)_{22}$ | 21.7 | 572000 | 1049400 | 4 | 0.45 |

The amphiphilic block copolymers examined here possess two types of arms: one arm is hydrophobic polystyrene (PS) and the other arm is a block copolymer of cationic poly(2-vinylpyridine) (P2VP) followed by anionic poly(acrylic acid) (PAA) with grafted poly(N-isopropylacrylamide) (PNIPAM) outer chains $PS_n$(P2VP-*b*-PAA-*g*-PNIPAM)$_n$ with n = 9 or 22 (Scheme 3.1). The grafted PNIPAM chains are thermally responsive with an LCST around 31-34 °C.[96,145,146]

### 3.1.2 Linear and Star Polymerized Ionic Liquids

The linear and star poly($VBBI^+TFSI^-$) PolyILs were synthesized by Prof. Krzysztof Matyjaszewski et al. (Carnegie Mellon University) using atom transfer radical polymerization (ATRP) and characterized by gel permeation chromatography (GPC), as described in a previously published procedure (Scheme 3.2).[147,148,149] Fourteen PolyIL arms were linked together by a β-cyclodextrin-14Br (BCD) initiator, which was synthesized according to previously published procedures[150]; the number of arms was held constant whereas the degree of polymerization (DP) and hence number average molecular weight ($M_n$) was varied, with an accompanying change in dispersity ($D$). DP was determined from NMR whereas $M_n$ was determined from GPC (Table 3.2). For star molecules, the theoretical molecular weight is higher than the $M_n$ ascertained by GPC using linear PS standards due to the different hydrodynamic volumes assumed by the star and linear topologies.[151]

**Scheme 3.2** Synthesis of the β-CD-$Br_{14}$ initiator (a) and molecular structure of poly($VBBI^+TFSI^-$) PolyIL with linear (b) and star (c) architectures.

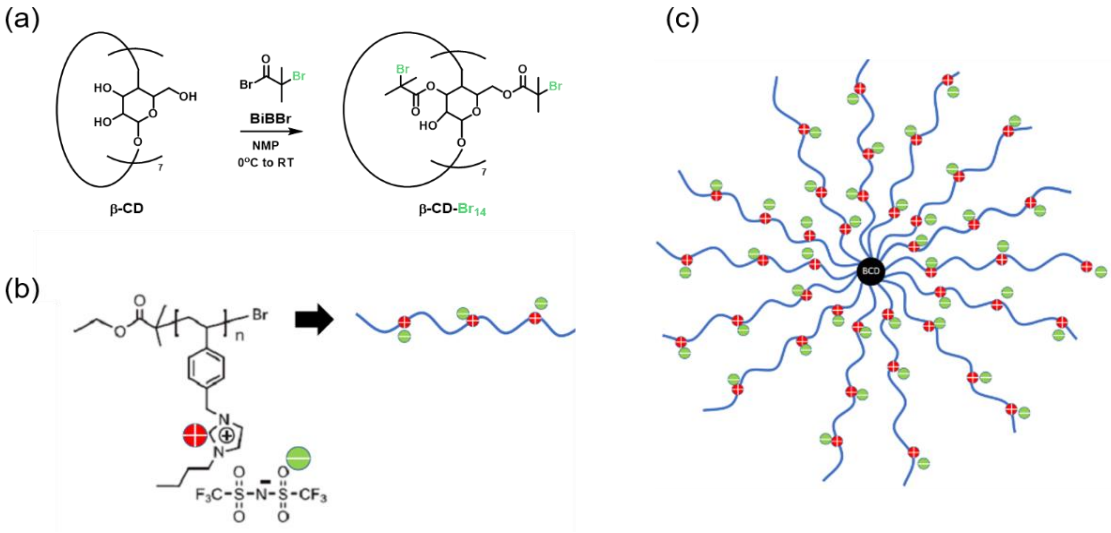


**Table 3.2** Molecular characteristics of the linear and star poly($VBBI^+TFSI^-$)s.

[a] From NMR. $N_{arm} = N$ for the linear $PIL_{76}$. [b] From GPC.

| sample | f | $N_{arm}$ [a] | $MW$ [b] | PDI [b] |
|---|---|---|---|---|
| $PIL_{76}$ | NA | 76 | 39 900 | 1.22 |
| $SPIL_{60}$ | 14 | 60 | 54 900 | 1.42 |
| $SPIL_{89}$ | 14 | 89 | 65 300 | 1.54 |
| $SPIL_{127}$ | 14 | 127 | 71 600 | 2.07 |

### 3.1.3 Hyperbranched Oligomeric Ionic Liquids

Hyperbranched oligomeric ionic liquids were synthesized by Prof. Valery Shevchenko et al. (National Academy of Sciences of Ukraine) with both hyperbranched polyester (HBP) and polyhedral oligomeric silsesquioxane (POSS) cores (Scheme 3.3).

**Scheme 3.3** Molecular models of (a) rigid, POSS-based cores and (b) flexible, HBP cores shown alongside diagrams of their different functionalizations. For comparison, linear oligomeric ionic liquids (c) are also synthesized.

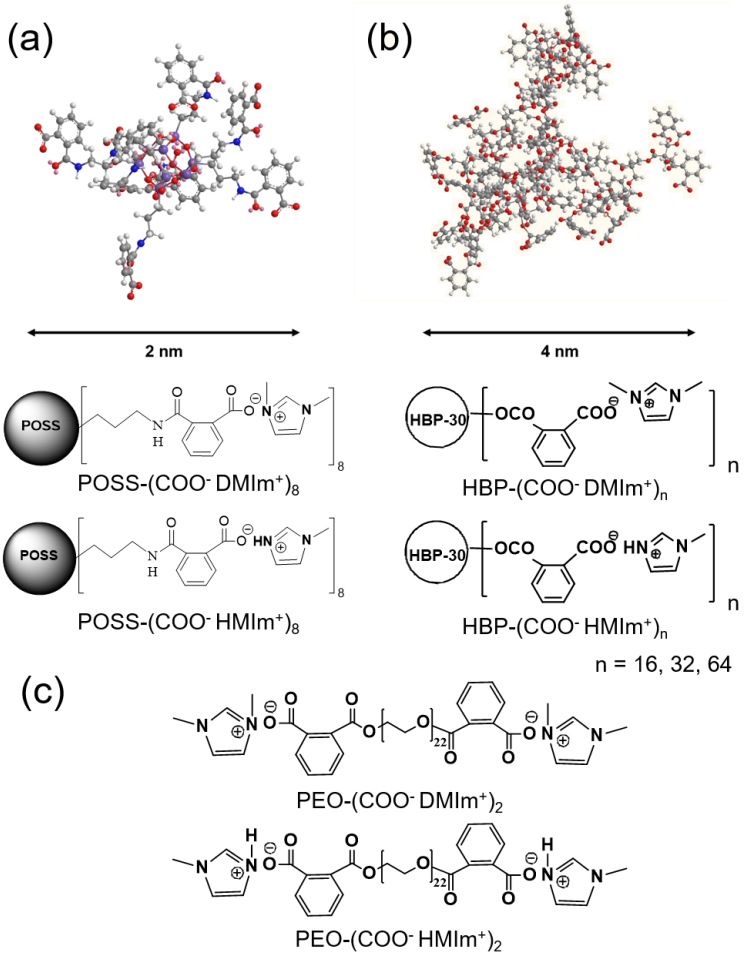


## 3.2 Polymer Assembly and Processing

### 3.2.1 Substrate Preparation

Freshly-cleaned silicon substrates were cut into dimensions of 1 cm x 2 cm in the [100] orientation (Semiconductor Processing). All substrates were cleaned with piranha solution (2:1 concentrated sulfuric acid to hydrogen peroxide mixture) for 1 h according to the usual procedure (caution: strong oxidizer!).[152] Substrates were then thoroughly rinsed with deionized water (Nanopure-Barnstead, ≥18.2 MΩ cm) and dried with a dry nitrogen stream. The treated Si wafers served as hydrophilic planar substrates for film deposition with a native oxide layer of ~1.9-2.0 nm.

### 3.2.2 Langmuir-Blodgett (LB) and Monolayer Films

The Langmuir-Blodgett method is an ideal characterization and nanofabrication technique for studying the surface interactions of amphiphilic molecules assembled at the air-water interface by measuring their surface tension of the confined monolayers in the two dimensional gaseous, liquid-expanded, liquid-condensed, and solid phases.[153,154] Furthermore, by immersing a solid substrate into the subphase (e.g., pretreated Si substrates), it is possible to transfer the interfacial monolayer into a well-defined monolayers with molecular precision at the solid-air interface.

Pressure-area (π-A) isotherms of the amphiphilic polyelectrolytes were collected at the air-water interface using a KSV2000 minitrough equipped with a Wilhelmy plate according to standard procedure.[155] Deionized water was used as the subphase for all isotherm measurements and film depositions. Sample solutions were prepared with a concentration of 0.2 mg/mL and dispersed uniformly onto the surface of deionized water in the minitrough in a dropwise fashion. The Langmuir monolayers were then left undisturbed for 30 minutes in order to let them equilibrate and allow the solvent to evaporate, after which they were compressed at a rate of 5 mm/min up until the minimum barrier separation distance (for π-A isotherms) or to the target pressure (for LB monolayer deposition). For compression-decompression hysteresis isotherms, monolayers were compressed to the maximum pressure before collapse, and then expanded to maximum trough area; three consecutive compression/expansion cycles were repeated.

### 3.2.3 Multilayer Thin Films

Layer-by-layer (LbL) assembly involves the cyclical adsorption of two or more materials into physically-bonded multilayer nanofilms.[156,157,158,159,160] The driving-forces directing the multilayer assembly can involve a diverse range of interactions, including electrostatic, hydrogen-bonding, hydrophobic, host-guest, among others. For example, electrostatic LbL self-assembly of polyelectrolyte multilayers (PEMs) involves the sequential and alternative absorption of oppositely charged polyelectrolytes onto a solid substrate, typically accompanied by an associated charge compensation and reversal for each deposited layer.

LbL self-assembly involves the sequential and alternative absorption of oppositely charged polyelectrolytes onto a solid substrate, typically accompanied by an associated charge compensation and reversal for each deposited layer.[161, 162, 163] Traditionally, LbL components are deposited by repeatedly dipping the substrate into the two or more component solutions; however, they can also be deposited by spin-assisted LbL assembly (SA-LbL) to induce highly ordered internal structure and drastically reduce the assembly time.[164, 165]

## 3.3 Characterization of Morphology and Physical Properties

### 3.3.1 Structure

#### *Atomic Force Microscopy (AFM)*

Surface morphology was examined using an AFM in the "light" tapping mode both in the dry state and in a fluid cell adjusted to various pH values using standard 8 nm n-type silicon tips according to well-established procedures.[166,167] For scanning in air, cantilevers had a force constant in the range of ~3-16 N/m (resonant frequency 115-200 kHz). The scanning speed was maintained in the range of 0.5-1.0 Hz for all scan sizes. For fluid topography scans, more compliant cantilevers were used to measure the hydrated membranes. In this case, spring constants ranged from 0.1-0.4 N/m (resonant frequency 15-18 kHz). Scanning speed was reduced to 0.3-0.5 Hz. The reported surface roughness $R_q$ corresponds to the root-mean-square height deviation taken from the mean image plane calculated from 1 x 1 $\mu m^2$ scan areas. $R_q$ values are determined from averaging at least 5 independent scan areas. Multilayer thicknesses were determined from AFM via scratch tests.

#### *Spectroscopic Ellipsometry (SE)*

Film thicknesses were obtained in the dry state and using a fluid cell for *in-situ* swelling experiments using a Woollam M-2000 U spectroscopic ellipsometer (SE) with WVASE32 analysis software. Unless otherwise stated, measurements are collected at three separate angles of incidence. The detected amplitude and phase shift are analyzed using a single Cauchy layer to simulate the optical properties of the polymer films. Nonlinear fitting of

the optical model to the experimental data is used to estimate the thickness. The procedure is repeated on multiple independent locations to acquire the average film thickness.

***Neutron Reflectivity (NR)***

The internal molecular organization of multilayer thin films were probed using neutron reflectivity measurements, which were carried out using the Liquids Reflectometer at Oak Ridge National Laboratory's Spallation Neutron Source.[168] The key advantage of using fluid-cell NR is the ability to nondestructively resolve film internal structure while applying multiple external stimuli. In a reflectivity measurement, the wave vector transfer $Q$ is defined as the difference between the incident and reflected neutron propagation vectors ($k_i$ and $k_o$). $Q$ has a magnitude $4\pi\sin(\theta)/\lambda$, where $\theta$ and $\lambda$ are the incident scattering angle and neutron wavelength respectively (Figure 3.1).

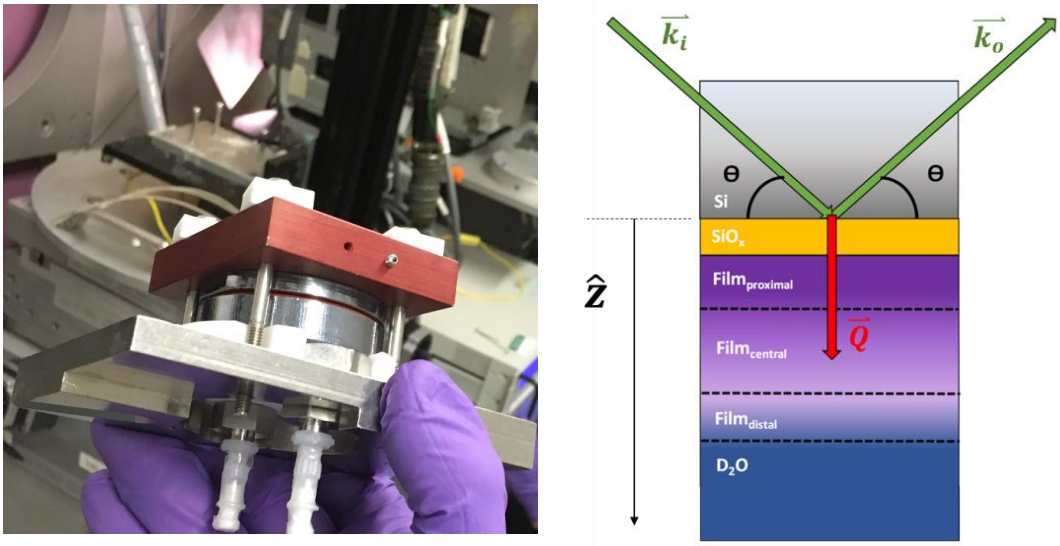


**Figure 3.1.** Picture of the liquids reflectometer cell and the corresponding schematic of the scattering geometry employed for specular neutron reflectivity. Incident neutrons are transmitted through the substrate (top silicon plate) and reflected at the coated interface from the silicon side.

In specular reflectivity, $Q$ is oriented parallel to the surface normal (defined here as the ***z*** direction), and thus probes the laterally averaged ($x$, $y$) variation of scattering length density (SLD) $\rho(z)$ throughout the thickness of the film. In the kinematic approximation, the reflectivity is given by the square of the Fourier transform of the real-space SLD gradient:

$$R(Q) \cong R_F(Q) \left| \int \frac{d\rho(z)}{dz} \exp(iQz)\, dz \right|^2 \qquad (3.1)$$

where $R_F(Q) \sim Q^{-4}$ is the Fresnel reflectivity of the bare Si-fluid interface.[169,170,171] Regions of high contrast (large $d\rho(z)/dz$) arising from the film/fluid interface are therefore easily distinguished in this technique. In practice, $R(Q)$ is computed by an exact optical treatment which considers the reflection and transmission coefficients for the neutron wavefunction in stratified media.[172]

Specular reflectivity measurements were performed using collimated beams incident onto films in air and in contact with $D_2O$-based buffer solutions. For the *in-situ* fluid cell measurements, the incident beam passes through the Si substrate and reflects from the solid-liquid interface. Specular reflectivity data were collected using a sequence of seven incident angles ($\theta$) and 3.3-Å-broad wavelength ($\lambda$) bands, spanning 0.008 $Å^{-1} < Q < 0.017$ $Å^{-1}$. The relative resolution, ($dQ/Q \sim d\theta/\theta$), was held constant at 2.3% to allow seamless assembly of a single $R$ vs. $Q$ data set and to maintain a constant illuminated beam footprint on the sample. For some samples, the rapid decay of reflectivity with $Q$ caused the reflected intensity to become negligible for $Q < 0.17$ $Å^{-1}$. In these instances, the data were truncated at the wave vector transfer where the reflected intensity became indistinguishable from the background scattering ($R < 10^{-6}$).

The fluid cell pH was adjusted analogously to the *in-situ* SE measurements, flushing several volumes for each aqueous condition and allowing ~30 minutes of equilibration time before measurements. The only difference is that for NR, a deuterated environment ($D_2O$, NaOD, DCl) is used to produce a large contrast gradient $d\rho(z)/dz$ with the hydrogenated membrane. The temperature was controlled using an Al block and cartridge heaters and stabilized before the 30-minute equilibration time.

***Molecular Modeling***

Molecular models were built using Materials Studio 3.1 software and their end-to-end distances $R_e$ were determined for both extended and "random coil" conformations. Simulation procedures are performed according to a previously established procedure: (1) a consistent-valence force-field (CVFF) energy minimization, (2) NVT thermodynamic

ensemble molecular dynamics employed to heat the polymer up to 473K (above Tg) and allow the chains to relax to the desired conformation, (3) a final CVFF energy minimization. “Extended confirmation” corresponds to a dihedral angle set to 0° while the dihedral angle was randomized for the “random coil” model.[145] The monomer length was approximated from the $R_e$ value calculated from the random coils. It was in turn used to estimate the radius of gyration $R_g$ of the linear and branched polymer architectures assuming random flight models.

***X-Ray Diffraction (XRD)***

The XRD patterns were recorded using an Empyrean X-ray Diffraction System (Panalytical) with an operating voltage of 45 kV, a current of 40 mA, and Cu Kα wavelength (θ = 1.54 Å).[173] The θ - 2θ scan was carried out in 2θ range from 3 to 30° using a fixed time mode with a step interval of 0.013° for all samples. Samples were dried under vacuum at 120 °C for 12 h before performing the measurements.

***Fourier-Transform Infrared Spectroscopy (FTIR)***

Attenuated total reflectance Fourier-transform infrared (ATR-FTIR) spectra were obtained using a Bruker Vertex 70 FTIR spectrophotometer (600-4000 $cm^{-1}$) with the resolution of 2 $cm^{-1}$ and the number of scans of 100. Polymers were dissolved in methanol (10 mg/mL), after which the solution was directly deposited onto a silicon ATR crystal and air-dried. Samples were then analyzed via FTIR with a grazing angle ATR accessory, which allows for analysis of the samples within 5 μm of the polymer-silicon interface.

### 3.3.2 Thermomechanical and Dynamic Properties

***Differential Scanning Calorimetry (DSC)***

Thermograms were collected in a dry nitrogen environment (TA Instruments). Samples were first dried under vacuum at 120 °C for 12 h and then placed in hermetically-sealed pans. Before starting the measurements, polymers were annealed at 80 °C for 35 min. Several heating/cooling cycles were recorded (constant rate of 10 °C/min), producing consistent, reproducible thermograms. Unless otherwise stated, the calorimetric glass

transition temperature $T_g$ was taken as the midpoint of the heat flow jump during the second cooling cycle.

***Rheology***

Small-amplitude oscillatory shear (SAOS) measurements were performed using an AR2000ex rheometer in the parallel plate geometry (4 mm plate diameter). The temperature was controlled by nitrogen gas in an environmental test chamber. The polymer samples were dried under vacuum at 120 °C for 12 h, after which they were viscous enough to load directly into the rheometer. Next, samples were briefly annealed at the same elevated temperature in the instrument before gradually cooling down to $T_g$. The final plate-to-plate distances were in the range of 600-800 μm. Samples were equilibrated for 5 min at each temperature, after which the viscoelastic response was recorded over a range of strain amplitudes to ensure the SAOS measurements were within the linear regime. Then, the constant-strain linear viscoelastic (LVE) response was examined at frequencies ω ranging from 100 rad/s to 0.1 rad/s. This procedure was repeated for all subsequent (increasing) temperatures for $T > T_g$.

***Broadband Dielectric Spectroscopy (BDS)***

Concentrated polyelectrolyte solutions (10 mg/mL) were slowly spun-cast onto a gold-plated electrode (diameter 10 mm) fitted with a Teflon spacer (thickness ~ 60 μm). The films were then dried under vacuum at 120 °C for 2-3 h, after which the upper electrode was pressed firmly against the film and returned to the oven. The assembled cells were further dried under these conditions for at least 24 h and then immediately transferred to the dielectric sample chamber for measurements under dry nitrogen atmosphere.

The dielectric spectra were measured using a Novocontrol Concept 80 system, including an Alpha-A impedance analyzer, a ZGS active sample cell interface, and a Quatro cryosystem temperature control unit. An AC voltage of 0.1 V was applied and the dielectric response was measured over a frequency range $10^{-2}$ - $10^{6}$ Hz and a temperature range 163 – 383 K (recorded from high to low temperatures). Each sample was equilibrated at the highest temperature for 35 min, during which the BDS measurements showed a steady-

state response. Unless otherwise stated, the reported spectra correspond to the decreasing temperature series.

In BDS, an ac electric field with frequency $f = 2\pi/\omega$ is applied to the sample and the dielectric response is evaluated.[174] In particular, the dynamic permittivity $\varepsilon^*$ is related to the capacitance $C^*$ of the system:

$$\varepsilon^*(\omega) = \varepsilon'(\omega) + i\varepsilon''(\omega) = \frac{C^*(\omega)}{C_0} \qquad (3.2)$$

where $C_0$ is the vacuum capacitance of the arrangement.

Experimentally, the permittivity data is found from measuring the complex impedance $Z^*$

$$\varepsilon^*(\omega) = \frac{1}{i\omega Z^*(\omega) C_0} \qquad (3.3)$$

In analyzing BDS results, it is useful to express the data using multiple different functions since some relaxation processes are not immediately obvious in the impedance or permittivity planes. For example, in assessing the ion transport of polymer electrolytes, it is useful to determine the complex conductivity $\sigma^*$. According to Maxwell's equations, $\sigma^*$ is related to the complex permittivity by

$$\sigma^*(\omega) = \sigma'(\omega) + i\sigma''(\omega) = i\omega\varepsilon_0\varepsilon^*(\omega) \qquad (3.4)$$

The dc conductivity is then generally taken as the frequency independent plateau of the $\sigma$' spectra. Meanwhile, the electric modulus $M^*$ is the reciprocal of $\varepsilon^*$:

$$M^*(\omega) \cdot \varepsilon^*(\omega) = 1 \qquad (3.5)$$

The transition from the higher frequency ac conductivity dispersion to the dc behavior is demarcated at a particular conductivity time $\tau_{dc}$ which corresponds to a Debye-like relaxation peak in the imaginary component of the electric modulus representation.

# CHAPTER 4. TUNABLE COMPARTMENTALIZED MORPHOLOGIES OF MULTILAYERED DUAL RESPONSIVE STAR BLOCK COPOLYMERS

## 4.1 Introduction

Different thermoresponsive, photosensitive, and ionizable functional groups are commonly incorporated into polymer backbones in order to influence interchain interactions and versatile stimuli-responsive behavior.[13,14,175] Responsive polymers are useful as functional building blocks in the guided assembly of metamorphosing materials that are capable of reorganizing at the molecular level as in, for example, phase-changing polymer networks, adaptive supramolecular structures, microgel systems, and self-healing gels.[176,177,178,179,180,181,182] Tuning the interactions of functional polymers assembled into organized morphologies at various interfaces is particularly important because the confined chain conformations and microstructures directly influence surface properties, including wetting characteristics, lubrication and adhesion, mechanical response, bioactivity, permeability, and charge transport.[14,15,16,20,145,159,183,184,185,186,187,188]

Stimuli-responsive polymeric materials are often based on weak polyampholytes, a subclass of polyelectrolytes whose charge and morphology depend on the dissociation equilibria of both acidic and basic functionalities in addition to their spatial locations along the backbone.[16,189,190,191,192] At low pH, acidic groups are protonated and the chain possesses a net positive charge, while at high pH, basic groups are deprotonated and the charge becomes negative. In both instances, the macromolecule is in the 'polyelectrolyte limit'; Coulombic forces promote chain extension and the charged segments tend to be more hydrophilic than the neutral segments.[193] But at the isoelectric point, balance between the ampholytic blocks produces a net charge neutrality of the overall molecular entity.[145] For sufficiently hydrophobic polyampholytes, the drive to minimize the electrostatic self-energy generally leads to association and precipitation at intermediate pH.[16]

More than one type of responsive group can be embedded into polymers to precisely control chain interactions, access complex morphologies, and expand functionality.

Multifunctional polymers, for instance, are often synthesized *via* copolymerization of polyelectrolytes with temperature-sensitive blocks.[184,194,195,196,197,198,199,200] When these materials are heated above the lower critical solution temperature (LCST), the hydrogen-bonded network of water in the first solvation layer is disrupted and hydrophobic interactions are enhanced.[201,202] Polyelectrolytes with LCST behavior therefore exhibit interesting temperature-dependent phase behavior that is dictated by the fluctuating balance of competing electrostatic and hydrophobic characters.[145,203] For example, when aqueous suspensions of weakly ionized hydrogels of N-isopropylacrylamide (NIPAM) copolymerized with acrylic acid (AA) are heated, the competition between pH-induced swelling of partially ionized acid groups and 'hydrophobicity'-driven collapse of NIPAM blocks results in a microphase-separated network containing densely-packed, de-swollen cores surrounded by a diffuse, ionized shells.[197]

Control of ionic and solvophobic interactions is accomplished by designing complex chemical architectures with different blocks within arms, grafts, and terminal groups.[189,190,191,204] Recently, polymers with branched architectures have been synthesized as an emerging class of responsive nanomaterials. Entropic repulsion of these "soft nanoparticles" limits their aggregation as they pack into more crowded environments, while the intramolecular partitioning of hydrophobic and hydrophilic blocks can lead to conformations analogous to those of block copolymer micelles, polymersomes, hierarchical dendrimers, and other multicompartmental colloidal nanoparticles.[89,178,204,101,205,206,207,208,209,]

The multifunctional architecture of the star-graft block quarterpolymers thus favors their integration into hierarchical, stimuli-responsive soft materials with complex intramolecular and intermolecular morphologies.[210] In particular, they are an advantageous component for layer-by-layer nanomaterials assembled by the cyclical adsorption of two or more materials into physically-bonded multilayer nanofilms.[178,145,211,212,213,214,215] LbL assembly produces ultrathin films with controlled thickness, composition, and structure and thus is a useful technique for modifying the properties of surfaces and colloids.[159,216] The hydrogen-bonding and ionic/thermosensitive functions of the SG quarterpolymers in particular allow for the independent control of film integrity and responsive properties. While branched

macromolecular architecture of copolymers is known influence interfacial interactions, polymer density, viscoelasticity and interfacial slip in polymer multilayers[217], the internal morphologies and multiresponsive behavior of hierarchical coatings assembled from polymers with complex, multifunctional architectures are poorly understood and rarely investigated *in-situ*.[218]

As such, there still remains a limited understanding of how compartmentalized morphologies are distributed throughout the interfacial assemblies and how heterogeneity and responsivity of these structures differ from those based on common linear polyelectrolyte counterparts. Herein, we study the dual pH and temperature responsive morphologies of LbL multilayers based on tannic acid (TA) and the heteroarm SG block-quarterpolymers PS$_n$(P2VP-*b*-PAA-*g*-PNIPAM)$_n$ with polyampholyte character (Figure 3.1).[96] The unique compartmentalized internal structures are observed to be dramatically different from the more uniform morphologies of conventional polyelectrolytes.

## 4.2 Experimental

### *Materials*

Poly(ethyleneimine) (PEI) ($M_w$ = 70,000) was obtained from Polysciences Inc. Tannic acid ($M_w$ = 1700), NaCl, and $D_2O$ were obtained from Sigma-Aldrich. Tris-HCl (1.0 M) was obtained from Rockland. All purchased chemicals were used as received. The synthesis and characterization of the PS$_n$(P2VP-*b*-PAA-*g*-PNIPAM)$_n$ is described above (Scheme 3.1). Silicon wafers (10 mm thickness, 5 cm diameter) of <100> orientation with a 2 nm native oxide layer were used as substrates for multilayer deposition (Electronic Materials Technology).

### *LbL Multilayers*

In this work, SG quarterpolymers (Table 3.1) are alternately co-deposited with polyphenol tannic acid (TA) as the H-bonding partner (Scheme 4.1).[145,178,211,212,213,214,215] Aqueous solutions (0.2 mg/mL) of PEI, SG2, SG3, and SG4 were prepared with ultrapure water (18.2 MΩ cm). To minimize electrostatic effects during the multilayer buildup and form the robust hydrogen bonds, the TA and washing solutions were prepared in diluted Tris-

HCl buffers (0.2 mg/mL and 0.1 M NaCl) with a pH adjusted to 5—near the neutral state of the star polyampholytes. During solution preparation and throughout the following experiments (except for neutron reflectivity measurements), the pH was adjusted using HCl and NaOH. For changing the pD in $D_2O$ for the neutron reflectivity measurements, NaOD and DCl were used.

The polished Si surfaces were cleaned using Piranha solution (2:1 concentrated sulfuric acid to hydrogen peroxide mixture) according to the normal procedure (*caution: strong oxidizer!)*.[145] In order to promote film adhesion and prevent delamination throughout the various experiments, the wafers were first submerged in a PEI solution for 15 minutes to form a strongly adsorbed pre-layer.[205] The pre-layer was washed by submerging the film in a fresh ultrapure water bath for one minute, repeated twice. For the film build-up, the substrate was sequentially and alternately submerged in TA and SG quarterpolymer solutions for 15-minute incubation times each and washed two times for 1 minute in the pH 5 buffer solution after the deposition of each individual layer (Scheme 4.1). LbL deposition proceeded to 10 bilayers, and the final surface assemblies were dried under a dry nitrogen stream.

**Scheme 4.1.** Hydrogen-bonding LbL assembly from aqueous tannic acid and star-graft quarterpolymer solutions

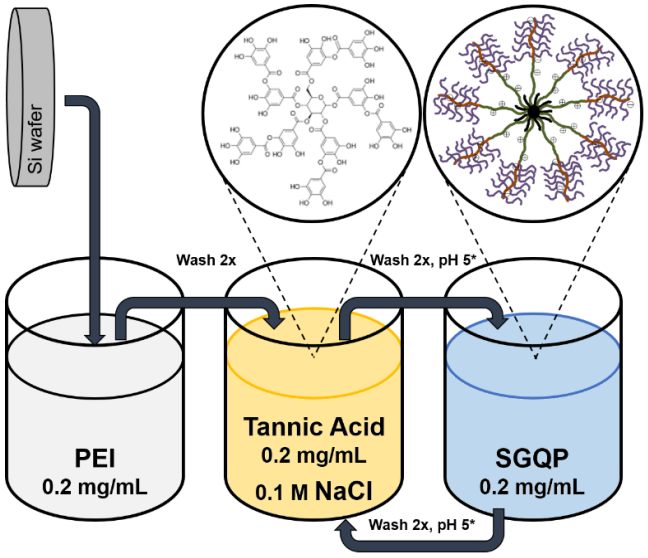


*Washed in 0.01 M Tris-HCl, adjusted to pH 5

***Film Characterization***

Spectroscopic ellipsometry was conducted in both the dry and fluid state. In the dry state, three angles of incidence were used: 65°, 70°, and 75°, while the fluid cell only allows for measurements at 70°. Dry film thickness was evaluated at 5 independent locations. To secure the fluid cell without any leakage, measurements were restricted to a single location at the center of the substrates for the *in-situ* experiments. Fluid cell environments were adjusted by flushing in several volumes (~10-15 mL) of the pH-adjusted ultrapure water. Membranes were allowed 30 minutes to equilibrate for each condition before measurements were recorded. The results are compared to thicknesses ascertained from AFM scratch measurements.

To investigate the film internal structure, neutron SLD profiles were acquired using neutron reflectivity. Values of $\rho$ are based on the number-average mass density ($D$ = 1.11 g/cm$^3$) of the different chemical blocks and their corresponding SLDs (Table S4.1). The multilayers can then be treated as homogenous in composition and density with a constant $\rho_{\text{film}}$ on the length scales investigated here, to which both components are assumed to make equivalent contributions due to equal mixing.[210,211] Buffer solution SLD $\rho_{\text{D2O}}$ was corrected by first fitting the room temperature data near the wave vector corresponding to the critical reflection $Q_c$, and was found to vary slightly from $5.9\times10^{-6}$ Å$^{-2}$ to $6.3\times10^{-6}$ Å$^{-2}$ (the pure $D_2O$ SLD is $6.34\times10^{-6}$ Å$^{-2}$ at $D$ = 1.11 g/cm$^3$). It follows that the modelled $\rho(z)$ should be within the limits established by $\rho_{\text{film}}$ and $\rho_{\text{D2O}}$.[219]

The film at any depth is composed of the TA/SG multilayer and $D_2O$, such that $\phi(z)$ + $\phi_{\text{D2O}}(z)$ = 1. Based on the considerations above, the volume fraction profile of the film is given by[220]

$$\phi(z) = \frac{\rho(z)-\rho_{D2O}}{\rho_{film}-\rho_{D2O}} \qquad (4.1)$$

Integrating the volume fraction profiles gives the total surface coverage $\Gamma$:

$$\Gamma = D \times \int_0^h \phi(z)\, dz \qquad (4.2)$$

where $z = 0$ corresponds to the substrate interface.[193] The upper limit of integration was set to the total film thickness $h$, defined as the height $z$ ($\phi$=0.05). Reported values of $\Gamma$ are scaled by the mass density $D$ of the film/$D_2O$ system and have units of mass/area:

$$\Gamma_{D2O} = D \times \int_0^h [1 - \phi(z)]\, dz = D \times \int_0^h \phi_{D2O}(z)\, dz \qquad (4.3)$$

Overall, Eqs. 4.2 and 4.3 can be used to find the mass average water composition $\langle\phi_{D2O}\rangle = \Gamma_{D2O} / (\Gamma + \Gamma_{D2O})$.

In this work, $\rho(z)$ profiles are simulated by dividing the adsorbed multilayer network into several homogeneous slabs (boxes), each parameterized by distinct values of $\rho_i$, thickness $h_i$, and interfacial width (between it and the layer above it) $\sigma_i$. Specifically, the SG2 and SG3 systems are comprised of a three layer box model where the parameters $h_i$, $\sigma_i$, and $\rho_i$ of each box depends on its local hydration (Table S4.2).[194,170,219,221,222,223] Here, $\sigma_i$ corresponds to the standard deviation of the error function used to model the mixing of adjacent layers. The PEI pre-layer ($\rho = 0.56\times10^{-6}$ Å$^2$) is implicitly considered as part of the initial, proximal layer.

This approach allows for the determination of a continuous volume fraction profile without making any assumptions regarding its analytical form (Eq. 4.1).[193] However, the solutions to $\rho(z)$ in Eq. 3.1 are not unique and must be constrained by additional parameters. In this work, SE measurements in air and fluid were used to constrain the $h_i$ values such that the overall thickness $h$ was within a reasonable range of the SE values. These initial fits were performed individually, allowing explicit constraint of mass balance and parameterization of hydration.[172] The initial fits were then optimized so that the surface coverage $\Gamma$ was constant within error.[220] In other words, it is assumed that desorption is negligible compared to the morphological changes induced under different fluid conditions. This assumption is justified by *in-situ* ellipsometry measurements, which detect no change in multilayer thickness upon exposure to solutions of different pH (2.5 to 8.5) over time (up to 4 hours). Additionally, for multilayers which showed negligible change to internal structure in response to external stimuli, $R(Q)$ and $\rho(z)$ measured at different temperatures and times were essentially identical, thus verifying the stability of the measurements. When reasonable fits were initially obtained, the resulting parameters were used for least

squares regression (Levenberg-Marquardt algorithm) using the Motofit software to yield the final SLD distributions.[224] Variation of the silicon and $SiO_2$ layer parameters had negligible effect on the simulations and were therefore fixed to known values.

## 4.3 Results and Analysis

### *Surface Morphology*

The PEI-$[TA/SG]_{10}$ multilayers deposited at pH 5.5 exhibits consistent growth in neutral conditions.[145] AFM imaging of the films in the dry state revealed granular topographies of the densely packed micellar morphologies over large surface areas (Figures 4.1 and S4.1).[178,204,205,206,207,225]

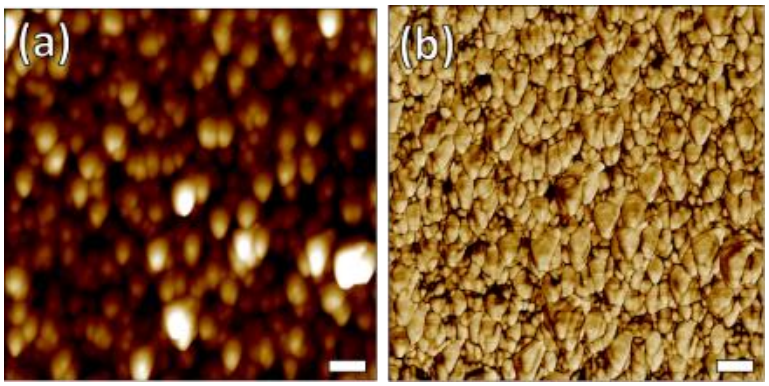


**Figure 4.1.** AFM topographical (a) and phase (b) images of the dry PEI-$[TA/SG3]_{10}$ films. Scale bars are 100 nm; Z scales are 50 nm and 35°.

Both the multilayer thickness and surface roughness increase with the degree of branching and the size of the polymers (Figure 4.2). The pronounced increase in thickness and roughness for the TA-SG4 films is attributed to their molecular characteristics: during LbL build-up, the SG4 stars with longer ampholytic blocks and more arms have stronger excluded volume effects associated with larger dimensions (Table 3.1).[101]

Previously, $\zeta$-potential measurements throughout the LbL deposition of anionic poly(styrene sulfonate) (PSS) and cationic $PS_nP2VP_n$ precursors on colloidal templates revealed charge compensation and reversal for each adsorption step.[204] In contrast, the TA/SG multilayers are characterized by negligible variations in the surface potential, which is always slightly negative regardless of whether the capping layer is the star

polymer or polyphenol.[145] These observations are consistent with the idea that the growth of the dual-responsive networks is mediated via hydrogen-bonding via the PNIPAM segments in the star corona.

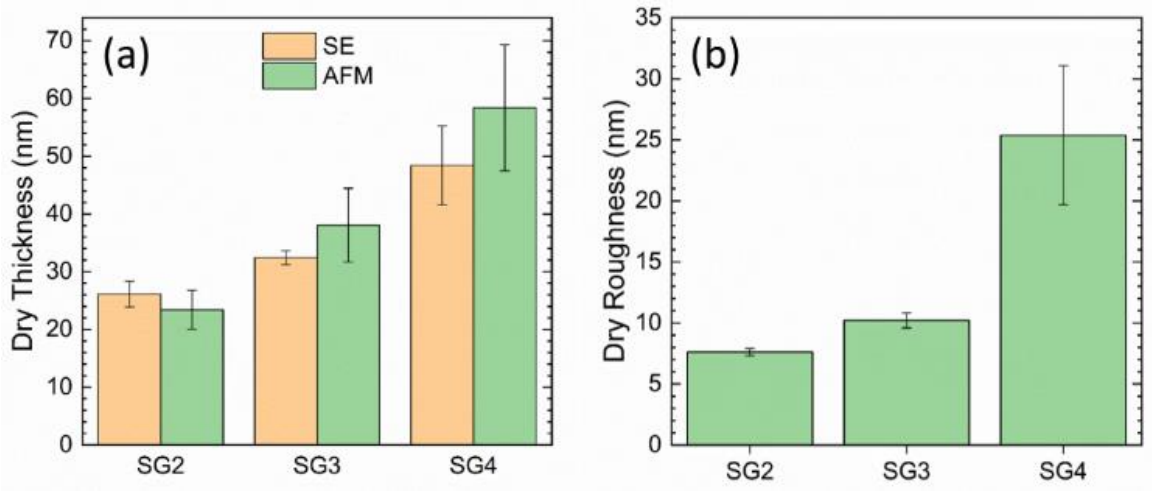


**Figure 4.2.** The average dry film thicknesses for the TA-SG multilayers as measured by SE and AFM (a) and the $R_q$ values determined using AFM images (b).

Next, submersion of the H-bonded multilayers into aqueous environments results in relatively smooth surface topographies with larger aggregated grains (Figure 4.3).[207] The surface textures feature the coexistence of collapsed and swollen domains reminiscent of the 'wormlike' surface structures observed for other pH-responsive star polymer LbL films and are attributed to the phase separation of the swollen and aggregated blocks.[226] The contrast between the heterogeneous domains is greatest at pH 5.5—corresponding to the roughest swollen surface—whereas these boundaries are more diffuse at pH 2.5 and 8.5.[193,204]

Although the measured roughness of the swollen films reflects the changes in morphology, the swelling is modest and essentially independent of the pH (Figure 4.4). The smooth interface with limited global swelling thus indicates a large volume filling factor likely caused by intermolecular association and strong H-bonding between LbL components at the surface.[204,225]

AFM scanning of the dried film after the swelling experiments confirmed the same micellar structure as before immersion, suggesting the surface morphological transitions are reversible. For comparison, *in-situ* AFM measurements of micellar monolayers and

multilayers normally reveal a granular texture in the swollen state.[178,206,207,225] From AFM measurements alone, it is difficult to determine whether or not such a micellar morphology is localized within the multilayers. Therefore, the internal structure is examined using NR.

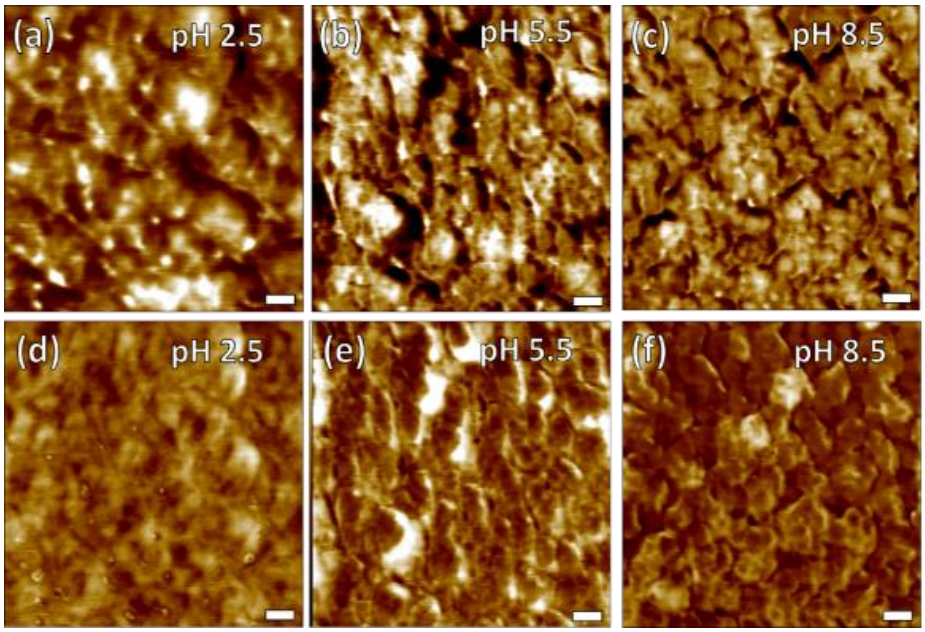


**Figure 4.3.** Surface morphologies of the swollen LbL multilayers at different pH. AFM topographical images (a-c) and phase images (d-f) of the PEI-$[TA/SG3]_{10}$ film collected *in-situ* with the aqueous fluid cell adjusted to the indicated pH. Scale bars are 100 nm; Z scales are 25 nm and 10°.

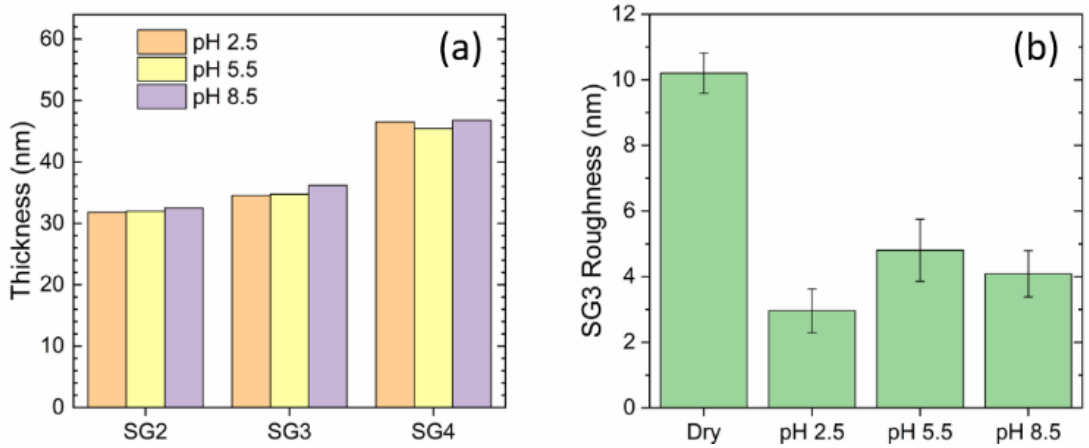


**Figure 4.4.** The swollen film thickness as determined by fluid cell SE (a) and $R_q$ values determined from *in-situ* AFM measurements in fluid cell (b).

### *Internal Morphology of Multilayer Films*

The film-liquid interface is probed *in-situ* using specular NR in a pD-adjusted $D_2O$ fluid cell. Notably, we found that the features in the reflectivity data for all samples could only be appropriately reproduced using multiple box layer models with non-monotonic $\rho(z)$ profiles (Figure 4.5, Tables S4.1, S4.2). Attempting to fit the data using simpler models with only one or two boxes representing the multilayer produced prohibitively large errors. The simple, monotonic $\rho(z)$ profiles often featured SLDs much smaller than those expected for any of the components in the multilayers. Secondly, the overall film thicknesses ascertained from these one- and two-box models were inconsistent with the independent SE and AFM data and the associated values of $\Gamma$ had unphysical variations.

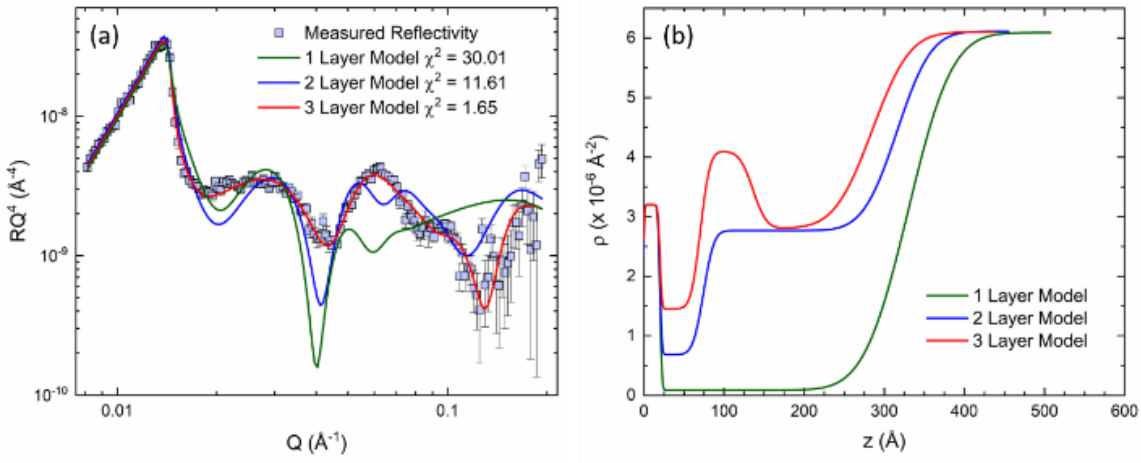


**Figure 4.5.** Comparison of different layer models for the PEI-[TA/SG2] multilayers. The reflectivity is scaled by $Q^4$ to remove the contribution of $R_F$ (Eq. 3.1).

Instead, a three-box model featuring a central layer with enhanced SLD enabled us to fit the neutron reflectivity measurements with very reliable and consistent values of $h$ and $\Gamma$ (red line, Figure 4.5). In the following analysis, the resulting $\rho(z)$ profiles are first correlated to features in the $R(Q)$ plots by observing their changes to external stimuli. Note that throughout this work, the reported $R(Q)$ is scaled by $Q^4$ to remove the contribution of the Fresnel reflectivity and isolate the interference originating from the film structure (Eq. 3.1).[169] The $\rho(z)$ distributions are then systematically converted to $\phi(z)$ profiles and compared at different pH and temperature conditions.

As an example, $R(Q)$ of the SG3 multilayers was found to depend strongly on both pH and temperature (Figure 4.6, see data for SG2 and SG4 in Figures S4 and S5). The pronounced drop in reflectivity at the critical wavevector $Q_c$ indicates sharp contrast between the $D_2O$ and hydrogenated multilayer. When the pH is switched to acidic/basic environments, the first minimum at $Q \sim 0.035$ Å$^{-1}$ becomes shallower while the maximum ca. Q ~ 0.06 Å$^{-1}$ increases slightly in intensity. Concurrently, there is an increase in $\rho(z)$ about 100 Å from the $SiO_2$ surface (Figure 4.6). Because a higher SLD indicates a larger contribution from $D_2O$, the changes simulated in $\rho(z)$ suggest more pronounced internal swelling at limiting pH 2.5 and 8.5.

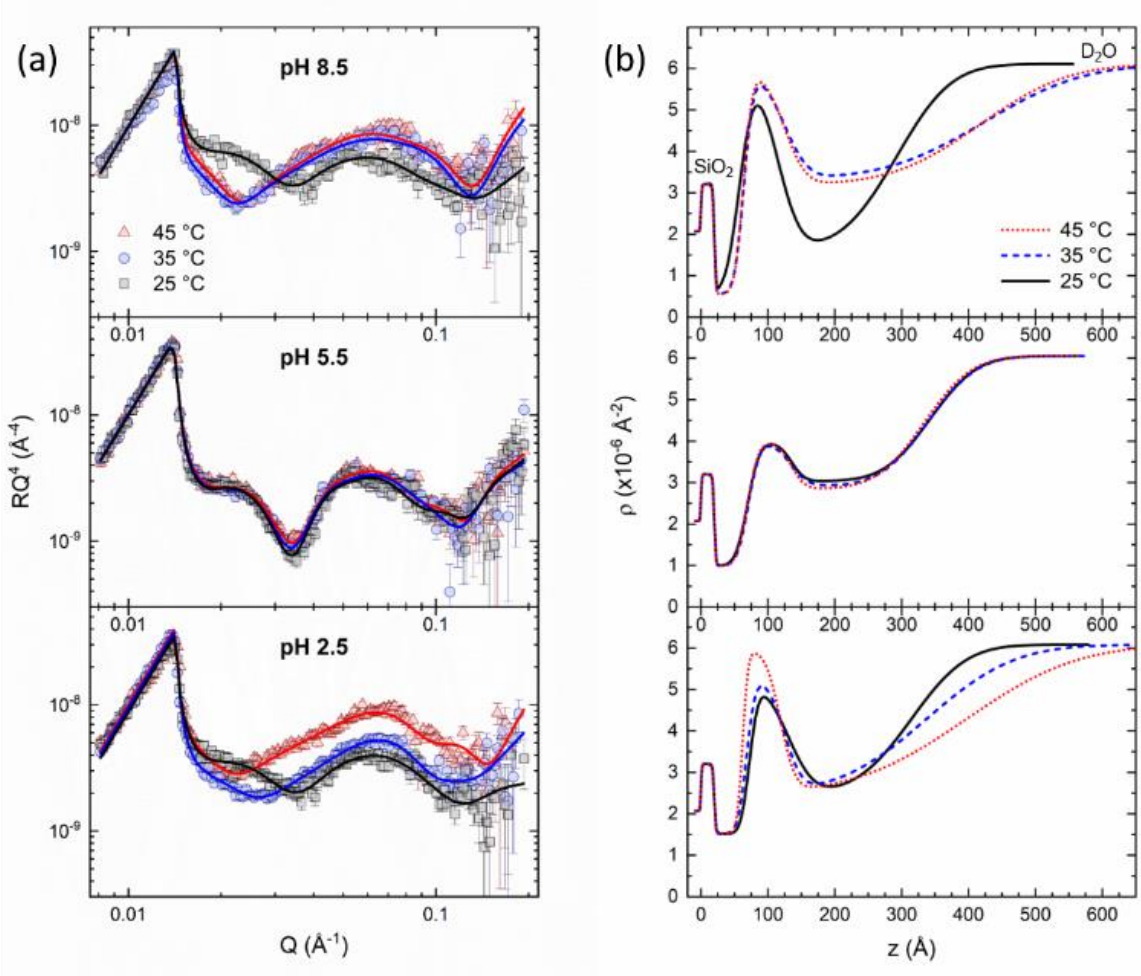


**Figure 4.6.** Neutron reflectivity (a) and the associated SLDs (b) of the PEI-$[TA/SG3]_{10}$ films with the solution pH set to 8.5, 5.5, and 2.5 for the top, middle, and bottom rows. Black squares, blue circles, and red triangles indicates measurements at temperatures of 25 °C, 35 °C, and 45 °C, respectively. The solid lines in the reflectivity plots represent the best fits generated by the SLD profiles in (b). The origin of the SLD plots corresponds to the $Si/SiO_2$ interface.

In addition, measurements for multilayers were recorded as the temperature increased from 25 °C to 45 °C (passing the LCST at ~31-34 °C).[96] For samples demonstrating clear temperature-responsive behavior, there are two prominent changes in the reflectivity for $T$ > 25 °C: (1) attenuation of the first maximum at a wave vector of $Q \sim 0.025$ Å$^{-1}$ and (2) further increase in the intensity of the high $Q$ feature ($Q \sim 0.06$ Å$^{-1}$). The broadening of the low $Q$ feature is consistent with the roughening of the film/fluid interface in $\rho(z)$ while the high $Q$ response indicates significant phase separation on the order of 10 nm resulting from heterogeneous swelling within the multilayer structure (Figure 4.6).[220]

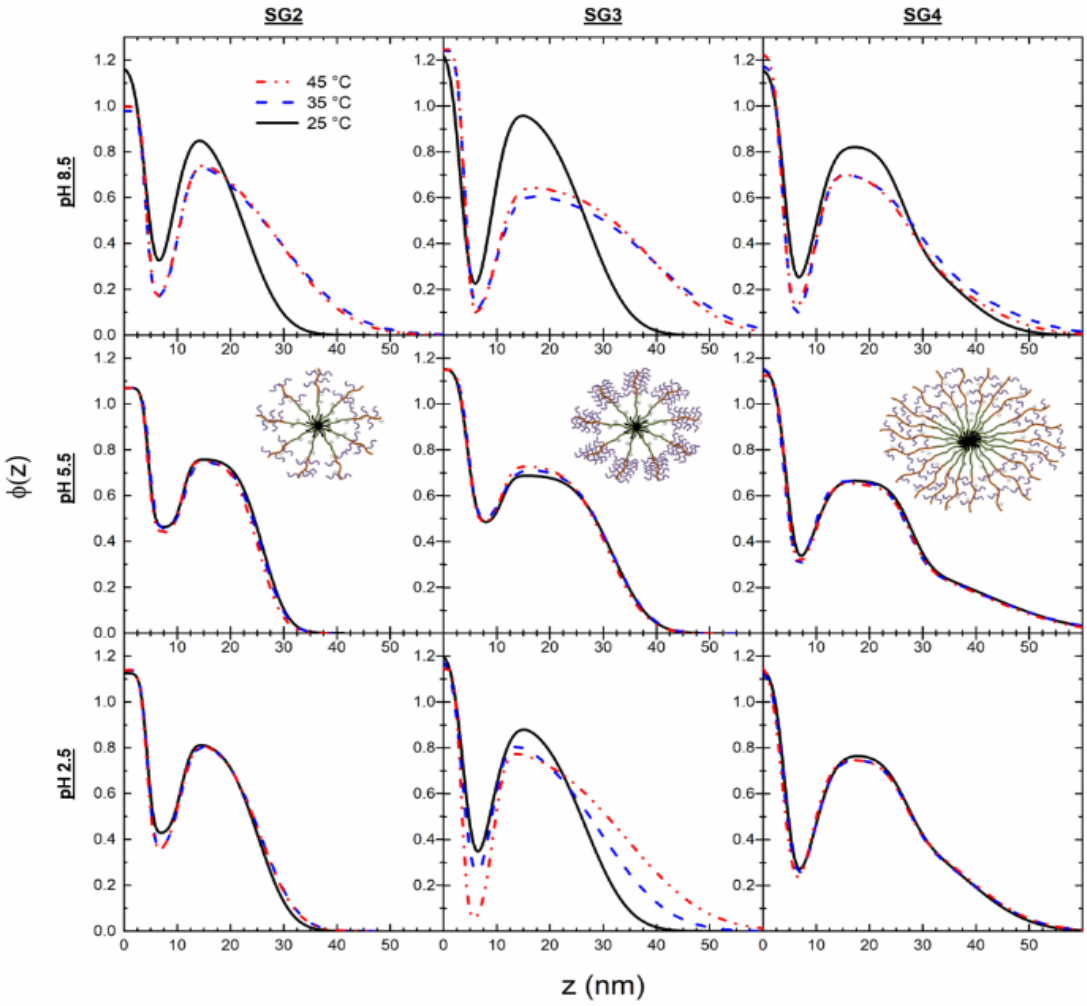


**Figure 4.7.** Volume fraction profiles for the SG2, SG3, and SG4 multilayers from NR data (left, middle, and right columns respectively, Table 2) with the fluid cell adjusted to a pH of 8.5, 5.5, and 2.5 (top, middle, and bottom rows respectively, Table 2). Each pH condition was measured for 3 temperatures: 25 °C (solid black lines), 35 °C (dashed blue lines), and 45 °C (dash-dotted red lines). Here, z = 0 coincides with the PEI pre-layer.

Notably, the temperature-responsive effects are only observed for certain star architectures and pH conditions. For example, while the thermally induced structural transitions are obvious in acidic/basic environments for the SG3 multilayers, the reflectivity is essentially invariant upon increasing temperatures near the isoelectric point—even up to 55 °C ($T >$ 45 °C data not shown). This observation demonstrates that the temperature-dependent variation of the internal structure is linked to specific functionalities belonging to the star polymers as opposed to extraneous effects, such as thermal expansion of the LbL multilayers.

The SLD distributions of the SG2 and SG4 films are similar to those observed for the SG3 films (Figures S4.3 and S4.4). Furthermore, the fitted $\rho(z)$ values are in good agreement with the range expected from Table S4.1 and the film thicknesses are all comparable to the SE measurements (Figure 4.4). Despite these structural similarities, however, the stimuli-responsive modulations of internal morphology depend on the different compositions and architectures.

The volume fraction $\phi(z)$ profiles enable real-space visualization of the internal structure at different pH and temperature conditions (Figure 4.7). For comparison to the SE and AFM measurements, the $z$ coordinate is redefined to originate at the PEI pre-layer. Note that values of $\phi(z)$ above unity for small $z$ are an artifact of the PEI pre-layer, which has a slightly lower SLD than the TA/SG components and is expected to interdigitate into the first layers (Table S4.1). In this representation, the high SLD interior corresponding to the high $Q$ reflectivity peak can be ascribed to a depletion of polymer in the highly swollen ~10-14 nm thick central region of the multilayer (cf. Figures 4.6 and 4.7). The total thicknesses determined from $\phi(z)$ are comparable to those measured by SE (Table 4.1; Figure 4.4). In addition, both the film thickness $h$ and dimension of the internal hydrated compartment $h_{int}$ at room temperature increases with star molecular weight. For the SG3 and SG4 films, it is noted that the thickness at pH 5.5 is somewhat larger than anticipated, which may be attributed to the larger roughness of the films under these conditions. Regardless, the internal restructuring (discussed below) at different pH is self-consistent within the NR models; while the thickness of the SG3 and SG4 films at pH 2.5 and 8.5 are

in better agreement with the corresponding SE values than $h$ at pH 5.5, $\Gamma$ changes only about 2% between all of the $\phi(z)$ profiles.

**Table 4.1.** Room Temperature Characteristics of Multilayers Determined by NR

[a] Film coverage, averaged from the three pH measurements, [b] film thickness, defined as the height $z(\phi=0.05)$, [c] thickness of internal hydrated compartment, defined as $\Delta z$ between the PEI layer and local $\phi_{max}$

| | | pH 2.5 | | | pH 5.5 | | | pH 8.5 | | |
|---|---|---|---|---|---|---|---|---|---|---|
| star component | $\Gamma$ (mg/m$^2$)[a] | $h$ (nm)[b] | $h_{int}$ (nm)[c] | $\langle \phi_{D2O} \rangle$ (%) | $h$ (nm) | $h_{int}$ (nm) | $\langle \phi_{D2O} \rangle$ (%) | $h$ (nm) | $h_{int}$ (nm) | $\langle \phi_{D2O} \rangle$ (%) |
| SG2 | 20.7 ± 0.95 | 32.5 | 10.9 | 40 | 31.5 | 10.3 | 39 | 31.8 | 12.0 | 44 |
| SG3 | 24.2 ± 0.60 | 36.9 | 12.5 | 42 | 39.6 | 11.5 | 43 | 37.3 | 13.2 | 41 |
| SG4 | 25.3 ± 0.49 | 49.3 | 14.9 | 53 | 55.8 | 14.0 | 59 | 45.4 | 15.0 | 50 |

At room temperature, $\Gamma$ ranged from 20.7 to 25.3 mg/m$^2$ for the SG films—similar to values reported for other LbL films (Table 4.1).[227] The increasing deposited mass with molecular weight is analogous to the thickness trend as measured by SE and AFM (Figures 4.2 and 4.4). Moreover, this trend mirrors that of multilayers assembled from neutral polymers: the adsorbed amount is proportional to the molecular weight.[170] This observation provides additional evidence that LbL build-up is for the most part non-ionic; it is not primarily driven by charge compensation because the SG polymers have a small net charge with highly screened interactions.

The total average $D_2O$ fraction (39-59%, Table 2) is in the higher range normally observed in traditional LbL assemblies (~4-56%) and comparable to that in common hydrogel films.[214,219,228,229,230] Comparison of $\phi(z)$ at different pH shows that the films expel $D_2O$ from the exterior in acidic/basic environments (Figure 4.7). For the rougher films, this leads to an overall drop in both $h$ and $<\phi_{D2O}>$ as well as decreased surface roughness as observed from *in-situ* AFM measurements when the pH is increased or decreased from pH 5.5 (Table 4.1, Figures 4.3, 4.4). At the same time, there is a deeper/wider minimum in the interior of the $\phi(z)$ distributions which signifies the increasing compartmentalization of water to internal micellar pockets (Figure 4.7).

Taking $\phi(z)$ of SG3 films as an example, the thickness of the internal hydrated compartment $h_{int}$ grows from 11.5 nm at pH 5.5 to 12.5 (pH 2.5) and 13.2 nm (pH 8.5). Furthermore, the maximum water volume fraction of the interior $\phi_{D2O,max}$ increases from 0.51 at the

isoelectric point to 0.65 (pH 2.5) and 0.77 (pH 8.5) while its position moves to lower $z$ (from 7.9 to 6.3 and 5.9 nm, respectively). Similar trends are observed for the SG2 and SG4 multilayers. It has previously been reported from $\zeta$-potential measurements that the degree of ionization of the star polymers generally increases in the order of pH 5.5 < pH 2.5 < pH 8.5.[96,145] Although the global charge of the multilayer assembly is not known, the pH dependence of the dimensions and characteristics of the hydrated layer in each sample follow that of the state of the corresponding stars in aqueous solution. From this, it is understood that the interior hydrophilic reservoirs swell and move closer to the substrate when the star polyampholytes are ionized in their known polyelectrolyte limits—especially in the alkaline regime.

Next, when the temperature is increased at basic pH, $\phi(z)$ in the depleted central region of the film decreases even further (larger SLD) and is accompanied by a spreading of the outer shell to a more diffuse, lower SLD periphery (Figures 4.6 and 4.7). This change reflects a larger permeability to $D_2O$ throughout the multilayer and resulting swelling, as quantified by a larger $\Gamma_{D2O}$ (Eq. 4.3). This behavior is different from the morphological transition observed in conventional thermoresponsive grafted films and multilayers. That is, the entropically-driven expulsion of water molecules surrounding the responsive PNIPAM blocks and collapse of the chains typically translates to partial dehydration of the coating interior.[194,200,205,222,223,231,232] In contrast to such uniform PNIPAM films, the transformation of SG micellar multilayers is instead more reminiscent of the thermally induced phase separation of microdomain morphology of block copolymers.[233] Indeed, only the compartmentalization of $D_2O$ into ~10 nm phase separated domains within the multilayers can account for the increased intensity at large $Q$ (Figure 4.5).[220]

To focus specifically on this thermally induced swelling caused by the porous morphology at different pH, we define a swelling ratio $SR = \frac{\Gamma_{D2O}(T)}{\Gamma_{D2O}(25\,^{\circ}C)}$ (where $T$ = 35 °C or 45 °C) and plot SR for each of the stars possessing different PNIPAM content (Figure 4.8). It is thus apparent that the LCST-triggered morphological transformation is coupled to both the pH and PNIPAM content. For instance, the swelling ratio of the multilayers increases with larger PNIPAM weight fractions (for pH ≠ 5.5). Likewise, the star polyampholytes with larger PNIPAM grafting densities are more sensitive to temperature changes in aqueous

solutions and at the air-water interface.[96,145] The composition-dependence of the LCST transition is therefore similar to the thermal behavior observed in other dual-responsive block copolymer systems: a larger fraction of thermoresponsive blocks increases the overall polymer hydrophobicity at the transition temperature.[195,196,199]

On the other hand, the LCST response is observable only when the stars are ionized at low/high pH whereas it is inhibited at the isoelectric point—regardless of the PNIPAM content (Figure 4.8). The effect of pH is therefore unusual, since ionization generally increases polyampholyte hydrophilicity, hinders hydrophobic association, and suppresses thermo-sensitive behavior.[96,195,196,198,199,203] The anomalous dual-responsive, compartmentalized morphologies are reconciled in the following section by considering the relationship between star topology, charge, and amphiphilicity in conjunction to hydrophobic and hydrogen-bonding interactions.

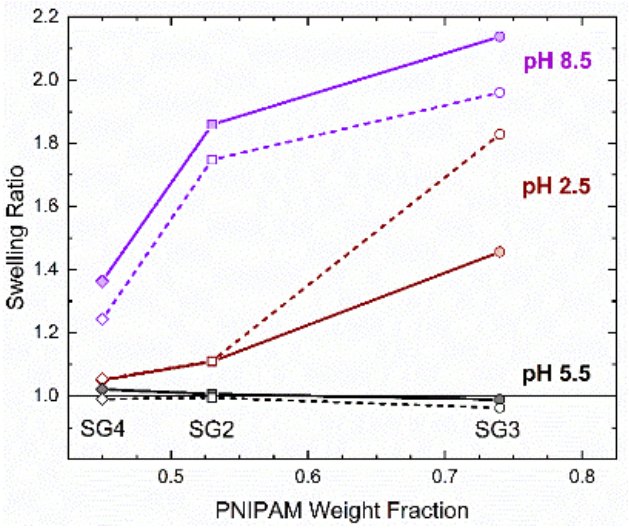


**Figure 4.8.** Thermally induced swelling of the H-bonded multilayers at T = 35 °C (filled symbols, solid lines) and 45 °C (open symbols, dashed lines) plotted as a function of the PNIPAM weight fraction (Table 4.1). The swelling ratio is calculated for the SG2 (squares), SG3 (circles), and SG4 (diamonds) multilayers at the indicated pH.

## 4.4 Discussion and Conclusions

Overall, we discovered that the hydrogen-bonded LbL multilayer assemblies containing the multicomponent and multifunctional star block quarterpolymers have a non-traditional, heterogeneous internal morphology wherein the water distribution depends on the polymer architecture and amphiphilicity (Figure 4.9).

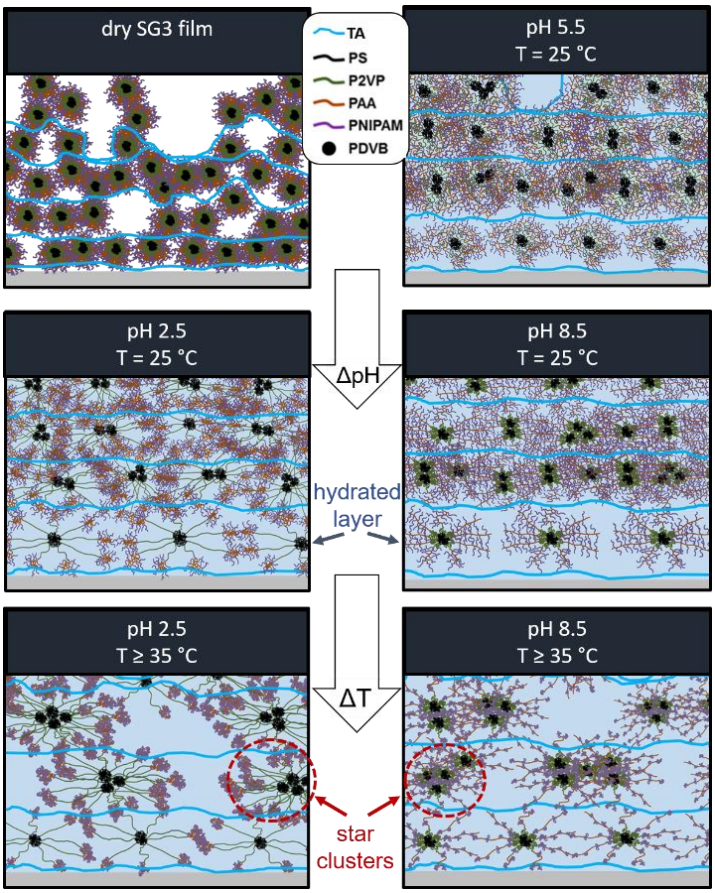


**Figure 4.9.** Suggested internal morphologies of the star polymer multilayers in the dry state and swollen state at various combination of pH and temperature.

We propose that the star polymers assume distinct micellar morphologies which are bonded into the multilayers close to the substrate surface. Due to the presence of molecular cavities within the hydrophilic-hydrophobic star macromolecules, hydrated pockets typify the solvation of these 'soft nanoparticles' at aqueous interfaces.[185,234] Accordingly, the SG4 multilayers had the highest water content in this region, which may be attributed to the highest arm number and longest PAA-*b*-P2VP arms. That the size and swelling capacity of these micellar regions increase with the degree of ionization further indicates that the

hydrated star conformations are stabilized by electrostatic interactions between the hydrophilic shells.[199,203,207]

We suggest that the presence of unimolecular micelles of star block quarterpolymers and their aggregates in solution prior to LbL assembly plays a critical role in the formation of multilayers with "empty" pockets in the vicinity of the solid substrates.[96] Because the films are deposited near the isoelectric point and in the presence of salt, electrostatic interactions are weaker due to lower star charge and/or charge screening effects. Indeed, $\zeta$-potential and adsorbed mass/thickness trends are consistent with neutral star behavior.[145] The interactions between the TA and SG components should therefore be stabilized by H-bonding—primarily between the PNIPAM periphery of the stars and the phenolic groups of TA, as is commonly observed in similar LbL assemblies.[210] While the 2VP and AA moieties may also participate in H-bonding, their interactions are likely less important because the multilayer films retain their structural integrity even when the ampholytic blocks are ionized at their respective limits.

The predominantly hydrogen-bond-driven assembly of soft nanoparticles differs significantly from that known for linear polyelectrolyte chains. During sequential adsorption steps, soft nanoparticles do not completely cover the preceding layers due to the significant entropic cost for packing additional stars into the limited spacing between adsorbed micelles. But as more layers are deposited, the complexation of micelles on the increasingly heterogeneous surfaces of preceding layers likely deforms the nanoparticle shape, driving them to associate further from the substrate to lower the interfacial tensions of their cores.[192,235] This scenario is very different from that observed for linear polyelectrolyte coils, for which extensive interlayer interdiffusion produces comparatively uniform and dense initial layers and more loosely organized morphologies further from the substrate.[159,229,236]

Due to the environment-sensitive intermolecular interactions of the PAA arms and PNIPAM grafts, the swelling of these multilayers and their aggregated morphologies were strongly dependent on pH and temperature (Figures 4.8 and 4.9). The temperature sensitivity (within the experimental window in this study, T = 25 – 45 °C) of the SG

polyampholytes depends on the multilayer microstructure as mediated by the star topology and the electrostatic, H-bonding, and hydrophobic interactions. Above the LCST, hydrophobic outer shells conjoin multiple stars into clusters (Figure 4.9).[145,203] Water permeability thereby increases due to the more porous film structure that directs water molecules into swollen compartments and structural voids.[215] The thermally induced restructuring is stronger not only for higher PNIPAM grafting densities, but also at limiting basic and acidic conditions, signaling that the temperature-triggered changes in morphology is controlled by the intramolecular partitioning of the star-graft blocks.

Internal heterogeneity is thus produced in basic/acidic pH due to compartmentalization of the ionized arms; at high enough grafting densities, the LCST morphological transition is observed.[197,203] The temperature-triggered phase separation is less pronounced at lower pH because the protonation and subsequent intramolecular H-bonding of the dehydrated PAA-*g*-PNIPAM compartments under these conditions partially suppresses the full collapse of the PNIPAM grafts.[196,210]

Additionally, the osmotic pressure and interchain repulsion which resists the temperature-driven inter-star clustering is greater within the inner P2VP portions of the star polymer at low pH compared to those between the charged outer PAA chains of the corona at high pH—especially for SG4 stars with the most arms.[192] The complexed shell at acidic pH may result in an additional level of compartmentalization, however phase separation at this length scale cannot be distinguished from the reflectivity measurements. Lastly, no changes are observed for any multilayers at pH 5.5 because the diminished charge near the isoelectric point minimizes internal heterogeneity and facilitates hydrophobic-hydrophobic interactions between the near-neutral amphoteric blocks and the PNIPAM grafts, thereby suppressing thermo-sensitivity.[237]

The observed behavior therefore indicates the strong coupling of the pH-dependent and the thermally responsive behavior exhibited by the H-bonded network of dual-responsive star block quarterpolymers. Increasing the number of ionizable arms and their length can lead to more hydrated interiors with a temperature response restricted only to pH above the isoelectric point (Figures 4.7). Alternatively, increasing the PNIPAM grafting density

expands temperature sensitivity to both acidic and alkaline conditions while maximizing the thermally induced swelling (Figure 4.8). In either case, the responsive groups and strong H-bonding functions are covalently bonded, resulting in limited localized swelling behavior rather than uniform swelling throughout the entire LbL films.

To emphasize, the heterogeneous distribution of hydrated domains and inner morphology in the micellar LbL assemblies of star-graft block quarterpolymers are in stark contrast to the more uniform swelling of conventional polyelectrolyte multilayers.[228,229,230] Furthermore, traditional multilayer LbL assemblies containing thermoresponsive block copolymers generally de-swell or have negligible responses at higher temperatures because the internal structure appears to be dominated by the hydration/collapse of the individual PNIPAM coils rather than their association and compartmentalization.[200] Meanwhile, conformations of the core-forming blocks are essentially independent of pH and temperature; the colloidal stability of the stars thus preserves creep-resistant, responsive morphologies during application of stimuli.[175]

In conclusion, multilayer LbL films assembled from dual-functional and multicomponent star polyampholytes reorganize into multiresponsive, compartmentalized micellar nanostructures with localized swelling/collapse of hydrophilic/hydrophobic domains. The result is an interior swollen micellar layer whose level of hydration depends on both pH and temperature. In their polyelectrolyte limits, stars with larger PNIPAM grafting densities associate their hydrophobic compartments into clusters when heated above the LCST, thereby opening up the interior film structure while the swollen fluid interface grows rougher with an aggregated morphology. We anticipate the heterogeneous, compartmentalized internal morphologies to be common for other branched, ampholytic molecules, grafted proteins, or micellar supramolecular structures. The particular advantage of this system is the capability to fine-tune the balance of intermolecular interactions while maintaining the overall integrity of the multilayer assembly, which is important for tuning organized colloidal networks of soft nanoparticles, internal reservoirs for cargo encapsulation/release, embedded reactors for localized chemical reactions in heterogeneous catalysts, and nanostructured channels for small molecule or ion transport.

**Chapter 4 Appendix: Supporting Information**

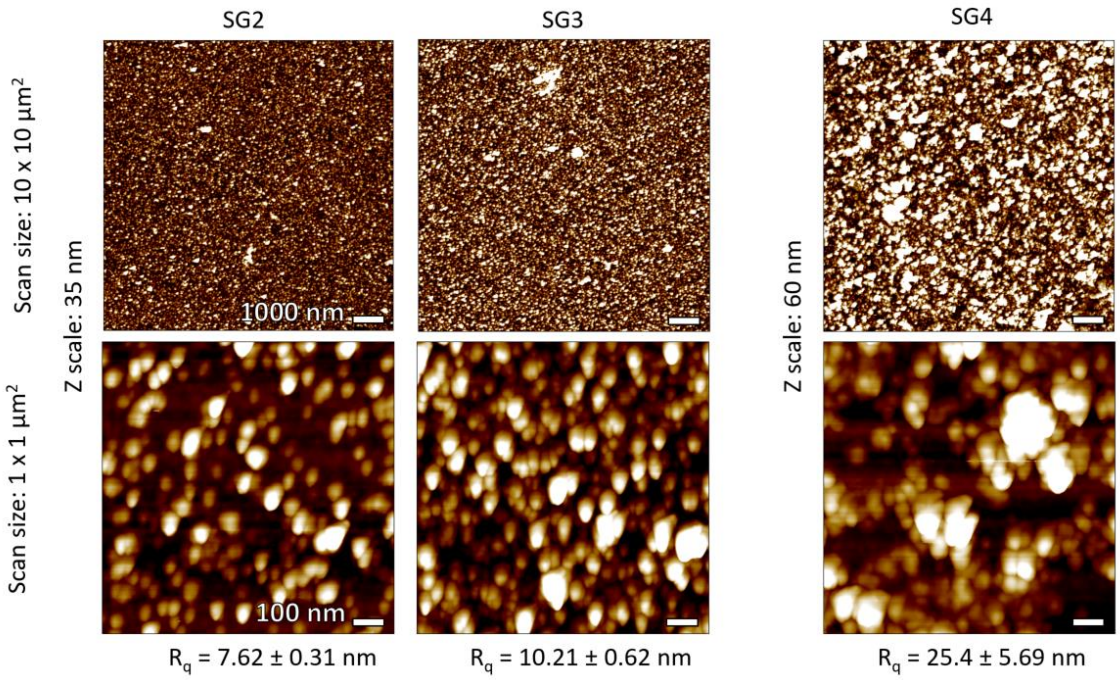


**Figure S4.1.** AFM height images of dry SG2 (left), SG3 (middle), and SG4 (right) PEI-$[TA/SG]_{10}$ multilayers. $R_q$ denotes the corresponding roughness measured from 5 independent 1 $\mu m^2$ areas. Scale bars for 10 μm x 10 μm scan areas (top) are 1000 nm. Scale bars for 1 μm x 1 μm scan areas (bottom) are 100 nm. Note the higher Z scale for the SG4 sample.

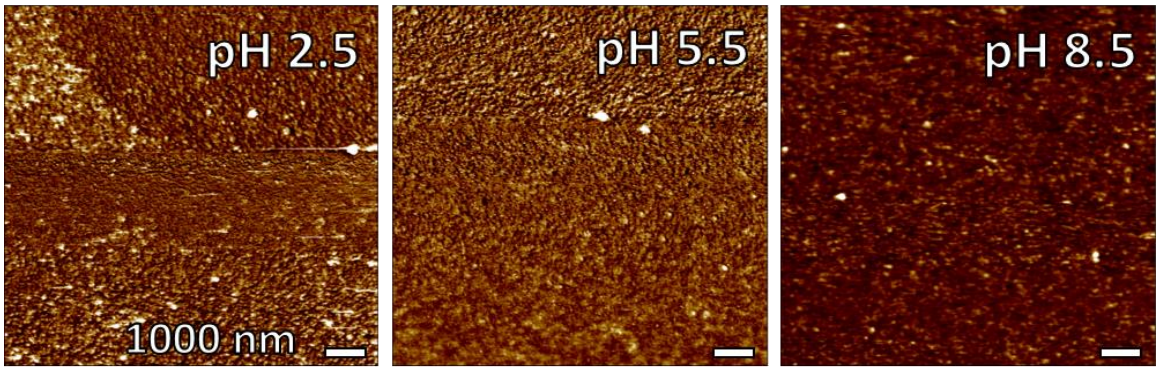


**Figure S4.2.** AFM height images of PEI-[TA/SG3] multilayers immersed in a fluid cell at the indicated pH. Scale bars for 10 μm x 10 μm scan areas are 1000 nm. Z scale is 40 nm.

**Table S4.1.** SLDs of the Individual Components and Multilayers

* Film SLDs are calculated under the assumptions: (i) the multilayer is about 50% TA composition and (ii) all components have the mass density 1.1 g/cm$^3$.[210,211]

| Component | SLD, $\rho$ ($10^{-6}$ A$^{-2}$) |
|---|---|
| PEI | 0.608 |
| PS | 1.48 |
| P2VP | 1.87 |
| PAA | 1.53 |
| PNIPAM | 0.814 |
| TA | 2.25 |
| TA/SG2 Film* | 1.76 |
| TA/SG3 Film* | 1.67 |
| TA/SG4 Film* | 1.79 |
| $D_2O$ | 6.34 |

**Table S4.2** Fitting Parameters for the PEI-[TA/SG3]$_{10}$ Multilayer at 25° C

| slab | pH 2.5 | | | pH 5.5 | | | pH 8.5 | | |
|---|---|---|---|---|---|---|---|---|---|
| | $h_i$ (Å) | $\rho_i$ ($10^{-6}$ Å$^{-2}$) | $\sigma_i$ (Å) | $h_i$ (Å) | $\rho_i$ ($10^{-6}$ Å$^{-2}$) | $\sigma_i$ (Å) | $h_i$ (Å) | $\rho_i$ ($10^{-6}$ Å$^{-2}$) | $\sigma_i$ (Å) |
| Si | ∞ | 2.07 | - | ∞ | 2.07 | - | ∞ | 2.07 | - |
| SiOx | 20 | 3.20 | 1 | 20 | 3.20 | 1 | 20 | 3.20 | 1 |
| $Film_{proximal}$ | 43 | 0.68 | 2 | 51 | 1.19 | 2 | 38 | 0.50 | 2 |
| $Film_{central}$ | 46 | 6.06 | 19 | 68 | 3.98 | 12 | 57 | 5.92 | 17 |
| $Film_{distal}$ | 181 | 1.97 | 32 | 204 | 3.09 | 13 | 178 | 1.65 | 27 |
| $D_2O$ | ∞ | 6.08 | 66 | ∞ | 6.05 | 55 | ∞ | 6.11 | 64 |

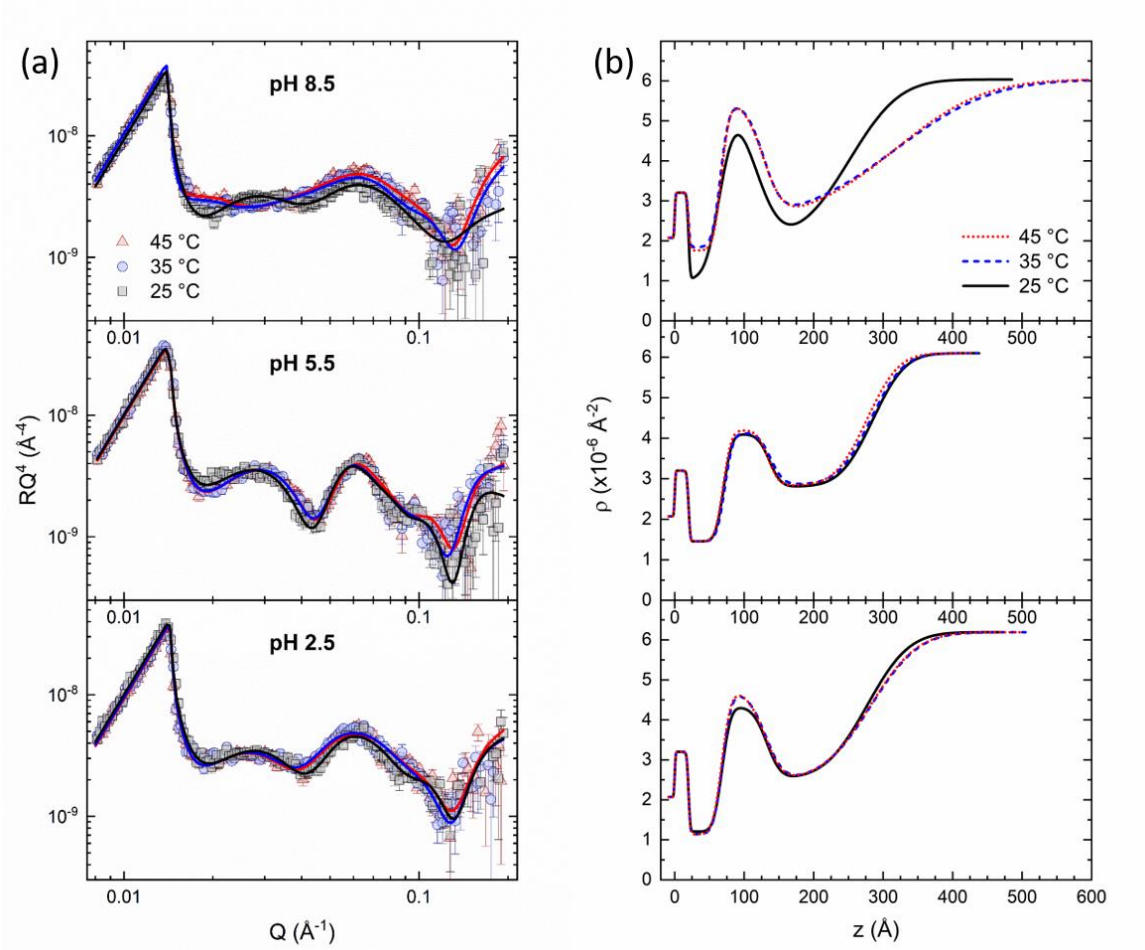


**Figure S4.3** Neutron reflectivity (a) and the associated SLD models (b) of the PEI-$[TA/SG2]_{10}$ films at the indicated pH. Black squares, blue circles, and red triangles indicates measurements at temperatures of 25 °C, 35 °C, and 45 °C, respectively. The solid lines in the reflectivity plots represent the best fits corresponding to the SLD profiles in (b). The origin of the SLD profiles corresponds to the $Si/SiO_2$ interface.

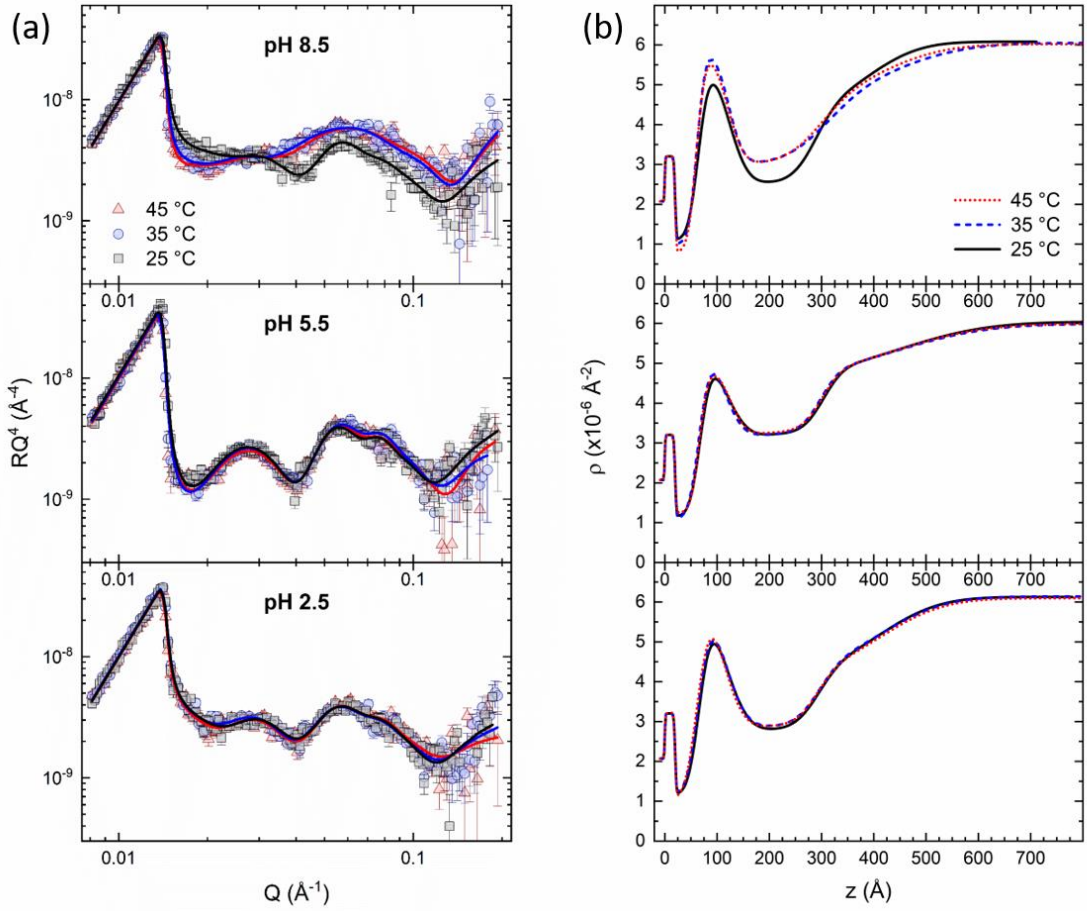


**Figure S4.4.** Neutron reflectivity (a) and the associated SLD models (b) of the PEI-$[TA/SG4]_{10}$ films at the indicated pH.

# CHAPTER 5. LINEAR AND STAR POLYMERIZED IONIC LIQUID ASSEMBLIES: SURFACE MONOLAYERS AND MULTILAYERS

## 5.1 Introduction

The polymerization of ILs provides the opportunity of combining the beneficial chemical properties of ILs outlined above with the improved mechanical stability and dimensional control provided by the macromolecular architecture and topology of the polymeric backbone.[34, 238, 239] Moreover, the facile processability and assembly of polymeric materials—spin coating, electrospinning, coacervation—affords a greater control over the two- and three-dimensional structure of PolyILs, and ultimately their integration into functional soft materials. For instance, gas separation membranes constructed from PolyIL assemblies combine the thermal stability and chemical selectivity inherent from the IL moieties while concurrently preventing the "blow-out" problem associated with their fluidic nature.[33, 240]

Polymerized ILs possess responsive behavior to environmental stimuli. However, in addition to the well-known stimuli commonly used to study many polyelectrolytes—ionic strength[241], pH[242], temperature[243], light[244]—the unique chemical properties of ILs with a wide selection of anions ranging from hydrophobic (bis(trifluoromethanesulfonyl)imide ($TF_2N^-$ or $TFSI^-$)) to hydrophilic (acetate or amino acid derivatives) introduces ion exchange as a particularly intriguing factor for affecting the post-assembly PolyIL morphology.[34, 245, 246] For example, in contrast to most polyelectrolytes, PolyILs are generally soluble in polar organic solvents rather than aqueous solutions.[32] But it has been demonstrated that an increase in hydrophilicity of PolyIL modified surfaces is possible via an anion exchange from $TFSI^-$ to $Cl^-$.[246] Likewise, alternatively flushing polymer brush surfaces with $TFSI^-$ and a highly hydrophilic polyphosphate yields large and reversible changes in the surface energy of a polyelectrolyte brush.[245] Conversely, Ma et al. have reported on the dewetting of polyIL films triggered by an anion exchange to a hydrophobic

counterion that induces mechanical stress relaxation associated with the autocondensation of hydrophobic droplets.[247]

Adjusting the chemical nature of the solvent conditions for a fixed IL counterion can also trigger conformational change of the PolyIL. In this regard, Yuan and coworkers have developed a synthesis route for porous PolyIL membranes by initiating ionic complexation between the PolyILs and weak acids in poor solvents, leading to a globular collapse that is restrained and fixed into place by the ionic network.[248] Small-angle X-ray scattering showed that the dimensions of these pores are related to the correlation length of the polymers—i.e., the extent of chain confinement induced by the poor solvent conditions.[249] Similarly, Firestone et al. investigated solvent-induced swelling and de-swelling as a means to manipulate a PolyIL gel containing gold nanoparticles.[46]

Synthesizing various polymer architectures of PolyIL molecules (e.g., star vs linear topology) is another means to exploit their functionality. Branched polyelectrolytes possess a unique charge redistribution and strong counterion confinement that enables interesting phase behavior depending on the balance of secondary interactions. Precisely controlling the configuration, composition, and architecture of PolyILs is now a feasible and promising approach to optimizing structure-property relationships of these materials.[238, 239 246, 250]

Because PolyILs are a subset of polyelectrolytes, their incorporation into electrostatically stabilized LbL polyelectrolyte thin films—also known as polyelectrolyte multilayers (PEMs)—is possible. Despite the diverse physical behavior demonstrated by ILs described above, very few studies considered PolyIL components for LbL assembly, with only cursory attention given to the assembly process itself.[251] A systematic and fundamental study on the molecular assembly of PolyILs as a function of the polymer shape, degree of polymerization, and environmental conditions is required if the beneficial IL properties are to be exploited to the fullest extent in their polymerized forms.

Hence, in this chapter, the surface organization of linear and star macromolecules of poly[1-(4-vinylbenzyl)-3-butylimidazolium bis- (trifluoromethylsulfonyl)imide] (poly($VBBI^+TFSI^-$)) with different molecular weights is investigated (Scheme 3.2). Since poly($VBBI^+TFSI^-$)'s polar interactions between its charged units partially balances the

hydrophobicity of the $TFSI^-$ ion and the repeat unit's high C/N ratio, its assembly at the air-water and air-solid interfaces is first investigated via the formation of Langmuir monolayers and their subsequent Langmuir-Blodgett (LB) deposition.[252] Secondly, its LbL assembly into multilayer films was studied by alternatively depositing the PolyIL with poly(styrene sulfonate) (PSS) onto Si substrates using dip-LbL and SA-LbL.[156]

## 5.2 Experimental

### *Materials*

Linear poly(styrene sulfonate) (PSS) ($M_w$ = 70,000) was obtained from Aldrich. Linear poly(ethyleneimine) (PEI) ($M_w$ = 70,000) was obtained from Polysciences Inc. NaCl was obtained from Sigma Aldrich. MeOH was obtained from BDH. All purchased chemicals were used as received. The synthesis and characterization of the linear and star poly($VBBI^+TFSI^-$) PILs used in this study are described above (Table 3.2).

### *Langmuir Monolayers and LB Deposition*

The pressure-area isotherms of polyILs assembled at the air-water interface were recorded using the Langmuir minitrough according to the standard procedure. PolyIL monolayers were then transferred via the vertical dipping method (from water to air) to silicon substrates at a rate of 1 mm/min at different pressures (5 and 20 mN/m). To assess monolayer stability and examine the responsive morphologies, LB monolayers were then submerged in deionized water and MeOH for ten minutes at room temperature.

### *Fabrication of LbL Films*

PSS and PEI were prepared in 0.2 mg/mL aqueous solutions, while all PIL samples were dissolved into 0.2 mg/mL MeOH solutions. LbL multilayers were constructed by both dip-LbL and SA-LbL in accordance to the standard procedure[242, 253]. To ensure uniform coverage and complete charge inversion of the initial layers, PEI was deposited onto the cleaned Si wafers first as a prelayer for all samples and washed by water twice, giving the substrate a net positive charge. Then, anionic PSS was deposited followed by the positively charged PIL sample of interest to form the first complete bilayer. PSS depositions were

followed by two washing steps with deionized water while PIL depositions were followed by two washing steps with either deionized water or MeOH. The PSS/PIL bilayer step was repeated 20 times to complete the PEI-$[PSS/PIL]_{20}$ sample. The spinning conditions were a constant 3000 rpm for 30 seconds for each deposited layer. Washing was performed by covering the substrate in $H_2O$ or MeOH and spinning with the same conditions twice. Dipping conditions involved complete submersion in polyelectrolytes for 10 minutes for each respective layer. Washing was conducted by rinsing thoroughly with $H_2O$ or MeOH twice after each submersion. LbL assemblies were submerged in deionized water or MeOH at 60°C for 1h each to examine morphological changes.

***Film Characterization***

Image analysis of the AFM scans, including flattening, roughness calculation, and producing fast Fourier transform (FFT) images and radially integrated power spectral density (PSD) profiles was performed using Gwyddion 2.45 software. All AFM images were first flattened, and roughness values were determined from the root mean square average of the height deviation taken from the mean image data plane for both the 10 x 10 $\mu m^2$ to 1 x 1 $\mu m^2$ areas. At least 3-5 independent locations on the sample were scanned and averaged for all roughness values.

To independently verify stable LbL growth of the films, layers were spun cast directly onto an ATR crystal (cleaned using the same procedure as the Si wafers) and analyzed using a Bruker Vertex 70 FTIR at several different deposition steps. 200 background scans on the crystal without the sample was collected, then measurements were performed with 100 averaged sample scans each with a resolution of 4 $cm^{-1}$. The contact angle of water on the assembled films in air was measured with a KSV CAM101 within 10 s of application of the drop, and at least on four separate locations on the sample.

## 5.3 Results and Analysis

***Langmuir Monolayers and LB Films***

The average end-to-end distance R of the LPIL and single arms of the SPILs as well as the radius of gyration $R_g$ of the whole molecules were estimated from molecular modelling and are summarized in Table 5.1.

**Table 5.1.** Molecular dimensions of polyILs. See Table 3.2 molecular characteristics.

[a] Determined from extrapolating the steep linear portion of the Langmuir isotherm down to 0 pressure. [b] Determined from the limiting MMA assuming a circular surface area.

| Sample Name | Limiting MMA[a] ($nm^2$) | Limiting Radius[b] (nm) | Extended *R* (nm) | Random Coil *R* (nm) | $R_g$ (nm) |
|---|---|---|---|---|---|
| LPIL | 10.5 | 1.83 | 13.8 | 10.0 | 4.08 |
| SPIL-1 | 16.0 | 2.26 | 17.4 | 10.9 | 1.64 |
| SPIL-2 | 16.5 | 2.29 | 20.3 | 12.6 | 2.00 |
| SPIL-3 | 18.6 | 2.43 | 29.1 | 19.7 | 2.39 |

As with all strong polyelectrolytes, PolyILs possess a polar head group associated the permanent ion pair in the repeat unit, bestowing a limited hydrophilicity to the IL monomers (Scheme 1). As discussed above, however, the ion pair is poorly coordinated and composed of the highly hydrophobic $TFSI^-$ ion.[32, 33, 34] The hydrophobic character is enhanced further by the prevalence of alkyl segments adjacent to the ionic moieties and the monomer's high C/N ratio.[254] Moreover, it should be noted that the star molecules are linked by a β-cyclodextrin (BCD) core which is known to act as a hydrophilic unit in self-assembled aggregates due to the hydroxyl groups that did not participate in the grafting reactions.[255] Therefore, it is expected that the macromolecule overall is largely hydrophobic (which is manifested in its insolubility in water), but that it also possesses limited amphiphilic character due to the charged backbone/core, which should stabilize the molecule at the air-water interface.[252]

Pressure-area isotherms for all PolyIL samples exhibit a classical three-phase shape throughout the compression of the monolayers, regardless of the topology or size of the molecule (Figure 5.1).[252] That is, large molecular area gaseous and liquid expanded phases are followed by a highly condensed phase and an eventual collapse at pressures just over 25 mN/m for all PolyIL samples, where the mean molecular area (MMA) of the molecules at these phase transitions was dependent on the size of the molecules. To quantify this, the limiting MMA was determined by extrapolating the linear portion of the steepest segment of the condensed phase portion in the π-A isotherm down to zero surface pressure, in accordance to the usual procedure.[243, 256, 257, 258, 259, 260]

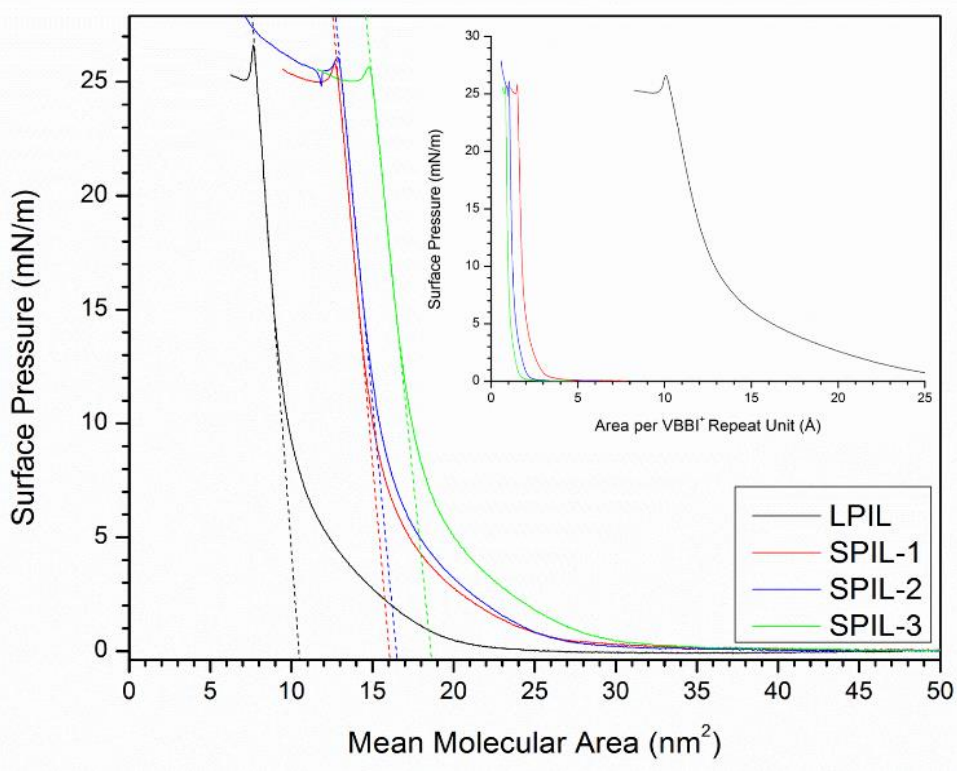


**Figure 5.1.** Surface pressure versus MMA isotherms of linear and star polyILs. Dashed lines indicate the linear extrapolations of the condensed phase used for the determination of the limiting MMA. The inset shows the same π-A isotherms normalized with respect to the number of ($VBBI^+$ $TFSI^-$) repeat units (note the scale of the inset is in square angstroms).

The results verify that the occupied limiting MMA increased with the size or molecular weight of the polymer. On the other hand, if the MMA is normalized with respect to the total DP of the polymer, a sense of the effective monomer packing can be ascertained.[261] The inset of Figure 5.1 shows the π-A isotherms normalized with respect to the number of

polyIL repeat units and demonstrates that the SPIL samples occupied much smaller interfacial areas on a per monomer basis than the LPIL. The normalized π-A isotherms therefore indicate that the SPILs are much more efficiently packed than the LPIL, with most monomer units being constrained in the vicinity of the core region.[262] The "extended" and "random coil" conformations do not represent appropriate models for the two dimensional organization of the polyIL monolayers, as their calculated chain dimensions are an order of magnitude larger than that determined experimentally from the limiting MMA of the π-A isotherms (Table 5.1).

On the other hand, $R_g$ is shown to agree much better with the observed dimensions, suggesting that cooperative molecular motion under compression is best described by considering their center of mass, rather than the stretched or coiled arms. This is interesting when compared to the assembly of traditional polyelectrolytes which are known to possess collapsed, globular conformations when hydrophobic interactions persist, but extend from Coulombic repulsion and excluded volume effects of the solvated side groups in the highly charged state.[243,245,259] That extended conformations are not observed here suggests that hydrophobic interactions dominate over the Coulombic repulsions, as tested by varying the salt concentration of the subphase to shield electrostatic forces and observing no change in the condensed phase (data not shown). Note that for the linear PolyIL, even $R_g$ appears to be an overestimation of the 2D dimensions, suggesting collapsed chain conformations, extensive inter-chain aggregation, and molecular overlap in the linear PolyIL assemblies.

To test the monolayer stability, the PolyIL dispersions were subjected to several compression/expansion cycles (Figure S5.1). The hysteresis curve for the star PolyILs exhibited superimposable compression/expansion in the condensed region, while the linear sample showed changing molecular areas at maximum compression for each cycle. It can therefore be concluded that the star PolyILs form stable condensed Langmuir monolayers, whereas monolayers formed by their linear analogue are susceptible to metastable changes under compression.[261] The difference in stability can be ascribed to the compact shape and dense packing of functional terminal groups of the star molecule which prevents the irreversible small-scale aggregation associated with its linear counterpart at very high

surface pressures. Additionally, the BCD serving as the star core acts as an anchor to the subphase.[255]

### *Surface Morphology of Monolayers*

PolyIL Langmuir monolayers deposited at surface pressures corresponding to both the liquid expanded (5 mN/m) and condensed (20 mN/m) phases possess regularly scattered granules of aggregated PolyIL chains with variable surface roughness (Figures 5.2, 5.3, S5.3, S5.4). Despite the extremely thin thicknesses of these films (~1-2 nm, as measured by ellipsometry), the uniform coverage of the surface is sufficient to yield hydrophobic ultrathin films with contact angles of 72-81° (Figure 5.3). The high surface roughness for the linear molecule for low pressures is consistent with observations of a more entangled and aggregated organization in the liquid expanded phase described above.

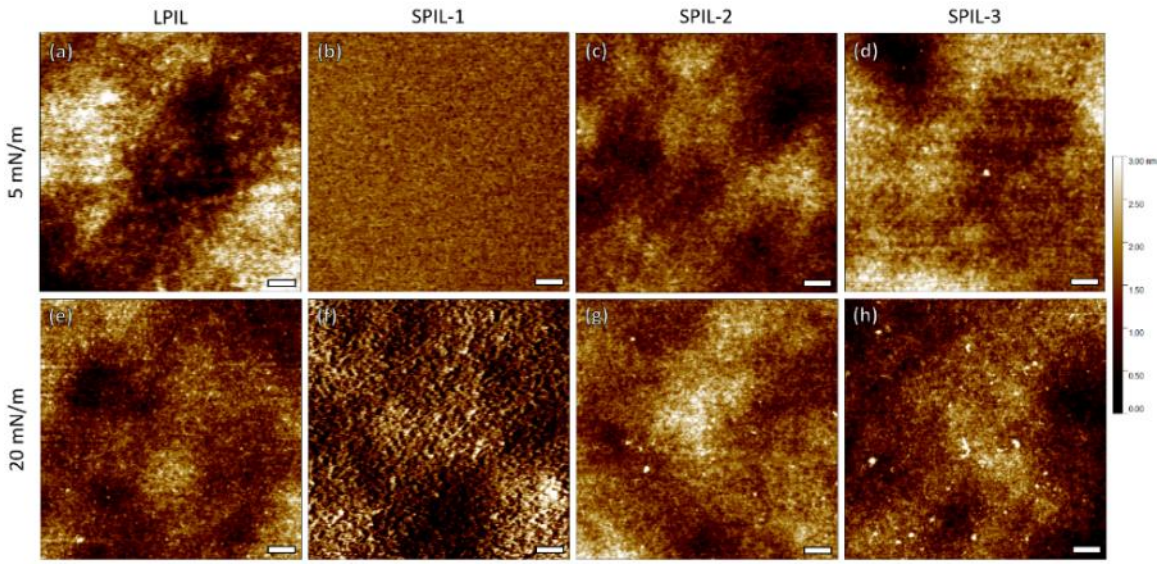


**Figure 5.2.** AFM topography images of LB monolayers deposited at a surface pressure of 5 mN/m (a-d) and 20 mN/m (e-h). The scale bar is 100 nm; the Z scale is 3 nm.

It is also apparent that the star molecule with the lowest DP, SPIL-1, shows the most distinct surface morphologies. Specifically, in the liquid expanded phase, the monolayer adopts a remarkably smooth surface which transitions into a highly rough, corrugated structure with pronounced ridges in the condensed phase (Figures 5.2b, 5.2f, 5.3). As the molecular weight of the arms increases—as for SPIL-2 and SPIL-3—surface morphology resembles the granular structure observed in the LPIL. For SPIL-2 and SPIL-3, the

increase in roughness can be associated with corrugation caused by high internal film stresses and pre-collapsed regions, whereas the roughness with SPIL-1 is dominated by a distinct structural transition.

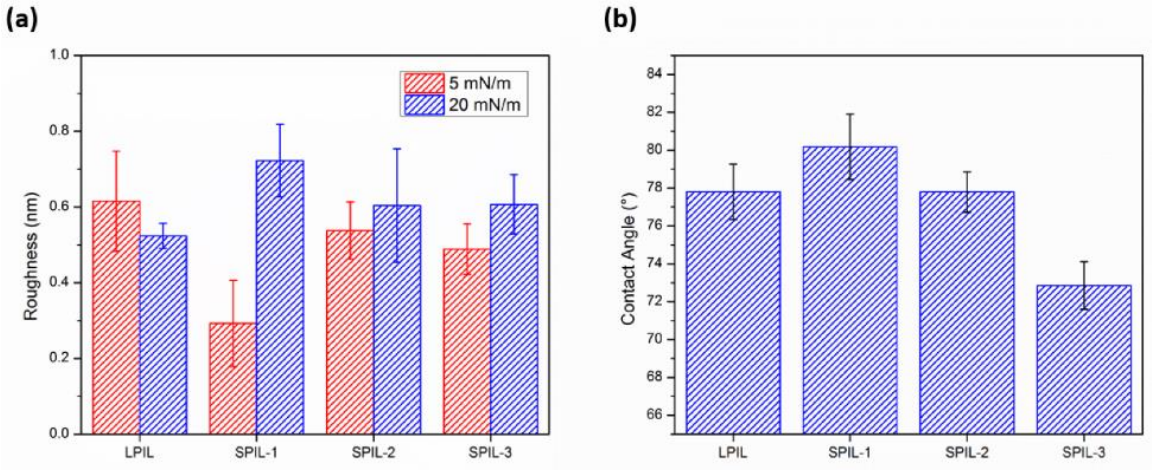


**Figure 5.3.** (a) Roughness values corresponding to the AFM topography images and contact angle measurements of LB monolayers deposited at a surface pressure of 5 mN/m (red) and 20 mN/m (blue). (b) The corresponding contact angle measurements. Reported $R_q$ values are collected from 1 x 1 $\mu m^2$ scan areas.

The responsivity of these monolayers was investigated by submerging the monolayers in water for 10 min, drying and scanning with AFM, and subsequently repeating these steps with submersion in methanol (Figure 5.4). Interestingly, upon water submersion almost all monolayers displayed a transition with an apparent dewetting of the film into polymeric droplets of approximate height 3.67 ± 0.9 nm with peak separations of 41.1 ± 9.2 nm, corresponding to droplet a droplet surface density of ~770 $\mu m^{-2}$.

Such high-density arrays of nanoscale droplets are probably accessible here due to the presence of strong electrostatic interactions to the silicon surface as well as the molecularly thin dimensions of the film wherein extensive, long-range migration is prohibited.[263] Given the scanned area of the AFM image *A*, the number of polymeric droplets within that area $N_d$, and the MMA $\sigma$ of each molecule in its Langmuir monolayer, the average number of molecules per droplet may be estimated from the relation: $\Gamma = A/(N_d\sigma)$.[243, 264] Each droplet contained approximately 70 star molecules (Figure 5.4b) or about 100 molecules of the linear analogue (data not shown). The lower aggregation number for star PolyILs is again consistent with the assertion that star topologies can limit interchain entanglement involved

in the collective dewetting into dense droplets. Moreover, it is demonstrated that subsequent submersion of the monolayers back into MeOH for 10 min results in a transition back to a uniform monolayer (Figure 5.4c). These transitions are reversible for 2-3 cycles, before irreversible dissolution of the absorbed PolyIL molecules.

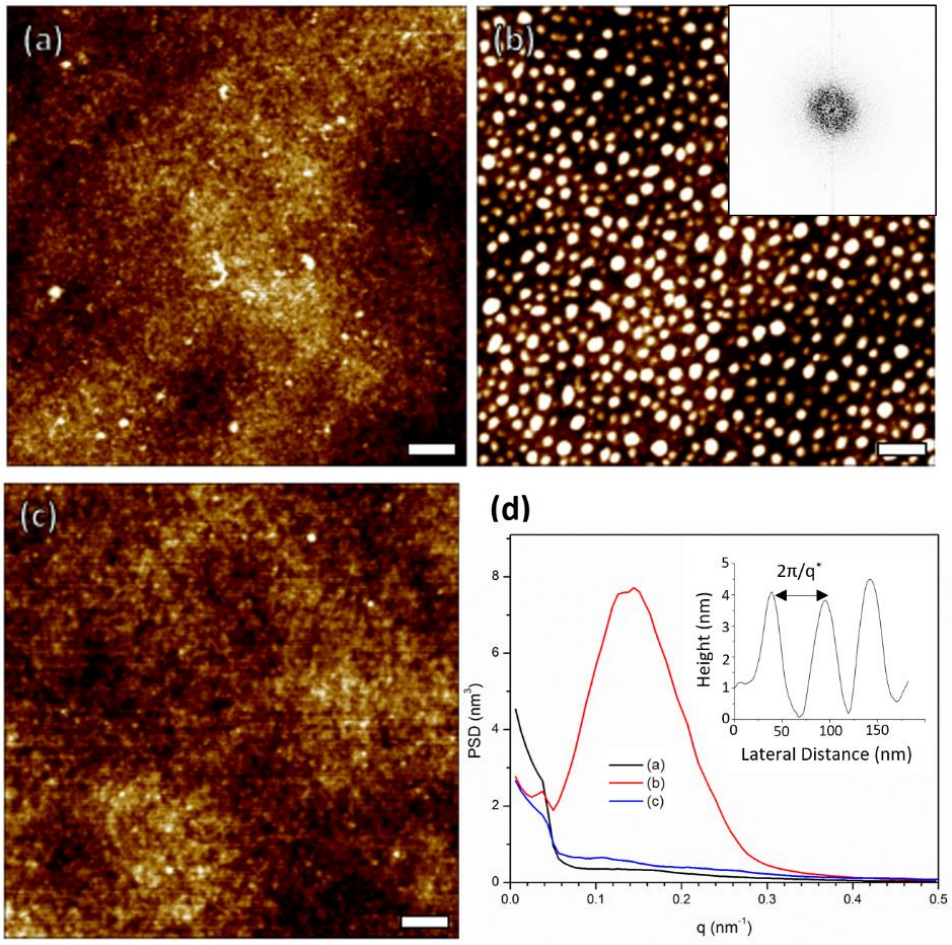


**Figure 5.4.** AFM topography images (a-c) of LB monolayers of SPIL-3 deposited at a surface pressure of 5 mN/m as-assembled (a), after 10 min submersion in water (b), and after a subsequent 10 min submersion in MeOH (c). (d) PSD profiles corresponding to the AFM images, with the inset displaying a height profile. The inset of (b) is the FFT image of the topography scan. The scale bar for the topography images is 100 nm; the Z scale is 3 nm.

The isotropic and highly ordered nature of the pattern is evidenced by the radial symmetry and a well-defined ring respectively in the 2D FFT of the topographical image of the hydrophobic droplets (Figure 4b, inset).[265] The integrated radial power spectral density (PSD) function can be used to select out a dominate isotropic wave vector $q^*$.[266, 267] The PSD profiles for the smooth monolayers are featureless, whereas that for the water-submerged film shows a pronounced peak at $q^* \sim 0.14$ nm$^{-1}$, or an in-plane correlation

length of $\Lambda = 2\pi/q^* \sim 46$ nm, which corresponds to the nearest distance of short-range ordered droplets (Figure 5.4d).

***Assembly of LbL Films***

The linear polyIL spin-casted from diluted solution formed polymeric droplets of height 5.0 ± 2.0 nm similar to those observed from the PolyIL monolayers (Figure 5.5). FFT analysis revealed a decreased q*, or an increased correlation length of $\Lambda$ = 63 nm. Furthermore, the star PolyILs—regardless of molecular weight—yielded interconnected aggregates of droplet clusters which are quite distinct from the LB monolayers (Figure 5.5b). As is known, an initial "spin-off" stage of polymer solution is immediately followed by a film thinning stage in which outward air-shearing and centrifugal forces are balanced by viscous forces near the substrate, all of which secure the fluid layer in place while rapid solvent evaporation quickly increases the PolyIL concentration until precipitation and solid film formation.[164,165] The dewetting rate of fluids is determined by a competition between capillary forces driven by upward solvent evaporation in addition to the interfacial tension of the PolyIL and viscous flow.[268] Star polymer solutions are known to be less viscous than their linear analogues due to the compact shape and smaller hydrodynamic radius of star molecules, and so it is likely that their higher mobility resulted in an increased dewetting stage.

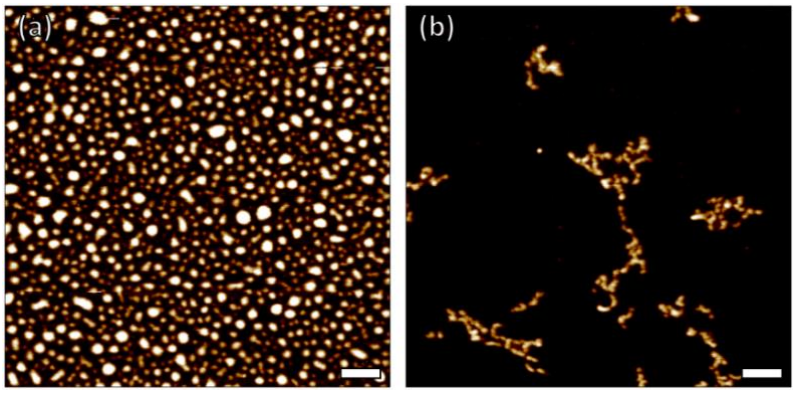


**Figure 5.5.** AFM images of dilute spin casting of LPIL (a) and SPIL-2 (b) onto bare Si substrates. Scale bar is 200 nm; Z scale is 5 nm.

PolyIL LbL films were assembled under a variety of different processing conditions using PSS as the strong negatively charged counterpart for the positively charged imidazolium cations. Stable LbL growth of the PEI-[PSS/PIL]$_{20}$ LbL assemblies is demonstrated by SE (Figure 5.6a) and ATR-FTIR (Figure S5.5), which show monotonically increasing thicknesses and mass deposition, respectively, as more layers are added. Moreover, assemblies constructed without salt show a highly linear thickness dependence on deposition cycle. This behavior is in contrast to studies which have shown polyelectrolytes with more cosmotropic anions (small hydration shells) capable of inducing exponential growth during LbL assembly.[269] Furthermore, contact angle measurements clearly demonstrate the alternating hydrophilic/hydrophobic character of the film following the buildup of sequential PSS/PIL bilayers, with contact angles of ~70-75° for PIL-capped films and ~40-55° for the PSS-capped films (Figure 5.6b).

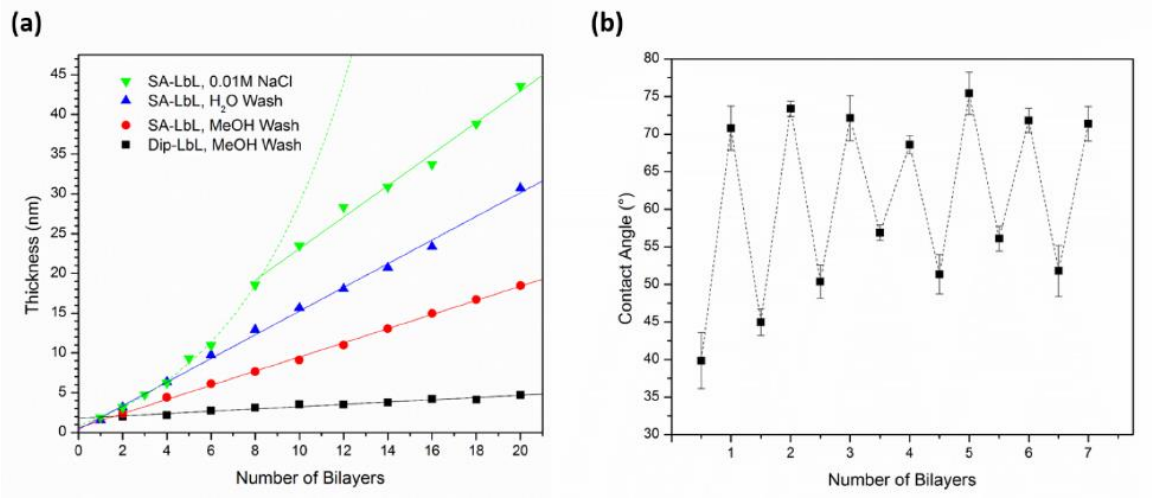


**Figure 5.6.** (a) Thickness of PEI-[PSS/LPIL]$_{20}$ LbL films vs the number of bilayers assembled by dip-LbL (black), SA-LbL with MeOH washing steps (red), SA-LbL with $H_2O$ washing steps (blue), and SA-LbL with $H_2O$ washing steps where all polymer/washing solutions were adjusted to 0.01 M NaCl (green). Solid and dashed lines denote linear and exponential fits to the data, respectively. (b) Contact angle measurements of PEI-[PSS/SPIL-2]$_{20}$ as a function of the number of bilayers.

Interestingly, the lower bound of the contact angle during PSS deposition is observed to increase with the bilayer number, suggesting a regular incorporation of $TFSI^-$ counterions that are free to diffuse throughout the multilayer structure, thereby rendering the top layer more hydrophobic than a pure PSS film. At around 3 bilayers, the overall surface

hydrophobicity appears to saturate for PSS-capped structures, indicating that an equilibrium concentration of counterions at the surface has been obtained.

In the ATR-FTIR spectra, the absorption peak at 1192 $cm^{-1}$ is ascribed to the $TFSI^-$ anion, whereas 2928 $cm^{-1}$ and 3150 $cm^{-1}$ designate respectively the C-H stretching vibration modes of the alkyl chains and imidazole ring corresponding to the $VBBI^+$ repeat unit.[270] The linear increase of the imidazole signal suggests a constant increase in mass per polyIL layer, whereas the sub-linear increase in the $TFSI^-$ signal provides further evidence of a gradual incorporation of counterions—referred to as extrinsic doping—which indicates that the fraction of complexed chains in the LbL assembly is decreasing with the number of bilayers.[271, 272] The exponential increase in counterion absorption with bilayer number is consistent with studies purporting a similar counterion charge density profile as a function of deposition cycle in strong polyelectrolytes at high salt content.[273] However, it is interesting that the same PolyIL counterion incorporation is observed here without any added salt, and is probably related to the strong binding affinity of the poorly hydrated $TFSI^-$ anion. The presence of the counterions within the structure will obviously affect the film properties, as reflected in the relatively large contact angle of the LbL films (Figures 5.6b). Film thickness, roughness, and contact angle measurements for LbL multilayers assembled under different preparation conditions are summarized in a comprehensive table in the supporting information (Table S1).

Clearly, the assembly conditions play a crucial role in determining the growth mode and final thickness. For example, using dip-LbL assembly to construct the films resulted in extremely thin films (4.8 ± 0.6 and 4.4 ± 0.4 nm for 20-bilayer LPIL and SPIL-2, respectively). Hence, at these concentrations, desorption and partial film dissolution facilitated by the high energy barrier to releasing $TFSI^-$ anions and hydrophobic aggregation of PolyIL molecules in the aqueous environment is likely occurring.[274] This is supported by AFM images of the dip-LbL films, in which small but regularly dispersed aggregates appear at the surface (Figure S5.6). In contrast, SA-LbL assembly is more effective in producing thicker films ranging from 18 to 30 nm for 20 bilayer films (Table S5.1).

For SA-LbL films, a drastic decrease in growth rate and final roughness was observed if the PolyIL layers were washed with MeOH instead of $H_2O$ (Figures 5.6a and Table S5.1). This is a consequence the PolyIL's insolubility in water, which resulted in incomplete washing of PolyIL chains that may not necessarily be complexed into the LbL film; uneven growth and coiled structures on the surface lead to thicker films.[165] On the other hand, MeOH is capable of dissolving the extraneous PolyILs and therefore yields much thinner and smoother surfaces. It should also be mentioned here that the structures are extremely sensitive to the ionic strength of solutions used in the assembly procedure. At just 0.01 M NaCl, the growth mode exhibits a transition from exponential to linear growth after about 8 bilayers assembly (Figure 5.6). The final thicknesses of LPIL and SPIL-2 LbL assemblies increased to 43.3 ± 4.0 and 42.9 ±1.2 nm respectively, accompanied by a dramatic increase in surface roughness (Table S5.1). Finally, it is noted that—as with studies of traditional polyelectrolyte LbL assembly[273]—the molecular weight and topology of the PolyIL molecules appear to have a negligible effect on the growth mode and film thickness. However, the film morphology was significantly influenced, as discussed below (Figure S5.7).

***LbL Film Morphology***

Various surface morphologies were observed for LbL films depending on the assembly procedure, topology, and molecular weight, with all exhibiting a highly textured surface of regularly dispersed spherical granules at the nanoscale (Figure 5.7). As molecular weight of the star PolyILs increases, the formation of highly porous morphology becomes more prevalent. This is to be compared to the linear PolyIL LbL film, in which more uniform films with minimal lateral reorganization (low density of defects) is observed. Similar trends are observed in the corresponding phase images of the water washed LbL films, which reveals an interconnected network of the granules for the linear PolyIL in contrast to highly segregated granular domains for star PILs that combine for higher molecular weight PolyILs (Figure 5.8).

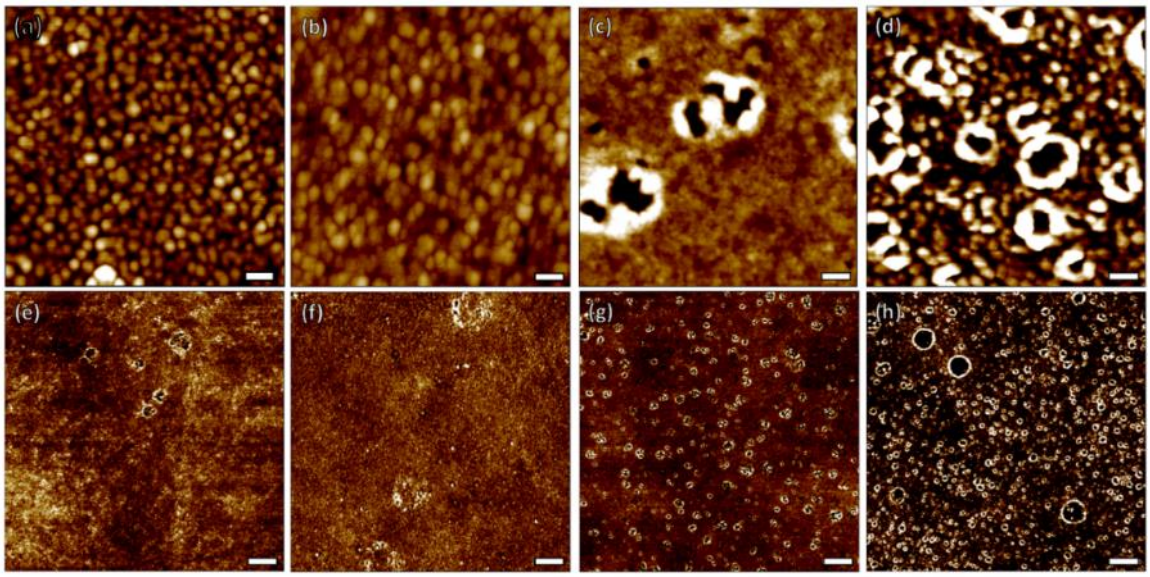


**Figure 5.7.** AFM topography images of PEI-$[PSS/PIL]_{20}$ containing (a,e) LPIL, (b,f) SPIL-1, (c,g) SPIL-2, (d,h) SPIL-3, where all layers were washed with water. Scale bar for (a-e) is 100 nm; scale bar for (e-h) is 1 μm. Z scale is 20 nm for all AFM images.

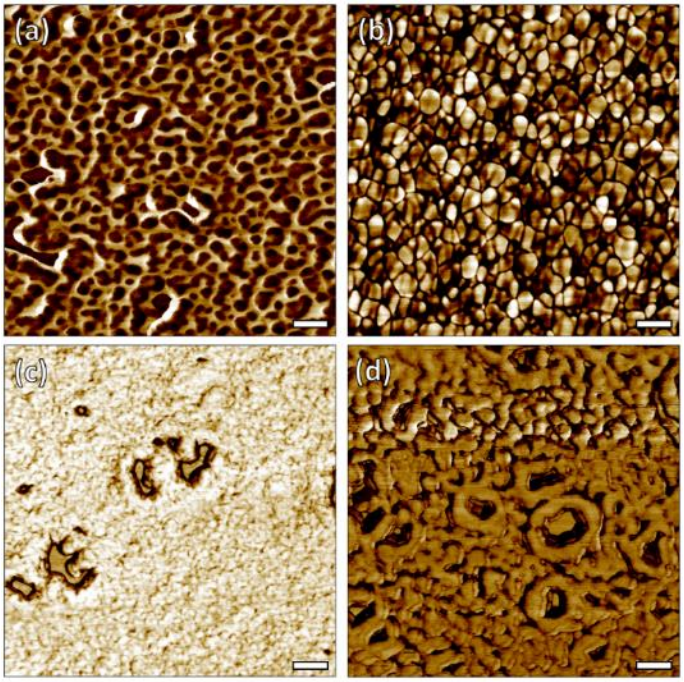


**Figure 5.8.** AFM phase images of SA-LbL PEI-$[PSS/PIL]_{20}$ containing (a) LPIL (b) SPIL-1 (c) SPIL-2 (d) SPIL-3 with water washing used in the assembly. Scale bar is 100 nm. Z scale is 30°.

As with the Langmuir monolayers, the organization of these features can be characterized by examining the radially integrated PSD profiles which feature more pronounced peak intensities at both the nano- and microscale as molecular weight increases (Figures S5.8,

S5.9). Note that the dimensions of the scan image used in generating the PSD function will determine the feature being inspected; for 1 x 1 $\mu m^2$ scans, the dominate contribution will be the peak-to-peak distances of the nanoscale granular structures or undulations $\Lambda$[267, 275] whereas the 10 x 10 $\mu m^2$ images are dominated by the density and size of dewetted pores[266]. This difference explains the large disparity between the peak locations in the PSD profiles: for smaller scan areas, the PSD peak intensity is small and broad for the lowest molecular weight star PILs, and appears to increase and sharpen at ~0.06 $nm^{-1}$, corresponding to inter-granular distances of around 100 nm. LPIL, however, shows an intermediate peak displaced at ~0.1 $nm^{-1}$ ($\Lambda$=63 nm), suggesting that linear molecules assemble into smaller surface undulations.

On the other hand, large scan areas reveal no peaks for LPIL and SPIL-1, consistent with the fact that no pore formation and few defects were observed from AFM images. However, SPIL-2 PSD profile shows a broad peak at about 0.046 $nm^{-1}$ (hole diameters of ~136 nm) while the peaks are significantly enhanced and split ($q_1$ = 0.004 $nm^{-1}$, $q_2$ = 0.0125 $nm^{-1}$, $q_3$ = 0.0205 $nm^{-1}$) for SPIL-3, representing the high-density multi-mode distribution of regularly dispersed pores ($d_1$ = 1570 nm, $d_2$ = 503 nm, $d_3$ = 307 nm). Accordingly, a consistent increase in surface roughness is observed at both length scales for the star molecules as molecular weight increases (Figure 5.9). The rougher samples were also associated with higher contact angles as well.

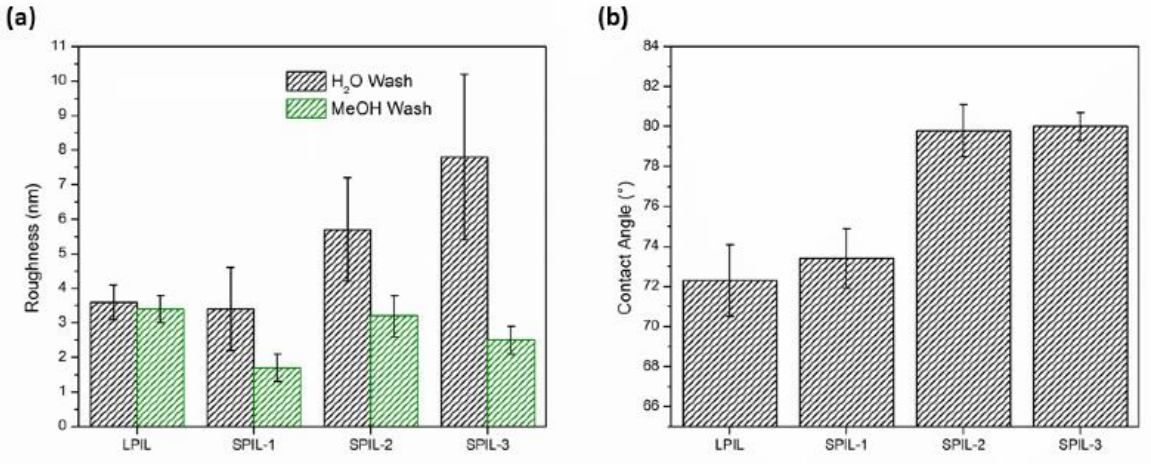


**Figure 5.9.** Roughness values (10 x 10 $\mu m^2$) (a) PEI-[PSS/PIL]$_{20}$ LbL films where PIL layers were washed with water (black) and methanol (green), and the associated contact angle measurements (b).

This is to be contrasted with the AFM images of the MeOH washed systems (Figure S5.10), which feature much smaller densities of smaller pores throughout the higher molecular weight films. This is consistent with the fact that the MeOH-washed samples show much flatter PSD profiles and smaller roughness values than do the water washed samples (Figures S5.9). These topological measurements can be compared to those of perforated LbL membranes fabricated by the dewetting of polyelectrolyte solutions on hydrophobic surfaces.[276] In comparison, the assemblies produced in this work are found to have roughness values up to twice as large for the star polyILs, indicating that mechanisms other than partial phase separation are generating the porous morphology (see general discussion below).

Figures S11 and S12 show the AFM images and PSD plots of the LPIL LbL films (from Figure 5.8) after being subjected to water submersion for 1 hour, followed by submersion in MeOH for 1 hour. Inter-granular dimensions for the linear PolyIL showed negligible shift (~60 nm) and became more pronounced upon water submersion, as shown in the PSD profile (Figure S12). This correlation length is slightly larger than—but on the same order—as those found from the LB monolayer for the linear PolyIL (about 36 nm). As in the case of the monolayers, subsequent immersion into MeOH completely erased the lateral correlations for granular texture, resulting in a marked decrease in surface roughness from $3.8 \pm 0.2$ nm to $1.3 \pm 0.2$ nm (1 x 1 $\mu m^2$ area). The similar dimensions and responsivity suggests that PolyIL molecules within LbL films organize themselves in a similar manner to those in the 2D monolayers. It is emphasized that the responsivity of PolyIL LbL films to ionic strength and environment can be combined to produce a variety of structures, ranging from molecularly smooth films formed from linear PILs in the absence of salt (Figure S11) to extremely rough and hierarchically porous, sponge-like morphologies of linear and star PolyILs assembled at 0.01 M NaCl (Figure 5.10).

Lastly, to explore the transition from single layer PolyILs to fully integrated multilayer structures, AFM images and corresponding $R_q$ values and PSD profiles were collected throughout the LbL process (Figure S5.13). As the number of bilayers increases, surface granules are seen to grow more prominent, with an associated increase in surface

roughness. Interestingly, at around 15 bilayers, surface pitting is observed, which could be the early stages of the pore nucleation in the LbL films.

## 5.4 General Discussion and Conclusions

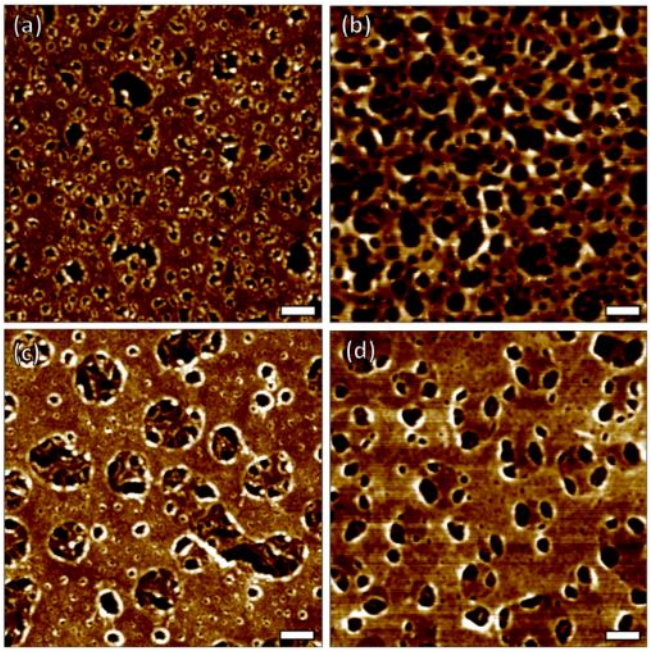


**Figure 5.10.** SA-LbL PEI-[PSS/LPIL]$_{20}$ (a,b) and PEI-[PSS/SPIL-2]$_{20}$ (c,d) as assembled at 0.01M NaCl and with water washing conditions (a,c), after 1 h immersion in water followed by 1 h in MeOH (b,d). Scale bar is 1 μm; Z scale is 40 nm in all images.

Throughout this study, the morphology of PolyILs within LB monolayers and LbL films has been shown to depend extensively on the interplay of electrostatic and hydrophobic interactions, as well as on how the molecular structure, size, and film environment influence this balance during the assembly process. Within Langmuir monolayers, the PolyIL molecules were observed to cooperatively assemble with tightly collapsed arms with their mean molecular surface dimensions closest to that of their estimated radius of gyration. It should be noted that most branched amphiphilic molecules studied at the air-water interface are usually synthesized such that they have clearly defined and localized hydrophobic/hydrophilic segments; that is, they typically are miktoarm stars[277], block copolymers[259, 261], star graft copolymers[243, 256], and hyperbranched/dendritic molecules[257, 260] in which the different cores, arms, block segments, and grafts are chemically distinct with different degrees of hydrophobicity/hydrophilicity. In this sense, these PolyIL

molecules are unique in that they have a "delocalized" amphiphilicity where the hydrophobic and hydrophilic balance is contested all the way down to the monomer scale.[258]

The observed collapsed morphologies are in stark contrast to that of ordinary strong polyelectrolytes, which tend to adopt stretched conformations to minimize electrostatic energy of the charged functional groups. Here, the large $TFSI^-$ anion with its small hydration shell exhibits a strong interaction with the PolyIL chains at the interface, bridging their hydration shells and inducing a pronounced decrease in chain dimensions. Evidently, the hydrophobic interactions inherent to the unique chemistry of ILs appear to dominate repulsive electrostatic interactions, despite the fact that the PolyILs are strong polyelectrolytes. This leads to a significant collapse, densification, and overlap between PolyIL chains at the interface, which in turn leads to the deposition of uniform, predominantly hydrophobic LB monolayers. Evidently, the PolyIL counterion ($TFSI^-$) is a critical agent that can be used to guide the assembly behavior.[277]

The PolyIL monolayers were highly susceptible to environmental changes; water submersion resulted in the reorganization of the uniform monolayer into regularly dispersed polymeric nanodroplets. Similar dewetting angles to previous studies suggest that stress relaxation to autocondensation mechanism is responsible for the dewetting.[247] However, the response was instigated here due to a change in environment in which the film thickness was restricted to molecular dimensions. Enhanced molecular control of the system thereby resulted in a monodisperse array of nanoscale aggregates with a characteristic length scale (intergranular distance) on the order of tens of nanometers—reminiscent of "spinodal dewetting".[275] Surface instabilities, structural relaxation, and capillary forces mediated by electrostatic and hydrophobic interactions all likely play roles in the migration of molecules and the resultant short-range lateral organization. But control of the feature sizes <100 nm with such a high surface density (two orders of magnitude higher than other dewetting mechanisms)[263] without the use of a template as observed here, in addition to their stimuli-responsive organization, does not appear to have been reported before using dewetting or anion-exchange procedures.

Interestingly, the results presented here demonstrate that PolyIL assembly characteristics as monolayers can be carried over to their integration into thicker LbL multilayers with control over the vertical and lateral organization. Therefore, the key component responsible for the similar physical interactions is likely the inclusion of the hydrophobic $TFSI^-$ ions (Figures 5.6, S5.5). The incomplete dissociation of $TFSI^-$ counterions upon PolyIL complexation within LbL multilayers is consistent with the hydration shell bridging effect, similar to the Langmuir monolayers. We suggest that for PSS-PolyIL complexation, the local aqueous environment associated with hydrated sulfonate groups will cause a retraction of PolyIL functional groups facilitated by the hydrophobic counterions, thereby decreasing the number of complexed linkages. Just as in the LB monolayers, the presence of these counterions in the multilayers will play a considerable role in the final film morphology, as observed in the wide diversity of surface structure, correlation length scale, roughness, and thickness achieved from different assembly conditions. Unique to the LbL films, however, was the opportunity to produce well-defined, stratified LbL multilayers in which one could induce long-range molecular migration to reversibly form porous morphologies and interconnected networks.

We propose that as the PSS aqueous solution is added to the substrate, exposed PolyIL segments will immediately contract as controlled by the $TFSI^-$ ions. Following this, dissociated $VBBI^+$ pendants will then coordinate with the free PSS chains in solution to form complex granules at the surface (Scheme 5.2).

**Scheme 5.2.** Illustration of the step by step LbL deposition process of the immiscible PIL/PE components. Note that the PEI prelayer and counterions are excluded for clarity.

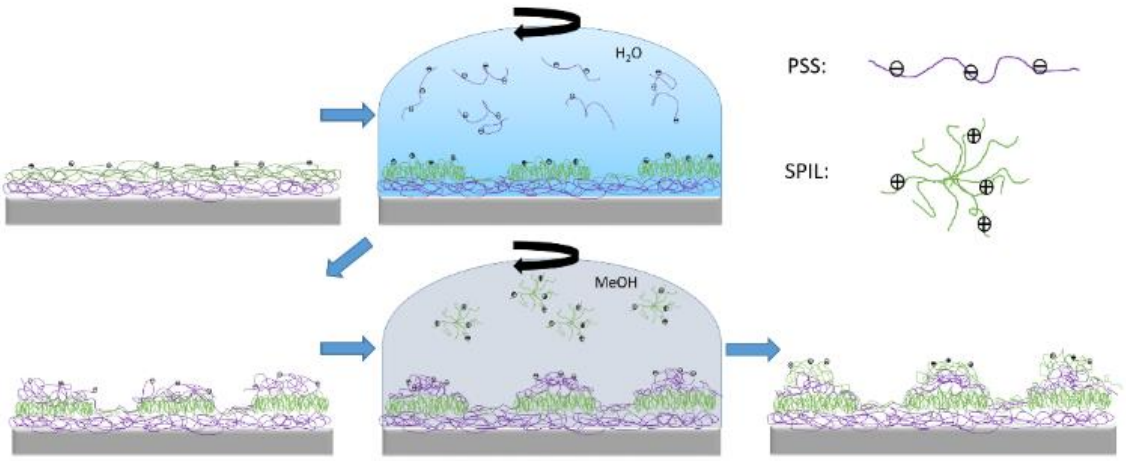

The PolyIL chains within these aggregates are then pinned into place by the ionic crosslinks joining the PolyIL molecules to the neighboring PSS layers. These constraints prevent expansion and reorganization of the PolyIL chains to a neat stratified layer during the next PolyIL deposition. In this manner, surface undulations will emerge and grow with each subsequent deposition, progressively increasing the surface roughness (Figure S13). This schematic also explains why the correlation length—distances between the surface granules within LbL multilayers—is almost twice that of the monolayers. The polymeric droplets which form in the LB monolayers are, throughout the LbL process, restrained by complexing PSS chains in the thicker LbL bilayers. As more layers are deposited, the characteristic wavelengths associated with the short-range ordered hydrophobic granules begin to emerge[265], and continuously shift to lower wavevectors reflecting the larger distances between the surface granules (Scheme 2). After a certain number of deposition cycles, deep surface pits with diameter on the order of a few hundred nanometers appear to emerge, manifesting the long-range structural reorganization of these regularly dispersed surface granules.

Polyelectrolyte complexation is known to occur via two extreme processes: "ladder-like" organization in which two oppositely charged polyelectrolytes linearly align to cooperatively stitch functional groups and the "scrambled salt" organization where multiple chains assume a stochastic pairing of ionic groups.[278] Given the topological mismatch of linear PSS/star PolyIL chains, the mechanism of association is likely dominated by the latter process, giving star molecules more freedom to detach and reorganize large segments into more energetically favorable conformations. It follows that star PolyILs, having a lower degree of ionic cross-linking and hastened interdiffusion, exhibit higher mobility during the spin-casting process. The resulting long-range migration into advanced dewetted structures at star PolyIL surfaces contrast considerably to the morphology observed in the linear analogues (Figure 5.5).[242]

In addition to capillary forces, residual stresses in confined, kinetically arrested systems have been shown to act as an extra driving force for dewetting.[279, 280] The fast evaporation of polymer solution effectively freezes chains into non-equilibrium, entangled configurations as the mixture passes through its glass transition, storing elastic energy that

can serve as a destabilizing factor in shrinking the film volume over time. Moreover, confinement of the polyelectrolytes into ultrathin glass layers at the interface is imposed by strong electrostatic interactions of the charged units within polyelectrolyte complexes, which restricts polymer chains from assuming entropically favored configurations of the melt state.[280] Supplementary sources of stress in the final LbL films is likely produced by the cyclic swelling/collapsing perturbations imposed on these crosslinks throughout the LbL assembly.[281] A glassy matrix would also seem to explain why the pore size distribution exhibited negligible changes following solvent annealing wherein long-range migration is inhibited by frozen mobility.

The results presented in this work point towards the combined effects of high star mobility in the casting process with large residual stresses generated by the long, entangled frozen arms as the likely driving forces to long-range restructuring of the surface into granular and porous morphologies of higher molecular weight PolyILs. Increasing the degree of polymerization of the star molecules results in a greater stored elastic energy, larger deformation of the PolyIL surface, and therefore the greatest density and size of nucleated holes as well as roughness and contact angle (Figure 5.9). Increasing the molecular mobility through salt addition or producing more surface aggregations via water washing steps are shown to be additional routes to facilitating lateral restructuring in PolyIL LbL films, regardless of the molecular weight and topology. It should be emphasized that previous studies of polymer thin film dewetting either require thermal annealing.[266] In contrast, no special post-assembly treatment was required to induce restructuring of LbL films, which is likely a consequence of its already low $T_g$ inherent to PolyILs (for poly($VBBI^+TFSI^-$), $T_g$~0 °C).

It should be added that the assembly of LbL films incorporating a highly hydrophobic, compartmentalized component has rarely been demonstrated. Rouse and Ferguson showed that hydrophobic polystyrene (PS) could be incorporated in a stepwise fashion[282], but in that study PS was not one of the intrinsic components but an extrinsic “interlayer” that attenuated subsequent growth. The regular and stable growth of alternating hydrophilic polyelectrolyte and hydrophobic PolyIL components demonstrated here should be useful for generating compartmentalized films. It is also shown that lateral organization can be

induced towards both porous and smooth, stratified films via dewetting mechanisms. Zhao et al. have shown PolyIL-based LbL to be a promising method for generating nitrogen-doped capsules with high surface area[251]; this work illustrates how knowledge of the assembly behavior specific to PolyILs can be used to provide additional handles on the nanoscale texture and thickness of such capsules. Moreover, controlling the pore size distribution in nanofabricated films enables their prospective application to molecular separation membranes with tunable nanostructures and uniform separation.[276] Establishing lateral control of LbL structures is generally relevant to applications in which transport properties require organization of the microstructure at the nanometer scale. [106,283]

In summary, the various inter- and intramolecular forces governing the stimuli-responsive chain conformations of PolyILs were examined in regards to controlling their assembly at interfaces and within three dimensional multilayers at both the nano- and microscale. Successful formation of stable star PolyIL and metastable linear PolyIL Langmuir monolayers at the air-water interface is demonstrated. It was shown that size and packing efficiency significantly depend on the molecular topology as well as molecular weight. Monolayers were then transferred to solid substrates to form hydrophobic, molecularly thin films with peculiar reversible stimuli-responsive behavior; exposure to water disrupted the hydrophobic and electrostatic interactions of PolyIL molecules to condense the monolayer into regular, monodisperse polymeric nanodroplets with a correlation length scale below 100 nm. This reorganization could be programmed by the deposition pressure and molecular topology. Furthermore, it was demonstrated that unique chemical nature of the hydrophobic PolyIL molecules could be combined with PSS to form robust, compartmentalized LbL membranes of hydrophobic character, distinct from conventional polyelectrolyte-based LbL films. The assembly procedure, ionic strength, molecular architecture of the PolyILs, and post-treatment of the as-assembled films can be exploited to tailor the final morphology, porosity, and thickness. The PolyIL assemblies explored in this study are relevant to the guided design of sophisticated coatings and nanostructured membranes with dynamically controlled permeability, encapsulation, and transport properties.

## Chapter 5 Appendix: Supporting Information

*Calculation of Macromolecular Dimensions*

End-to-end molecular dimensions R of linear PIL chains were calculated using Materials Studio Software according to the usual procedure.[284] From the calculated R value of the random coil linear molecule, the statistical monomer length b (~1.15 nm) can be ascertained based on its degree of polymerization N. This in turn allows for the determination of the radius of gyration $R_g$ for linear chains assuming random walk configurations in three dimensions (i.e. at the θ temperature):

$$R_{g,linear}^2 = \frac{Nb^2}{6} \qquad (5.1)$$

For star macromolecules with f arms, the linear and branched $R_g$ values can be related from the ratio:

$$g = \frac{R_{g,linear}^2}{R_{g,star}^2} = \frac{(3f-2)}{f^2} \qquad (5.2)$$

thereby allowing for a simple estimation of the radius of gyration of the star PILs in this report.[285] Note that this model makes the assumption that excluded volume effects for branched molecules are similar to those in their linear analogues. Furthermore, it is also assumed for these calculations that full initiation of the polyILs from all 14 initiating arms occurred. This is justified by the well-defined star architectures and low polydispersity in arm lengths as measured by GPC of star polymers and their cleaved arms formed via ATRP from BCD cores in similar studies.[286]

*Pressure-Area Isotherms*

An increase in surface pressure of the gaseous phase following the initial compression was observed for all samples, indicating a residual surface tension in the monolayer (Figure S5.1). This tension is likely a product of strong secondary intermolecular forces that lead to enhanced hydrophobic interactions and chain entanglement.[284] The residual pressure disappears only at very large expansions, suggesting that intermingled molecules are

kinetically locked together upon expansion, and only after sufficiently long times can they recover their initial conformation. This is supported by AFM phase images of LB monolayers deposited from the gaseous phase before and after compression (Figure S5.2).

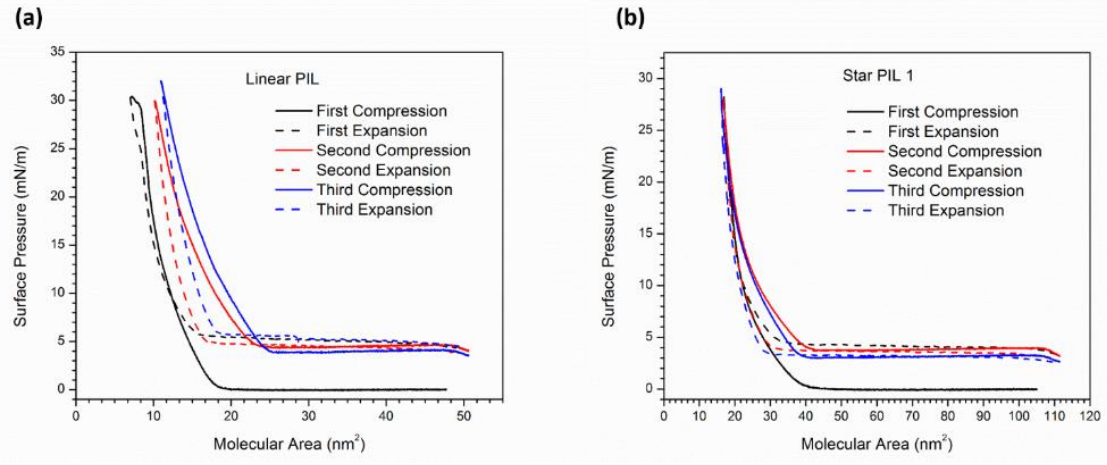


**Figure S5.1**. Compression/expansion hysteresis pressure-area isotherms of the linear (a) and a star (b) PIL sample. Solid and dashed lines indicate compressions and expansions, respectively. Black, red, and blue curves represent the first, second, and third cycles, respectively.

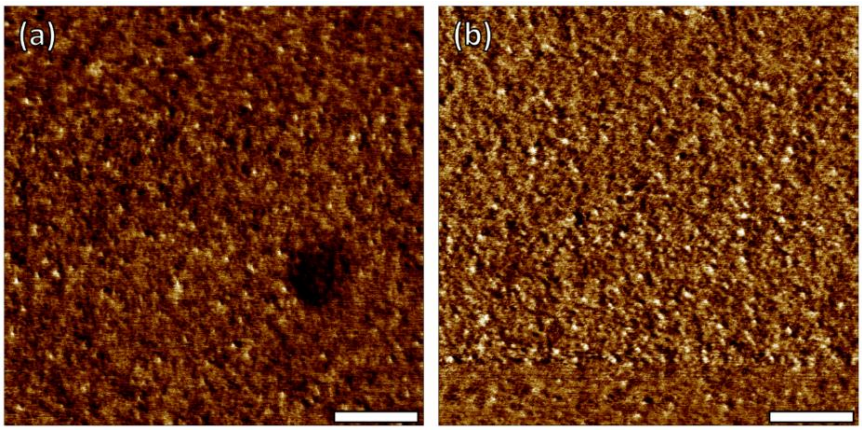


**Figure S5.2**. High resolution AFM phase images of LB monolayers of SPIL-2 in the gaseous phase before (a) and after (b) the first compression/expansion at the same trough area. Scale bar is 100 nm; Z scale is 5°.

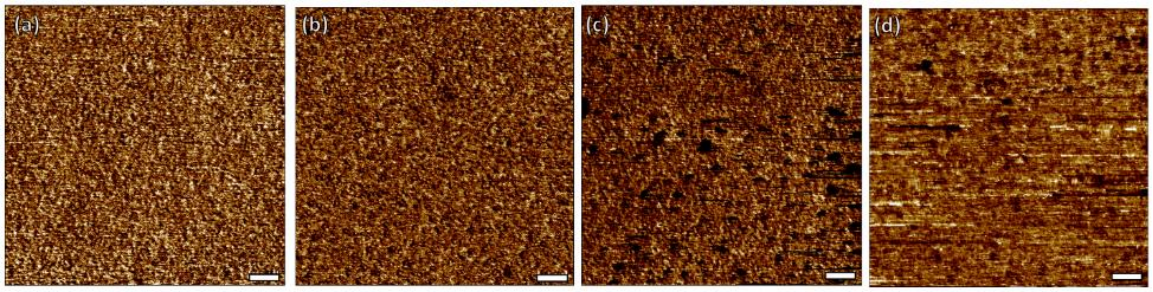


**Figure S5.3**. AFM phase images of LB monolayers LPIL (a), SPIL-1 (b), SPIL-2 (c), and SPIL-3 (d) at a surface pressure of 5 mN/m. Scale bar is 100 nm; Z scale is 5°.

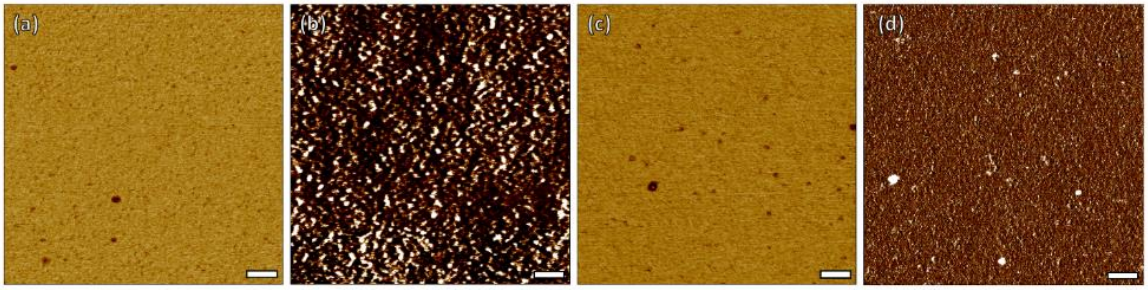


**Figure S5.4**. AFM phase images of LB monolayers LPIL (a), SPIL-1 (b), SPIL-2 (c), and SPIL-3 (d) at a surface pressure of 20 mN/m. Scale bar is 100 nm; Z scale is 15°.

**Table S5.1**. Thickness, roughness, and contact angle measurements for LbL films.

| Assembly Condition | Sample | Growth Rate (nm/bilayer) | Ellipsometry Thickness (nm) | 1μm x 1μm Rq (nm) | 10μm x 10μm Rq (nm) | Contact Angle (°) |
|---|---|---|---|---|---|---|
| Dip-LbL MeOH Wash | LPIL | 0.14 ± 0.01 | 4.8 ± 0.6 | 1.3 ± 0.4 | 1.8 ± 0.3 | 67.6 ± 2.4 |
| | SPIL-2 | 0.10 ± 0.02 | 4.4 ± 0.4 | 2.0 ± 0.2 | 2.4 ± 0.3 | 65.1 ± 2.8 |
| SA-LbL MeOH Wash | LPIL | 0.89 ± 0.01 | 18.4 ± 0.7 | 3.3 ± 0.4 | 3.4 ± 0.4 | 70.9 ± 2.9 |
| | SPIL-1 | 0.97 ± 0.01 | 21. 4 ± 0.9 | 1.5 ± 0.3 | 1.7 ± 0.4 | 72.5 ± 3.0 |
| | SPIL-2 | 0.89 ± 0.01 | 16.9 ± 0.8 | 2.5 ± 0.4 | 3.2 ± 0.6 | 70.6 ± 0.8 |
| | SPIL-3 | 1.10 ± 0.01 | 24.0 ± 1.5 | 1.8 ± 0.4 | 2.5 ± 0.4 | 75.2 ± 1.3 |
| SA-LbL H2O Wash | LPIL | 1.49 ± 0.03 | 30.7 ± 2.1 | 4.6 ± 1.4 | 3.6 ± 0.5 | 72.3 ± 1.8 |
| | SPIL-1 | 1.45 ± 0.21 | 28.8 ± 0.6 | 3.8 ± 1.6 | 3.4 ± 1.2 | 74.3 ± 1.5 |
| | SPIL-2 | 1.84 ± 0.02 | 27.8 ± 6.6 | 5.8 ± 1.9 | 5.7 ± 1.5 | 79.8 ± 1.3 |
| | SPIL-3 | 1.50 ± 0.06 | 29.0 ± 0.7 | 8.8 ± 1.9 | 7.8 ± 2.4 | 80.0 ± 0.7 |
| SA-LbL H2O Wash 0.01M NaCl | LPIL | 2.27 ± 0.06 | 43.3 ± 4.0 | 8.2 ± 2.1 | 10.9 ± 2.3 | 70.6 ± 2.2 |
| | SPIL-2 | 2.30 ± 0.08 | 42.9 ± 1.2 | 6.8 ± 2.3 | 10.4 ± 0.7 | 77.5 ± 2.1 |

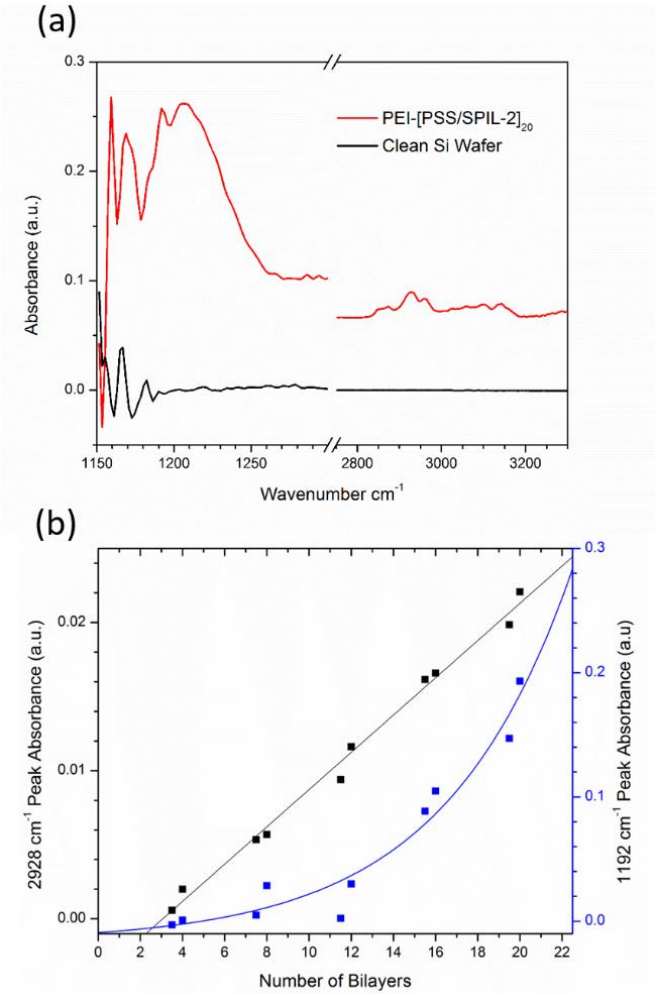


**Figure S5.5.** ATR-FTIR spectra (a) measured from a bare Si substrate (black) and 20 bilayer PSS/SPIL-2 LbL films (red). Peak absorbance values corresponding to the $VBBI^+$ repeat unit (black) and the $TFSI^-$ anion (blue) are displayed as a function of the bilayer number (b). Note that FTIR measurements were performed for both PSS-capped (half integer number of bilayers) and SPIL-capped (integer) films. The black and blue lines denote linear and exponential fits to the data, respectively.

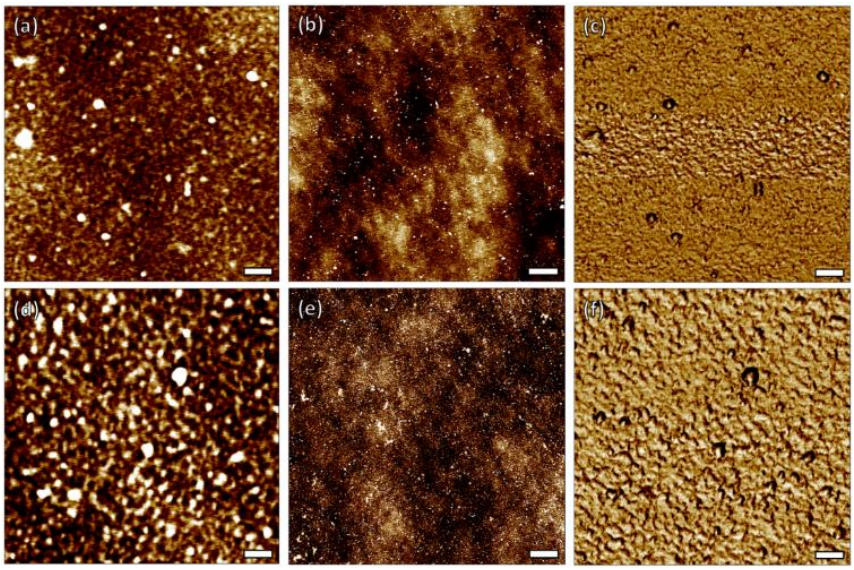


**Figure S5.6**. (a,b,d,e) AFM topography and (c,f) phase images for dip-LbL PEI-$[PSS/PIL]_{20}$ films containing (a-c) LPIL and (d-f) SPIL-2. PSS layers were washed with water; PIL layers were washed with MeOH. Scale bar for (a,c,d,f) is 100 nm; scale bar for (b,e) is 1 μm. Z scale is 6 nm for topography images and 7° for phase images.

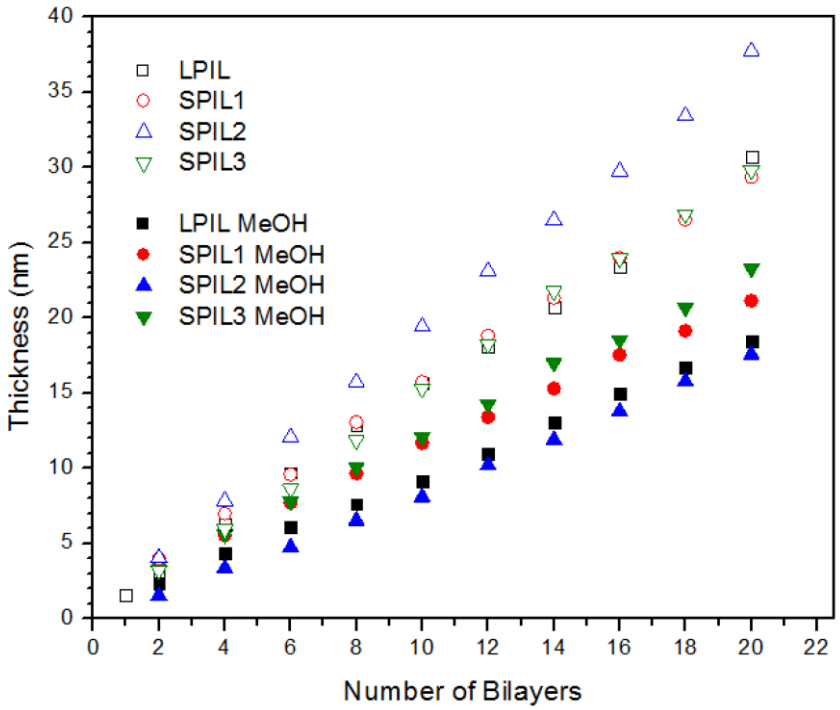


**Figure S5.7**. Thicknesses of SA-LbL films as a function molecular weight. Open and filled symbols denote LbL films assembled under water-washing and MeOH-washing conditions, respectively.

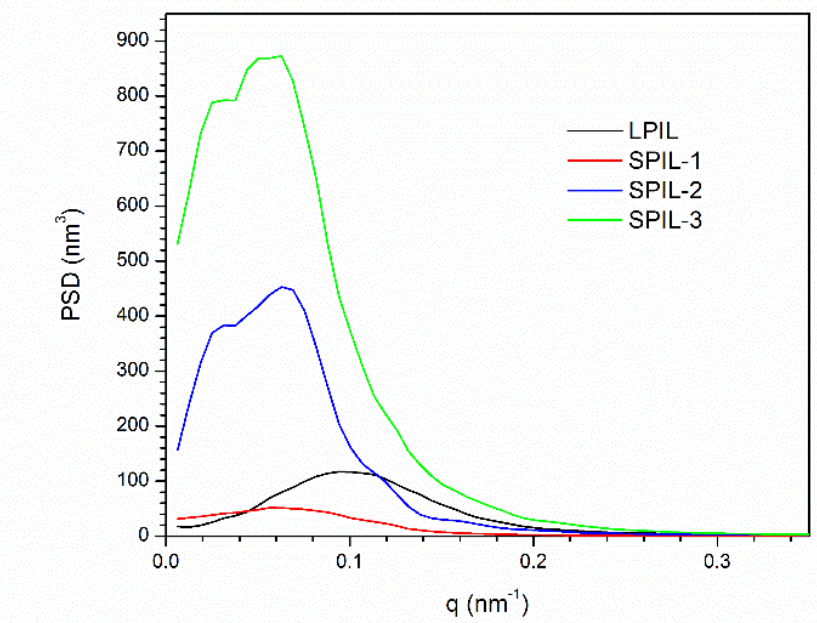


**Figure S5.8**. Radially integrated PSD profiles corresponding to 1 x 1 μm$^2$ AFM scans of SA-LbL films washed by water.

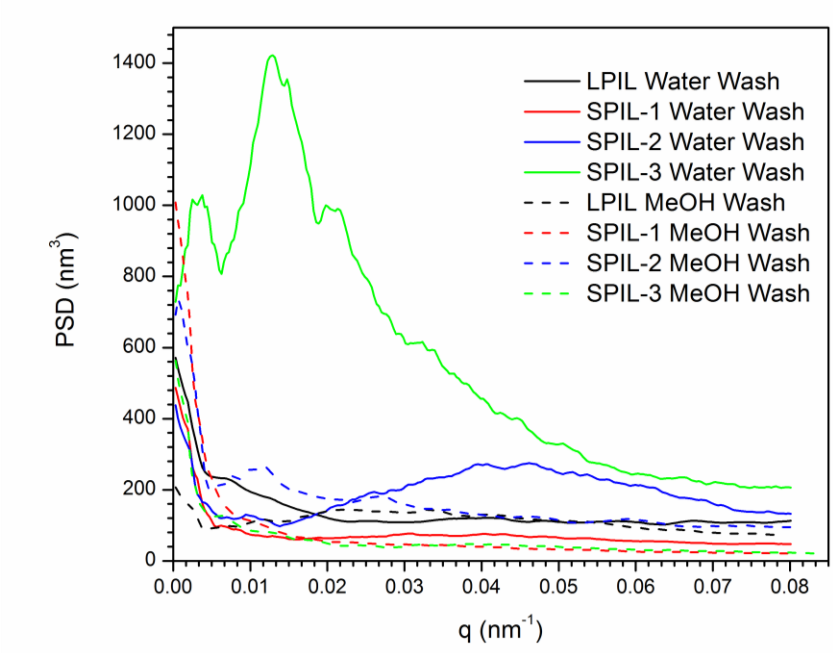


**Figure S5.9**. Radially integrated PSD profiles corresponding to 10 x 10 μm$^2$ AFM scans of SA-LbL films washed by water (solid lines) and methanol (dashed lines).

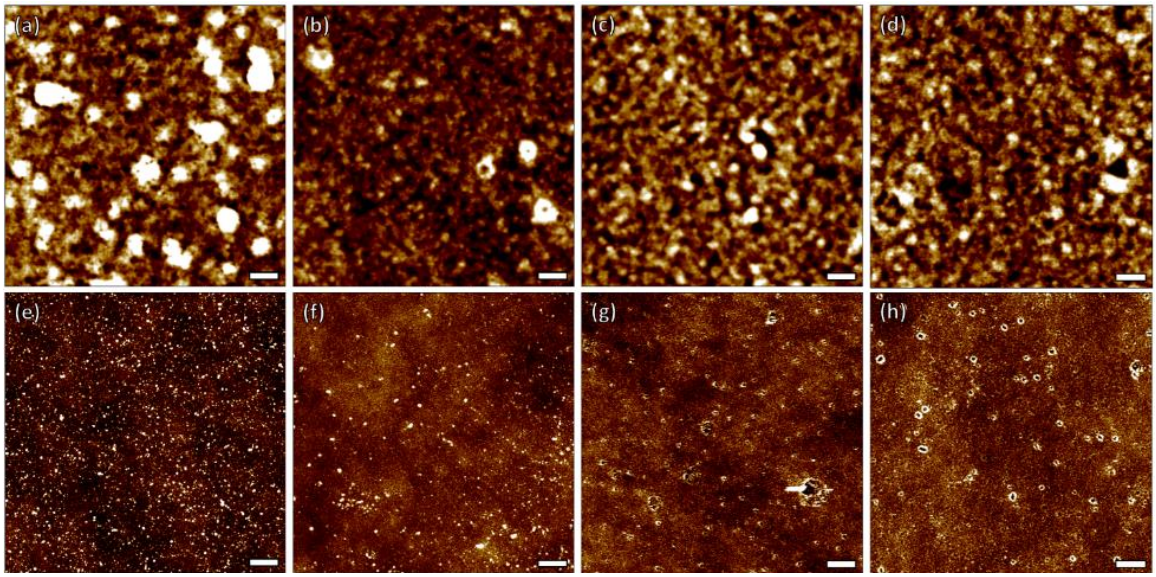


**Figure S5.10**. AFM topography images of SA-LbL PEI-[PSS/PIL]$_{20}$ film containing (a,e) LPIL, (b,f) SPIL-1, (c,g) SPIL-2, (d,h) SPIL-3. PSS layers were washed with water; polyIL layers were washed with MeOH. Scale bar for (a-e) is 100 nm; scale bar for (e-h) is 1 μm. Z scale is 10 nm for top; 15nm for bottom.

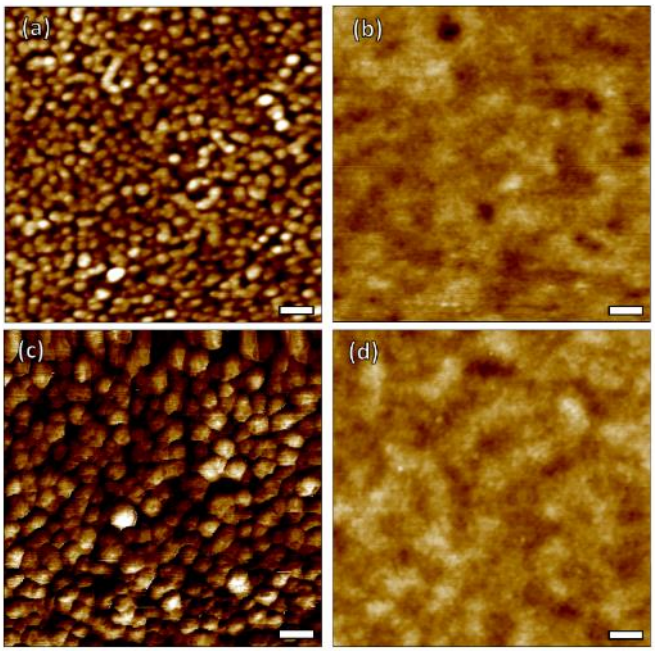


**Figure S5.11.** SA-LbL PEI-[PSS/LPIL]$_{20}$ (a,b) and PEI-[PSS/SPIL-2]$_{20}$ (c,d), after 1 h immersion in water (a,c), and then after 1 h in MeOH (b,d). Scale bar is 100 nm; Z scale is 20 nm.

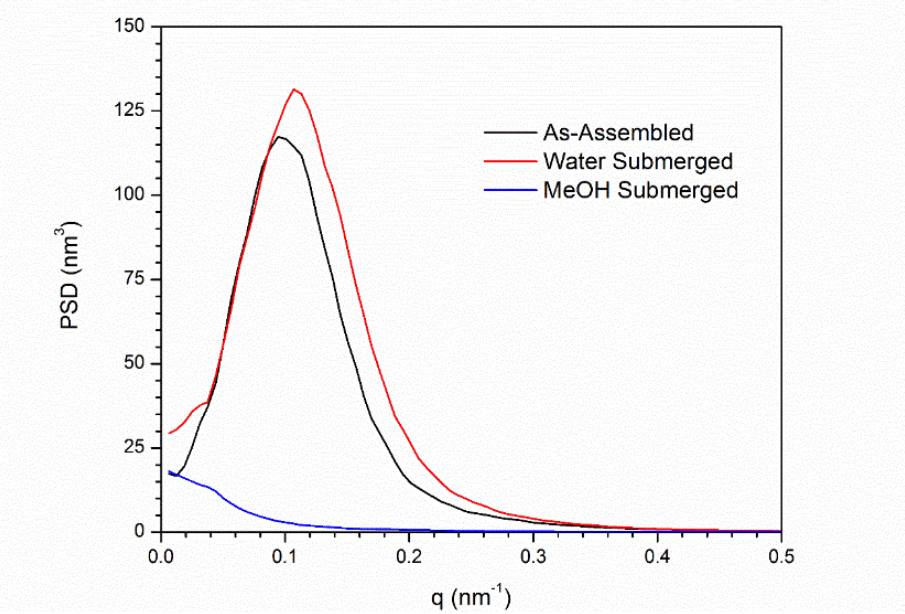


**Figure S5.12**. Radially integrated PSD profiles corresponding to 1 x 1 μm$^2$ AFM scans of as-assembled SA-LbL films washed by water (black line), followed by water submersion (red line), and then MeOH submersion (blue line).

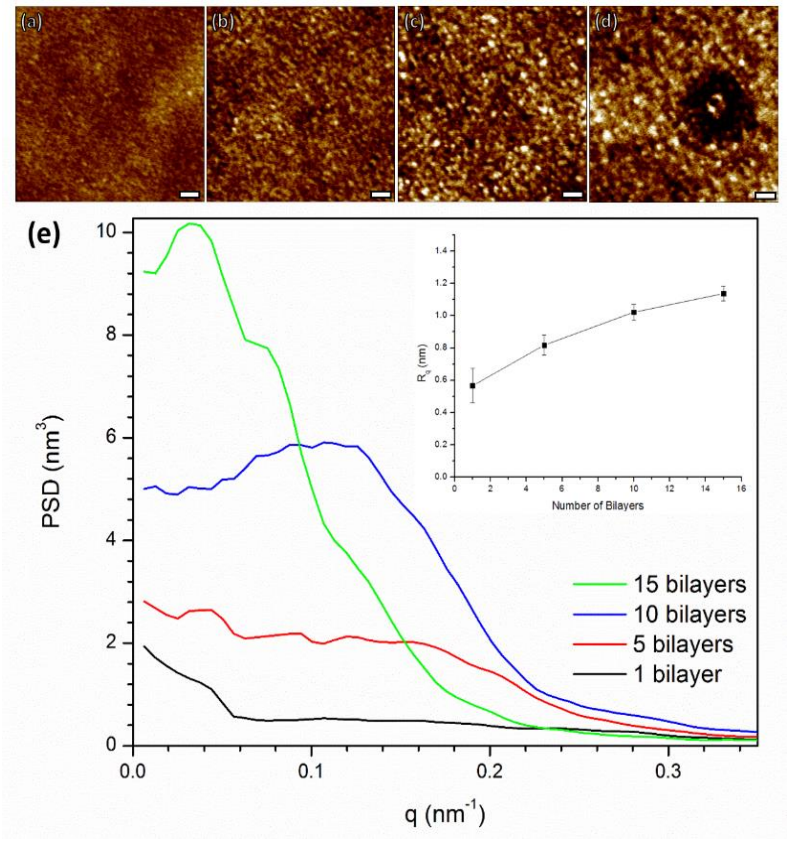


**Figure S5.13.** AFM topographical images of SA-LbL PEI-[PSS/SPIL-2] with one complete bilayer (a), 5 bilayers (b), 10 bilayers (c), and 15 bilayers (d), and their corresponding PSD profiles (e). Inset of (e) shows $R_q$ as a function of the number of bilayers, collected from 5 independent 1 x 1 μm$^2$ scanning areas. Scale bar is 100 nm; Z scale is 6 nm.

# CHAPTER 6. VISCOELASTIC PROPERTIES AND ION DYNAMICS IN STAR-SHAPED POLYMERIZED IONIC LIQUIDS

## 6.1 Introduction

Solid polymer electrolytes are central to the design of many functional ionic materials due to their ability to perform the primary function of their low molecular weight analogues (e.g., ion transport) while improving upon their thermal, mechanical, and electrochemical stability, in addition to overall safety.[287] The ionic and viscoelastic duality of PolyILs has therefore been variously exploited in the design of flexible supercapacitors, soft actuators, responsive hydrogels, thin film transistors, gas separation membranes, and redox-active materials.[288,289,290,291,292,293] Due to the polymerization and single-ion conductivity inherent to PolyILs, the viscoelasticity, gas permeability, and other physical properties of ILs can potentially be tailored independently of the ion transport.

Recent studies of chain rigidity, molecular weight, chemical constitution, counterion type, and monomer structure reveal a diverse range of melt morphologies and dynamic properties of PolyILs.[294,295,296,297,298,299,300,301,302,303,304,305,306,307,308] In contrast, the role of star polymer architecture on the morphology and dynamic behavior has received comparatively little attention.[309,310,311] Few relationships between the branching architecture and ion transport have been established. For example, the opposing contributions of ion density and chain flexibility have been proposed to be important considerations but have not been thoroughly explored.[312]

Star-shaped polymers are particularly interesting because at different length scales, the monomers, arms, and macromolecule will influence the segmental, chain, and 'particle-like' ordering respectively. Depending on the star functionality $f$ and arm length $N_{arm}$, organization in melts can result in hierarchical relaxation processes with distinct dynamic behavior.[313,314,315,316,317,318,319] For instance, the coupling between the retracting chain-like arms and rigid cores in polymers with high branching ratios $f/N_a$ can greatly enhance melt elasticity while having a relatively limited effect on viscosity.[319,320] Moreover, nonuniform

segmental densities, intermolecular entropic repulsions, and anomalous packing of branched polymers have been reported to influence the glass transition temperature, fragility, structural organization, and ion confinement.[309,319,321,322,323,324,325,326] To date, little is known regarding how the different dynamics and thermomechanical behavior of neutral or traditional polyelectrolyte stars translate to PolyIL systems. In this chapter, we ascertain the role of star polymer architecture on the dynamics, mechanical properties, and single-ion conductivity in PolyILs by examining the viscoelastic and dielectric response of several imidazolium-based, linear and star-shaped macromolecules with different molecular weights.

## 6.2 Experimental

### *Film Preparation for FTIR and AFM*

PolyILs were dissolved in methanol (10 mg/mL) and spin-coated on cleaned silicon wafers (AFM) and an ATR crystal (FTIR) and air dried to form PolyIL films with microscale thickness. Afterward, the samples were thermally annealed at 100 ℃ for 12 h under vacuum prior to AFM imaging.

## 6.3 Results and Analysis

### Thermal, Chemical, and Structural Characterization

The $VBBI^+TFSI^-$ monomer volume $V_m$ is estimated to be approximately ~0.67 $nm^3$ based on literature values for the analogous poly(1-butyl-3-vinylimidazolium TFSI) monomer (0.473 $nm^3$) and an added ethylbenzene unit.[295] Using the known inverse correlation between the glass transition temperature $T_g$ and $V_m$, the PolyILs studied here are expected to possess a $T_g$ ca. 270 K.[327,328] Indeed, DSC measurements reveal $T_g$ values within the range 266-274 K, in good agreement with that expected from the literature (Figure 6.1a). In addition, all samples are amorphous with no crystallization observed in the investigated temperature window (193 to 353 K). Accordingly, XRD data reveals two broad peaks at roughly $q_1$ ~ 8 $nm^{-1}$ and $q_2$ ~ 14 $nm^{-1}$, corresponding to distances of $d_1$ ~ 0.8 nm and $d_2$ ~ 0.45 nm, respectively (Figure 6.1b). These features are commonly observed in imidazolium/TFSI (ImTFSI) systems and correspond to the anion-anion correlations and

the short-range ordering of polymer backbones, respectively.[295,305,306] Note that the predicted monomer size $r_m \cong V_m^{1/3} \cong 0.88$ nm corresponds well to the anion-anion correlation distance $d_1$.

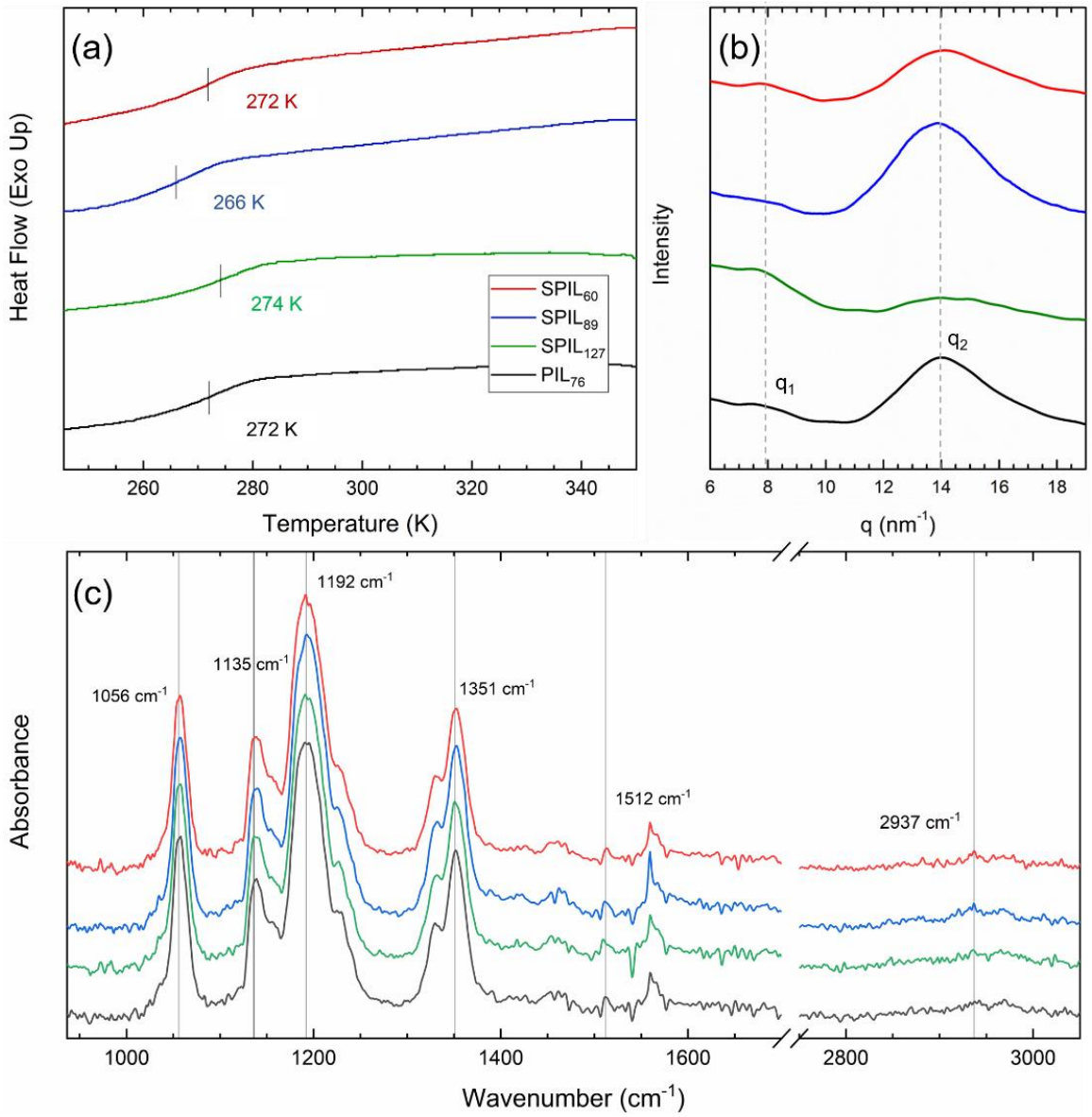


**Figure 6.1.** Thermal, structural, and chemical characterization of the PolyILs. The data are shifted vertically for clarity (a-c). (a) DSC thermograms show the glass transition on cooling. (b) XRD data reveal broad peaks corresponding to the ion correlations ($q_1$) and the amorphous ordering ($q_2$). (c) IR spectra confirm the chemical composition and indicate no shifts in the positions of the adsorptions peaks corresponding to the ionic liquid groups.

The expected chemical composition is confirmed by IR to be independent of the PolyIL architecture (Figure 6.1c). Typically, shifts in the adsorption peaks of the ionic liquid moieties imply changing ion interactions, dissociation, or aggregation behavior.[307,374,329,330] Neither the adsorption peaks normally attributed to the TFSI counterions (1056 $cm^{-1}$ for the asymmetric S-N-S stretching; 1192 $cm^{-1}$ and 1351 $cm^{-1}$ for the sulfonyl group) nor the imidazolium side chain (1512 $cm^{-1}$ and 2850-3000 $cm^{-1}$) exhibit appreciable shifts within experimental resolution.[309,374,329] Just as previous reports have determined there to be no correlation between counteranion size and ionic interactions in imidazolium-based PolyILs, neither does molecular architecture appear to have any influence on the ionic environment.[307] This is consistent with the XRD data, which shows no significant changes in the inter-chain and inter-ion distances between different Poly($VBBI^+TFSI^-$)s.

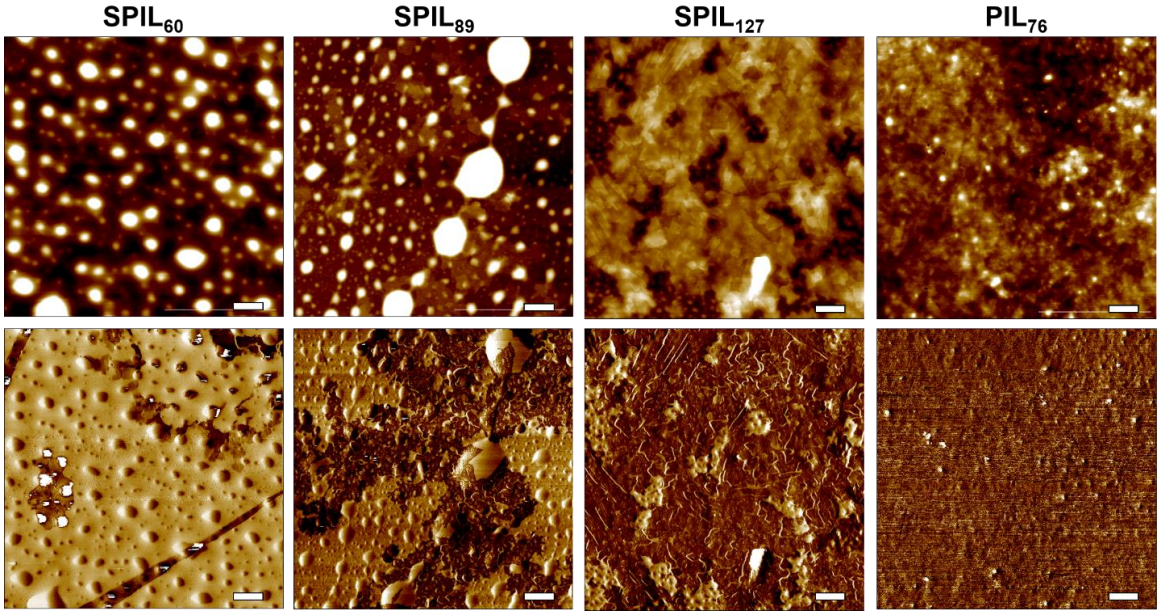


**Figure 6.2.** AFM height (top) and phase (bottom) images of the indicated PolyILs. Z scales for the star PolyILs are 55 nm and 25 °; Z scales for the linear PolyIL are 10 nm and 15 °. All scale bars are 500 nm.

On the other hand, AFM imaging, reveals a considerable dependence of the microscale PolyIL surface morphology on the macromolecular architecture (Figure 6.2). Star PolyILs with shorter arms (smaller $N_{arm}$) appear to form discrete, submicron aggregated clusters (size within ~100-500 nm) which may be clearly distinguished from the smoother, more homogenous morphology observed in the linear counterpart. Stars with longer arms—the intermediate case—feature a heterogeneous surface; high-resolution phase maps outline

long-chain aggregates that percolate through domains of the discrete clusters (Figure S6.1). The star PolyIL surface morphologies are reminiscent of the 'micellar-like' organization that arises from the limited-aggregation of other branched polymers in thin films.[309,323,324,326]

***Viscoelastic Response***

To examine dynamic processes over a wider frequency range, time-temperature superposition (tTS) is used to construct the SAOS master curves (Figure 6.3).[303,307,331,332,333] The horizontal shift factor $a_T$ follows the empirical Williams-Landel-Ferry (WLF) relationship:

$$\log a_T = \frac{-C_1(T-T_r)}{C_2-(T-T_r)} \qquad (6.1)$$

where $C_1$ and $C_2$ are constants related to the apparent activation energy and fragility (Figure S6.2).[295,307,334] The fitted parameters for the WLF equation are provided in Table S6.1.

The master curve of the linear poly(VBBI$^+$TFSI$^-$) is qualitatively similar to LVE spectra reported for other ImTFSI-based PolyILs.[295,331,332,333] The response is mostly elastic ($G' > G''$) in the glassy regime at the highest frequencies while, at intermediate frequencies, the real and imaginary components cross at the glass-to-rubber transition and the PolyIL exhibits viscoelastic behavior. This dynamic transition is associated with a characteristic rate of segmental dynamics $\omega_s$ which is defined here by the intersection of the $G'$ and $G''$ (Figure 6.3).[296,297] The temperature dependence of $\omega_s$ is compared to other dynamic processes later on (Table 6.1). In the viscoelastic regime ($\omega < \omega_s$), an apparent power-law scaling of $G' \sim G'' \sim \omega^{2/3}$ is observed. Although the scaling exponent is reminiscent of Zimm relaxation, this result is frequently reported in other PolyILs, as well as some hyperbranched and star polymers.[295,316,320] It is usually attributed to the coupling of the

segmental dynamics to the high frequency Rouse modes and results in a broader glass-to-rubber transition.[316,333,335]

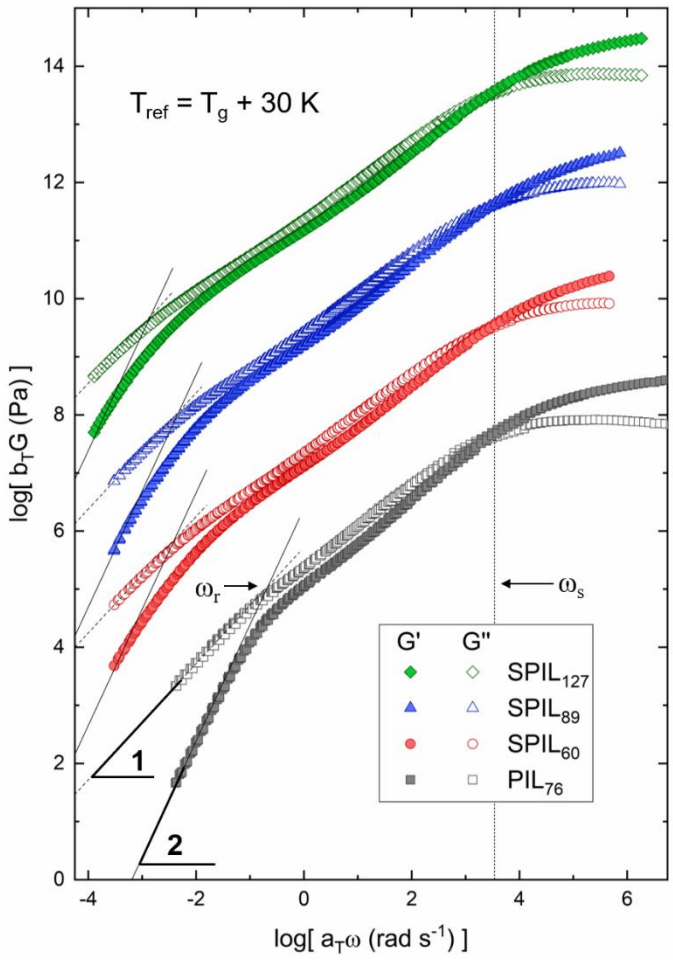


**Figure 6.3.** LVE spectra, represented by the storage *G'* (filled symbols) and loss *G''* (open symbols) moduli. Master curves were constructed from tTS using the reference temperature $T_r = T_g + 30$ K. Adjacent curves from different samples are offset by 2 decades for clarity. The dotted vertical line indicates the rate of segmental relaxation $\omega_s$. Thin lines at the lowest frequencies represent best fits applied to the limiting terminal flow behavior in the determination of $\eta$.

At the lowest frequencies, terminal relaxation and flow is observed. It is apparent that as $M_n$ of the star PolyILs increases, the separation between the terminal and segmental timescales grows larger. No rubbery plateau nor a second crossover of the shear moduli components are observed in any of the samples at longer times, suggesting the absence of chain entanglements in the poly(VBBI$^+$TFSI$^-$) melts.[320,336] This is not surprising, considering that the critical chain length for observing entanglement effects in other

poly(ImTFSI)s is reported to be quite high—ca. $N_c \sim 100$.[331] That the $SPIL_{127}$ melt shows no obvious signs of entanglement effects may be related to the additional phenyl group in the poly($VBBI^+TFSI^-$)s, the star architecture, or the higher polydispersity for this sample (Table 3.2). In fact, the rotational hindrance imposed by the bulky IL pendant/counterion composition as well as the steric crowding around branch points in nonlinear polymers are both known to increase the dynamic chain rigidity.[320,333,337]

Instead, the LVE response approaches characteristic viscous liquid behavior at the lowest frequencies: $G' = J_{eq}\eta^2\omega^2$ and $G'' = \eta\omega$.[335] The real and imaginary components are thus simultaneously fitted in the terminal regime with the steady state compliance $J_{eq}$ and zero shear viscosity $\eta$ as freely varying parameters (Figure 6.3). The analysis allows for the estimation of $\eta$ for the linear and star PolyILs and confirms the pronounced effect of both chain length and branched architecture on the slower, long-range structural organization in PolyIL melts (Figure 6.4).

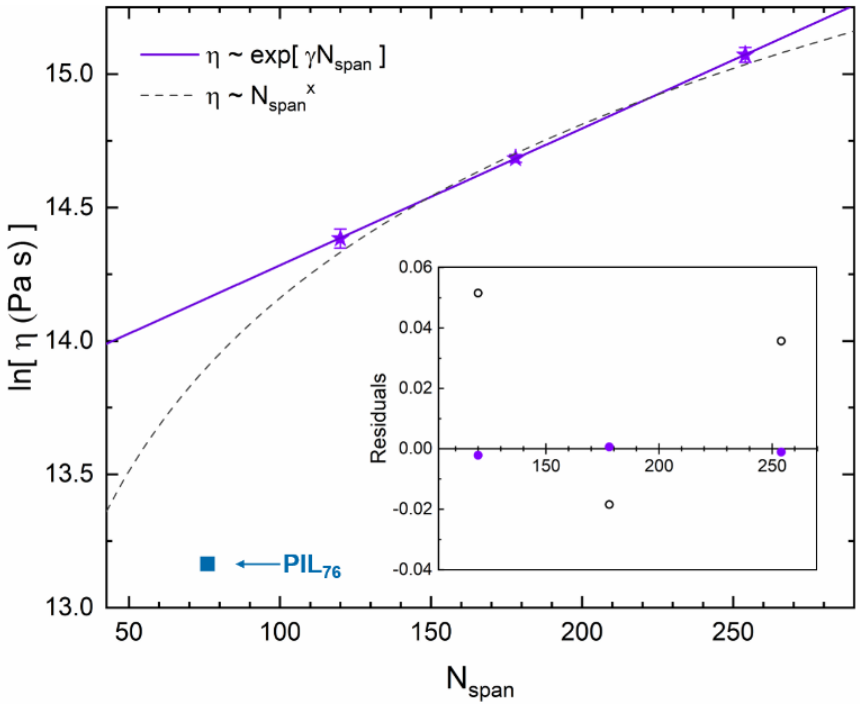


**Figure 6.4.** Zero-shear viscosity vs. the star span length. The solid purple line shows the fitted exponential dependence of star $\eta$ on $N_{span}$ (purple star symbols). For comparison, the dashed gray line represents a fitted power law dependence with exponent $x = 0.93$. The corresponding residuals are presented in the inset. For reference, the linear PolyIL is also indicated by the blue square with $N_{span} = N$, but is not included in the fitting.

In particular, $\eta$ for the star melts is more than an order of magnitude greater than that of the linear, despite $N_{arm}$ being similar in size to $N$ of the linear polymer. Even if $N$ is compared to the longest molecular strand, or span length $N_{span} = 2N_{arm}$ of the stars, the expected power law scaling of viscosity on the effective linear chain size $\eta \sim N_{span}^{x}$ cannot adequately describe the abrupt increase in $\eta$ between PolyILs of different architectures. This finding indicates the arms do not relax independently of one another as single chains; a separate description of the star terminal dynamics should consider covalent connectivity at the core. Specifically, the exponential dependence of $\eta$ on the arm/span length that is typically encountered in traditional star polymer melts is found to be a better description of the star-shaped poly(VBBI$^{+}$TFSI$^{-}$)s (Figure 6.4 inset).[319,335,338] The low frequency LVE data therefore suggest star PolyILs relax via a distinct arm retraction mechanism that is qualitatively similar to that of neutral star polymers.

Lastly, the specific overall influence of nonlinear polymer architectures can be distinguished by plotting the phase angle $\delta$ against the shear modulus magnitude in the Van Gurp-Palmen (vGP) representation (Figure 6.5).[336,337,339] Minima in the vGP plots indicate relaxation processes whose elastic character is proportional to the depth or amplitude of the feature. It is clear that all samples—regardless of chain architecture or size—show identical segmental/glassy dynamics at the high-modulus end; below $\delta_s = 45°$, $G' > G''$ and the phase angle drops to a high-frequency minimum outside the experimental window. A recent BDS study on PDMS bottlebrush polymers similarly demonstrated that while branched polymers can slightly slower segmental relaxations, as the molecular weight of the side chains increase, the alpha relaxation time becomes indistinguishable from the linear counterpart; the effect of branched architecture on the dynamics becomes negligible.[340] Hence, the star PolyILs examined here likely have arms which are too long to manifest any branching effects on the segmental relaxation in these viscoelastic experiments.

There is a second minimum around $10^5$ Pa whose position and elastic character are sample dependent. For the linear analogue, this feature is less pronounced as a weak shoulder. The effect of star architecture on the overall viscoelastic dynamics of PolyIL melts is thus demonstrated to be qualitatively similar to that reported for neutral polymers: branching

predominately influences terminal relaxation at long timescales while the faster segmental dynamics remain essentially unchanged (Figures 6.3 and 6.5).[313,314,316,336,337]

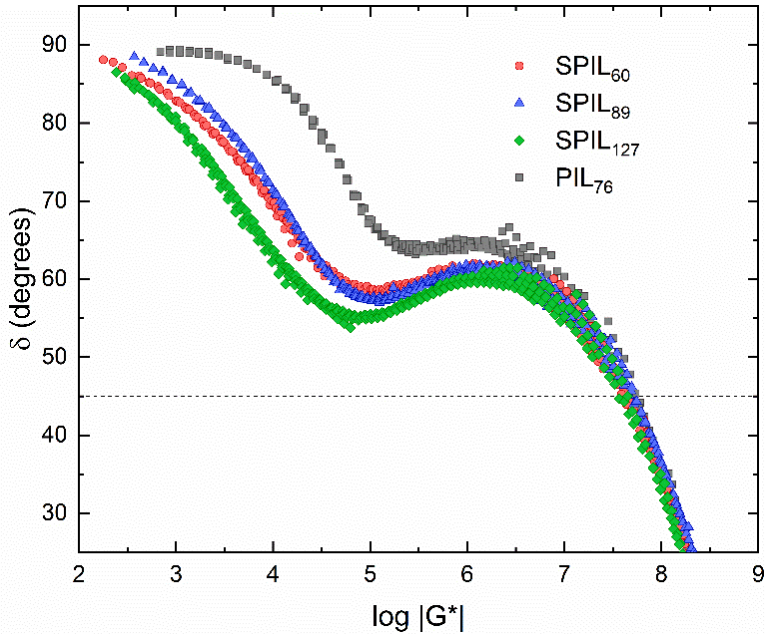


**Figure 6.5.** The vGP representation of the SAOS data. The dashed line at the phase angle $\delta_s$ = 45° indicates the position of the crossover ($G$' = $G$" at $\tau_s$).

Multiple minima and low-frequency shoulders in the vGP plot have also been observed in bottlebrush, H-shaped, and other branched polymers wherein the distinct features are ascribed to the sequential relaxation of the polymer backbone and the shorter side/brush chains.[336,337,339] On the other hand, neutral linear polymers normally exhibit only the single segmental minimum with no low-frequency feature; a single relaxation process should dictate their mechanical spectra.[341] That the linear PolyIL examined here instead also exhibits a low-frequency shoulder therefore evidences an additional relaxation in PolyILs which may be similar to the 'sticky Rouse' motions observed in ionomers: dissociation/association of the ionic liquids into ion clusters extends elastic character to lower frequencies and delays molecular flow.[342,343] The prominence of ion aggregation is consistent with the relatively large PolyIL viscosities (~$10^6$ Pa s) when compared to those of neutral polystyrenes with similar molecular weight (~$10^4$ Pa s) at $T_r \sim T_g + 30$ K.[320]

Similar to the ionic effects in the linear poly(VBBI$^+$TFSI$^-$)s discussed above, sequential relaxation in neutral stars typically results in weak shoulders in the vGP plot.[339] In the latter

case, enhancement in elasticity at lower frequencies arises due to increased arm rigidity associated with the internal microstructure of symmetric star architectures—especially for segments in the vicinity of the core.[317,318,319,320] For the star PolyILs examined, however, the low-frequency feature manifests as a pronounced minimum (Figure 6.5). The rheological data thus highlight the synergistic effect ionic liquid clustering in combination with the star-like relaxation in extending strong elastic character to the low-frequency response of branched PolyIL melts.

***Dielectric Response***

The BDS data reveal dc ion conductivity, the conductivity relaxation, a secondary β-relaxation, and electrode polarization (Figure 6.6). The dc ion conductivity is identified by the frequency-independent plateau in the real part of the complex conductivity $\sigma^*$ plot. A complete presentation of the $\sigma'$ data for each PolyIL sample is provided in the SI (Figure S6.3). Polymer electrolytes whose ion dynamics are completely coupled to the segmental relaxations are expected to have a dc conductivity of $10^{-15}$ S cm$^{-1}$ at $T_g$.[344] In contrast, the PolyILs in this report have $\sigma_{dc}(T_g) \sim 10^{-10}$ S cm$^{-1}$, indicating that the ion dynamics are decoupled from the segmental process by about 5 orders (Figure 6.7). Overall, ion conductivity at $T_g$ is found to be essentially independent of the polymer architecture. Similarly, star-branched poly(ethylene oxide) doped with LiTFSI salt also showed comparable ionic conductivity to its linear counterpart in the amorphous state.[345]

The conductivity plateau corresponds to times longer than $\tau_{dc} \sim \omega_{dc}^{-1}$, in which ion motions are long-range and diffusive. Above a characteristic frequency $\omega_{dc}$, $\sigma'(\omega)$ begins to rise due to the onset of ac conductivity; at timescales shorter than $\tau_{dc}$, the subdiffusive ion motions are confined to a local, disordered environment.[344] In ionic systems, the onset of ac conductivity thus manifests as a dielectric relaxation caused by ion rearrangement—i.e., the reorientation of the dipole moment corresponding to the ion-cage system.[296,297,298,299,303,304,307] The time $\tau_{dc}$ of this 'conductivity relaxation' is related to the average ion-association lifetimes; in the present system, this is the duration a TFSI

counterion spends trapped in a cage (of size ~$d_1$, Figure 6.1) of neighboring imidazolium groups.

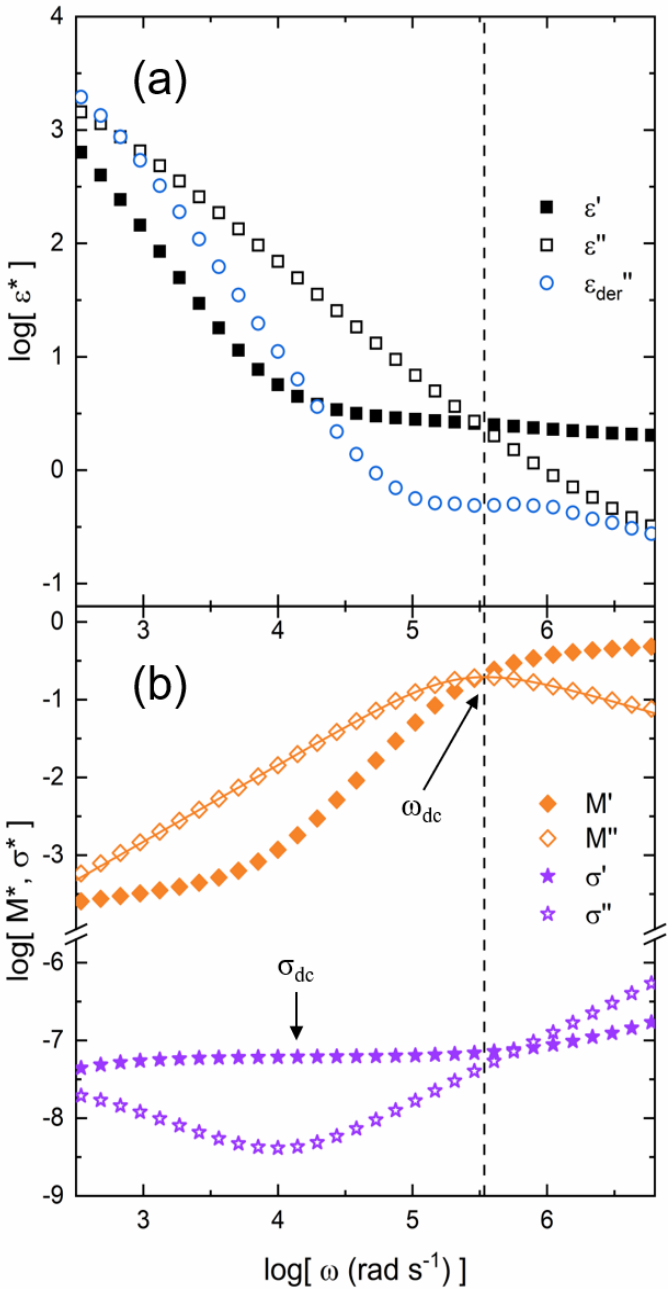


**Figure 6.6.** BDS spectra for SPIL$_{127}$ at $T$ = 303 K. Frequency-dependent complex permittivity $\varepsilon^*$ components are plotted alongside the derivative curve (a) and compared to the electric modulus $M^*$ and conductivity $\sigma^*$ (b). The solid line is the best fit of the CD function to $M$", where the peak position is used for the determination of $\omega_{dc} = \tau_{dc}^{-1}$ (dashed vertical line).

The peak position in the imaginary component of the electric modulus $M^*$ follows the ion rearrangements.[344] Specifically, the Cole-Davidson (CD) function is shown to be a satisfactory approximation to $M''$:

$$M''(\omega) = \frac{\Delta M}{(1+i\omega\tau_{CD})^{\gamma}} \qquad (6.2)$$

where $\Delta M$, $\tau_{CD}$, and $\gamma$ (with values $0 < \gamma \leq 1$) are fitting parameters corresponding to the strength, characteristic time, and asymmetric stretching of the CD relaxation function, respectively (Figure 6.6b).[344] From the best fits, the conductivity relaxation rate is then calculated from the peak position:

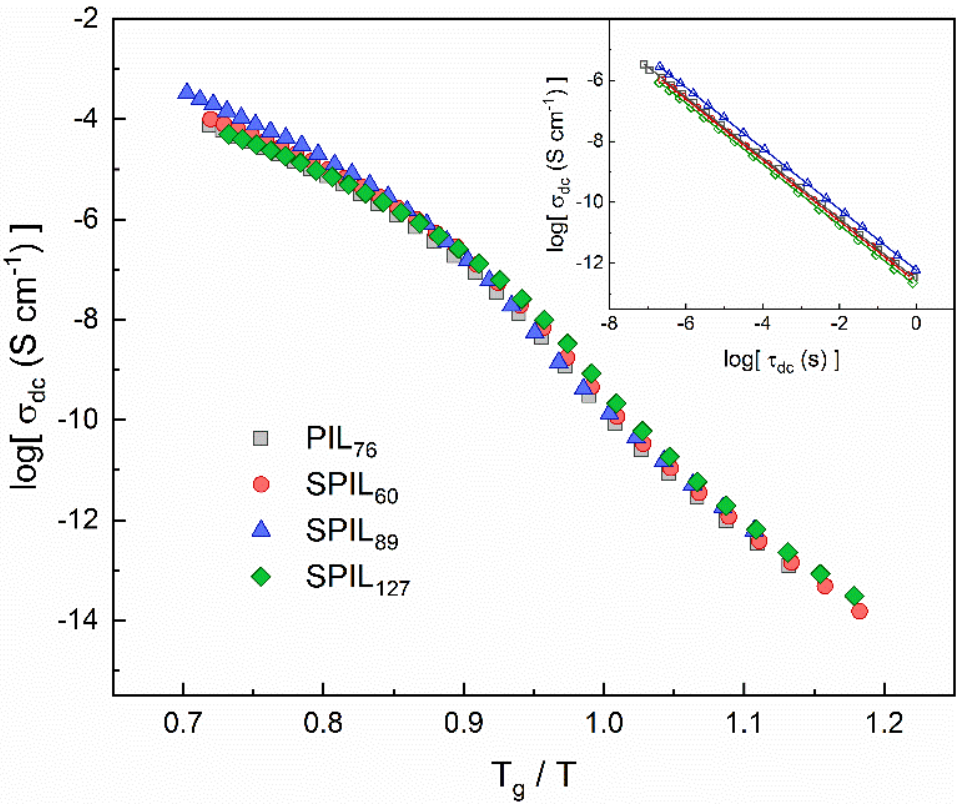


**Figure 6.7.** dc ion conductivity of PolyILs vs. reciprocal temperature as scaled by the respective calorimetric $T_g$s. The inset shows the BNN scaling relationship confirmed for each sample.

$$\omega_{dc} = \frac{1}{\tau_{dc}} = \frac{1}{\tau_{CD}} \frac{\sin\left(\frac{\pi}{2+2\gamma}\right)}{\sin\left(\frac{\gamma\pi}{2+2\gamma}\right)} \qquad (6.3)$$

As expected, the Barton, Nakajima, and Namikawa (BNN) scaling relationship $\sigma_{dc} \sim \tau_{dc}^{-1}$ is recovered for these PolyILs, further confirming the assignment of the conductivity relaxation to $\tau_{dc}$ (Figure 6.7 inset).[298,299,303,174]

Lastly, a high frequency dielectric relaxation emerges in $\varepsilon^*$ for temperatures below about 263 K (Figure 6.8). This process is attributed to the secondary or β-relaxation with time $\tau_\beta$ and strength $\Delta\varepsilon_\beta$ and is generally related to the fluctuation of the ionic liquid pendant groups.[298,299,304] The Cole-Cole function is used to simultaneously fit both the real and imaginary components of the permittivity:

$$\varepsilon^*(\omega) = \varepsilon_\infty + \frac{\Delta\varepsilon_\beta}{1+(i\omega\tau_\beta)^\alpha} \qquad (6.4)$$

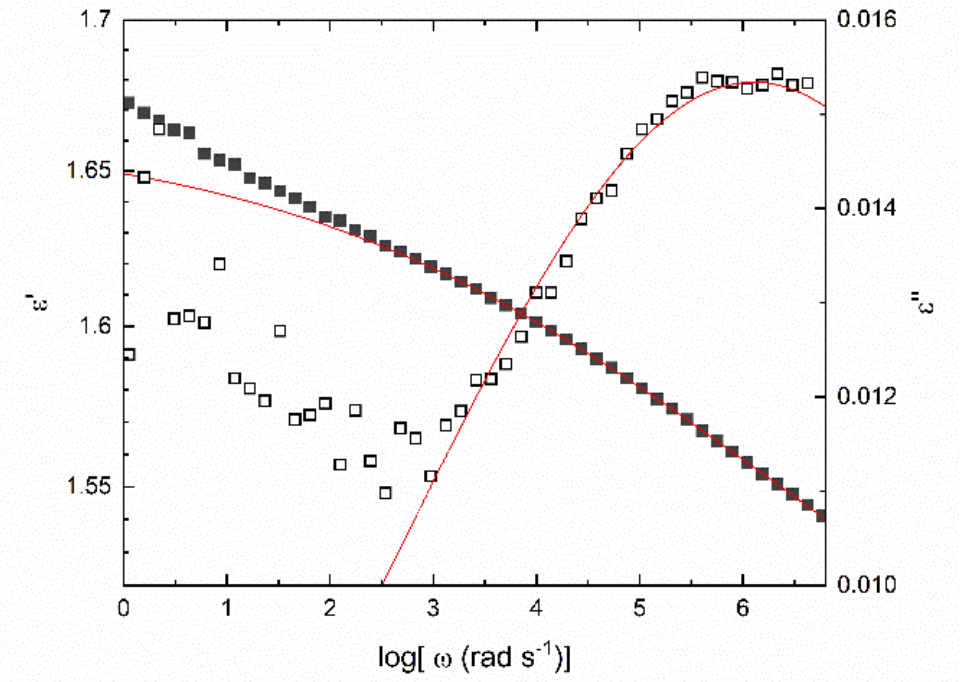


**Figure 6.8.** Representative fitting of Eq. 6.4 (red lines) to the real and imaginary components (filled and open symbols, respectively) of ε* in the region corresponding to the secondary β-relaxation for $SPIL_{127}$ at T = 203 K.

where $\alpha$ is a symmetric broadening parameter. Eq. 6.4 is able to fit both $\varepsilon$' and $\varepsilon$'' components well (solid red lines in Figure 6.8). The temperature dependence of both the conductivity and secondary relaxations are analyzed and compared between the different macromolecular characteristics in the following section (Table 6.2).

***Comparison of Dynamic Processes***

The influence of PolyIL architecture and molecular weight on the various relaxation processes is further evaluated by comparing the temperature dependence of their respective timescales (Figure 6.9). In particular, the time constants are generally described using either Arrhenius or empirical Vogel-Fulcher-Tamman (VFT) equations, the latter having the form

$$\tau = \tau_o \exp\left(\frac{DT_0}{T-T_0}\right) \qquad (6.5)$$

where $\tau_0$ is the time constant in the high temperature limit, $D$ is a material-specific strength parameter inversely related to the dynamic fragility, and $T_0$ is the Vogel temperature.[334] The VFT (Eq. 6.5) and WLF (Eq. 6.1) equations are the same equation, only presented in different forms. In a plot of log$\tau$ vs. 1/$T$, the Arrhenius expression yields a straight line whereas super-Arrhenius VFT behavior has an upwards curvature.[346]

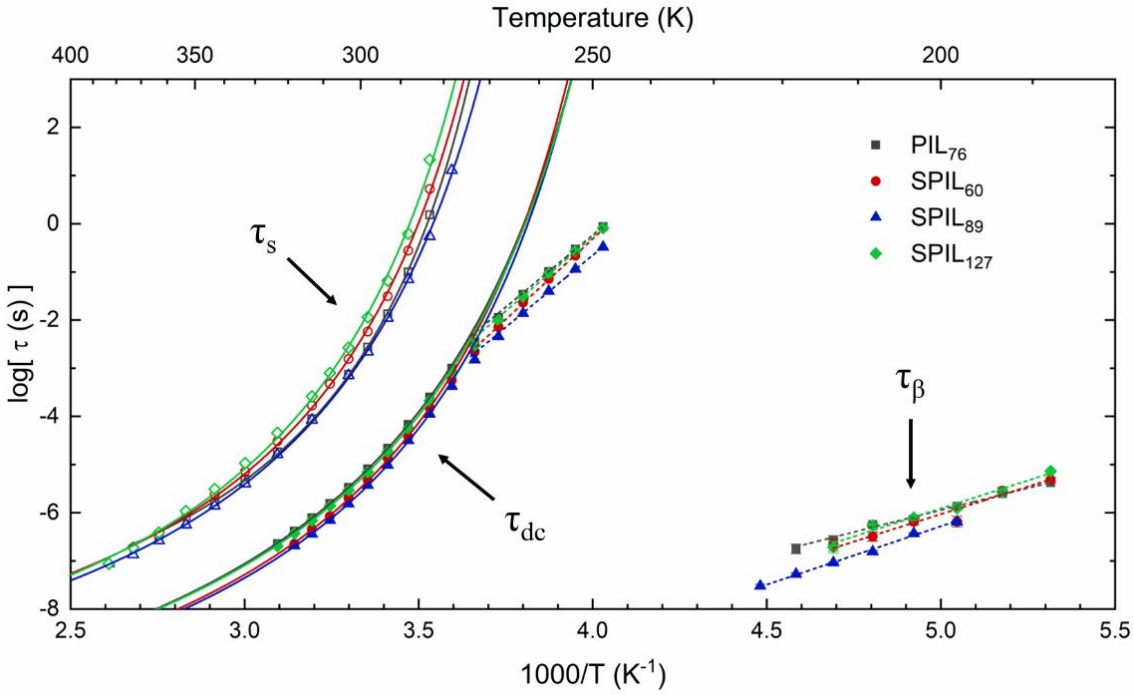


**Figure 6.9.** Time constants corresponding to the segmental $\tau_s$, conductivity $\tau_{dc}$, and secondary $\tau_\beta$ relaxations vs. reciprocal temperature. Open symbols represent time constants determined from the rheological data (Figure 3) while closed symbols indicate the fitted parameters to the BDS spectra (Figures 6.6 and 6.9). Solid and dashed lines are fits to the VFT (Eq. 6.5) and Arrhenius equations, respectively.

Consistent with studies on other PolyILs, the rheological measurements reveal a super-Arrhenius temperature dependence of the segmental relaxation times for $T > T_g$. As such, Eq. 6.5 is a good fit to $\tau_s$ in the measured temperature window (Figure 6.9). Note that the glass transition temperatures may also be independently determined via rheological measurements by extrapolating the fitted VFT function to the structural relaxation time of $\tau_s$ = 1000 s. Hence, Eq. 6.5 is also substantiated by the agreement in rheological $T_g$s with the corresponding DSC values (Table 6.1).

**Table 6.1** Fitted parameters to the viscoelastic data.

[a] To compare to the rheology experiments (data collected with increasing $T$), the calorimetric $T_g$ here is taken from the heating curve (10 K/min).

| | $\tau_s$, VFT | | | | | DSC[a] |
|---|---|---|---|---|---|---|
| sample | $\tau_0$ ($10^{-11}$ s) | $D$ | $T_0$ (K) | $T_g$ (K) | $m$ | $T_g$ (K) |
| $SPIL_{60}$ | 7.20 ± 3.6 | 4.39 ± 0.29 | 241 ± 2.0 | 275 | 106 ± 7.1 | 276 |
| $SPIL_{89}$ | 2.90 ± 0.50 | 5.12 ± 0.13 | 233 ± 0.91 | 272 | 91.8 ± 2.3 | 269 |
| $SPIL_{127}$ | 4.53 ± 2.5 | 4.64 ± 0.34 | 241 ± 2.4 | 277 | 103 ± 7.6 | 281 |
| $PIL_{76}$ | 45.6 ± 1.89 | 3.33 ± 0.19 | 246 ± 1.4 | 274 | 122 ± 6.8 | 275 |

From the VFT expression, the fitted $D$ is found to be larger for stars than linear PolyILs; the star architecture increases the effective fragility strength throughout the measured temperature range.[342] The fragility index $m$ is defined strictly at $T_g$ and can be extrapolated from the VFT parameters:

$$m = \left| \frac{d\log\tau_s}{d\left(T_g/T\right)} \right|_{T=T_g} = \frac{DT_0T_g}{\left(T_g - T_0\right)^2 \ln(10)} \qquad (6.6)$$

Similarly, $m$ is found to decrease (greater glass-forming "strength") for the star PolyILs relative to the linear analogue (Table 6.1). Depressed fragility has also been reported for both star-shaped and hyperbranched polystyrene melts and is suggested to arise due to the nonlinear architecture, viz. limited chain interpenetration, stronger intermolecular interactions, and particle-like ordering of the branched polymer cores.[319,325] Additionally,

the disparity in the WLF parameters between linear and star samples is compatible with the latter possessing a measurable degree of density heterogeneity (Table S6.1).[318]

On the other hand, the VFT expression fails to describe the conductivity relaxation throughout the measured temperatures. Specifically, there is a dynamic crossover from the super-Arrhenius to an Arrhenius dependence at temperature $T_x$.[346] The crossover signifies the temperature at which the ions begin to move through the frozen structure and is found to be close to $T_g$ (Table 6.2). This increases the extent of decoupling as defined by the ratio $R_\tau = \tau_s/\tau_{dc}$ of the segmental to ion relaxation times in the PolyIL melts at $T_g$.[296] In systems for which ion conductivity is coupled to structural relaxations, log$R_\tau$ is close to zero or negative, while PolyILs instead typically show log$R_\tau$ in the range of 3 to 8.[296] For the poly(VBBI$^+$TFSI$^-$) examined here, log$R_\tau$ = 5.0 ± 0.2, confirming the result from the $\sigma_{dc}$ data that the ion dynamics for each PolyIL is about 5 orders of magnitude faster than the segmental dynamics—regardless of the chain architecture (Figure 6.7).

**Table 6.2** Fitted parameters to the BDS data.

[a] Estimated from the intersection of the VFT and Arrhenius fits to the $\tau_{dc}$ data

| sample | $\tau_{dc}$, VFT | | | $T_x$ (K)[a] | $E_{a,dc}$ (kJ mol$^{-1}$) | $E_{a,\beta}$ (kJ mol$^{-1}$) |
|---|---|---|---|---|---|---|
| | $\tau_0$ (E-12) | $D$ | $T_0$ (K) | | | |
| $SPIL_{60}$ | 3.22 ± 0.40 | 4.83 ± 0.05 | 222 ± 0.64 | 273 | 128 ± 2.6 | 43.8 ± 3.7 |
| $SPIL_{89}$ | 3.13 ± 1.7 | 4.80 ± 0.38 | 222 ± 2.9 | 275 | 115 ± 1.5 | 46.4 ± 1.7 |
| $SPIL_{127}$ | 3.95 ± 0.89 | 5.12 ± 0.16 | 220 ± 1.2 | 274 | 118 ± 1.5 | 44.6 ± 3.4 |
| $PIL_{76}$ | 3.32 ± 0.35 | 5.32 ± 0.08 | 219 ± 0.50 | 274 | 115 ± 1.6 | 35.0 ± 1.2 |

From the slope of the Arrhenius region (at $T < T_g$), the activation energy $E_{a,dc}$ for the 'ion hopping' in the frozen structure is determined to be essentially invariant for all samples except for the star PolyIL with the shortest arms ($SPIL_{60}$). Because this particular melt is comprised of the highest density of cores, and thus the greatest proportion of segments confined to these crowded regions, it is conceivable that ions encounter a higher energy barrier to hopping between ion cages in these more heterogeneous environments. But if the arms are long enough, there are evidently enough percolating low-density regions requiring less energy for the ions to diffuse through. Likewise, fitting $\tau_\beta$ with the Arrhenius expression yields larger $E_{a,\beta}$ values for the star polymers as compared to their linear

counterpart. This effect can also arise from inhomogeneous segmental densities associated with the branched topology; the average local fluctuations of the ionic liquid moieties are expected to be more restricted and require more energy in the crowded core regions of the frozen matrices.

The higher activation energies found for the β relaxation process is consistent with QENS studies on PDMS bottlebrush polymers which similarly showed higher activation energies for the short-time, localized methyl group rotations.[97] Such phenomena are similarly ascribed to more congested monomer densities near branching points in polymers with the nonlinear backbones.

## 6.4 General Discussion and Conclusions

Ionic transport is mostly determined by short-range interactions and monomer chemistry, whereas the polymer architecture is less important in this regard. Accordingly, XRD, FTIR, and BDS distinguish no obvious dependence of counterion-counterion distance, ionic interactions, or $\sigma_{dc}(T_g)$ on the molecular characteristics of the PolyILs (Figures 6.1 and 6.7). On the other hand, polymer branching may have some weaker secondary effects on the temperature dependence of the conductivity and β relaxation dynamics, such as increased energy barriers to the decoupled ion hopping and β fluctuations for the more branched PolyILs.

At longer timescales, however, ionic pairs behave as 'sticky' segments which repeatedly associate and dissociate.[342,343] From the rheological data, it is obvious the effects of chain entanglements are negligible (Figure 6.3). Rather, it is mainly the sticky ionic groups which slow down polymer diffusion and delay structural relaxation of the melt, thereby providing additional elastic character to the LVE response at lower frequencies (Figures 6.3 and 6.5). Notably, chain connectivity and branching are important in this region; star PolyILs have a terminal relaxation time which is more than an order of magnitude longer than that of linear chains—even when the linear chain size was greater than $N_{arm}$ of the star.

This disparity in $\tau_r$ arises due to the distinct terminal relaxation mechanism of star-shaped polymers. While terminal flow of linear PolyILs occurs upon chain relaxation as mediated

by the sticky ionic interactions, stars must also sequentially retract their arms away from obstacles (likely ion clusters) towards their cores before the overall polymer center of mass can diffuse. In support of this description, the characteristic scaling $\eta \sim \exp(N_{arm})$ expected for non-ionic star polymers is also obtained for the star-shaped poly($VBBI^+TFSI^-$)s investigated in this study.[335] Because arm retraction is strongly opposed by entropy, terminal relaxation is much slower for stars than for their linear counterparts.[319,338]

In addition, both the rheological fragility and surface morphology are dependent on the PolyIL architecture at longer length scales (Figure 6.2). While the bulk microstructure may differ somewhat from the observed surface morphologies, the interfacial assembly is still relevant to the organization of PolyILs at electrode interfaces, which will affect the electrode polarization. As in melts of neutral branched polymers, the decrease in $m$ and emergence of limited-aggregate surface morphologies for the nonlinear PolyILs are attributed to their intermolecular interactions, limited chain interpenetration, and particle-like organization.

To summarize, investigation of the viscoelastic and dielectric properties of linear and star-shaped PolyILs reveals that branched polymer architectures primarily control the slower dynamic properties and morphologies on the molecular/chain length scale whereas effects on the faster, more local segmental and ion dynamics as well as structural organization at the monomer scale are secondary or absent altogether. This work highlights a key advantage of polymerized ionic liquids: the assembled morphology and thermorheological properties can be tuned independently of the ion conductivity by processing polymers with controlled architectures. Moreover, because ion transport is facilitated by localized ion rearrangements, the results further emphasize that improvements to single-ion conductivity in solid polymer electrolytes should focus on controlling polymer chemistry at the segmental/monomer scale. However, further investigation is required to elucidate the range of functionality $f/N_{arm}$ over which the findings discussed above can be expected and how the effect of architecture on PolyIL dynamics might manifest for more flexible or hydrophilic PolyILs with different counterions and/or nanoparticle-like conformations. This study nonetheless lays the groundwork for understanding how branched polymer

architectures can be used to help guide the development of functional ionic liquid materials with finely tuned mechanical and transport properties.

## Chapter 6 Appendix: Supporting Information

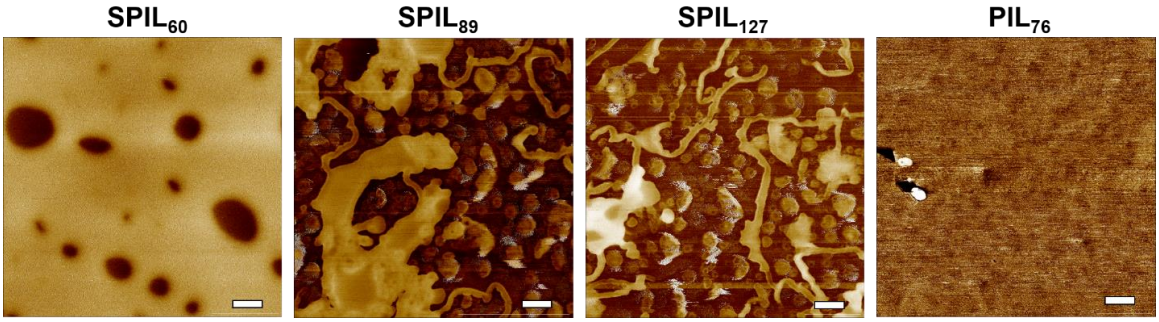


**Figure S6.1.** High-resolution AFM phase images of the indicated PILs at high magnification. Z scales for $PIL_{76}$ and $SPIL_{60}$ are 10 °; Z scales for $SPIL_{89}$ and $SPIL_{127}$ are 20 °. All scale bars are 100 nm.

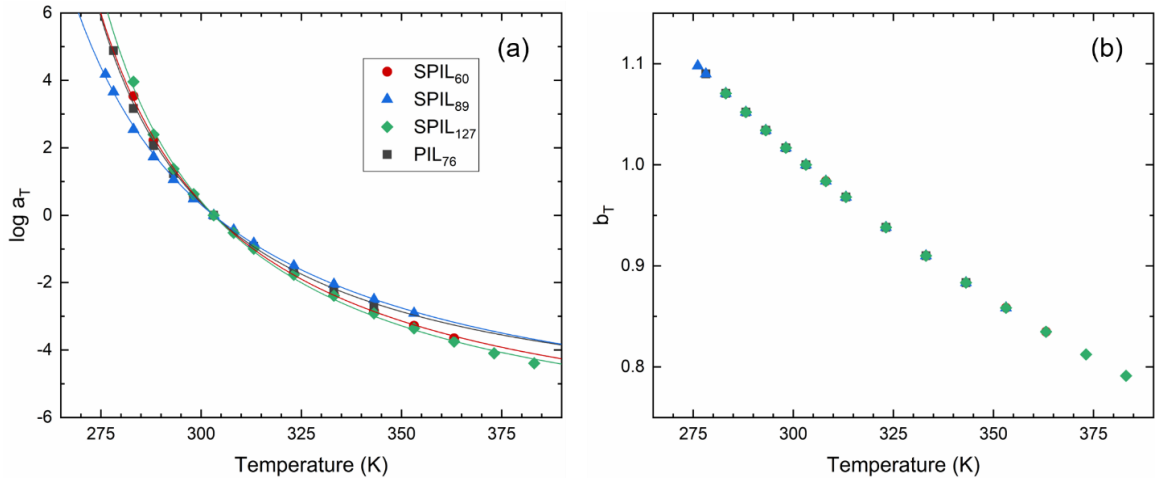


**Figure S6.2.** Temperature dependence of the horizontal shift factor $a_T$ (a) and vertical shift factor $b_T$ (b) used to construct the SAOS master curves, referenced to $T_r$ = 303 K. Solid lines represent best fits to the WLF equation.

**Table S6.1** Fitted WLF constants to the viscoelastic data at the reference temperature $T_r$ = 303 K.

| | $a_T$, WLF | |
|---|---|---|
| sample | $C_1$ | $C_2$ |
| $SPIL_{60}$ | 7.33 ± 0.14 | 62.6 ± 1.3 |
| $SPIL_{89}$ | 7.07 ± 0.14 | 73.4 ± 1.2 |
| $SPIL_{127}$ | 7.43 ± 0.16 | 59.2 ± 1.6 |
| $PIL_{76}$ | 6.47 ± 0.27 | 59.1 ± 1.7 |

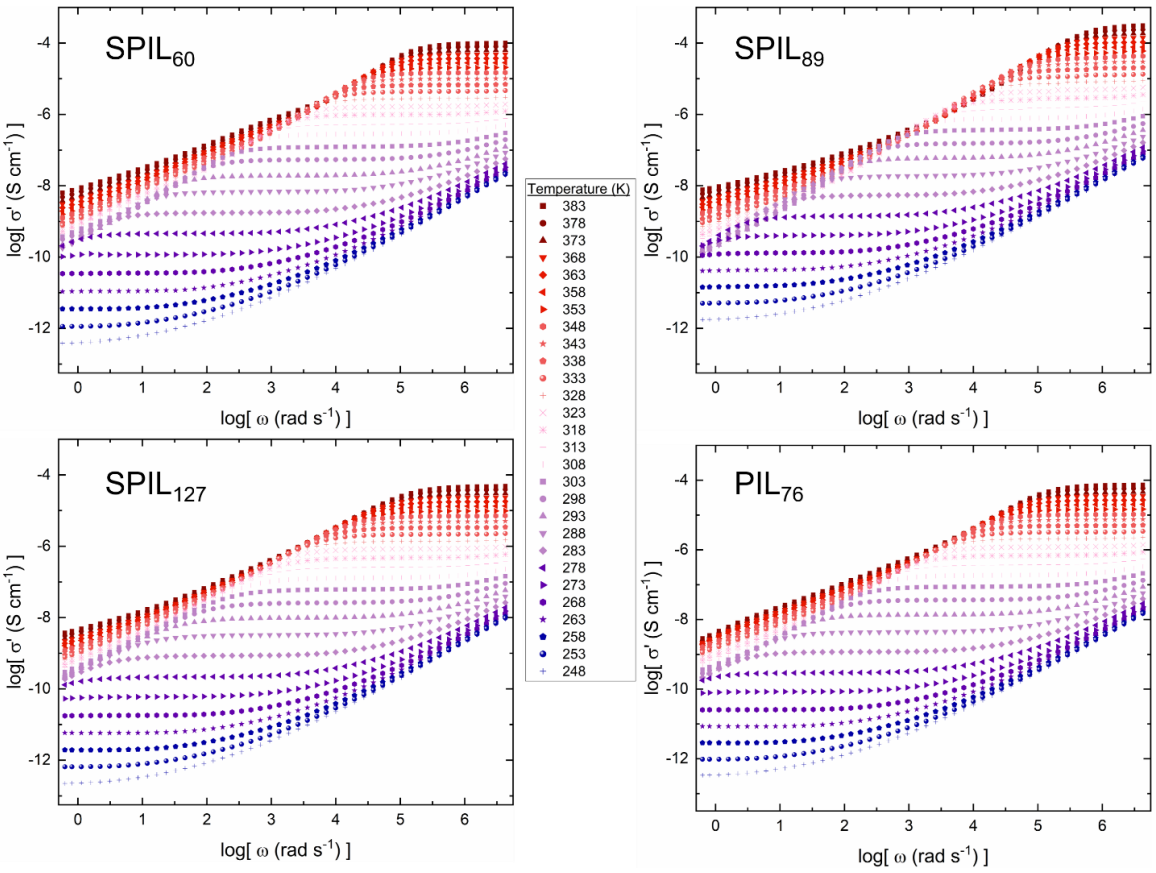


**Figure S6.3.** The frequency dependence of the real part of the complex conductivity, plotted at different temperatures for the indicated linear/star PolyILs.

# CHAPTER 7. IONIC LIQUID FUNCTIONALIZED HYPERBRANCHED NANOPARTICLES

## 7.1 Introduction

The proliferation of new electrochemical energy storage and harvesting technologies has spurred the development of a diverse range of functional branched soft nanoparticle electrolytes with tunable ion transport, viscoelasticity, and thermal properties.[347] A variety of approaches have been employed in order to achieve solid polymer electrolytes with high ionic conductivity. Zhang et al. developed a bottom-up assembly technique consisting of the covalent tethering of poly(ethylene oxide) (PEO) chains to organic building blocks prior to their organization into covalent organic frameworks (COFs) doped with LiTFSI salt, however such electrolyte materials are only suitable for high temperatures (~200 °C) and are susceptible to efficiency loss and instability due to the mobile anion species.[348]

Archer and coworkers have investigated both single-ion conducting nanoparticle salts[349] as well as organic hybrid electrolytes based on grafted nanoparticles[350,351]. The inclusion of the rigid inorganic phase generally improves the mechanical stability of the electrolyte by preventing liquid-like flow while simultaneously introducing internal interfaces which can alter the transport of ions. Moreover, by tethering one of the ionic species to a functionalized nanoparticle, it is possible to control the flow of charge and polarization, as in polymer electrolytes. Branched particle functionalization is therefore an attractive approach towards tuning the functional response of ionic media.[352,353,354,355,356]

Highly branched particles such as star-shaped polymers, hyperbranched oligomers, dendrimers, microgels, and polymer-grafted nanoparticles have been demonstrated to be versatile components in the modular assembly of a wide range of functional soft materials.[357,358] Owing to nontrivial elastic forces, excluded volume effects, particle localization, and interdigitation and entanglement of the peripheral (corona) regions, interparticle interactions can range from ultrasoft potentials to effectively hard sphere repulsions. Consequently, glasses formed from branched particles can exhibit a variety of vitrification behavior wherein assembly fragility is determined by the nature and strength

of such interactions.[359] Ultrahigh branching functionalities can lead to colloidal-like jamming in the molten state, which can make them easily processable while leaving the segmental dynamics relatively unchanged.[360] Despite the long-range disorder of such amorphous materials, a well-defined local structure may emerge which can profoundly impact the mechanical, optical, and transport properties of so-called 'hyperuniform materials'.[361]

The decoupling phenomenon in PolyILs has been related to the sequential formation and breaking of ion associations which give rise to intra- and intermolecular ion hopping through a relatively immobilized, glassy matrix. As known, the ionic interactions in ionic liquids are unique in that they are considerably delocalized in comparison to other salts. In fact, counterions have been shown to exhibit delocalized coordination with multiple tethered (polymerized) ions from different chains.[362,363,364] It is therefore expected that tailoring polymer structure and architecture, which dictates the arrangement of such tethered groups, can potentially lead to control over the spatial allocation of ionic functionalities and thus the hopping motions of ions. For example, PolyILs have been shown to exhibit higher conductivity when imidazolium groups are polymerized along the backbone than when they are incorporated as pendant groups.[308]

Branched PolyILs feature distinct arrangements of functional IL groups but have received little attention. Moreover, covalent chain connectivity restricts the organization of dipoles and their rotational motions in PolyILs and can therefore lead to pronounced changes in dielectric constant.[365] Insofar as the excluded volume effects of ionic groups are tuned by polymer branching, it should be possible to direct the collective dipole orientations, offering molecular branching as a potential design parameter for electrolytes with tunable dielectric environment and ion transport. And as with increasing polymer chain rigidity, nonlinear molecular architectures can likewise frustrate chain packing, which in the case of PolyILs is believed to result in greater free volume at temperatures near $T_g$ and therefore further decouple the ion dynamics.[366]

In the previous chapter, however, it was demonstrated that long-chain branching in the star-shaped PolyILs produced negligible changes in the dynamic and thermal properties at

shorter timescales because the architectural branching was tuned at length scales much larger than the segmental. The question remains how branching at much smaller length scales as in branched functionalized nanoparticles and hyperbranched compounds might affect the ion behavior in these electrolyte materials. While some dynamic properties of hyperbranched and dendritic oligomeric ionic liquids have been reported, few relationships between the branching architecture and ion transport have been established.[367,368,369,370,371,372,373,374,375] For example, it is not yet known whether or not highly branched architectures can tune the coupling and decoupling of ion dynamics from the segmental motions in the glassy state, which is relevant to the performance of solid-state electrolytes. To better understand this, the dynamic properties of IL-tethered macromolecules consisting of both POSS and hyperbranched polyester cores with varying degrees of branching and different ionic functionality are probed (Scheme 3.3).

## 7.2 Experimental

### *Temperature-Modulated DSC*

Following the regular sample preparation procedure where standard DSC measurements at 10 °C/min reliably produce consistent thermograms, temperature-modulated measurements were then used to more precisely determine the $T_g$. In the T-modulated DSC measurements, an average rate of 2 °C/min was used with a temperature modulation amplitude and period of 0.5 °C and 60 s, respectively. Unless otherwise stated, the calorimetric glass transition temperature $T_g$ was taken as the midpoint of the reversible heat capacity jump from the modulated heating step.

### *BDS Sample Preparation*

Solutions of the hyperbranched and linear ionic liquids were all prepared in ethanol and POSS-$[COO^-\ DMIm^+]_8$ and POSS-$[COO^-\ HMIm^+]_8$ solutions were prepared in ethanol and chloroform, respectively (all ~17 mg/mL). Solutions were then slowly spun-cast onto a gold-plated electrode (diameter 10 mm) fitted with a Teflon spacer (thickness ~ 60 µm). The films were subsequently dried under vacuum at 70 °C for 2-3 h, after which the upper electrode was pressed firmly against the film and returned to the oven. The assembled cells

were further dried under these conditions for at least 24 h and then immediately transferred to the dielectric sample chamber for measurements under dry nitrogen atmosphere.

## 7.3 Results and Analysis

### Thermal, Chemical, and Structural Characterization

The hyperbranched samples were found to be thermally stable up to 125-150 °C from TGA analysis. In contrast, POSS-based samples did not thermally decompose until reaching temperatures up to 250-350 °C, demonstrating the enhanced thermal stability of the electrolytes possessing the nanoscale inorganic cores.[353]

Changing the molecular architecture or core structure while keeping the ionic liquid functionality the same can lead to profound effects on the vitrification behavior of the electrolytes (Figure 7.1). For example, increasing the branching generation of carboxyl-terminated HBP particles generally leads to an increase in the $T_g$—although depending on the counterion, this relationship may not be monotonic (Table 7.1). For this series, the increase in $T_g$ is likely due to a greater density of ions whose electrostatic interactions reinforce the electrolyte matrix. More significant is the effect of changing the core structure from hyperbranched polyester to POSS nanoparticles, which can lead to an increase in $T_g$

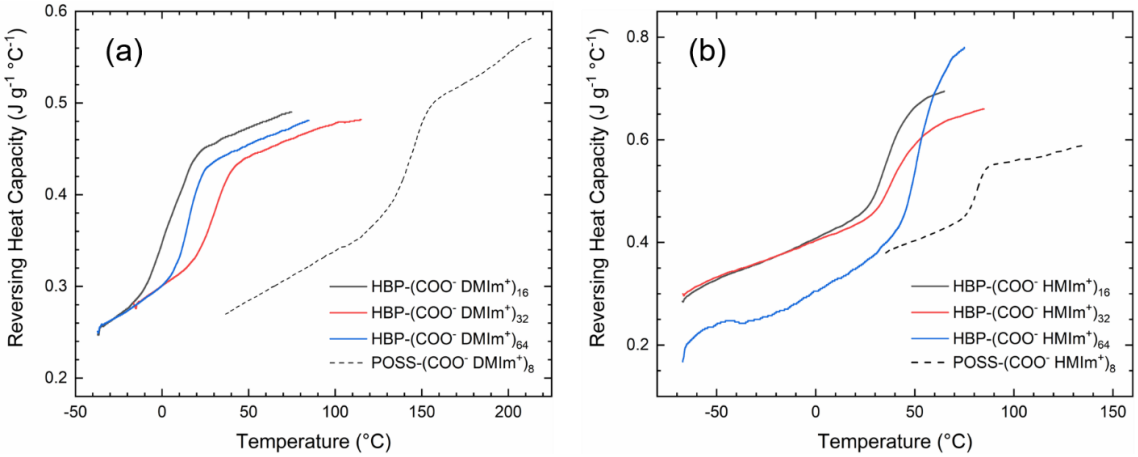


**Figure 7.1.** Scaled reversing heat capacities for HBP (solid lines) and POSS (dashed lines) based ionic liquids end-functionalized by carboxyl groups bearing aprotic $DMIm^+$ (a) and protic $HMIm^+$ (b) counterions. Each DSC curve is multiplied by a scaling factor in order to compare hyperbranched cores possessing n = 16 (gray), 32 (red), and 64 (blue) terminal groups.

of up to ~140 °C. Incorporation of the inorganic component evidently results in the percolation of a rigid phase that substantially enhances the glassy properties of the matrix.[376]

**Table 7.1** Thermal characteristics of IL particles with both rigid (POSS) and soft (HBP) cores.

[a] Determined from BDS. [b] Determined from T-modulated DSC. [c] Temperature width of the $T_g$ jump from the DSC thermograms.

| Sample | $T_x$ (°C)[a] | $T_g$ (°C)[b] | $\Delta T_g$ (°C)[c] |
|---|---|---|---|
| POSS-$(COO^- K^+)_8$ | 180 | 190 | 19 |
| HBP-$(COO^- K^+)_{32}$ | 115 | 51 | 10 |
| POSS-$(COO^- DMIm^+)_8$ | 140 | 143 | 22 |
| HBP-$(COO^- DMIm^+)_{16}$ | 5 | 10 | 26 |
| HBP-$(COO^- DMIm^+)_{32}$ | 20 | 30 | 18 |
| HBP-$(COO^- DMIm^+)_{64}$ | 20 | 15 | 7 |
| POSS-$(COO^- HMIm^+)_8$ | 90 | 81 | 9 |
| HBP-$(COO^- HMIm^+)_{16}$ | 45 | 36 | 23 |
| HBP-$(COO^- HMIm^+)_{32}$ | 32 | 40 | 22 |
| HBP-$(COO^- HMIm^+)_{64}$ | 49 | 52 | 8 |
| POSS-$(SO_3^- HMIm^+)_8$ | 148 | 130 | 72 |
| HBP-$(SO_3^- HMIm^+)_{32}$ | 29 | -6 | 13 |
| HBP-$(SO_3^- DMIm^+)_{32}$ | 47 | 24 | 24 |

Likewise, tuning the ion pair interactions has a significant effect on the glass transition (Figure 7.2). For HBP particles of identical generation (32 end groups), the melt $T_g$s increase for the following ionic liquid chemistries: $(SO_3^- HMIm^+) < (COO^- DMIm^+) \sim (SO_3^- DMIm^+) < (COO^- HMIm^+) < (COO^- K^+)$. These results point to two predominant contributions to the glass transition: electrostatic interactions and hydrogen-bonding. HBPs with small counterions (e.g., $K^+$) will generally have large charge densities and strong, directional Coulombic forces. These electrolytes tend to form ionic aggregates which can serve as physical crosslinks, thereby increasing $T_g$. In contrast, larger counterions with delocalized charges (imidazoliums) tend to have weaker interactions and lower $T_g$s.

At the same time, compounds with strong, directional hydrogen bonding interactions such as HBPs terminated by the $(COO^- HMIm^+)$ pair can have a larger $T_g$ owing to their

propensity to form hydrogen bonding networks. This is distinct from the extremely low $T_g$ of the ($SO_3^-$ $HMIm^+$) sample. The greater stability of the sulfate ion possibly results in the incomplete proton transfer and therefore a lower density of hydrogen bonds.

It is interesting to note that for both carboxyl and sulfate terminated HBPs the jump in heat capacity $\Delta C_p$ at $T_g$ is consistently larger for systems containing the protic counterions ($\Delta C_p \approx 0.18$ $Jg^{-1}K^{-1}$) than for their counterparts bearing aprotic counterions ($\Delta C_p \approx 0.12$ $Jg^{-1}K^{-1}$). In addition, the heat capacity of HBP-($COO^-$ $HMIm^+$)$_n$ is generally greater than that of HBP-($COO^-$ $DMIm^+$)$_n$ throughout the measured temperature range (Figure 7.1). This result indicates the presence of extra degrees of freedom in the protic systems due to the configurational entropy of a hydrogen-bonded network, which becomes especially pronounced in the melt state. Notably, both the heat capacity and $\Delta C_p(T_g)$ for the POSS protic system lack this particular signature in its thermogram. The lack of a hydrogen-bonded network in this sample might explain its low $T_g$ in comparison to the other POSS particles.

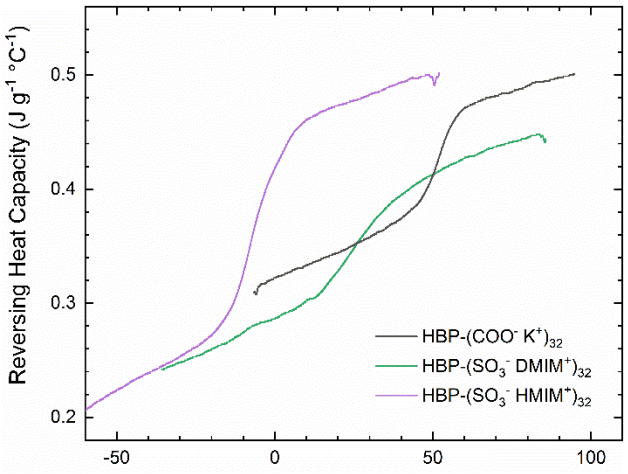


**Figure 7.2.** Reversing heat capacities for HBP samples end-functionalized by different ionic liquid chemistries.

A broadening of the calorimetric glass transition with decreasing branching generation for is observed for both protic and aprotic samples. This broadening indicates the presence of a more diverse local dynamic associated with the structural partitioning of the polar ionic groups from the cores due to their mutual immiscibility.'[377] The effect thus becomes more significant for hyperbranched samples with the lowest branching number—and therefore the lowest density of ionic groups—in which the core constitutes a considerable portion of

each molecule. At the highest ionic densities for higher generation branching, the $T_g$ is dominated by the ionic and H-bonding interactions of the terminal functional groups, and the jump in heat capacity occurs over a much narrower range.

***Ion Dynamics and Conductivity***

As with star PolyILs, the dielectric spectra distinguish four relaxation processes: electrode polarization, segmental relaxation, ion reorientation motion, and dc ionic conductivity. Because the derivative curve in the permittivity plane $\varepsilon''_{der}$ suppresses contribution of the ion conductivity, this representation is useful for identifying the peaks corresponding to segmental and ion reorientation dynamics (Figure 7.3).[378] Havriliak-Negami (HN) functions are employed to fit these processes in the permittivity spectra:

$$\varepsilon''_{der}(\omega) = -\frac{\pi}{2}\frac{\partial \varepsilon'(\omega)}{\partial(\ln\omega)} = A\omega^{-s} - \frac{\pi}{2}\frac{\partial \sum \mathrm{Re}\left(\frac{\Delta\varepsilon_i}{\left(1+(i\omega\tau_i)^{\beta_i}\right)^{\gamma_i}}\right)}{\partial(\ln\omega)} \qquad (7.1)$$

where $\omega$ is the radial frequency, $\Delta\varepsilon_i$ is the dielectric relaxation strength, $\tau_i$ is the relaxation time, and $\beta_i$ and $\gamma_i$ are symmetric and asymmetric broadening parameters, respectively.[379,380,381] For samples with sufficient conductivity, electrode polarization dominates the spectra at the lowest frequencies and is accounted for by a power law term $A\omega^{-s}$. In the following, the subscripts $i$ = s and $i$ = ion correspond to the segmental and ion reorientation motions, respectively.

In addition to these relaxations, the complex conductivity σ* reveals the long-range ion diffusion corresponding to dc conductivity, which is approximated here using the random barrier model (RBM):

$$\sigma^*(\omega) = \frac{\sigma_{dc} i\omega\tau_{RBM}}{\ln(1+i\omega\tau_{RBM})} + i\omega\varepsilon_0\left(\sum\frac{\Delta\varepsilon_i}{\left(1+(i\omega\tau_i)^{\beta_i}\right)^{\gamma_i}} + \varepsilon_\infty\right) \qquad (7.2)$$

where $\sigma_{dc}$ is the frequency-independent dc ionic conductivity and $\tau_{RBM}$ is the characteristic 'ion-hopping' time constant.[382,383,384] In particular, $\tau_{RBM}$ distinguishes the short-range, subdiffusive dynamics at high frequencies (i.e., conductivity dispersion) from the long-

range, diffusive dynamics at lower frequencies (conductivity plateau) and it corresponds roughly to the intersection of the $\sigma$' and $\sigma$'' components. It is evident that $\tau_{ion}$ and $\tau_{RBM}$ are closely related; namely, the onset of long-range diffusion is precipitated by the ion reorientation motion, since $\tau_{ion} < \tau_{RBM}$. For simplicity, the portion of $\sigma^*(\omega)$ due to electrode polarization was omitted from the fitting.

The representative results shown in Figure 7.3 are measured as the temperature approaches $T_g$ from above. They demonstrate two general cases: (1) the ion reorientation and hopping rates are several orders of magnitude *faster* than the segmental motions, indicating that ion transport is entirely decoupled from the glassy dynamics of the electrolyte and (2) ion motions and the onset of dc ion conductivity are *slower* than the segmental motions, indicating that the particle segments must fully relax before ions can diffuse. In either case, Eqs. 7.1 and 7.2 fit the data well. Moreover, comparison to rheology data confirms unambiguous identification of the segmental mode. This comparison is particularly useful in cases for which segmental motions are largely obscured by conductivity in the dielectric spectra (Figure 7.3a).

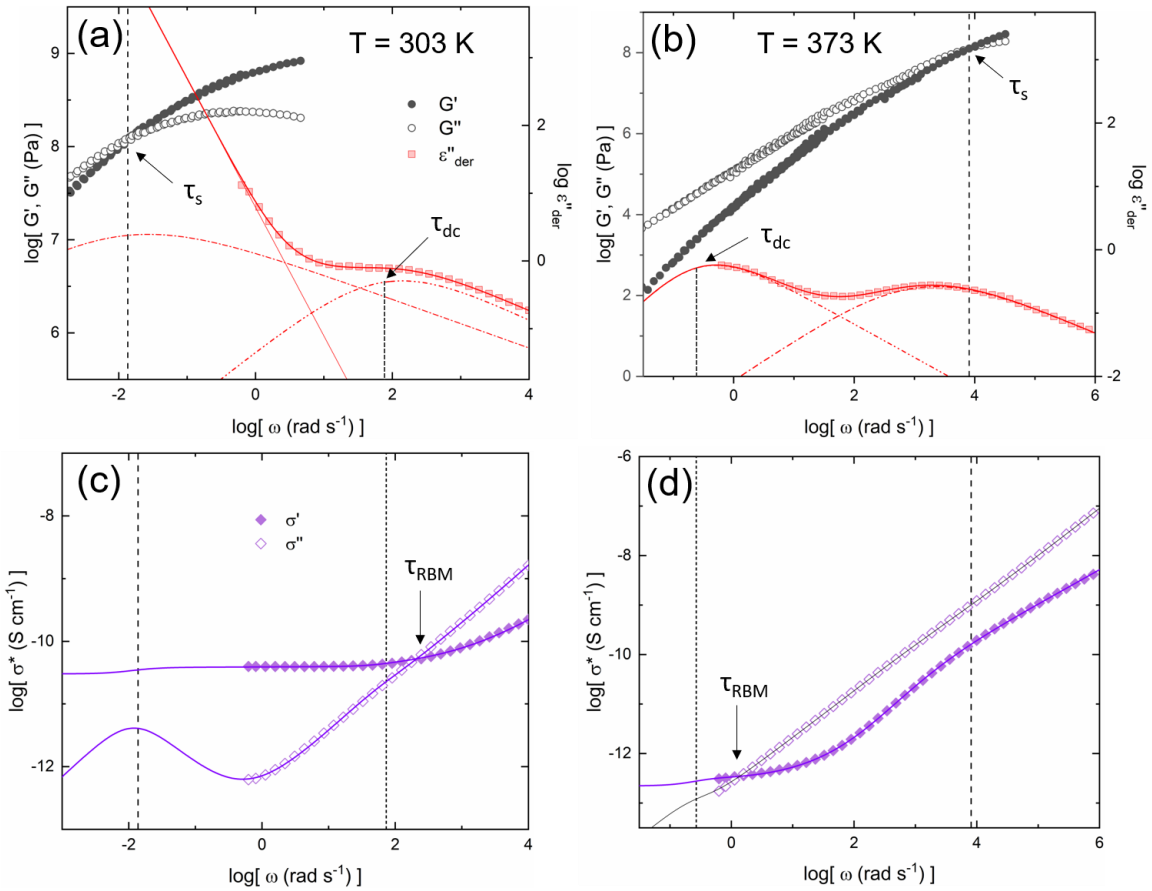


**Figure 7.3.** Representative dynamic spectra of HBP-$(COO^{-}\ DMIM^{+})_{32}$ (a, c) and POSS-$(COO^{-}\ HMIM^{+})_{8}$ (b, d) recorded at the temperature $T = T_g + 10$ K for each sample. Eq. 7.1 is used to fit the segmental and ion reorientation processes in the permittivity derivative curves (a, b); their respective contributions are indicated by the red dash-dotted lines. The thin red line is the contribution of electrode polarization (a). The complex shear moduli, as measured by rheometry, are shown for comparison. The intersection of the storage and loss components G' and G'' is used to determine the segmental relaxation rate $\omega_s = \tau_s^{-1}$, as denoted by the black dashed line. $\tau_s$ and $\tau_{ion}$ are inserted into Eq. 7.2, which is used to fit the associated data in the $\sigma^*(\omega)$ plane (c, d).

**Effect of Molecular Architecture and Core Structure**

Ionic liquid particles are synthesized from both soft HBP cores and rigid POSS nanoparticles in order to evaluate the extent to which core structure—composition, flexibility, and functional density—influences the dynamic behavior of their melts. Furthermore, the particles are compared to their approximate linear counterparts, which consist of short PEO oligomeric 'linear cores' with two ends terminated by ionic liquids. In this section, attention is restricted to carboxyl-terminated molecules with either aprotic $DMIM^+$ or protic $HMIM^+$ countercations.

The dominating effect of the glass transition is immediately apparent from a comparison the dc ion conductivities (Figure 7.4). For example, conductivities of the aprotic series at room temperature fall from ~$10^{-5}$ S $cm^{-1}$ for the liquid-like linear oligomers ($T_g$ = -5 °C) to ~$10^{-9}$-$10^{-11}$ for the rubbery hyperbranched particles. On the other hand, the POSS-based ionic liquid particles are glassy solids at room temperature and consequently have immeasurably low conductivities. Note however that the measured $\sigma_{dc}$ do not necessarily follow the observed dependence of $T_g$ on the branching generation for the HBP samples.

In order to compare the ion transport decoupling character, the same $\sigma_{dc}$ data are plotted against reciprocal temperatures as scaled by their respective glass transition temperatures (Figure 7.5). In this representation, there is a clear discontinuity in the temperature dependence of $\sigma_{dc}$ as it transitions from VFT to Arrhenius-like behavior at a dynamic crossover temperature $T_x$ located in the vicinity of $T_g$. Notably, the linear samples feature a sharp drop in conductivity at temperatures well above their recorded values of $T_g$, owing to their crystallization during the BDS measurements. Regardless, the samples approach similar levels of conductivity at temperatures well above the glass transition; at the highest temperatures the ion chemistry is the dominating factor. The exception is POSS-$[COO^-HMIM^+]_8$ which appears to saturate at lower conductivities for high temperatures, possibly due to limited ionicity for this particular sample.

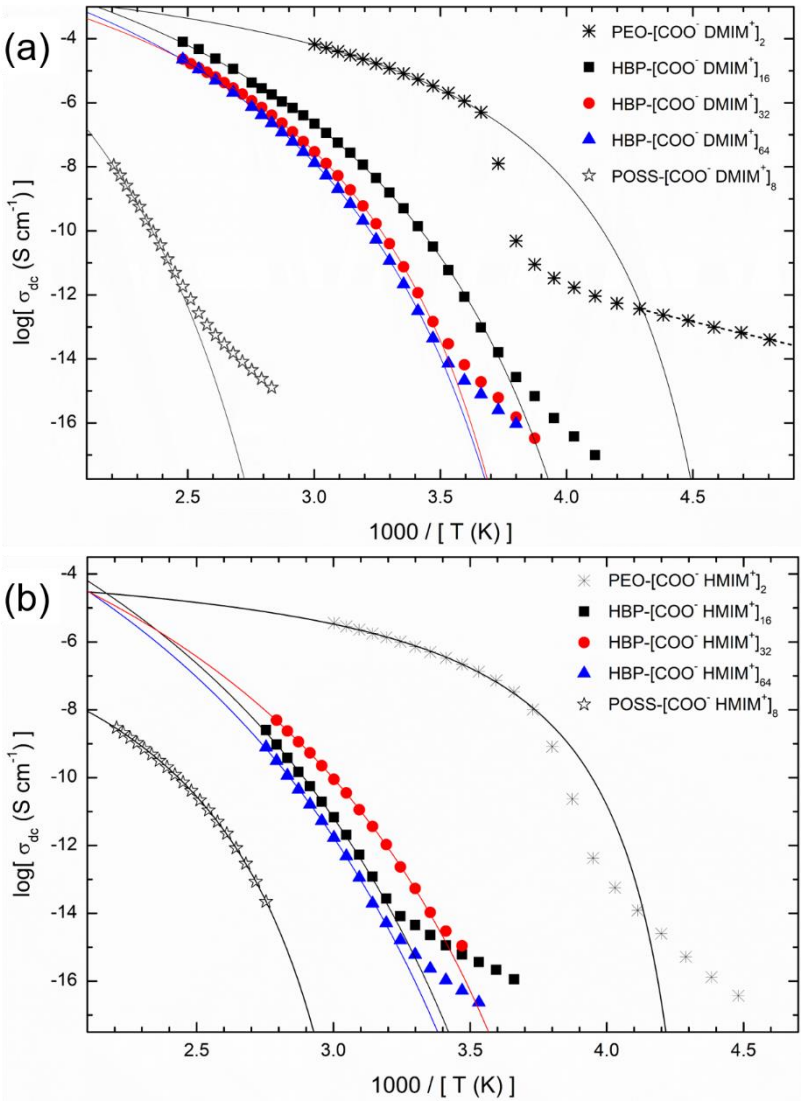


**Figure 7.4.** dc ion conductivity vs reciprocal temperature of linear and branched carboxyl-based ionic liquids functionalized by either the aprotic $DMIM^+$ (a) or protic $HMIM^+$ (b) countercations. Solid lines are VFT fits to data above the glass transition temperature.

Above $T_g$, the linear oligomer sample possesses a significantly larger conductivity in both aprotic/protic systems than the branched particles, despite having a lower ion density. This is likely a consequence of a larger ionicity (weaker ion-pair association) due to the highly solvating ethylene oxide chains; i.e., EO segments have a dilution effect on ion aggregates thereby producing a higher density of free ions.[380] Additionally, it may result from a more decoupled ion mobility in the former chain-like systems. In contrast, a higher segmental density in the vicinity of branched particle cores may have a smaller free volume which precludes passage of ions.

In the case of the aprotic ionic liquids, conductivity of the linear oligomer remains higher and decays more slowly with temperature when cooled below $T_g$ in comparison to the branched HBP and POSS samples. From the linear dependence of $\sigma_{dc}(T)$ for $T < T_g$, an activation energy $E_{a,dc}$ of 35.6 ± 0.07 kJ/mol can be ascribed to a low temperature 'hopping' barrier for ions in PEO-[$COO^-$ $DMIM^+$]$_2$. The relatively high conductivity and low $E_{a,dc}$ below $T_g$ indicate the existence of an efficient pathway for ion diffusion even as the segmental motions are frozen and that electrostatic interactions and ion aggregation do not significantly hinder ion transport.

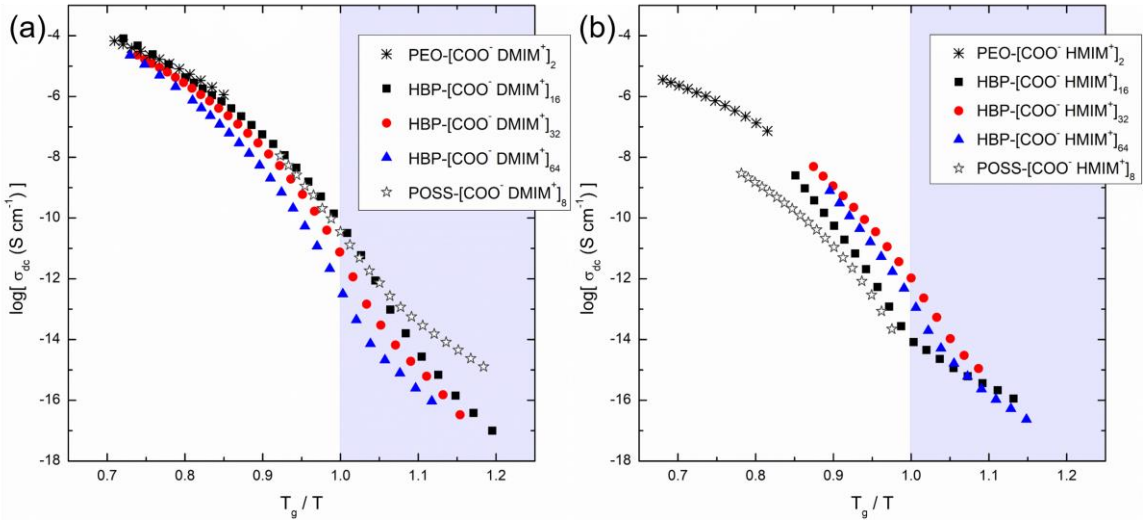


**Figure 7.5.** dc ion conductivity vs $T_g$-scaled reciprocal temperature plotted for linear and branched carboxyl-based ionic liquids functionalized by either the aprotic $DMIM^+$ (a) or protic $HMIM^+$ (b) countercations. The gray area encompasses the glassy regime. For the linear samples, only the conductivity data above crystallization is scaled to their reported $T_g$ values.

The otherwise identical $\sigma_{dc}$ values for $T >> T_g$ contrasts with those at lower temperatures where core structure and branching generation begin to have considerable effects on the conductivity in the kinetically arrested state. For example, with each increase in branching generation in the aprotic series, there is a corresponding one order of magnitude drop in the conductivity at $T = T_g$. That is, for HBP-[$COO^-$ $DMIM^+$]$_n$, $\sigma_{dc} \approx 1 \times 10^{-10}$, $1 \times 10^{-11}$, and $1 \times 10^{-12}$ S/cm at $T_g$ for n = 16, 32, and 64, respectively. In contrast, protic molecules with higher branching numbers feature the higher conductivities. HBP-[$COO^-$ $HMIM^+$]$_{16}$ ($\sigma_{dc} \approx 2 \times 10^{--14}$ S/cm) has a conductivity approximately 2 orders of magnitude lower than its more branched counterparts ($\sigma_{dc} \approx 2 \times 10^{-12}$ and $5 \times 10^{-13}$ S/cm at $T_g$ for n = 32 and 64, respectively).

Soft, flexible HBP cores are compared to rigid, inorganic POSS cores in regards to their effects on ion dynamics. Similar to the examination of molecular architecture, the influence core structure also depends on the ion-pair interactions (Figure 7.5). Interestingly, the POSS compounds showed similar values of $\sigma_{dc}(T_g)$ to those of the HBP-ILs with the lowest number of terminal groups for both protic and aprotic samples. As such, POSS-[$COO^-$ $DMIM^+$]$_8$ maintains one of the highest scaled conductivities of the aprotic ionic liquids throughout the entire temperature range. Moreover, $\sigma_{dc}$ of this sample decreases more gradually as it is cooled below $T_g$. It appears that in the absence of hydrogen-bonding, the organosilate composition may enhance ion hopping motions and/or prevent the formation of large ionic aggregates in the glassy state. On the other hand, the POSS-based protic electrolytes exhibited the lowest conductivities at temperatures above its $T_g$. Due to the very small conductivity and overlap with the segmental relaxation, $\sigma_{dc}$ of POSS-[$COO^-$ $HMIM^+$]$_8$ could not be unambiguously determined below $T_g$ (Figure 7.3). From the available data, ion dynamics may be accelerated or decelerated by tuning the core structure, depending on ionic liquid functionality.

**Effect of Ion-Pair Chemistry**

Given the importance of ion-pair interactions in considering how branched molecular design can tune the properties of solid electrolytes, several hyperbranched particles with different ionic liquid end groups were also compared to elucidate the effect of ion-pair interactions (Figure 7.6). Overall, it is found that both the tethered anion and free cation control the extent of ion/segmental decoupling. The results indicate that, regardless of the anionic end group (i.e., $COO^-$ vs. $SO_3^-$), substitution of the aprotic $DMIm^+$ for the protic $HMIm^+$ decreases $\sigma_{dc}(T_g/T)$. Note that this effect is similarly observed in the samples with the POSS-based cores (Figure 7.5). This result suggests an incomplete proton transfer and ionic association, thereby limiting ionicity and conductivity at $T_g$ for the particles bearing protic cations.[385]

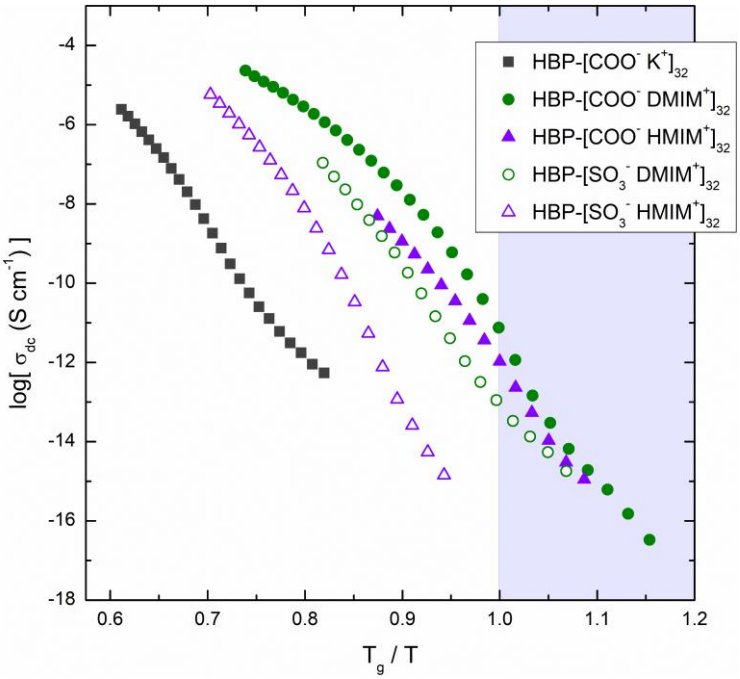


**Figure 7.6.** dc ion conductivity of hyperbranched particles functionalized with different ion pair chemistries plotted as a function of the $T_g$-scaled reciprocal temperature.

On one hand, this finding indicates that proton conductivity in the protic samples is essentially negligible, as is typically observed in protic ILs. Instead of diffusing, the proton on the methylimidazolium cation more likely acts as a strong hydrogen donor in hydrogen-bonding interactions with acceptor groups on either the anion or the polyester/POSS core. This highly directional interaction is anticipated to increase the energy barrier to ion-pair disassociation, thereby leading to decreased ionicity and lower ion conductivity. On the other hand, the inductive effect of the additional methyl group on the $DMIm^+$ counterions produces an electron-donating effect to the heterocyclic nitrogen, thereby decreasing the cation acidity and effectively shielding the charge-transfer of the ion pair.[386] As a result, the diminished ionic interactions of the $DMIm^+$ system effectively facilitates the counterion migration and increases the ion conductivity.

To confirm the changes in ion interactions, FTIR measurements on carboxyl-terminated POSS particles containing $K^+$, $DMIm^+$, and $HMIm^+$ are compared to examine any changes in the hydrogen bonding environment (Figure 7.7). In the spectra of nanoparticles with the aprotic $K^+$ and $DMIm^+$ cations, broad and bimodal peaks are identified in the range of 3200 $cm^{-1}$ to 3600 $cm^{-1}$, attributed a wide distribution of O—H and N—H stretching vibrations

in a heterogeneous environment. In contrast, POSS particles with the protic $HMIm^+$ cations show relatively narrow peaks shifted to higher wavenumbers, which suggest the presence of stronger, more directional bonding in the case of protic cations.[387,388]

Furthermore, tethering the more basic sulfate anions to the particle end groups depresses $\sigma_{dc}(T_g/T)$ relative to the carboxyl-terminated counterparts. That is, when the highly directional electrostatic interactions are enhanced between ion pairs, counterions are less likely to dissociate from these pairs and the scaled ionic conductivity decreases.[389] This effect is especially dramatic for sulfate-terminated molecules with protic counterions, due to the limited proton conductivity of the cation.

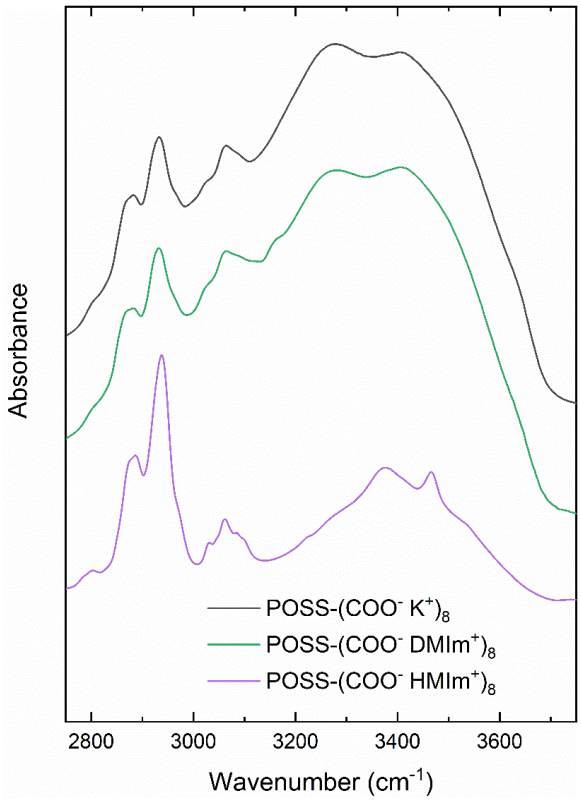


**Figure 7.7.** FT-IR spectra of POSS-ILs. Curves are shifted vertically for clarity.

The system with the lowest conductivities was HBP-$[COO^- K^+]_{32}$, even when its large glass transition temperature is taken into account. This result emphasizes the importance of electrostatic interactions, which for the small $K^+$ cation are much stronger than those with the comparatively delocalized $DMIm^+$ cation; in the absence of hydrogen-bonding, a counterion trapped within a strong coulombic potential well would need to overcome a

considerable energy barrier to undergo long-range diffusion. It is worthwhile mentioning that, in comparison to molecules terminated by the ($COO^-$ $DMIM^+$) and ($COO^-$ $HMIM^+$) ion pairs, samples functionalized with ($COO^-$ $K^+$), ($SO_3^-$ $DMIM^+$), and ($SO_3^-$ $HMIM^+$) exhibited the largest discrepancies between $T_g$ and $T_x$. Hyperbranched ILs with the strongest electrostatic interactions tend to exhibit the dynamic crossover from super-Arrhenius temperature dependence to Arrhenius at temperatures considerably higher than their glass transition temperatures. Though there is precedent for this behavior, it is beyond the scope of the present work.[346]

## 7.4 Conclusions

As expected, the glass transition temperature is demonstrated to be a significant property in determining the dynamic properties of the electrolytes studied in this report. In this regard, molecular architecture (i.e., branched vs. linear), core structure (hyperbranched polyester vs. POSS), and ion interactions (electrostatic vs. hydrogen-bonding) are all shown to be adjustable synthetic parameters for tuning the glass transition. Overall, ionic liquids with the inorganic POSS cores existed as rigid, glassy solids over a wide range of temperatures. As such, these samples tended to have extremely poor conductivity. In contrast, compounds with the more flexible hyperbranched polyester cores featured glass transitions closer to room temperature and therefore exhibited intermediate conductivities. The extent of branching density was demonstrated to have a subtle effect of generally increasing the $T_g$ for the more branched HBP-ILs. A dense periphery of ions with strong electrostatic and hydrogen-bonding interactions would explain the shift in $T_g$, and is consistent with the narrower jump in heat capacity as the HBP core plays a more diminished role in the higher generation HBP-ILs.

Lastly, the 'linear cores' show the lowest $T_g$s and therefore the highest $\sigma_{dc}$s. However, these electrolytes are liquid at temperatures above 0 °C, which precludes their integration into devices which require a stable, mechanically robust electrolytes at room temperature. Due to growing interest in such solid-state electrolytes, it is critical to develop a fundamental understanding of how dynamic properties evolve when the electrolytes are cooled to the

glassy state. Hence, in this report ion transport is compared in the different electrolytes at temperatures which are scaled by their respective $T_g$s.

In this respect, the design variables explored above are shown to have additional effects beyond simply shifting the glass transition temperature; tuning particle branching, core structure, and ionic species can drastically change the coupling of segmental and ion relaxations, influencing ionicity and the temperature dependence of ion conductivity. The most striking result was the disparity in the conductivities in the aprotic vs protic samples: compounds baring the protic $HMIm^+$ counterion were demonstrated to have significantly lower conductivities than their aprotic $DMIm^+$ counterparts even after the higher $T_g$s of the former series were taken into account (Figure 7.5). The absence of proton conductivity and the immobilization of counterions in the hydrogen-bonded networks severely limits ion transport in such systems.[390] Likewise, strong electrostatic interactions such as those found in compounds with tethered sulfates or baring the small $K^+$ cation limit the density of free ions and decrease $\sigma_{dc}(T_g)$ (Figure 7.6).

Regardless of molecular architecture and core structure, electrolytes containing the aprotic cations therefore always showed a greater degree of ion/segmental decoupling than their protic counterparts. Examples of this effect are clearly discerned from their dielectric spectra, wherein the ion reorientation process can be either several orders of magnitude faster than the segmental relaxation for aprotic systems (Figure 7.3). Accordingly, when the molar conductivity is plotted against the segmental relaxation rate in the Walden plot, the aprotic hyperbranched samples exhibit 'superionic' behavior with the decoupling exponent $\varepsilon = 1 - \alpha$ (where $\alpha$ is the slope) increasing with decreasing branching density (Figure 7.8). In contrast, many protic ionic liquids tend to exhibit sub-ionic properties: the presence of neutral clusters and hydrogen-bonding networks manifest as a lower ionicity.[388]

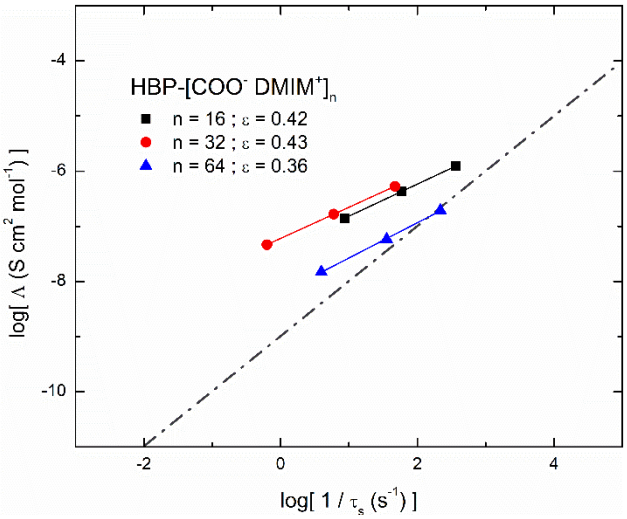


**Figure 7.8.** Walden plot featuring the molar conductivity Λ vs the structural relaxation rate $\tau_s^{-1}$ for the HBP-[COO⁻ DMIM⁺]$_n$ melts. The dash-dotted line corresponds to an aqueous solution of LiCl, used as a reference for the ideal Walden line.

In addition to the effects of the ion-pair chemistry on the $T_g$ and ionicity, the influence of the core structure and branching architecture on the ion dynamics was also dependent of the presence of protic vs aprotic counterions. For HBP-ILs with $DMIm^+$ cations, higher generation HBP-ILs with a greater functional group density exhibited lower conductivities at $T_g$ than the first generation and the POSS-IL counterparts. This is apparent in the Walden plot, where HBP-(COO⁻ $DMIm^+$)$_n$ exists further "above" in the superionic regime for n =16 and 32, whereas compound with n = 64 lies below, closer to the ideal behavior. The reverse trend is observed for the $HMIm^+$ series: the greater generation HBP-ILs exhibit a greater degree of decoupling of the ion transport from the segmental dynamics.

On one hand, in both the protic and aprotic series, more terminal IL groups in the more branched samples should translate to higher potential concentration of free ions to contribute to the ion conductivity. While increasing the end group number in the protic series corresponds to progressively glassier electrolytes due to the greater number of hydrogen-bonds, it may be this larger population of ions that also contributes to their higher conductivities when the $T_g$ effect is taken into account. On the other hand, this benefit to $\sigma_{dc}(T_g)$ is seemingly absent in the aprotic series. In this case, the presence of the core—which constitutes a larger portion of the compounds for the POSS and HBP-ILs of lower

generations—may provide a high-mobility route for mobile ions in the glassy state that manifests in ion dynamics that are ~ 5 orders of a magnitude faster than the segmental process. Conversely, it is also possible that the POSS and HBP cores, both of which possess hydrogen-bonding sites, may present additional "traps" that could hinder $HMIm^+$ transport in the protic series, resulting in ion dynamics that are almost completely coupled to the segmental motions of the electrolyte.

To summarize, a series of protic and aprotic branched ionic liquid particles with different IL chemistries were systematically investigated to explore how synthetically tuning the core structure and molecular architecture can control the resulting thermodynamic and ionic properties. In prior studies, the influence of the polymer architecture of larger star-shaped PolyILs on dynamic properties was limited to molecular scale; stars with different arm lengths could be used to tailor the melt viscosity or to assemble thin films with an assortment of different morphologies, whereas the segmental and ion dynamics were relatively unchanged. In contrast, tuning the molecular architecture for the branched ILs explored here not only substantially altered the glass transition behavior but could also be used to enhance or weaken the coupling of the segmental motions to the ion dynamics in the electrolyte, depending on the IL chemistry. In particular, it was found that branched aprotic PolyILs with lowest degree of branching show the most decoupled ion dynamics.

## Chapter 7 Appendix: Supporting Information

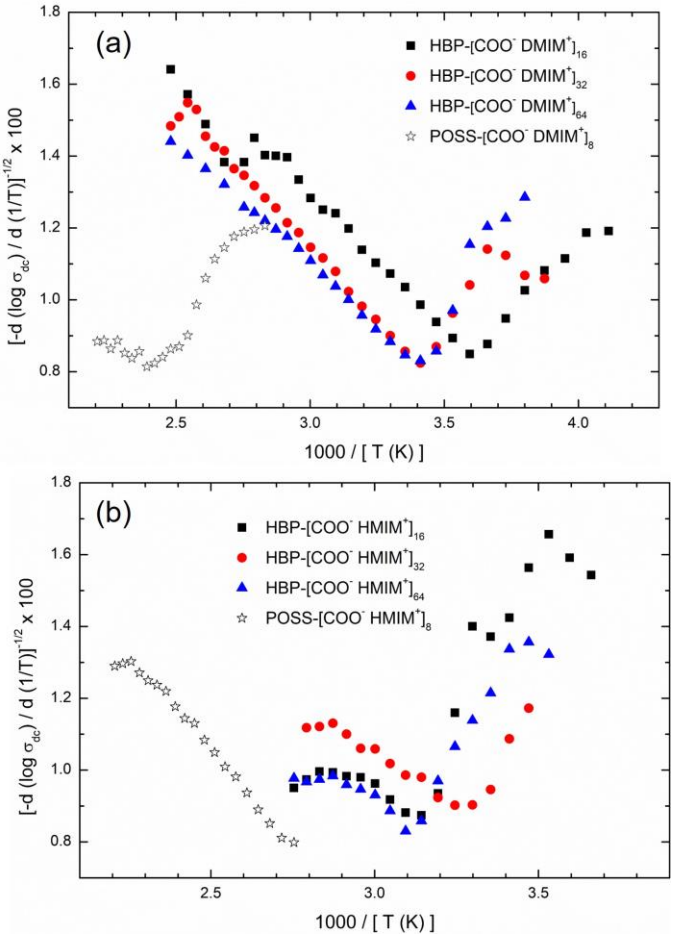


**Figure S7.1.** Plots of the BDS data used in the determination of the dynamic crossover in aprotic (a) and protic (b) compounds. The approximate $T_x$ is taken as the minimum, which corresponds to the shift from VFT to Arrhenius temperature dependence of the dc ion conductivity.

# CHAPTER 8. GENERAL CONCLUSIONS AND BROADER IMPACT

## 8.1 Major Results and Significance

Studies of polymerized ionic liquids have traditionally focused on the influence of molecular structure and ion chemistry on polymer conformations, interfacial and bulk assembly, morphology, phase behavior, and other physical properties. While significant advances in synthetic chemistry have opened up a broad library of various macromolecular architectures, there is a critical lack of understanding in regards to how branched architectures introduces an additional level of control over the polymer interactions, and further how these modified interactions translate to unique responsive assembly behavior and emergent properties in soft electrolyte materials.

The major results presented throughout this work address this gap in knowledge by investigating the effect of branched polymer architecture in polyelectrolytes and PolyILs with various ionic chemistries in regards to: (1) the interfacial assembly at different interfaces in connection to the resultant stimuli-responsive morphologies and (2) the polymer dynamics as manifested in the thermomechanical properties and ion transport. Due to the complex, hierarchical relationship of the nonlinear polymer building blocks to their nano- and microscale organization and macroscopic properties, a broad range of spatial and temporal scales are considered in this approach.

### *8.1.1 Part I: Stimuli-Responsive Assembly of Star Polyelectrolytes and PolyILs*

Branched polyelectrolytes are first investigated in this dissertation to examine how tuning the molecular architecture modifies intra- and intermolecular interactions which govern their self-assembly into stimuli-responsive morphologies. The star-graft block-quarterpolymer [$PS_n$(P2VP-*b*-PAA-*g*-PNIPAM)$_n$] is a unique branched polyampholyte of particular interest because its wide range of available compositional and structural parameters—grafting density, arm number, block length—translate to a complex assortment of interactions ideal for a systematic investigation of its multiresponsive

microstructures. Prior studies had examined the sensitivity of SGQP solutions to pH and temperature and it was shown that they could be integrated into the shells of microcapsules which demonstrated outstanding performance for drug delivery. However there existed a critical gap in understanding how the individual SGQP responsive conformations translated to their interactions organization into multicomponent films and shells, how the internal structure of these organized systems was changing at the nanoscale in response to pH and temperature shifts, and how the organization and responsivity might be controlled via the synthetic parameters of the SGQPs. In the work presented here, these points are addressed so as to both rationalize their performance in prior applications (e.g., the aforementioned microcapsules) as well as to provide a fundamental understanding of branched polyampholytes as versatile building blocks for multifunctional polymer electrolytes.

In this spirit, SGQPs with different molecular architectures and composition were integrated into hydrogen-bonded multilayer films and their assembled surface and internal morphologies were evaluated *in-situ* using surface probe microscopy and neutron reflectivity under different conditions. The block-specific swelling was found to promote the heterogeneous partitioning of hydrophobic and hydrophilic reservoirs within the interior of the swollen films, which generated unique compartmentalized morphologies distinct from those observed in traditional LbL assemblies.

By subjecting the multilayers to aqueous environments with variable pH and temperature, the balance of amphiphilicity afforded by the SGQP architecture was determined to be the chief factor governing the responsive internal structures. The route to achieving the various hierarchical morphologies was successfully mapped out, illustrating how internal porosity and thermally-induced swelling could be programed via the star composition and solution pH. Ultimately, the nanoscale characterization employed in this study allowed for an assessment of the global film organization and swelling in conjunction to the conformational changes and aggregation of SGQPs into star-like clusters at the molecular scale. The results not only elucidated the interactions relevant to the responsive properties observed in other studies of dual responsive stars, but could also be more broadly applied to understanding the assembly of other complex ampholytic molecules such as proteins

and supramolecular nanoparticles. The study thus provides the groundwork necessary for designing multicompartmental polymer electrolytes films which can be dynamically controlled to influence localized reactions, molecular separation, targeted encapsulation and release, on-off switching, and ion transport.

In contrast to multiresponsive star polymers, the assembly, morphology, and properties of branched PolyILs has received much less attention. This dissertation therefore provides a fundamental basis of knowledge in this respect by reporting on the organization and surface morphology of linear and star-shaped poly($VBBI^+TFSI^-$) under different adsorption conditions and following various post-assembly treatments, and furthermore demonstrates how PolyILs with star architectures exhibit assembly behavior distinct from both that observed from linear PolyILs as well as traditional polyelectrolytes. In probing the surface tension of the poly($VBBI^+TFSI^-$)s at the air-water interface, the limited-aggregation phenomena of branched polymers is found to stabilize the PolyIL monolayer under repeated compression and expansion, packing IL repeat units much more efficiently than its linear counterpart. For the first time, Langmuir-Blodgett monolayers of PolyILs are formed and are shown to exhibit peculiar reversible condensation into nanodroplet arrays. Furthermore, the PolyILs are successfully used as a building block in the layer-by-layer assembly of multilayer films for the first time. In contrast to traditional polyelectrolyte multilayers, the PolyIL films feature compartmentalized hydrophobic ions that drive a microstructural reorganization towards a diverse set of highly textured, porous, and interconnected network morphologies which depend on both the architecture of the polyIL.

Overall, the results provide important insight into how the lower glass transition temperature of polymers based on bulky ionic liquids with weaker ionic interactions and unique miscibility behavior organize into much more dynamic or malleable assemblies when compared to the normal glassy polyelectrolytes that possess more strongly-attracted ion pairs. The work further emphasizes the significance of the counterion in driving the aggregation, dewetting, and pore formation in the PolyIL monolayers and multilayers—a feature that would otherwise be overlooked in traditional polyelectrolyte assemblies. Lastly, this portion provides a into how the distinct rheological behavior of linear and star PolyILs manifest into different surface topographies as a result to their disparate flow

behavior. This dissertation thus introduces the salient factors governing the organization of branched PolyILs and distinguishes them from those normally considered in linear polyelectrolyte films. Such information is necessary if polymerized ionic liquids are to realize the full potential of polymer viscoelasticity and assembly in the development of state-of-the-art ionic liquid materials for textured smart coatings, separation membranes, conductive films, and interconnected carbonaceous networks.

### *8.1.2 Part II: Viscoelasticity and Ion Transport of Star and Hyperbranched PolyILs*

Polymerization of ions affords greater dimensional control to electrolyte materials and it has been shown how branched macromolecular architectures can influence the interactions guiding polyelectrolyte and PolyIL assembly. Yet the extent to which branching in the polymer backbone might also affect the polymer dynamics and the transport of ionic charge in PolyILs had not yet been explored. In this dissertation, the star poly($VBBI^+TFSI^-$)s, which were already evaluated for their assembly into responsive surface monolayers and multilayers, were then studied in regards to their viscoelastic and ion conducting properties over a broad range of frequencies and temperatures.

At longer timescales, star PolyILs arms exhibited more sluggish and elastic dynamics compared to those found in linear chains of comparable size. That is, arm retraction was shown to delay the terminal relaxation of the stars in the melt and, consequently, the zero-shear viscosity increased exponentially with the arm length. Yet at the shorter timescales, long-chain branching was found to have minor effects on the segmental and ion motions. The glass transition temperature, rates of segmental relaxation, short-range ordering of polymer backbones, ion disassociation, and dc conductivity were similar regardless of the polymer architecture and arm length.

These results illustrate how tailoring molecular architecture on the scale of larger star arm lengths translates changes in the polymer viscoelasticity at commensurate timescales—namely, the dissociation of chains from sticky ionic clusters and arm retraction which preclude star diffusion in the melt. However, since the PolyIL remains essentially unchanged at the monomer scale, differences between the samples with different branching architectures were comparatively muted. From a synthetic design standpoint, the results

are of interest because they demonstrate modification at a particular scale can selectively control morphology and physical properties of interest. In the case of the star PolyILs, tuning the arm length allows one to control the melt viscosity independently of the ionic conductivity. This can be of interest to the design of solar cell electrolytes, for example, for which processing demands require a certain viscosity or in the operation of batteries where the swelling associated with charging and discharging of electrodes requires an elastic and creep-resistant electrolyte without compromising the conductivity.

The question then remains of how the dynamic properties might be affected when ionic liquids are tethered onto more highly branched soft and rigid particles, rather than long-chain stars. In this case, the chain architecture begins to materialize on a scale comparable to the size of the chain segments. As such, changes on even faster timescales relevant to ion conductivity were anticipated. To explore this hypothesis, a similar set of dynamic experiments were conducted on a series of IL-tethered macromolecules consisting of both POSS and hyperbranched polyester cores with varying degrees of branching.

The results revealed that changes in the branching architecture had significant effects on not only the glass transition, but also ion dynamics and their coupling to the segmental motions of the electrolyte. For one, introducing branching architecture to the ILs substantially increased their glass transition temperature relative to the linear chain counterpart—increases to branching generation generally further promoted the $T_g$ to higher temperatures. The increase in $T_g$ was of course accompanied by decreased ionic conductivities.

An unexpected discovery was that the branching effect on the extent of ion/segmental dynamic coupling in the PolyILs is dependent on the ionic liquid chemistry used in functionalizing the HBPs. For compounds baring aprotic counterions, increasing the extent of HBP branching resulted in suppressed conductivities as samples approached the glassy state; conversely, it was the more branched HBPs which exhibited the higher conductivities at $T_g$ when the IL counterions were protic. Controlling the ion transport in PolyILs near the $T_g$ important implications towards the development of solid-state electrolytes in which it is desirable to have high conductivities in the glassy phase.

This is the first time that polymer architecture has been reported to affect the ion dynamics in PolyILs and the results suggest competing effects arising from the ion density from the terminal groups in addition to the ion interactions with the different cores—this balance is in turn influenced by the nature of the diffusing counterion.

## 8.2 Future Trends and Suggestions

There still remain a number of unresolved challenges which have precluded a full understanding of the behavior of branched polyelectrolytes and their properties. Such issues require attention from the community if the pressing demands of current state-of-the-art electrolyte technologies are to be met. For one, there are many additional polymer architectures, such as brush and miktoarm copolymers, whose morphologies and dynamic properties with different ion chemistries are still unknown. And from a practical standpoint, the performance of many polymer electrolytes in terms of their thermorheological behavior and ion transport are still prohibitively poor for many applications in energy storage and conversion.

There are a number of unexplored avenues, for example, in regards to tuning the assembly and stimuli-responsive morphologies of branched polymer electrolytes. This work examined exposure to shifts to pH, temperature, and various solvents. Even more dynamic and unprecedented structural responses may be expected from counterion exchange as the stimulus. For instance, the exchange of monovalent to multivalent counterions are especially interesting in branched polyelectrolytes due to the capacity of the latter to bridge multiple charged arms into a collapsed conformation in solution while producing ionic cross-linking sites between polymers in the melt. Such changes would lead to large shifts in the morphology, glass transition, viscoelasticity, among other properties.

Moreover, because the results discussed throughout this dissertation point towards the importance of hydrophobic and hydrogen-bonding interactions in addition to electrostatic forces in the determination of molecular aggregation, multicomponent assembly, and responsive morphologies, future studies should focus on the exchange of ions with different hydrogen donor and acceptor sites, in addition to ions with variable ionicity, hydrophobicity, size, polarity, and so on. While this area has received cursory attention for

linear polyelectrolytes and for—in this work—some hyperbranched polyILs, it is believed that these approaches can be used to exercise a much greater degree of control over branched polymers in the search for more sophisticated and dynamic morphologies. Efforts in directing polymer assembly should focus on facilitating the organization of percolating phases with long-range order that permit the coordinated motion of diffusing ions on macroscopic length scales.

The scope of this dissertation was focused mainly on branched polyelectrolytes as building blocks in relatively simple systems comprised of the polymer melt or multilayer assemblies. However, many of the more complex electrolytes being considered in cutting-edge applications have many unique components whose synergistic performance result in outstanding properties. In particular, ionogels incorporate a fluid-like ion phase that not only maintains functional ionic properties, but also can plasticize the electrolyte and promote stimuli-responsive behavior. Phase separated morphologies between the polymer and ionic phases can thereby be controlled by miscibility differences as mediated, for example, by the temperatures or ion species present.

Alternatively, nanoparticles with different intrinsic properties may be introduced to modify, for example, the dielectric constant, free volume, viscoelasticity, ion dissociation, and diffusion in nanocomposite polymer electrolytes. Branched polymers are an especially suitable component in these systems because, as discussed in the first part of this dissertation, their compact architectures and functional group densities increase the energetic drive to their physical adsorption at interfaces.

Future studies should focus efforts on reinforcing branched polymer electrolytes using nanofillers with specific advantageous properties targeted for both passive and active effects. For instance, ferroelectric nanoparticles can be considered for tuning the dielectric environment and ion dissociation. Incorporating ‘Garnet-type’ ceramics should also be explored due to their strong anion-withdrawing capacity, high ionic conductivity, and large shear moduli. Additionally, these ceramic particles provide new transport pathways through their bulk and modified interfacial regions. Considerable increases in macroscopic conductivity care therefore anticipated by self-assembling the oxide phase into an

interconnected, percolating network for high performance, flexible composite polymer electrolytes. Studies investigating the co-assembly of a ceramic conducting phase, however, need to emphasize the ion behavior at the inorganic-polymer interface where the disparate resistances of the two media can impede transport.

In theory, there exist $10^{18}$ possible combinations in IL pairs and there are roughly 1000 and counting IL compounds reported in the literature. When considering the myriad of different polymer architectures for which these different ILs can be polymerized into—not to mention their copolymerization into multifunctional block copolymers—the possibilities are boundless. Future studies would therefore benefit from a more targeted, collaborative approach in which the constructure of IL databases and a machine learning can be used to screen for chemistries and macromolecular architectures that might be suitable for polymerization towards a particular application or in understanding new physical phenomena. In addition, molecular dynamics simulations and other computational approaches can serve not only to help rationalize results observed form experimental work, but can be used in tandem with machine learning to help identify the structural and physical characteristics required in a polymer electrolyte at a molecular level. Such information is expected to greatly accelerate the experimental efforts of the electrolyte community.

In pursuing the ideas suggested above, investigators should keep in mind a number of unsettled fundamental issues which are of broader relevance to the soft matter community. This includes unravelling the significance of "decoupled" dynamic properties and how they change as disordered electrolytes are cooled into the glassy state. There is still much to learn regarding the interrelated effects of free volume of chain ends, inhomogenous segmental packing, and ion aggregation in branched polymers and densely functionalized nanoparticles, and further how these factors affect their local conformations, glass transition, viscoelasticity, and assembly in the melt and at interfaces. While the dielectric constant of the electrolyte is understood to influence dipole-dipole interactions, ionic aggregation, and counterion dissociation, more research is necessary to better understand which length scales the local dielectric environment is relevant in this regard—and furthermore whether or not the local morphology can play a role. Furthermore, although the work presented here demonstrates that the generality of descriptions of ion transport

such as the random barrier model can be applied to branched polymer electrolytes, researchers should continue to refine the physical description of ion transport in these materials to better understand ion reorganization, hopping, and conductivity in relation to electrolyte structure. And lastly, as the demands for electrolyte materials require nanostructured components and interfaces, it is increasingly important to consider how the organization and physical properties of branched polymers, such as the distribution of dynamic timescales, differs under confinement at the nanoscale as compared to in bulk electrolytes.

While the field of polymer electrolytes has already been active for several decades, the prominence of a new classes of ionic polymers—PolyILs—and the design of increasingly complex polymer architectures together promise many more fruitful years of discoveries in this area to come.

## 8.3 Dissemination of Work

The contents of this dissertation have been distributed to the research community in the following major publications and presentations:

[1] **Erwin, A. J.**; Lee, H.; Ge, S.; Sokolov, A. P.; Tsukruk, V. V., Ionic Liquid Functionalized Nanoparticles. *Manuscript in preparation*

[2] Kumar, R.; Mahalik, J. P.; Silmore, K. S.; Wojnarowska, Z.; **Erwin, A.**; Ankner, J. F.; Sokolov, A. P.; Sumpter, B. G.; Bocharova, V. Capacitance of thin films containing polymerized ionic liquids. *Sci. Adv.* **2020**, DOI: 10.1126/sciadv.aba7952

[3] Stryutsky, A. V.; Korolovych, V. F.; Lee, H.; Mikan, E.; **Erwin, A.**; Sobko, O.; Gumenna, M. A.; Klimenko, N. S.; Shevchenko, V. V.; Bulavin, L. A.; Tsukruk, V. V. Oligomeric and Polymeric Ionic Liquids: Engineering Architecture and Morphology. In book: *International Conference Physics of Liquid Matter: MPPLS*; Springer, Cham. 2018, Vol. *223*, pp 93-118

[4] **Erwin, A. J.**; Lee, H.; Ge, S.; Zhao, S.; Korolovych, V. F.; He, H.; Matyjaszewski, K.; Sokolov, A. P.; Tsukruk, V. V., Viscoelastic Properties and Ion Dynamics in Star-Shaped Polymerized Ionic Liquids. *Eur. Polym. J.* **2018**, *109*, 326-335 (*part of special issue: Poly(ionic liquid)s: innovative electrolytes for cutting-edge applications*)

[5] **Erwin, A. J**.; Korolovych, V. F.; Iatridi, Z.; Tsitsilianis, C.; Ankner, J. F.; Tsukruk, V. V., Tunable Compartmentalized Morphologies of Multilayered Dual Responsive Star Block Polyampholytes. *Macromolecules* **2018**, *51*, 4800-4812

[6] Korolovych, V. F.; **Erwin, A.**; Stryutsky, A.; Lee, H.; Heller, W. T.; Shevchenko, V. V.; Tsukruk, V. V., Thermally Responsive Hyperbranched Poly (ionic liquid) s: Assembly and Phase Transformations. *Macromolecules* **2018**, *51*, 4923-4937

[7] **Erwin, A. J.**; Xu, W.; He, H.; Matyjaszewski, K.; Tsukruk, V. V., Linear and Star Poly (ionic liquid) Assemblies: Surface Monolayers and Multilayers. *Langmuir* **2017**. *33*, 3187-3199

[8] Korolovych, V.; **Erwin, A.**; Stryutsky, A.; Mikan, E.; Shevchenko, V.; Tsukruk, V., Self-Assembly of Hyperbranched Protic Poly (ionic liquid) s with Variable Peripheral Amphiphilicity. *Bull. Chem. Soc. Jpn.* **2017**, 90, 919-923.

# REFERENCES


[1] Chu, S.; Majumdar, A. Opportunities and challenges for a sustainable energy future. *Nature* **2012,** *488*, 294-303.

[2] Wu, F.; Zhang, K.; Liu, Y.; Gao, H.; Bai, Y.; Wang, X.; Wu, C. Polymer electrolytes and interfaces toward solid-state batteries: Recent advances and prospects. *Energy Storage Mater.* **2020**, *33*, 26-54.

[3] Manthiram, A.; Yu, X.; Wang, S. Lithium battery chemistries enabled by solid-state electrolytes. *Nat. Rev. Mater.* **2017,** *2*, 16103.

[4] Osada, I.; de Vries, H.; Scrosati, B.; Passerini, S. Ionic-Liquid-Based Polymer Electrolytes for Battery Applications. *Angew. Chem. International Edition* **2016,** *55* (2), 500-513.

[5] Gebert, F.; Knott, J.; Gorkin, R.; Chou, S. L.; Dou, S. X. Polymer electrolytes for sodium-ion batteries. *Energy Stor. Mater.* **2020**, DOI: 10.1016/j.ensm.2020.11.030

[6] Wang, X.; Salari, M.; Jiang, D. E.; Varela, J. C.; Anasori, B.; Wesolowski, D. J.; Dai, S.; Grinstaff, M. W.; Gogotsi, Y. Electrode material–ionic liquid coupling for electrochemical energy storage. *Nat. Rev. Mater.* **2020**, *5*, 787-808.

[7] Bocharova, V.; Sokolov, A. P. Perspectives for polymer electrolytes: A view from fundamentals of ionic conductivity. *Macromolecules* **2020**, *53*, 4141-4157.

[8] Yu, S.; Schmidt, R. D.; Garcia-Mendez, R.; Herbert, E.; Dudney, N. J.; Wolfenstine, J. B.; Sakamoto, J.; Siegel, D. J. Elastic properties of the solid electrolyte Li7La3Zr2O12 (LLZO). *Chem. Mater.* **2015,** *28*, 197-206.

[9] Tikekar, M. D.; Choudhury, S.; Tu, Z.; Archer, L. A. Design principles for electrolytes and interfaces for stable lithium-metal batteries. *Nat. Energy* **2016,** *1*, 16114.

[10] Hallinan Jr, D. T.; Balsara, N. P. Polymer electrolytes. *Annu. Rev. Mater. Res.* **2013,** *43*, 503-525.

[11] Cotessat, M.; Flachard, D.; Nosov, D.; Lozinskaya, E. I.; Ponkratov, D. O.; Schmidt, D. F.; Drockenmuller, E.; Shaplov, A. S. Effects of repeat unit charge density on the physical and electrochemical properties of novel heterocationic poly (ionic liquid) s. *New J. Chem.* **2020**, DOI: 10.1039/d0nj04143b

[12] Fernandez-Nieves, A.; Puertas A. M., *Fluids, Colloids and Soft Materials: An Introduction to Soft Matter Physics*. John Wiley & Sons: 2016; Vol. 7.

[13] Stuart, M. A. C.; Huck, W. T.; Genzer, J.; Müller, M.; Ober, C.; Stamm, M.; Sukhorukov, G. B.; Szleifer, I.; Tsukruk, V. V.; Urban, M.; Winnik, F.; Zauscher, S.; Luzinov, I.; Minko, S. Emerging applications of stimuli-responsive polymer materials. *Nat. Mater.* **2010**, *9*, 101-113.

[14] Xu, W.; Ledin, P. A.; Shevchenko, V. V.; Tsukruk, V. V. Architecture, assembly, and emerging applications of branched functional polyelectrolytes and poly (ionic liquid) s. *ACS Appl. Mater. Interfaces* **2015**, *7*, 12570-12596.

[15] Dobrynin, A. V.; Rubinstein, M. Theory of polyelectrolytes in solutions and at surfaces. *Prog. Polym. Sci.* **2005,** *30*, 1049-1118.

[16] Dobrynin, A. V.; Colby, R. H.; Rubinstein, M. Polyampholytes. *J. Polym. Sci., Part B: Polym. Phys.* **2004,** *42*, 3513-3538.
[17] Hiemenz, P. C.; Lodge, T. P. *Polymer chemistry*. CRC press: 2007.
[18] Rubinstein, M.; Colby, R. H. *Polymer physics*. Oxford University Press New York: 2003; Vol. 23.
[19] De Gennes, P.-G. *Scaling concepts in polymer physics*. Cornell university press: 1979.
[20] De Gennes, P. Polymers at an interface; a simplified view. *Adv. Colloid Interface Sci.* **1987,** *27* (3-4), 189-209.
[21] Sperling, L. H. *Introduction to physical polymer science*. John Wiley & Sons: 2005.
[22] Chen, Q.; Bao, N.; Wang, J. H. H.; Tunic, T.; Liang, S.; Colby, R. H. Linear viscoelasticity and dielectric spectroscopy of ionomer/plasticizer mixtures: A transition from ionomer to polyelectrolyte. *Macromolecules* **2015**, *48*, 8240-8252.
[23] Tanford, C., *Physical chemistry of macromolecules*. Wiley: 1961.
[24] Weiss, R. A.; Zhao, H. Rheological behavior of oligomeric ionomers. *J. Rheol.* **2009**, *53*, 191-213.
[25] Chen, Q.; Tudryn, G. J.; Colby, R. H. Ionomer dynamics and the sticky Rouse model. *J. Rheol.* **2013**, *57*, 1441-1462.
[26] Chen, Q.; Liang, S.; Shiau, H. S.; Colby, R. H. Linear viscoelastic and dielectric properties of phosphonium siloxane ionomers. *ACS Macro Lett.* **2013**, *2*, 970-974.
[27] Cheng, Y.; Yang, J.; Hung, J. H.; Patra, T. K.; Simmons, D. S. Design rules for highly conductive polymeric ionic liquids from molecular dynamics simulations. *Macromolecules* **2018**, *51*, 6630-6644.
[28] Choi, U. H.; Mittal, A.; Price Jr, T. L.; Lee, M.; Gibson, H. W.; Runt, J.; Colby, R. H. Molecular volume effects on the dynamics of polymerized ionic liquids and their monomers. *Electrochim. Acta* **2015**, *175*, 55-61.
[29] Cui, J.; Li, Y.; Chen, D.; Zhan, T. G.; Zhang, K. D. Ionic Liquid-Based Stimuli-responsive Functional Materials. *Adv. Funct. Mater.* **2020**, 2005522.
[30] Welton, T. Room-temperature ionic liquids. Solvents for synthesis and catalysis. *Chem. Rev.* **1999,** *99*, 2071-2084.
[31] Huddleston, J. G.; Visser, A. E.; Reichert, W. M.; Willauer, H. D.; Broker, G. A.; Rogers, R. D. Characterization and comparison of hydrophilic and hydrophobic room temperature ionic liquids incorporating the imidazolium cation. *Green Chem.* **2001,** *3*, 156-164.
[32] Mecerreyes, D. Polymeric ionic liquids: Broadening the properties and applications of polyelectrolytes. *Prog. Polym. Sci.* **2011,** *36*, 1629-1648.
[33] Yuan, J.; Mecerreyes, D.; Antonietti, M. Poly (ionic liquid) s: An update. *Prog. Polym. Sci.* **2013,** *38*, 1009-1036.
[34] Green, O.; Grubjesic, S.; Lee, S.; Firestone, M. A. The design of polymeric ionic liquids for the preparation of functional materials. *Polym. Rev.* **2009,** *49*, 339-360.
[35] Qian, W.; Texter, J.; Yan, F. Frontiers in poly (ionic liquid) s: syntheses and applications. *Chem. Soc. Rev.* **2017**, *46*, 1124-1159.
[36] Liu, Y.; Wang, B.; Dong, Y.; Zhao, X.; Yin, J. Distinctly different electroresponsive electrorheological effect in low-molecular-weight and polymerized ionic liquids: rheological and dielectric relaxation studies. *J. Phys. Chem. B.* **2018**, *122*, 12184-12193.

[37] Cowan, M. G.; Gin, D. L.; Noble, R. D. Poly (ionic liquid)/ionic liquid ion-gels with high "free" ionic liquid content: platform membrane materials for CO2/light gas separations. *Acc. Chem. Res.* **2016**, *49*, 724-732.

[38] Wu, J.; Mu, L.; Feng, X.; Lu, X.; Larsson, R.; Shi, Y. Poly (alkylimidazolium bis (trifluoromethylsulfonyl) imide)-Based Polymerized Ionic Liquids: A Potential High-Performance Lubricating Grease. *Adv. Mater. Interfaces* **2019**, *6*, 1801796.

[39] Wheatle, B. K.; Fuentes, E. F.; Lynd, N. A.; Ganesan, V. Influence of Host Polarity on Correlating Salt Concentration, Molecular Weight, and Molar Conductivity in Polymer Electrolytes. *ACS Macro Letters* **2019**, *8*, 888-892.

[40] Wei, S.; Choudhury, S.; Xu, J.; Nath, P.; Tu, Z.; Archer, L. A. Highly stable sodium batteries enabled by functional ionic polymer membranes. *Adv. Mater*. **2017**, *29*, 1605512.

[41] Zhao, S.; Zhang, Y.; Pham, H.; Carrillo, J. M. Y.; Sumpter, B. G.; Nanda, J.; Dudney, N. J.; Saito, T.; Sokolov, A. P.; Cao, P. F. Improved Single-Ion Conductivity of Polymer Electrolyte via Accelerated Segmental Dynamics. *ACS Appl. Energy Mater.* **2020**, DOI: 10.1021/acsaem.0c02079

[42] Kokubo, H.; Sano, R.; Murai, K.; Ishii, S.; Watanabe, M., Ionic polymer actuators using poly (ionic liquid) electrolytes. *Eur. Polym. J.* **2018**, 106, 266-272.

[43] Zhao, D.; Martinelli, A.; Willfahrt, A.; Fischer, T.; Bernin, D.; Khan, Z.U.; Shahi, M.; Brill, J.; Jonsson, M.P.; Fabiano, S.; Crispin, X., Polymer gels with tunable ionic Seebeck coefficient for ultra-sensitive printed thermopiles. *Nat. Commun.* **2019**, *10*, 1093.

[44] Hayes, R.; Warr, G. G.; Atkin, R. Structure and nanostructure in ionic liquids. *Chem. Rev.* **2015**, *115*, 6357-6426.

[45] Yoshio, M.; Kagata, T.; Hoshino, K.; Mukai, T.; Ohno, H.; Kato, T. One-dimensional ion-conductive polymer films: alignment and fixation of ionic channels formed by self-organization of polymerizable columnar liquid crystals. *J. Am. Chem. Soc.* **2006,** *128*, 5570-5577.

[46] Batra, D.; Seifert, S.; Varela, L. M.; Liu, A. C.; Firestone, M. A. Solvent-Mediated Plasmon Tuning in a Gold-Nanoparticle–Poly (Ionic Liquid) Composite. *Adv. Funct. Mater.* **2007,** *17*, 1279-1287.

[47] Yuan, J.; Soll, S.; Drechsler, M.; Müller, A. H.; Antonietti, M. Self-assembly of poly (ionic liquid) s: Polymerization, mesostructure formation, and directional alignment in one step. *J. Am. Chem. Soc.* **2011**, *133*, 17556-17559.

[48] Vijayakrishna, K.; Mecerreyes, D.; Gnanou, Y.; Taton, D., Polymeric vesicles and micelles obtained by self-assembly of ionic liquid-based block copolymers triggered by anion or solvent exchange. *Macromolecules* **2009,** *42*, 5167-5174.

[49] Pothanagandhi, N.; Sivaramakrishna, A.; Vijayakrishna, K., Chiral anion-triggered helical poly (ionic liquids). *Polym. Chem.* **2017**, *8*, 918-925.

[50] He, H.; Rahimi, K.; Zhong, M.; Mourran, A.; Luebke, D. R.; Nulwala, H. B.; Möller, M.; Matyjaszewski, K. Cubosomes from hierarchical self-assembly of poly (ionic liquid) block copolymers. *Nat. Commun.* **2017**, *8*, 1-8.

[51] Ricks-Laskoski, H. L.; Snow, A. W., Synthesis and electric field actuation of an ionic liquid polymer. *J. Am. Chem. Soc.* **2006,** *128*, 12402-12403.

[52] Zhang, K.; Feng, X.; Ye, C.; Hempenius, M. A.; Vancso, G. J. Hydrogels with a memory: dual-responsive, organometallic poly (ionic liquid) s with hysteretic volume-phase transition. *J. Am. Chem. Soc.* **2017**, *139*, 10029-10035.

[53] Zhao, Q.; Heyda, J.; Dzubiella, J.; Täuber, K.; Dunlop, J. W.; Yuan, J. Sensing solvents with ultra-sensitive porous poly (ionic liquid) actuators. *Adv. Mater.* **2015**, *27*, 2913-2917

[54] Mori, H.; Ebina, Y.; Kambara, R.; Nakabayashi, K. Temperature-responsive self-assembly of star block copolymers with poly (ionic liquid) segments. *Polym. J.* **2012**, *44*, 550-560.

[55] Sun, J. K.; Zhang, W.; Guterman, R.; Lin, H. J.; Yuan, J. Porous polycarbene-bearing membrane actuator for ultrasensitive weak-acid detection and real-time chemical reaction monitoring. *Nat. Commun.* **2018**, *9*, 1-8.

[56] Zhao, Q.; Yin, M.; Zhang, A. P.; Prescher, S.; Antonietti, M.; Yuan, J. Hierarchically structured nanoporous poly (ionic liquid) membranes: Facile preparation and application in fiber-optic pH sensing. *J. Am. Chem. Soc.* **2013**, *135*, 5549-5552.

[57] Chen, F.; Guo, J.; Xu, D.; Yan, F. Thermo-and pH-responsive poly (ionic liquid) membranes. *Polym. Chem.* **2016**, *7*, 1330-1336.

[58] Xiao, S.; Lu, X.; Lu, Q. Photosensitive polymer from ionic self-assembly of azobenzene dye and poly (ionic liquid) and its alignment characteristic toward liquid crystal molecules. *Macromolecules* **2007,** *40*, 7944-7950.

[59] Darabi, A.; Jessop, P. G.; Cunningham, M. F. CO 2-responsive polymeric materials: synthesis, self-assembly, and functional applications. *Chem. Soc. Rev.* **2016**, *45*, 4391-4436.

[60] Angell, C. A. Formation of glasses from liquids and biopolymers. Science **1995**, *267*, 1924-1935.

[61] Wojnarowska, Z.; Paluch, M. Recent progress on dielectric properties of protic ionic liquids. J. Phys.: Condens. Matter **2015**, *27*, 073202.

[62] Dyre, J. C. Colloquium: The glass transition and elastic models of glass-forming liquids. Rev. Mod. Phys. **2006**, *78*, 953.

[63] Mogurampelly, S.; Keith, J. R.; Ganesan, V., Mechanisms Underlying Ion Transport in Polymerized Ionic Liquids. *J. Amer. Chem. Soc.* **2017,** *139*, 9511-9514.

[64] Keith, J. R.; Mogurampelly, S.; Aldukhi, F.; Wheatle, B. K.; Ganesan, V. Influence of molecular weight on ion-transport properties of polymeric ionic liquids. *Phys. Chem. Chem. Phys.* **2017**, *19*, 29134-29145

[65] Bartels, J.; Sanoja, G. E.; Evans, C. M.; Segalman, R. A.; Helgeson, M. E. Decoupling Mechanical and Conductive Dynamics of Polymeric Ionic Liquids via a Trivalent Anion Additive. *Macromolecules* **2017**, *50*, 22, 8979–8987

[66] Wang, Y.; Agapov, A. L.; Fan, F.; Hong, K.; Yu, X.; Mays, J.; Sokolov, A. P. Decoupling of ionic transport from segmental relaxation in polymer electrolytes. *Phys. Rev. Lett.* **2012,** *108*, 088303.

[67] Kinsey, T.; Glynn, K.; Cosby, T.; Iacob, C.; Sangoro, J. Ion Dynamics of Monomeric Ionic Liquids Polymerized In Situ within Silica Nanopores. *ACS Appl. Mater. Interfaces* **2020**, *12*, 44325-44334.

[68] Do, C.; Lunkenheimer, P.; Diddens, D.; Götz, M.; Weiß, M.; Loidl, A.; Sun, X.-G.; Allgaier, J.; Ohl, M. Li+ transport in poly (ethylene oxide) based electrolytes: neutron scattering, dielectric spectroscopy, and molecular dynamics simulations. *Phys. Rev. Lett.* **2013,** *111*, 018301.

[69] Mallamace, F.; Branca, C.; Corsaro, C.; Leone, N.; Spooren, J.; Chen, S.-H.; Stanley, H. E. Transport properties of glass-forming liquids suggest that dynamic crossover

temperature is as important as the glass transition temperature. *PNAS* **2010,** *107*, 22457-22462.

[70] Sangoro, J.; Iacob, C.; Serghei, A.; Naumov, S.; Galvosas, P.; Kärger, J.; Wespe, C.; Bordusa, F.; Stoppa, A.; Hunger, J. Electrical conductivity and translational diffusion in the 1-butyl-3-methylimidazolium tetrafluoroborate ionic liquid. *J. Chem. Phys.* **2008**, *128*, 214509.

[71] Griffin, P.; Agapov, A. L.; Kisliuk, A.; Sun, X.-G.; Dai, S.; Novikov, V. N.; Sokolov, A. P. Decoupling charge transport from the structural dynamics in room temperature ionic liquids. *J. Chem. Phys.* **2011,** *135*, 114509.

[72] Fan, F.; Wang, Y.; Hong, T.; Heres, M. F.; Saito, T.; Sokolov, A. P. Ion conduction in polymerized ionic liquids with different pendant groups. *Macromolecules* **2015,** *48*, 4461-4470.

[73] Fan, F.; Wang, W.; Holt, A. P.; Feng, H.; Uhrig, D.; Lu, X.; Hong, T.; Wang, Y.; Kang, N.-G.; Mays, J.; Sokolov, A. P. Effect of molecular weight on the ion transport mechanism in polymerized ionic liquids. *Macromolecules* **2016,** *49*, 4557-4570.

[74] Wojnarowska, Z.; Paluch, K. J.; Shoifet, E.; Schick, C.; Tajber, L.; Knapik, J.; Wlodarczyk, P.; Grzybowska, K.; Hensel-Bielowka, S.; Verevkin, S. P. Molecular origin of enhanced proton conductivity in anhydrous ionic systems. *J. Am. Chem. Soc.* **2015,** *137*, 1157-1164.

[75] Napolitano, S.; Glynos, E.; Tito, N. B. Glass transition of polymers in bulk, confined geometries, and near interfaces. *Rep. Prog. Phys.* **2017**, *80*, 036602.

[76] Shusharina, N.; Rubinstein, M., Concentration regimes in solutions of polyelectrolyte stars. *Macromolecules* **2008,** *41*, 203-217.

[77] Song, J.; Cho, B.-K. Glass Transition Behavior of Dendritic Polymers Containing Mobile Aliphatic Polyether Cores and Glassy Peripheral Polystyrenes. *Bull. Korean Chem. Soc.* **2008**, *29*, 1167-1172.

[78] Glynos, E.; Frieberg, B.; Oh, H.; Liu, M.; Gidley, D. W.; Green, P. F. Role of molecular architecture on the vitrification of polymer thin films. *Phys. Rev. Lett.* **2011**, *106*, 128301.

[79] Glynos, E.; Frieberg, B.; Chremos, A.; Sakellariou, G.; Gidley, D. W.; Green, P. F., Vitrification of thin polymer films: from linear chain to soft colloid-like behavior. *Macromolecules* **2015**, *48*, 2305-2312.

[80] Dobrynin, A. V. Theory and simulations of charged polymers: From solution properties to polymeric nanomaterials. *Curr. Opin. Colloid Interface Sci.* **2008**, *13*, 376-388.

[81] Kodiyath, R.; Choi, I.; Patterson, B.; Tsitsilianis, C.; Tsukruk, V. V. Interfacial behavior of pH responsive ampholytic heteroarm star block terpolymers. *Polymer* **2013,** *54*, 1150-1159.

[82] Choi, I.; Malak, S. T.; Xu, W.; Heller, W. T.; Tsitsilianis, C.; Tsukruk, V. V. Multicompartmental microcapsules from star copolymer micelles. *Macromolecules* **2013,** *46*, 1425-1436.

[83] Chen, G.; Hoffman, A. S. Graft copolymers that exhibit temperature-induced phase transitions over a wide range of pH. *Nature* **1995,** *373*, 49-52.

[84] Zhou, Y.; Huang, W.; Liu, J.; Zhu, X.; Yan, D. Self-assembly of hyperbranched polymers and its biomedical applications. *Adv. Mater.* **2010**, *22*, 4567-4590.

[85] Jing, Y. N.; Li, S. S.; Su, M.; Bao H.; Wan, W. M. Barbier Hyperbranching polymerization-induced emission toward facile fabrication of white light-emitting diode and light-harvesting film. *J. Am. Chem. Soc.* **2019**, *141*, 16839-16848.

[86] Lezov, A.; Gubarev, A.; Kaiser, T.; Tobaschus, W.; Tsvetkov, N.; Nischang, I.; Schubert, U. S.; Frey, H.; Perevyazko, I. "Hard" Sphere Behavior of "Soft", Globular-like, Hyperbranched Polyglycerols–Extensive Molecular Hydrodynamic and Light Scattering Studies. *Macromolecules* **2020**, DOI: 10.1021/acs.macromol.0c01340

[87] Yang, D. P.; Oo, M. N. N. L.; Deen, G. R.; Li, Z.; Loh, X. J. Nano-star-shaped polymers for drug delivery applications. *Macromol. Rapid Commun.* **2017**, *38*, 1700410.

[88] Uhlík, F.; Košovan, P.; Zhulina, E. B.; Borisov, O. V. Charge-controlled nano-structuring in partially collapsed star-shaped macromolecules. *Soft Matter* **2016**, *12*, 4846-4852.

[89] Huo, H.; Liu, J.; Kannan, S.; Chen, L.; Zhao, Y.; Zhang, L.; Chang, G.; Zhang, Q.; Liu, F. Multicompartment Nanoparticles Bearing Hydrophilic/Hydrophobic Subdomains by Self-Assembly of Star Polymers in Aqueous Solution. *Macromolecules* **2020**, DOI: 10.1021/acs.macromol.0c02213

[90] Harn, Y. W.; He, Y.; Wang, Z.; Chen, Y.; Liang, S.; Li, Z.; Li, Q.; Zhu, L.; Lin, Z. Synthesis of Amphiphilic and Double Hydrophilic Star-like Block Copolymers and the Dual pH-Responsiveness of Unimolecular Micelle. *Macromolecules* **2020**, *53*, 8286-8295.

[91] Liu, H.; Zhang, J.; Dai, W.; Zhao, Y. Synthesis and self-assembly of a dual-responsive monocleavable ABCD star quaterpolymer. *Polym. Chem.* **2017**, *8*, 6865-6878.

[92] Lebedeva, I. O.; Zhulina, E. B.; Borisov, O. V. Theory of Linear–Dendritic Block Copolymer Micelles. *ACS Macro Lett.* **2018**, *7*, 42-46.

[93] Xue, X.; Chen, Y.; Liang, K.; Huang, W.; Yang, H.; Jiang, L.; Jiang, Q.; Jiang, B.; Pu, H. (2020). A facile approach for preparing tadpole and barbell-shaped cyclic polymers through combining ATRP and atom transfer radical coupling (ATRC) reactions. *Polym. Chem.* **2020**, *11*, 6529-6538.

[94] Plamper, F. A.; Reinicke, S.; Elomaa, M.; Schmalz, H.; Tenhu, H. Pearl necklace architecture: New threaded star-shaped copolymers. *Macromolecules* **2010,** *43*, 2190-2203.

[95] Pelras, T.; Mahon, C. S.; Müllner, M. Synthesis and applications of compartmentalised molecular polymer brushes. *Angew. Chem. Int. Ed.* **2018**, *57*, 6982-6994.

[96] Iatridi, Z.; Lencina, M. S.; Tsitsilianis, C. PNIPAM-based heteroarm star-graft quarterpolymers: synthesis, characterization and pH-dependent thermoresponsiveness in aqueous media. *Polym. Chem.* **2015**, *6*, 3942-3955.

[97] Bichler, K. J.; Jakobi, B.; Sakai, V. G.; Klapproth, A.; Mole, R. A.; Schneider, G. J. Short-Time Dynamics of PDMS-g-PDMS Bottlebrush Polymer Melts Investigated by Quasi-Elastic Neutron Scattering. *Macromolecules* **2020**, DOI: 10.1021/acs.macromol.0c01846

[98] Lin, X.; He, Q.; Li, J. Complex polymer brush gradients based on nanolithography and surface-initiated polymerization. *Chem. Soc. Rev.* **2012,** *41*, 3584-3593.

[99] Peleshanko, S.; Tsukruk, V. V. The architectures and surface behavior of highly branched molecules. *Prog. Polym. Sci.* **2008**, *33*, 523-580.

[100] Polymeropoulos, G.; Zapsas, G.; Ntetsikas, K.; Bilalis, P.; Gnanou, Y.; Hadjichristidis, N. 50th Anniversary perspective: polymers with complex architectures. *Macromolecules* **2017**, *50*, 1253-1290.

[101] Jusufi, A.; Likos, C.; Löwen, H., Conformations and interactions of star-branched polyelectrolytes. *Phys. Rev. Lett.* **2001,** *88*, 018301.

[102] Likos, C.; Löwen, H.; Watzlawek, M.; Abbas, B.; Jucknischke, O.; Allgaier, J.; Richter, D., Star polymers viewed as ultrasoft colloidal particles. *Phys. Rev. Lett.* **1998,** *80*, 4450.

[103] Vlassopoulos, D., Colloidal star polymers: Models for studying dynamically arrested states in soft matter. *J. Polym. Sci. Part B Polym. Phys.* **2004,** *42*, 2931-2941.

[104] Chremos, A.; Douglas, J. F., Communication: When does a branched polymer become a particle? *J. Chem. Phys.* **2015**, *143*, 111104.

[105] Johnson, K. J.; Glynos, E.; Sakellariou, G.; Green, P., Dynamics of Star-Shaped Polystyrene Molecules: From Arm Retraction to Cooperativity. *Macromolecules* **2016**, *49*, 5669-5676.

[106] Kim, B.-S.; Gao, H.; Argun, A. A.; Matyjaszewski, K.; Hammond, P. T. All-star polymer multilayers as pH-responsive nanofilms. *Macromolecules* **2008,** *42*, 368-375.

[107] McConney, M. E.; Singamaneni, S.; Tsukruk, V. V. Probing soft matter with the atomic force microscopies: imaging and force spectroscopy. *Polym. Rev.* **2010,** *50*, 235-286.

[108] Panyukov, S. V.; Sheiko, S. S.; Rubinstein, M., Amplification of tension in branched macromolecules. *Phys. Rev. Lett.* **2009,** *102*, 148301.

[109] Berezney, J. P.; Marciel, A. B.; Schroeder, C. M.; Saleh, O. A., Scale-Dependent Stiffness and Internal Tension of a Model Brush Polymer. *Phys. Rev. Lett.* **2017,** *119*, 127801.

[110] Chremos, A.; Glynos, E.; Green, P. F. Structure and dynamical intra-molecular heterogeneity of star polymer melts above glass transition temperature. *J. Chem. Phys.* **2015**, *142*, 044901.

[111] Zamponi, M.; Pyckhout-Hintzen, W.; Wischnewski, A.; Monkenbusch, M.; Willner, L.; Kali, G. r.; Richter, D. Molecular observation of branch point motion in star polymer melts. *Macromolecules* **2009**, *43*, 518-524.

[112] Panagopoulou, A.; Napolitano, S. Irreversible Adsorption Governs the Equilibration of Thin Polymer Films. *Phys. Rev. Lett.* **2017**, *119*, 097801.

[113] Frieberg, B. R.; Glynos, E.; Stathouraki, M.; Sakellariou, G.; Green, P. F., Glassy Dynamics of Polymers with Star-Shaped Topologies: Roles of Molecular Functionality, Arm Length, and Film Thickness. *Macromolecules* **2017,** *50*, 3719-3725.

[114] Saigal, T.; Riley, J. K.; Golas, P. L.; Bodvik, R.; Claesson, P. M.; Matyjaszewski, K.; Tilton, R. D., Poly (ethylene oxide) star polymer adsorption at the silica/aqueous interface and displacement by linear poly (ethylene oxide). *Langmuir* **2013,** *29*, 3999-4007.

[115] Wang, H. S.; Khan, A.; Choe, Y.; Huh, J.; Bang, J., Architectural Effects of Organic Nanoparticles on Block Copolymer Orientation. *Macromolecules* **2017**, *50*, 5025-5032.

[116] Plamper, F. A.; Walther, A.; Müller, A. H.; Ballauff, M. Nanoblossoms: light-induced conformational changes of cationic polyelectrolyte stars in the presence of multivalent counterions. *Nano Lett.* **2007**, *7*, 167-171.

[117] Xu, W.; Choi, I.; Plamper, F. A.; Synatschke, C. V.; Muller, A. H.; Tsukruk, V. V. Nondestructive light-initiated tuning of layer-by-layer microcapsule permeability. *ACS Nano* **2012**, *7*, 598-613.

[118] Wang, X.; Gao, P.; Yang, Y.; Guo, H.; Wu, D. Dynamic and programmable morphology and size evolution via a living hierarchical self-assembly strategy. *Nat. Commun.* **2018**, *9*, 1-15.

[119] Steinschulte, A. A.; Gelissen, A. P.; Jung, A.; Brugnoni, M.; Caumanns, T.; Lotze, G.; Mayer, J.; Pergushov, D. V.; Plamper, F. A. Facile screening of various micellar

morphologies by blending miktoarm stars and diblock copolymers. *ACS Macro Lett.* **2017**, *6*, 711-715.

[120] Moghimi, E.; Chubak, I.; Statt, A.; Howard, M. P.; Founta, D.; Polymeropoulos, G.; Ntetsikas, K.; Hadjichristidis, N.; Panagiotopoulos, A. Z.; Likos, C. N.; Vlassopoulos, D. Self-Organization and Flow of Low-Functionality Telechelic Star Polymers with Varying Attraction. *ACS Macro Lett.* **2019**, *8*, 766-772.

[121] Qian, Z.; Koh, Y. P.; Pallaka, M. R.; Chang, A. B.; Lin, T. P.; Guzmán, P. E.; Grubbs, R. H.; Simon, S. L.; McKenna, G. B. Linear rheology of a series of second-generation dendronized wedge polymers. *Macromolecules* **2019**, *52*, 2063-2074.

[122] Stowe, M. K.; Liu, P.; Baker, G. L. Star poly (ethylene oxide) as a low temperature electrolyte and crystallization inhibitor. *Chem. Mater*. **2005**, *17*, 6555-6559.

[123] Hawker, C. J.; Chu, F.; Pomery, P. J.; Hill, D. J. Hyperbranched poly (ethylene glycol) s: a new class of ion-conducting materials. *Macromolecules* **1996**, *29*, 3831-3838.

[124] Tseng, S. K.; Wang, R. H.; Wu, J. L.; Jyothibasu, J. P.; Wang, T. L.; Chu, C. Y.; Lee, R. H. Synthesis of a series of novel imidazolium-containing ionic liquid copolymers for dye-sensitized solar cells. *Polymer* **2020**, *210*, 123074.

[125] Elwan, H. A.; Mamlouk, M.; Scott, K. A review of proton exchange membranes based on protic ionic liquid/polymer blends for polymer electrolyte membrane fuel cells. *J. Power Sources* **2020**, 229197.

[126] Lee, J.; Lau, V. M.; Ren, Y.; Evans, C. M.; Moore, J. S.; Sottos, N. R. Effect of Polymerized Ionic Liquid Structure and Morphology on Shockwave Energy Dissipation. *ACS Macro Lett.* **2019**, *8*, 535-539.

[127] Nulwala, H.; Mirjafari, A.; Zhou, X. Ionic liquids and poly (ionic liquid) s for 3D printing–A focused mini-review. *Eur. Polym. J.* **2018**, *108*, 390-398.

[128] Wiedmann, S.; Kerscher, B.; Lienert, C.; Böcherer, D.; Mülhaupt, R. Tailoring Poly (2-oxazoline)-Based Polymeric Ionic Liquids as Thermoresponsive Molecular Brushes and Programmable Dispersants for Silver Nanoparticles. *Macromolecules* **2020**, *53*, 6703-6710.

[129] Tran, T. S.; Dutta, N. K.; Choudhury, N. R. Poly (ionic liquid)-Stabilized Graphene Nanoinks for Scalable 3D Printing of Graphene Aerogels. *ACS Appl. Nano Mater.* **2020**, DOI: 10.1021/acsanm.0c02781

[130] Yang, J.; Chen, H.; Xiao, S.; Shen, M.; Chen, F.; Fan, P.; Zhong, M.; Zheng, J. Salt-responsive zwitterionic polymer brushes with tunable friction and antifouling properties. *Langmuir* **2015**, *31*, 9125-9133.

[131] Zhang, S. Y.; Miao, H.; Zhang, H. M.; Zhou, J. H.; Zhuang, Q.; Zeng, Y. J.; Gao, Z.; Yuan, J.; Sun, J. K. Accelerating Crystallization of Open Organic Materials by Poly(ionic liquid)s. *Angew. Chem. Int. Ed.* **2020**, *59*, 22109-22116

[132] Gou, H.; Ma, X.; Su, Q.; Liu, L.; Ying, T.; Qian, W.; Dong, Li.; Cheng, W. Hydrogen bond donor functionalized poly (ionic liquid) s for efficient synergistic conversion of CO 2 to cyclic carbonates. *Phys. Chem. Chem. Phys.* **2020**, DOI: 10.1039/x0xx00000x

[133] Ren, Y.; Zhang, J.; Guo, J.; Chen, F.; Yan, F. Porous poly (ionic liquid) membranes as efficient and recyclable absorbents for heavy metal ions. *Macromol. Rapid Commun.* **2017**, *38*, 1700151.

[134] Kammakakam, I.; Bara, J. E.; Jackson, E. M. Dual Anion–Cation Crosslinked Poly (ionic liquid) Composite Membranes for Enhanced CO2 Separation. *ACS Appl. Polym. Mater.* **2020**, DOI: 10.1021/acsapm.0c00877

[135] Li, X.; Sun, Y.; Wang, S.; Jia, X. Ru–Pd Thermoresponsive Nanocatalyst Based on a Poly (ionic liquid) for Highly Efficient and Selectively Catalyzed Suzuki Coupling and Asymmetric Transfer Hydrogenation in the Aqueous Phase. *ACS Appl. Mater. Interfaces* **2020**, *12*, 44094-44102.

[136] Guo, J.; Xu, Q.; Zheng, Z.; Zhou, S.; Mao, H.; Wang, B.; Yan, F. Intrinsically Antibacterial Poly (ionic liquid) Membranes: The Synergistic Effect of Anions. *ACS Macro Letters* **2015,** *4*, 1094-1098.

[137] Wang, F.; Hu, Z.; Fan, Y.; Bai, W.; Wu, S.; Sun, H.; Li, A. Salt-Rejection Solar Absorbers Based on Porous Ionic Polymers Nanowires for Desalination. *Macromol. Rapid Commun.* **2020**, 2000536.

[138] Yuan, J.; Márquez, A. G.; Reinacher, J.; Giordano, C.; Janek, J.; Antonietti, M. Nitrogen-doped carbon fibers and membranes by carbonization of electrospun poly (ionic liquid) s. *Polymer Chemistry* **2011,** *2*, 1654-1657.

[139] Xiao, S.; Lu, X.; Lu, Q. Photosensitive polymer from ionic self-assembly of azobenzene dye and poly (ionic liquid) and its alignment characteristic toward liquid crystal molecules. *Macromolecules* **2007,** *40*, 7944-7950.

[140] Kim, T. Y.; Lee, H. W.; Stoller, M.; Dreyer, D. R.; Bielawski, C. W.; Ruoff, R. S.; Suh, K. S. High-performance supercapacitors based on poly (ionic liquid)-modified graphene electrodes. *ACS Nano* **2010,** *5*, 436-442.

[141] Tang, G.; Niu, J.; Tang, J.; Yang, J.; Zhou, Z.; Gao, Y.; Chen, X.; Tang, R.; Tian, Y.; Li, Y.; Li, J.; Cao, Y. Development of poly (ionic liquids) based on mepiquat chloride with improved rainfastness and long-lasting activity on growth regulation of cotton plant. *ACS Sustainable Chem. Eng.* **2020**, *8*, 14996-15004

[142] Greaves, T. L.; Drummond, C. J. Protic ionic liquids: properties and applications. *Chem. Rev.* **2008,** *108*, 206-237.

[143] Fellinger, T. P.; Thomas, A.; Yuan, J.; Antonietti, M. 25th Anniversary article:"cooking carbon with salt": carbon materials and carbonaceous frameworks from ionic liquids and poly (ionic liquid) s. *Adv. Mater.* **2013,** *25*, 5838-5855.

[144] Iatridi, Z.; Roiter, Y.; Stavrouli, N.; Minko, S.; Tsitsilianis, C., Phase behavior and self-assembly of PS n (P2VP-b-PAA) n multiarmed multisegmented star terpolymers with ampholytic arms. *Polym. Chem.* **2011,** *2*, 2037-2044.

[145] Xu, W.; Ledin, P. A.; Iatridi, Z.; Tsitsilianis, C.; Tsukruk, V. V., Multiresponsive Star-Graft Quarterpolymer Monolayers. *Macromolecules* **2015,** *48*, 3344-3353.

[146] Xu, W.; Ledin, P. A.; Iatridi, Z.; Tsitsilianis, C.; Tsukruk, V. V., Multicompartmental Microcapsules with Orthogonal Programmable Two-Way Sequencing of Hydrophobic and Hydrophilic Cargo Release. *Angew. Chem.* **2016,** *128*, 4992-4997.

[147] He, H.; Averick, S.; Roth, E.; Luebke, D.; Nulwala, H.; Matyjaszewski, K. Clickable poly (ionic liquid) s for modification of glass and silicon surfaces. *Polymer* **2014,** *55*, 3330-3338.

[148] He, H.; Zhong, M.; Adzima, B.; Luebke, D.; Nulwala, H.; Matyjaszewski, K. A simple and universal gel permeation chromatography technique for precise molecular weight characterization of well-defined poly (ionic liquid)s. *J. Am. Chem. Soc.* **2013,** *135*, 4227-4230.

[149] He, H.; Luebke, D.; Nulwala, H.; Matyjaszewski, K. Synthesis of Poly (ionic liquid) s by Atom Transfer Radical Polymerization with ppm of Cu Catalyst. *Macromolecules* **2014,** *47*, 6601-6609.

[150] Chmielarz, P.; Park, S.; Sobkowiak, A.; Matyjaszewski, K. Synthesis of β-cyclodextrin-based star polymers via a simplified electrochemically mediated ATRP. *Polymer* **2016,** *88*, 36-42.

[151] Matyjaszewski, K.; Miller, P. J.; Pyun, J.; Kickelbick, G.; Diamanti, S. Synthesis and characterization of star polymers with varying arm number, length, and composition from organic and hybrid inorganic/organic multifunctional initiators. *Macromolecules* **1999,** *32*, 6526-6535.

[152] Sheller, N. B.; Petrash, S.; Foster, M. D.; Tsukruk, V. V. *Langmuir* **1998**, *14*, 4535-4544.

[153] Petty, M. C., *Langmuir-Blodgett films: an introduction.* Cambridge University Press: 1996.

[154] Ariga, K.; Yamauchi, Y.; Mori, T.; Hill, J. P. 25th Anniversary article: What can be done with the Langmuir-Blodgett method? Recent developments and its critical role in materials science. *Adv. Mater.* **2013**, *25*, 6477-6512.

[155] Larson, K.; Vaknin, D.; Villavicencio, O.; McGrath, D. V.; Tsukruk, V. V. *J. Phys. Chem. B* **2002**, *106*, 7246-7251.

[156] Decher, G. Fuzzy nanoassemblies: toward layered polymeric multicomposites. *Science* **1997,** *277*, 1232-1237.

[157] Borges, J. O.; Mano, J. F. Molecular interactions driving the layer-by-layer assembly of multilayers. *Chem. Rev.* **2014,** *114*, 8883-8942.

[158] Ariga, K.; Hill, J. P.; Ji, Q. Layer-by-layer assembly as a versatile bottom-up nanofabrication technique for exploratory research and realistic application. *PCCP* **2007,** *9*, 2319-2340.

[159] Richardson, J. J.; Björnmalm, M.; Caruso, F. Technology-driven layer-by-layer assembly of nanofilms. *Science* **2015**, 348, aaa2491.

[160] Richardson, J. J.; Cui, J.; Björnmalm, M.; Braunger, J. A.; Ejima, H.; Caruso, F. Innovation in layer-by-layer assembly. *Chem. Rev.* **2016**, *116*, 14828-14867.

[161] Decher, G. Fuzzy nanoassemblies: toward layered polymeric multicomposites. *Science* **1997,** *277*, 1232-1237.

[162] Borges, J. O.; Mano, J. F. Molecular interactions driving the layer-by-layer assembly of multilayers. *Chem. Rev.* **2014,** *114*, 8883-8942.

[163] Ariga, K.; Hill, J. P.; Ji, Q. Layer-by-layer assembly as a versatile bottom-up nanofabrication technique for exploratory research and realistic application. *PCCP* **2007,** *9*, 2319-2340.

[164] Lee, S.-S.; Hong, J.-D.; Kim, C. H.; Kim, K.; Koo, J. P.; Lee, K.-B. Layer-by-layer deposited multilayer assemblies of ionene-type polyelectrolytes based on the spin-coating method. *Macromolecules* **2001,** *34*, 5358-5360.

[165] Cho, J.; Char, K.; Hong, J. D.; Lee, K. B. Fabrication of highly ordered multilayer films using a spin self-assembly method. *Adv. Mater.* **2001,** *13*, 1076-1078.

[166] McConney, M. E.; Singamaneni, S.; Tsukruk, V. V., Probing soft matter with the atomic force microscopies: imaging and force spectroscopy. *Polym. Rev.* **2010,** *50*, 235-286.

[167] Tsukruk, V. V.; Singamaneni, S. Scanning Probe Microscopy of Soft Matter: Fundamentals and Practices, Wiley-VCH, Weinheim, **2012**.

[168] Ankner, J. F.; Tao, X.; Halbert, C. E.; Browning, J. F.; Michael Kilbey, S.; Swader, O. A.; Dadmun, M. S.; Kharlampieva, E.; Sukhishvili, S. A. The SNS liquids reflectometer. *Neutron News* **2008**, 19, 14-16.

[169] Russell, T., X-ray and neutron reflectivity for the investigation of polymers. *Mater. Sci. Rep.* **1990,** *5*, 171-271.

[170] Roe, R.-J., *Methods of X-ray and neutron scattering in polymer science*. Oxford University Press on Demand: 2000; Vol. 739.

[171] Büscher, K.; Graf, K.; Ahrens, H.; Helm, C. A., Influence of adsorption conditions on the structure of polyelectrolyte multilayers. *Langmuir* **2002,** *18*, 3585-3591.

[172] Ankner, J. F.; Majkrzak, C. F. In *Subsurface profile refinement for neutron specular reflectivity*, San Diego'92, International Society for Optics and Photonics: 1992; pp 260-269.

[173] Korolovych, V. F.; Cherpak, V.; Nepal, D.; Ng, A.; Shaikh, N. R.; Grant, A.; Xiong, R.; Bunning, T. J.; Tsukruk, V. V., Cellulose nanocrystals with different morphologies and chiral properties. *Polymer* **2018,** *145*, 334-347.

[174] Schönhals, A.; Kremer, F., *Broadband dielectric spectroscopy*, Springer: 2003.

[175] Dewald, I.; Fery, A., Polymeric Micelles and Vesicles in Polyelectrolyte Multilayers: Introducing Hierarchy and Compartmentalization. *Adv. Mater. Interf.* **2017**, *4*, 1600317

[176] Honda, S.; Toyota, T., Photo-triggered solvent-free metamorphosis of polymeric materials. *Nat. Commun.* **2017,** *8*, 502

[177] Ilmain, F.; Tanaka, T.; Kokufuta, E., Volume transition in a gel driven by hydrogen bonding. *Nature* **1991**, *349*, 400.

[178] Zhu, Z.; Sukhishvili, S. A., Layer-by-layer films of stimuli-responsive block copolymer micelles. *J. Mater. Chem.* **2012,** *22*, 7667-7671.

[179] Wang, Y.; Sukhishvili, S. A., All-Aqueous Nanoprecipitation: Spontaneous Formation of Hydrogen-Bonded Nanoparticles and Nanocapsules Mediated by Phase Separation of Poly (N-Isopropylacrylamide). *Macromol. Rapid Commun.* **2017**, doi: 10.1002/marc.201700242

[180] Scotti, A.; Gasser, U.; Herman, E. S.; Pelaez-Fernandez, M.; Han, J.; Menzel, A.; Lyon, L. A.; Fernández-Nieves, A., The role of ions in the self-healing behavior of soft particle suspensions. *Proc. Natl. Acad. Sci. U.S.A.* **2016,** *113*, 5576-5581.

[181] Wei, Z.; Yang, J. H.; Zhou, J.; Xu, F.; Zrínyi, M.; Dussault, P. H.; Osada, Y.; Chen, Y. M., Self-healing gels based on constitutional dynamic chemistry and their potential applications. *Chem. Soc. Rev.* **2014**, *43*, 8114-8131.

[182] Plamper, F. A.; Richtering, W., Functional microgels and microgel systems. *Acc. Chem. Res.* **2017**, *50*, 131-140.

[183]Russell, T. P.; Chai, Y., 50th Anniversary Perspective: Putting the Squeeze on Polymers: A Perspective on Polymer Thin Films and Interfaces. *Macromolecules* **2017**, *50*, 4597-4609.

[184] Dedinaite, A.; Thormann, E.; Olanya, G.; Claesson, P. M.; Nyström, B.; Kjøniksen, A.-L.; Zhu, K., Friction in aqueous media tuned by temperature-responsive polymer layers. *Soft Matter* **2010,** *6*, 2489-2498.

[185] Pasche, S.; Textor, M.; Meagher, L.; Spencer, N. D.; Griesser, H. J., Relationship between interfacial forces measured by colloid-probe atomic force microscopy and protein resistance of poly (ethylene glycol)-grafted poly (L-lysine) adlayers on niobia surfaces. *Langmuir* **2005,** *21*, 6508-6520.

[186] Akers, P. W.; Dingley, A. J.; Swift, S.; Nelson, A. R.; Martin, J.; McGillivray, D. J., Using Neutron Reflectometry to Characterize Antimicrobial Protein Surface Coatings. *J. Phys. Chem. B* **2017**, *121*¸5908-5916

[187] Folkertsma, L.; Zhang, K.; Czakkel, O.; de Boer, H. L.; Hempenius, M. A.; van den Berg, A.; Odijk, M.; Vancso, G. J., Synchrotron SAXS and Impedance Spectroscopy Unveil Nanostructure Variations in Redox-Responsive Porous Membranes from Poly (ferrocenylsilane) Poly (ionic liquid) s. *Macromolecules* **2016**, *50*, 296-302

[188] Dishari, S. K.; Rumble, C. A.; Maroncelli, M.; Dura, J. A.; Hickner, M., Unraveling the Complex Hydration Behavior of Ionomers Under Thin Film Confinement. *J. Phys. Chem. C* **2018**, *122*, 3471-3481

[189] Iatridi, Z.; Tsitsilianis, C., pH responsive self assemblies from an A n-core-(B-b-C) n heteroarm star block terpolymer bearing oppositely charged segments. *Chem. Commun.* **2011,** *47*, 5560-5562.

[190] Iatridi, Z.; Roiter, Y.; Stavrouli, N.; Minko, S.; Tsitsilianis, C., Phase behavior and self-assembly of PS n (P2VP-b-PAA) n multiarmed multisegmented star terpolymers with ampholytic arms. *Polym. Chem.* **2011,** *2*, 2037-2044.

[191] Kodiyath, R.; Choi, I.; Patterson, B.; Tsitsilianis, C.; Tsukruk, V. V., Interfacial behavior of pH responsive ampholytic heteroarm star block terpolymers. *Polymer* **2013,** *54*, 1150-1159.

[192] Dewald, I.; Gensel, J.; Betthausen, E.; Borisov, O. V.; Müller, A. H.; Schacher, F. H.; Fery, A., Splitting of Surface-Immobilized Multicompartment Micelles into Clusters upon Charge Inversion. *ACS Nano* **2016**, *10*, 5180-5188.

[193] Sanjuan, S.; Tran, Y., Stimuli-responsive interfaces using random polyampholyte brushes. *Macromolecules* **2008,** *41*, 8721-8728.

[194] Lazzara, G.; Campbell, R. A.; Bayati, S.; Zhu, K.; Nyström, B.; Nylander, T.; Schillén, K., On the formation of inclusion complexes at the solid/liquid interface of anchored temperature-responsive PNIPAAM diblock copolymers with γ-cyclodextrin. *Colloid. Polym. Sci.* **2017**, *8*, 1327-1341

[195] Han, X.; Zhang, X.; Zhu, H.; Yin, Q.; Liu, H.; Hu, Y., Effect of composition of PDMAEMA-b-PAA block copolymers on their pH-and temperature-responsive behaviors. *Langmuir* **2013**, 29, 1024-1034.

[196] Chen, G.; Hoffman, A. S., Graft copolymers that exhibit temperature-induced phase transitions over a wide range of pH. *Nature* **1995,** *373*, 49-52.

[197] Hyatt, J. S.; Douglas, A. M.; Stanley, C.; Do, C.; Barker, T. H.; Fernández-Nieves, A., Charge segregation in weakly ionized microgels. *Phys. Rev. E* **2017,** *95*, 012608.

[198] Okhapkin, I. M.; Nasimova, I. R.; Makhaeva, E. E.; Khokhlov, A. R., Effect of complexation of monomer units on pH-and temperature-sensitive properties of poly (N-vinylcaprolactam-co-methacrylic acid). *Macromolecules* **2003**, *36*, 8130-8138.

[199] Xu, L.; Zhu, Z.; Borisov, O. V.; Zhulina, E. B.; Sukhishvili, S. A., pH-Triggered Block Copolymer Micelle-to-Micelle Phase Transition. *Phys. Rev. Lett.* **2009**, *103*, 118301.

[200] Tan, W. S.; Zhu, Z.; Sukhishvili, S. A.; Rubner, M. F.; Cohen, R. E., Effect of block copolymer architecture on the thermally induced swelling of micelle-containing multilayer thin films. *Macromolecules* **2011**, *44*, 7767-7774.

[201] Tamai, Y.; Tanaka, H.; Nakanishi, K., Molecular dynamics study of polymer− water interaction in hydrogels. 1. Hydrogen-bond structure. *Macromolecules* **1996,** *29*, 6750-6760.

[202] Deshmukh, S. A.; Sankaranarayanan, S. K.; Suthar, K.; Mancini, D. C., Role of solvation dynamics and local ordering of water in inducing conformational transitions in

poly (N-isopropylacrylamide) oligomers through the LCST. *J. Phys. Chem. B* **2012,** *116*, 2651-2663.

[203] Xu, W.; Choi, I.; Plamper, F. A.; Synatschke, C. V.; Müller, A. H.; Melnichenko, Y. B.; Tsukruk, V. V., Thermo-induced limited aggregation of responsive star polyelectrolytes. *Macromolecules* **2014,** *47*, 2112-2121.

[204] Choi, I.; Malak, S. T.; Xu, W.; Heller, W. T.; Tsitsilianis, C.; Tsukruk, V. V., Multicompartmental microcapsules from star copolymer micelles. *Macromolecules* **2013,** *46*, 1425-1436.

[205] Zhu, Z.; Sukhishvili, S. A., Temperature-induced swelling and small molecule release with hydrogen-bonded multilayers of block copolymer micelles. *ACS Nano* **2009,** *3*, 3595-3605.

[206] Smith, E. G.; Webber, G. B.; Sakai, K.; Biggs, S.; Armes, S. P.; Wanless, E. J., Direct visualization of a self-organized multilayer film of low Tg diblock copolymer micelles. *J. Phys. Chem. B* **2007,** *111*, 5536-5541.

[207] Webber, G. B.; Wanless, E. J.; Armes, S. P.; Tang, Y.; Li, Y.; Biggs, S., Nano-Anemones: Stimulus-Responsive Copolymer-Micelle Surfaces. *Adv. Mater.* **2004,** *16*, 1794-1798.

[208] Xu, W.; Ledin, P. A.; Iatridi, Z.; Tsitsilianis, C.; Tsukruk, V. V., Multicompartmental Microcapsules with Orthogonal Programmable Two-Way Sequencing of Hydrophobic and Hydrophilic Cargo Release. *Angew. Chem.* **2016,** *128*, 4992-4997.

[209] Xu, W.; Steinschulte, A. A.; Plamper, F. A.; Korolovych, V. F.; Tsukruk, V. V., Hierarchical assembly of star polymer polymersomes into responsive multicompartmental microcapsules. *Chem. Mater.* **2016**, 28, 975-985.

[210] Costa, E.; Coelho, M.; Ilharco, L. M.; Aguiar-Ricardo, A.; Hammond, P. T., Tannic acid mediated suppression of PNIPAAm microgels thermoresponsive behavior. *Macromolecules* **2011,** *44*, 612-621.

[211] Shutava, T.; Prouty, M.; Kommireddy, D.; Lvov, Y., pH responsive decomposable layer-by-layer nanofilms and capsules on the basis of tannic acid. *Macromolecules* **2005,** *38*, 2850-2858.

[212] Erel-Unal, I.; Sukhishvili, S. A., Hydrogen-bonded multilayers of a neutral polymer and a polyphenol. *Macromolecules* **2008,** *41*, 3962-3970.

[213] Kozlovskaya, V.; Kharlampieva, E.; Drachuk, I.; Cheng, D.; Tsukruk, V. V., Responsive microcapsule reactors based on hydrogen-bonded tannic acid layer-by-layer assemblies. *Soft Matter* **2010,** *6*, 3596-3608.

[214] Kharlampieva, E.; Kozlovskaya, V.; Sukhishvili, S. A., Layer-by-layer hydrogen-bonded polymer films: from fundamentals to applications. *Adv. Mater.* **2009,** *21*, 3053-3065.

[215] Kharlampieva, E.; Kozlovskaya, V.; Tyutina, J.; Sukhishvili, S. A., Hydrogen-bonded multilayers of thermoresponsive polymers. *Macromolecules* **2005**, *38*, 10523-10531.

[216] Ariga, K.; Hill, J. P.; Ji, Q., Layer-by-layer assembly as a versatile bottom-up nanofabrication technique for exploratory research and realistic application. *PCCP* **2007**, *9*, 2319-2340.

[217] Lu, B.; Bondon, A.; Touil, I.; Zhang, H.; Alcouffe, P.; Pruvost, S.; Liu, C.; Maazouz, A.; Lamnawar, K. Role of the Macromolecular Architecture of Copolymers at Layer–Layer Interfaces of Multilayered Polymer Films: A Combined Morphological and Rheological Investigation. *Ind. Eng. Chem. Res.* **2020**, DOI: 10.1021/acs.iecr.0c04731

[218] Zhuk, A.; Xu, L.; Ankner, J. F.; Sukhishvili, S. A., Selective water uptake within micelle-containing layer-by-layer films of various architectures: a neutron reflectometry study. *Soft Matter* **2013,** *9*, 410-417.

[219] Higgins, W.; Kozlovskaya, V.; Alford, A.; Ankner, J.; Kharlampieva, E., Stratified Temperature-Responsive Multilayer Hydrogels of Poly (N-vinylpyrrolidone) and Poly (N-vinylcaprolactam): Effect of Hydrogel Architecture on Properties. *Macromolecules* **2016,** *49*, 6953-6964.

[220] DeCaluwe, S. C.; Kienzle, P. A.; Bhargava, P.; Baker, A. M.; Dura, J. A., Phase segregation of sulfonate groups in Nafion interface lamellae, quantified via neutron reflectometry fitting techniques for multi-layered structures. *Soft Matter* **2014**, *10*, 5763-5776.

[221] Wallet, B.; Kharlampieva, E.; Campbell-Proszowska, K.; Kozlovskaya, V.; Malak, S.; Ankner, J. F.; Kaplan, D. L.; Tsukruk, V. V., Silk Layering as Studied with Neutron Reflectivity. *Langmuir* **2012,** *28*, 11481-11489.

[222] Lazzara, G.; Campbell, R. A.; Bayati, S.; Zhu, K.; Nyström, B.; Nylander, T.; Schillén, K., On the formation of inclusion complexes at the solid/liquid interface of anchored temperature-responsive PNIPAAM diblock copolymers with γ-cyclodextrin. *Colloid. Polym. Sci.* **2017**, *8*, 1327-1341

[223] Yim, H.; Kent, M.; Huber, D.; Satija, S.; Majewski, J.; Smith, G., Conformation of end-tethered PNIPAM chains in water and in acetone by neutron reflectivity. *Macromolecules* **2003,** *36*, 5244-5251.

[224] Nelson, A., Co-refinement of multiple-contrast neutron/X-ray reflectivity data using MOTOFIT. *J. Appl. Crystallogr.* **2006,** *39*, 273-276.

[225] Gensel, J.; Dewald, I.; Erath, J.; Betthausen, E.; Müller, A. H.; Fery, A., Reversible swelling transitions in stimuli-responsive layer-by-layer films containing block copolymer micelles. *Chem. Sci.* **2013,** *4*, 325-334.

[226] Connal, L. A.; Li, Q.; Quinn, J. F.; Tjipto, E.; Caruso, F.; Qiao, G. G., pH-responsive poly (acrylic acid) core cross-linked star polymers: morphology transitions in solution and multilayer thin films. *Macromolecules* **2008,** *41*, 2620-2626

[227] Schlenoff, J. B.; Ly, H.; Li, M., Charge and mass balance in polyelectrolyte multilayers. *J. Am. Chem. Soc.* **1998,** *120*, 7626-7634.

[228] Wong, J. E.; Rehfeldt, F.; Hänni, P.; Tanaka, M.; Klitzing, R. V., Swelling behavior of polyelectrolyte multilayers in saturated water vapor. *Macromolecules* **2004,** *37*, 7285-7289.

[229] Lösche, M.; Schmitt, J.; Decher, G.; Bouwman, W. G.; Kjaer, K., Detailed structure of molecularly thin polyelectrolyte multilayer films on solid substrates as revealed by neutron reflectometry. *Macromolecules* **1998**, 31, 8893-8906.

[230] Steitz, R.; Leiner, V.; Siebrecht, R.; Klitzing, R. V. Influence of the ionic strength on the structure of polyelectrolyte films at the solid/liquid interface. *Colloids Surf. A* **2000**, *163*, 63-70.

[231] Gao, X.; Kucerka, N.; Nieh, M.-P.; Katsaras, J.; Zhu, S.; Brash, J. L.; Sheardown, H., Chain conformation of a new class of PEG-based thermoresponsive polymer brushes grafted on silicon as determined by neutron reflectometry. *Langmuir* **2009,** *25*, 10271-10278.

[232] Steitz, R.; Leiner, V.; Tauer, K.; Khrenov, V.; Klitzing, R. V., Temperature-induced changes in polyelectrolyte films at the solid–liquid interface. *Appl. Phys. A* **2002**, *74*, s519-s521.

[233] Anastasiadis, S.; Russell, T.; Satija, S.; Majkrzak, C., Neutron reflectivity studies of the surface-induced ordering of diblock copolymer films. *Phys. Rev. Lett.* **1989,** *62*, 1852.

[234] Banquy, X.; Le Dévédec, F.; Cheng, H.-W.; Faivre, J.; Zhu, J. X.; Valtiner, M., Interaction Forces Between Pegylated Star-Shaped Polymers at Mica Surfaces. *ACS Appl. Mater. Interfaces* **2017**, *9*, 28027-28033

[235] Witten, T. A.; Pincus, P. A., *Structured fluids: polymers, colloids, surfactants*. Oxford University Press: 2004.

[236] Kharlampieva, E.; Kozlovskaya, V.; Ankner, J. F.; Sukhishvili, S. A., Hydrogen-bonded polymer multilayers probed by neutron reflectivity. *Langmuir* **2008,** *24*, 11346-11349.

[237] Wang, Y.; Sukhishvili, S. A., Hydrogen-bonded polymer complexes and nanocages of weak polyacids templated by a Pluronic® block copolymer. *Soft Matter* **2016**, *12*, 8744-8754.

[238] Shaplov, A. S., Ponkratov, D. O., & Vygodskii, Y. S. Poly (ionic liquid) s: Synthesis, properties, and application. *Polym. Sci. Ser. B.* **2016**, *58*, 73-142.

[239] Obadia, M. M., & Drockenmuller, E. Poly (1, 2, 3-triazolium) s: a new class of functional polymer electrolytes. *Chem. Commun.* **2016** *52*, 2433-2450.

[240] Bara, J. E.; Lessmann, S.; Gabriel, C. J.; Hatakeyama, E. S.; Noble, R. D.; Gin, D. L. Synthesis and performance of polymerizable room-temperature ionic liquids as gas separation membranes. *Ind. Eng. Chem. Res.* **2007,** *46*, 5397-5404.

[241] Dubas, S. T.; Schlenoff, J. B. Swelling and smoothing of polyelectrolyte multilayers by salt. *Langmuir* **2001,** *17*, 7725-7727

[242] Choi, I.; Suntivich, R.; Plamper, F. A.; Synatschke, C. V.; Müller, A. H.; Tsukruk, V. V. pH-controlled exponential and linear growing modes of layer-by-layer assemblies of star polyelectrolytes. *J. Am. Chem. Soc.* **2011,** *133*, 9592-9606.

[243] Xu, W.; Ledin, P. A.; Iatridi, Z.; Tsitsilianis, C.; Tsukruk, V. V. Multiresponsive Star-Graft Quarterpolymer Monolayers. *Macromolecules* **2015,** *48*, 3344-3353.

[244] Xu, W.; Choi, I.; Plamper, F. A.; Synatschke, C. V.; Müller, A. H.; Tsukruk, V. V. Nondestructive light-initiated tuning of layer-by-layer microcapsule permeability. *ACS Nano* **2012,** *7*, 598-613.

[245] Azzaroni, O.; Brown, A. A.; Huck, W. T. Tunable wettability by clicking counterions into polyelectrolyte brushes. *Adv. Mater.* **2007,** *19*, 151-154.

[246] He, H.; Averick, S.; Roth, E.; Luebke, D.; Nulwala, H.; Matyjaszewski, K. Clickable poly (ionic liquid) s for modification of glass and silicon surfaces. *Polymer* **2014,** *55*, 3330-3338.

[247] Ma, X.; Ashaduzzaman, M.; Kunitake, M.; Crombez, R.; Texter, J.; Slater, L.; Mourey, T. Stimuli responsive poly (1-[11-acryloylundecyl]-3-methyl-imidazolium bromide): dewetting and nanoparticle condensation phenomena. *Langmuir* **2011,** *27*, 7148-7157.

[248] Zhao, Q.; Zhang, P.; Antonietti, M.; Yuan, J. Poly (ionic liquid) complex with spontaneous micro-/mesoporosity: template-free synthesis and application as catalyst support. *J. Am. Chem. Soc.* **2012,** *134*, 11852-11855.

[249] Folkertsma, L.; Zhang, K.; Czakkel, O.; de Boer, H. L.; Hempenius, M. A.; van den Berg, A.; Odijk, M.; Vancso, G. J., Synchrotron SAXS and Impedance Spectroscopy Unveil Nanostructure Variations in Redox-Responsive Porous Membranes from Poly

(ferrocenylsilane) Poly (ionic liquid) s. *Macromolecules* **2016**, doi: 10.1021/acs.macromol.6b02318

[250] Adzima, B. J.; Taylor, S. C.; He, H.; Luebke, D. R.; Matyjaszewski, K.; Nulwala, H. B. Vinyl-triazolium monomers: Versatile and new class of radically polymerizable ionic monomers. *J. Polym. Sci., Part A: Polym. Chem.* **2014,** *52*, 417-423.

[251] Zhao, Q., Fellinger, T. P., Antonietti, M., & Yuan, J. Nitrogen-Doped Carbon Capsules via Poly (ionic liquid)-Based Layer-by-Layer Assembly. *Macromol. Rapid Commun.* **2013**. 33, 1149-1153.

[252] Petty, M. C., *Langmuir-Blodgett films: an introduction*. Cambridge University Press: 1996.

[253] Kharlampieva, E.; Kozlovskaya, V.; Chan, J.; Ankner, J. F.; Tsukruk, V. V. Spin-Assisted Layer-by-Layer Assembly: Variation of Stratification as Studied with Neutron Reflectivity†. *Langmuir* **2009,** *25*, 14017-14024.

[254] Yuan, J.; Antonietti, M. Poly (ionic liquid) latexes prepared by dispersion polymerization of ionic liquid monomers. *Macromolecules* **2011,** *44*, 744-750.

[255] Kakuchi, T.; Narumi, A.; Matsuda, T.; Miura, Y.; Sugimoto, N.; Satoh, T.; Kaga, H. Glycoconjugated polymer. 5. Synthesis and characterization of a seven-arm star polystyrene with a β-cyclodextrin core based on TEMPO-mediated living radical polymerization. *Macromolecules* **2003,** *36*, 3914-3920.

[256] Choi, I.; Gunawidjaja, R.; Suntivich, R.; Tsitsilianis, C.; Tsukruk, V. Surface Behavior of PS n (P2VP-b-P t BA) n Heteroarm Stars. *Macromolecules* **2010,** *43*, 6818-6828.

[257] Zhai, X.; Peleshanko, S.; Klimenko, N.; Genson, K.; Vaknin, D.; Vortman, M. Y.; Shevchenko, V.; Tsukruk, V. Amphiphilic dendritic molecules: hyperbranched polyesters with alkyl-terminated branches. *Macromolecules* **2003,** *36*, 3101-3110.

[258] Dhanabalan, A.; Dabke, R.; Kumar, N. P.; Talwar, S.; Major, S.; Lal, R.; Contractor, A. A study of Langmuir and Langmuir-Blodgett films of polyaniline. *Langmuir* **1997,** *13*, 4395-4400.

[259] Chung, B.; Choi, M.; Ree, M.; Jung, J. C.; Zin, W. C.; Chang, T. Subphase pH effect on surface micelle of polystyrene-b-poly (2-vinylpyridine) diblock copolymers at the air-water interface. *Macromolecules* **2006,** *39*, 684-689.

[260] Korolovych, V. F.; Ledin, P. A.; Stryutsky, A.; Shevchenko, V. V.; Sobko, O.; Xu, W.; Bulavin, L. A.; Tsukruk, V. V. Assembly of Amphiphilic Hyperbranched Polymeric Ionic Liquids in Aqueous Media at Different pH and Ionic Strength. *Macromolecules* **2016**, *49*, 8697-8710.

[261] Joncheray, T. J.; Denoncourt, K. M.; Mathieu, C.; Meier, M. A.; Schubert, U. S.; Duran, R. S. Langmuir and Langmuir-Blodgett films of poly (ethylene oxide)-b-poly (ε-caprolactone) star-shaped block copolymers. *Langmuir* **2006,** *22*, 9264-9271.

[262] Kerscher, B.; Appel, A.-K.; Thomann, R.; Mülhaupt, R. Treelike polymeric ionic liquids grafted onto graphene nanosheets. *Macromolecules* **2013,** *46*, 4395-4402.

[263] Verma, A.; Sharma, A. Enhanced Self-Organized Dewetting of Ultrathin Polymer Films Under Water-Organic Solutions: Fabrication of Sub-micrometer Spherical Lens Arrays. *Adv. Mater.* **2010,** *22*, 5306-5309.

[264] Logan, J. L.; Masse, P.; Dorvel, B.; Skolnik, A. M.; Sheiko, S. S.; Francis, R.; Taton, D.; Gnanou, Y.; Duran, R. S. AFM Study of Micelle Chaining in Surface Films of Polystyrene-b lock-Poly (ethylene oxide) Stars at the Air/Water Interface. *Langmuir* **2005,** *21*, 3424-3431.

[265] Higgins, A. M.; Jones, R. A. Anisotropic spinodal dewetting as a route to self-assembly of patterned surfaces. *Nature* **2000,** *404*, 476-478.

[266] Qin, S.; Wei, D.; Liao, Q.; Jin, X. Dewetting process of polyelectrolyte multilayer films in hot water. *Macromol. Rapid Commun.* **2006,** *27*, 11-14.

[267] Bollinne, C.; Cuenot, S.; Nysten, B.; Jonas, A. M. Spinodal-like dewetting of thermodynamically-stable thin polymer films. *Eur. Phys. J. E Soft Matter* **2003,** *12*, 389-396.

[268] Redon, C.; Brochard-Wyart, F.; Rondelez, F. Dynamics of dewetting. *Phys. Rev. Lett.* **1991,** *66*, 715.

[269] Wong, J. E.; Zastrow, H.; Jaeger, W.; von Klitzing, R. Specific ion versus electrostatic effects on the construction of polyelectrolyte multilayers†. *Langmuir* **2009,** *25*, 14061-14070.

[270] Chen, X.; Zhao, J.; Zhang, J.; Qiu, L.; Xu, D.; Zhang, H.; Han, X.; Sun, B.; Fu, G.; Zhang, Y. Bis-imidazolium based poly (ionic liquid) electrolytes for quasi-solid-state dye-sensitized solar cells. *J. Mater. Chem.* **2012,** *22*, 18018-18024.

[271] Lourenço, J. M.; Ribeiro, P. A.; do Rego, A. M. B.; Raposo, M. Counterions in layer-by-layer films—Influence of the drying process. *J. Colloid Interface Sci.* **2007,** *313*, 26-33.

[272] Fu, J.; Schlenoff, J. B. Driving Forces for Oppositely Charged Polyion Association in Aqueous Solutions: Enthalpic, Entropic, but Not Electrostatic. *J. Am. Chem. Soc.* **2016,** *138*, 980-990.

[273] Dubas, S. T.; Schlenoff, J. B. Factors controlling the growth of polyelectrolyte multilayers. *Macromolecules* **1999,** *32*, 8153-8160.

[274] Kovacevic, D.; Van der Burgh, S.; De Keizer, A.; Cohen Stuart, M. Kinetics of formation and dissolution of weak polyelectrolyte multilayers: role of salt and free polyions. *Langmuir* **2002,** *18*, 5607-5612.

[275] Xie, R.; Karim, A.; Douglas, J.; Han, C.; Weiss, R. Spinodal dewetting of thin polymer films. *Phys. Rev. Lett.* **1998,** *81*, 1251.

[276] Zimnitsky, D.; Shevchenko, V. V.; Tsukruk, V. V. Perforated, freely suspended layer-by-layer nanoscale membranes. *Langmuir* **2008,** *24*, 5996-6006.

[277] Genson, K. L.; Hoffman, J.; Teng, J.; Zubarev, E. R.; Vaknin, D.; Tsukruk, V. V. Interfacial micellar structures from novel amphiphilic star polymers. *Langmuir* **2004,** *20*, 9044-9052.

[278] Mendelsohn, J.; Barrett, C. J.; Chan, V.; Pal, A.; Mayes, A.; Rubner, M. Fabrication of microporous thin films from polyelectrolyte multilayers. *Langmuir* **2000,** *16*, 5017-5023.

[279] Reiter, G.; Hamieh, M.; Damman, P.; Sclavons, S.; Gabriele, S.; Vilmin, T.; Raphaël, E. Residual stresses in thin polymer films cause rupture and dominate early stages of dewetting. *Nat. Mater.* **2005,** *4*, 754-758.

[280] Suh, K.; Lee, H. H. Dynamic instability of strongly confined thin polymer films in spinodal dewetting. *Phys. Rev. Lett.* **2001,** *87*, 135502.

[281] Zhang, J.; Fredin, N. J.; Lynn, D. M. Apparent dewetting of ultrathin multilayered polyelectrolyte films incubated in aqueous environments. *Langmuir* **2007,** *23*, 11603-11610.

[282] Rouse, J. H.; Ferguson, G. S. Stepwise incorporation of nonpolar polymers within polyelectrolyte multilayers. *Langmuir* **2002,** *18*, 7635-7640.

[283] Shim, B. S.; Podsiadlo, P.; Lilly, D. G.; Agarwal, A.; Lee, J.; Tang, Z.; Ho, S.; Ingle, P.; Paterson, D.; Lu, W. Nanostructured thin films made by dewetting method of layer-by-layer assembly. *Nano Lett.* **2007,** *7*, 3266-3273.

[284] Xu, W.; Ledin, P. A.; Iatridi, Z.; Tsitsilianis, C.; Tsukruk, V. V. Multiresponsive Star-Graft Quarterpolymer Monolayers. *Macromolecules* **2015,** *48*, 3344-3353.

[285] Mazur, J.; McCrackin, F. Configurational properties of star-branched polymers. *Macromolecules* **1977,** *10*, 326-332.

[286] Chmielarz, P., Park, S., Sobkowiak, A., & Matyjaszewski, K. Synthesis of β-cyclodextrin-based star polymers via a simplified electrochemically mediated ATRP. *Polymer* **2016,** 88, 36-42.

[287] Manthiram, A.; Yu, X.; Wang, S., Lithium battery chemistries enabled by solid-state electrolytes. *Nat. Rev. Mater.* **2017,** *2*, 16103.

[288] Taghavikish, M.; Subianto, S.; Gu, Y.; Sun, X.; Zhao, X. S.; Choudhury, N. R. A Poly (ionic liquid) Gel Electrolyte for Efficient all Solid Electrochemical Double-Layer Capacitor. *Sci. Rep.* **2018**, *8*, 10918.

[289] Sun, J.-K.; Zhang, W.; Guterman, R.; Lin, H.-J.; Yuan, J., Porous polycarbene-bearing membrane actuator for ultrasensitive weak-acid detection and real-time chemical reaction monitoring. *Nat. Comm.* **2018**, *9*, 1717

[290] Zhang, K.; Feng, X.; Ye, C.; Hempenius, M. A.; Vancso, G. J., Hydrogels with a memory: dual-responsive, organometallic poly (ionic liquid) s with hysteretic volume-phase transition. *J. Am. Chem. Soc.* **2017**, *139*, 10029-10035.

[291] Choi, J.-H.; Xie, W.; Gu, Y.; Frisbie, C. D.; Lodge, T. P., Single Ion Conducting, Polymerized Ionic Liquid Triblock Copolymer Films: High Capacitance Electrolyte Gates for n-type Transistors. *ACS Appl. Mater. Interfaces* **2015,** *7*, 7294-7302.

[292] Cowan, M. G.; Gin, D. L.; Noble, R. D. Poly (ionic liquid)/ionic liquid ion-gels with high "free" ionic liquid content: platform membrane materials for CO2/light gas separations. *Acc. Chem. Res.* **2016**, *49*, 724-732.

[293] Montoto, E. C.; Cao, Y.; Hernández-Burgos, K.; Sevov, C. S.; Braten, M. N.; Helms, B. A.; Moore, J. S.; Rodríguez-López, J., Effect of the Backbone Tether on the Electrochemical Properties of Soluble Cyclopropenium Redox-Active Polymers. *Macromolecules* **2018**, *51*, 3539-3546.

[294] Wojnarowska, Z.; Feng, H.; Fu, Y.; Cheng, S.; Carroll, B.; Kumar, R.; Novikov, V. N.; Kisliuk, A. M.; Saito, T.; Kang, N.-G., Effect of chain rigidity on the decoupling of ion motion from segmental relaxation in polymerized ionic liquids: Ambient and elevated pressure studies. *Macromolecules* **2017**, *50*, 6710-6721.

[295] Choi, U. H.; Ye, Y.; Salas de la Cruz, D.; Liu, W.; Winey, K. I.; Elabd, Y. A.; Runt, J.; Colby, R. H., Dielectric and viscoelastic responses of imidazolium-based ionomers with different counterions and side chain lengths. *Macromolecules* **2014,** *47*, 777-790.

[296] Fan, F.; Wang, Y.; Hong, T.; Heres, M. F.; Saito, T.; Sokolov, A. P., Ion conduction in polymerized ionic liquids with different pendant groups. *Macromolecules* **2015,** *48*, 4461-4470.

[297] Fan, F.; Wang, W.; Holt, A. P.; Feng, H.; Uhrig, D.; Lu, X.; Hong, T.; Wang, Y.; Kang, N.-G.; Mays, J.; Sokolov, A. P., Effect of molecular weight on the ion transport mechanism in polymerized ionic liquids. *Macromolecules* **2016,** *49*, 4557-4570.

[298] Frenzel, F.; Folikumah, M. Y.; Schulz, M.; Anton, A. M.; Binder, W. H.; Kremer, F., Molecular dynamics and charge transport in polymeric polyisobutylene-based ionic liquids. *Macromolecules* **2016,** *49*, 2868-2875.

[299] Frenzel, F.; Guterman, R.; Anton, A. M.; Yuan, J.; Kremer, F., Molecular Dynamics and Charge Transport in Highly Conductive Polymeric Ionic Liquids. *Macromolecules* **2017,** *50*, 4022-4029.

[300] Keith, J. R.; Mogurampelly, S.; Aldukhi, F.; Wheatle, B. K.; Ganesan, V., Influence of molecular weight on ion-transport properties of polymeric ionic liquids. *Phys. Chem. Chem. Phys.* **2017**, *19*, 29134-29145.

[301] Bartels, J.; Sanoja, G. E.; Evans, C. M.; Segalman, R. A.; Helgeson, M. E., Decoupling Mechanical and Conductive Dynamics of Polymeric Ionic Liquids via a Trivalent Anion Additive. *Macromolecules* **2017**, *50*, 8979-8987.

[302] Griffin, P. J.; Freyer, J. L.; Han, N.; Geller, N.; Yin, X.; Gheewala, C. D.; Lambert, T. H.; Campos, L. M.; Winey, K. I., Ion Transport in Cyclopropenium-Based Polymerized Ionic Liquids. *Macromolecules* **2018,** *51*, 1681-1687.

[303] Choi, U. H.; Mittal, A.; Price Jr, T. L.; Gibson, H. W.; Runt, J.; Colby, R. H., Polymerized ionic liquids with enhanced static dielectric constants. *Macromolecules* **2013,** *46*, 1175-1186.

[304] Harris, M. A.; Heres, M. F.; Coote, J.; Wenda, A.; Strehmel, V.; Stein, G. E.; Sangoro, J., Ion Transport and Interfacial Dynamics in Disordered Block Copolymers of Ammonium-Based Polymerized Ionic Liquids. *Macromolecules* **2018**. *51*, 3477-3486.

[305] Delhorbe, V.; Bresser, D.; Mendil-Jakani, H.; Rannou, P.; Bernard, L.; Gutel, T.; Lyonnard, S.; Picard, L., Unveiling the Ion Conduction Mechanism in Imidazolium-Based Poly (ionic liquids): A Comprehensive Investigation of the Structure-to-Transport Interplay. *Macromolecules* **2017,** *50*, 4309-4321.

[306] Iacob, C., Matsumoto, A., Brennan, M., Liu, H., Paddison, S. J., Urakawa, O.; Inoue, T.; Sangoro, J.; Runt, J., Polymerized Ionic Liquids: Correlation of Ionic Conductivity with Nanoscale Morphology and Counterion Volume. *ACS Macro Lett.* **2017**, 6, 941-946.

[307] Matsumoto, A.; Iacob, C.; Noda, T.; Urakawa, O.; Runt, J.; Inoue, T., Introducing Large Counteranions Enhances the Elastic Modulus of Imidazolium-Based Polymerized Ionic Liquids. *Macromolecules* **2018**, *51*, 4129-4142.

[308] Evans, C. M.; Bridges, C. R.; Sanoja, G. E.; Bartels, J.; Segalman, R. A., Role of Tethered Ion Placement on Polymerized Ionic Liquid Structure and Conductivity: Pendant versus Backbone Charge Placement. *ACS Macro Lett.* **2016**, *5*, 925-930.

[309] Erwin, A. J.; Xu, W.; He, H.; Matyjaszewski, K.; Tsukruk, V. V., Linear and Star Poly (ionic liquid) Assemblies: Surface Monolayers and Multilayers. *Langmuir* **2017**. *33*, 3187-3199

[310] Mori, H.; Ebina, Y.; Kambara, R.; Nakabayashi, K., Temperature-responsive self-assembly of star block copolymers with poly (ionic liquid) segments. *Polym. J.* **2012,** *44*, 550-560.

[311] Mori, H.; Ebina, Y.; Kambara, R.; Nakabayashi, K. Temperature-responsive self-assembly of star block copolymers with poly (ionic liquid) segments. *Polym. J.* **2012,** *44*, 550-560.

[312] Shevchenko, V.; Stryutsky, A.; Klymenko, N.; Gumenna, M.; Fomenko, A.; Bliznyuk, V.; Trachevsky, V.; Davydenko, V.; Tsukruk, V., Protic and aprotic anionic oligomeric ionic liquids. *Polymer* **2014,** *55*, 3349-3359.

[313] Pakula, T.; Vlassopoulos, D.; Fytas, G.; Roovers, J., Structure and dynamics of melts of multiarm polymer stars. *Macromolecules* **1998,** *31*, 8931-8940.

[314] Vlassopoulos, D.; Fytas, G.; Pakula, T.; Roovers, J., Multiarm star polymers dynamics. *J. Phys. Condens. Matter* **2001,** *13*, R855.

[315] Likos, C.; Löwen, H.; Watzlawek, M.; Abbas, B.; Jucknischke, O.; Allgaier, J.; Richter, D., Star polymers viewed as ultrasoft colloidal particles. *Phys. Rev. Lett.* **1998,** *80*, 4450.

[316] Van Ruymbeke, E.; Muliawan, E. B.; Vlassopoulos, D.; Gao, H.; Matyjaszewski, K., Melt rheology of star polymers with large number of small arms, prepared by crosslinking poly (n-butyl acrylate) macromonomers via ATRP. *Eur. Polym. J.* **2011,** *47*, 746-751.

[317] Helgeson, M. E.; Wagner, N. J.; Vlassopoulos, D., Viscoelasticity and shear melting of colloidal star polymer glasses. *J. Rheol.* **2007**, 51, 297-316.

[318] Snijkers, F.; Cho, H. Y.; Nese, A.; Matyjaszewski, K.; Pyckhout-Hintzen, W.; Vlassopoulos, D., Effects of core microstructure on structure and dynamics of star polymer melts: from polymeric to colloidal response. *Macromolecules* **2014**, 47, 5347-5356.

[319] Johnson, K. J.; Glynos, E.; Sakellariou, G.; Green, P., Dynamics of Star-Shaped Polystyrene Molecules: From Arm Retraction to Cooperativity. *Macromolecules* **2016**, *49*, 5669-5676.

[320] Dorgan, J. R.; Knauss, D. M.; Al-Muallem, H. A.; Huang, T.; Vlassopoulos, D., Melt rheology of dendritically branched polystyrenes. *Macromolecules* **2003,** *36*, 380-388.

[321] Napolitano, S.; Glynos, E.; Tito, N. B., Glass transition of polymers in bulk, confined geometries, and near interfaces. *Rep. Prog. Phys.* **2017,** *80*, 036602.

[322] van der Scheer, P.; van de Laar, T.; van der Gucht, J.; Vlassopoulos, D.; Sprakel, J., Fragility and strength in nanoparticle glasses. *ACS nano* **2017,** *11*, 6755-6763.

[323] Xu, W.; Ledin, P. A.; Shevchenko, V. V.; Tsukruk, V. V., Architecture, assembly, and emerging applications of branched functional polyelectrolytes and poly (ionic liquid) s. *ACS Appl. Mater. Interfaces* **2015,** *7*, 12570-12596.

[324] Xu, W.; Choi, I.; Plamper, F. A.; Synatschke, C. V.; Müller, A. H.; Melnichenko, Y. B.; Tsukruk, V. V., Thermo-induced limited aggregation of responsive star polyelectrolytes. *Macromolecules* **2014,** *47*, 2112-2121.

[325] Akabori, K. I.; Atarashi, H.; Ozawa, M.; Kondo, T.; Nagamura, T.; Tanaka, K., Glass transition behavior of hyper-branched polystyrenes. *Polymer* **2009**, 50, 4868-4875.

[326] Erwin, A. J.; Korolovych, V. F.; Iatridi, Z.; Tsitsilianis, C.; Ankner, J. F.; Tsukruk, V. V., Tunable Compartmentalized Morphologies of Multilayered Dual Responsive Star Block Polyampholytes. *Macromolecules* **2018**, *51*, 4800-4812

[327] Choi, U. H.; Mittal, A.; Price, T. L.; Lee, M.; Gibson, H. W.; Runt, J.; Colby, R. H., Molecular volume effects on the dynamics of polymerized ionic liquids and their monomers. *Electrochim. Acta* **2015,** *175*, 55-61.

[328] Bocharova, V.; Wojnarowska, Z.; Cao, P.-F.; Fu, Y.; Kumar, R.; Li, B.; Novikov, V. N.; Zhao, S.; Kisliuk, A.; Saito, T., Influence of Chain Rigidity and Dielectric Constant on the Glass Transition Temperature in Polymerized Ionic Liquids. *J. Phys. Chem. B* **2017,** *121*, 11511-11519.

[329] He, R.; Kyu, T., Effect of plasticization on ionic conductivity enhancement in relation to glass transition temperature of crosslinked polymer electrolyte membranes. *Macromolecules* **2016,** *49*, 5637-5648.

[330] Lu, M.; Runt, J.; Painter, P., An infrared spectrocopic study of a polyester copolymer ionomer based on poly (ethylene oxide). *Macromolecules* **2009,** *42*, 6581-6587.

[331] Nakamura, K.; Saiwaki, T.; Fukao, K.; Inoue, T., Viscoelastic Behavior of the Polymerized Ionic Liquid Poly (1-ethyl-3-vinylimidazolium bis (trifluoromethanesulfonylimide)). *Macromolecules* **2011,** *44*, 7719-7726.

[332] Nakamura, K.; Fukao, K.; Inoue, T., Dielectric relaxation and viscoelastic behavior of polymerized ionic liquids with various counteranions. *Macromolecules* **2012,** *45*, 3850-3858.

[333] Inoue, T.; Matsumoto, A.; Nakamura, K., Dynamic viscoelasticity and birefringence of poly (ionic liquids) in the vicinity of glass transition zone. *Macromolecules* **2013**, *46*, 6104-6109.

[334] Qin, Q.; McKenna, G. B., Correlation between dynamic fragility and glass transition temperature for different classes of glass forming liquids. *J. of Non-Cryst. Solids* **2006,** *352*, 2977-2985.

[335] Rubinstein, M.; Colby, R. H., *Polymer physics*. Oxford university press New York: 2003; Vol. 23.

[336] Dalsin, S. J.; Hillmyer, M. A.; Bates, F. S., Linear rheology of polyolefin-based bottlebrush polymers. *Macromolecules* **2015,** *48*, 4680-4691.

[337] Hu, M.; Xia, Y.; McKenna, G. B.; Kornfield, J. A.; Grubbs, R. H., Linear rheological response of a series of densely branched brush polymers. *Macromolecules* **2011,** *44*, 6935-6943.

[338] Kapnistos, M.; Semenov, A. N.; Vlassopoulos, D.; Roovers, J., Viscoelastic response of hyperstar polymers in the linear regime. *J. Chem. Phys.* **1999**, *111*, 1753-1759.

[339] Trinkle, S.; Walter, P.; Friedrich, C., Van Gurp-Palmen plot II–classification of long chain branched polymers by their topology. *Rheol. Acta* **2002,** *41*, 103-113.

[340] Jakobi, B.; Bichler, K. J.; Sokolova, A.; Schneider, G. J. Dynamics of PDMS-g-PDMS Bottlebrush Polymers by Broadband Dielectric Spectroscopy. *Macromolecules* **2020**, *53*, 8450-8458

[341] Trinkle, S.; Friedrich, C., Van Gurp-Palmen-plot: a way to characterize polydispersity of linear polymers. *Rheol. Acta* **2001,** *40*, 322-328.

[342] Chen, Q.; Tudryn, G. J.; Colby, R. H., Ionomer dynamics and the sticky Rouse model. *J. Rheol.* **2013,** *57*, 1441-1462.

[343] Chen, Q.; Bao, N.; Wang, J. H. H.; Tunic, T.; Liang, S.; Colby, R. H., Linear viscoelasticity and dielectric spectroscopy of ionomer/plasticizer mixtures: A transition from ionomer to polyelectrolyte. *Macromolecules* **2015**, *48*, 8240-8252.

[344] Gainaru, C.; Stacy, E. W.; Bocharova, V.; Gobet, M.; Holt, A. P.; Saito, T.; Greenbaum, S.; Sokolov, A. P., Mechanism of conductivity relaxation in liquid and polymeric electrolytes: Direct link between conductivity and diffusivity. *J. Phys. Chem. B* **2016,** *120*, 11074-11083.

[345] Marzantowicz, M.; Dygas, J. R.; Krok, F.; Tomaszewska, A.; Florjańczyk, Z.; Zygadło-Monikowska, E.; Lapienis, G., Star-branched poly (ethylene oxide) LiN (CF3SO2) 2: A promising polymer electrolyte. *J. Power Sources* **2009**, 194, 51-57.

[346] Mallamace, F.; Branca, C.; Corsaro, C.; Leone, N.; Spooren, J.; Chen, S.-H.; Stanley, H. E., Transport properties of glass-forming liquids suggest that dynamic crossover temperature is as important as the glass transition temperature. *PNAS* **2010,** *107*, 22457-22462.

[347] Srivastava, S.; Schaefer, J. L.; Yang, Z.; Tu, Z.; Archer, L. A. 25th anniversary article: polymer–particle composites: phase stability and applications in electrochemical energy storage. *Adv. Mater.* **2014**, *26*, 201-234.

[348] Zhang, G.; Hong, Y. L.; Nishiyama, Y.; Bai, S.; Kitagawa, S.; Horike, S. Accumulation of Glassy Poly (ethylene oxide) Anchored in a Covalent Organic Framework as a Solid-State Li+ Electrolyte. *J. Am. Chem. Soc.* **2018**, *141*, 1227-1234.

[349] Schaefer, J. L.; Yanga, D. A.; Archer, L. A. High lithium transference number electrolytes via creation of 3-dimensional, charged, nanoporous networks from dense functionalized nanoparticle composites. *Chem. Mater.* **2013**, *25*, 834-839.

[350] Nugent, J. L.; Moganty, S. S.; Archer, L. A. Nanoscale organic hybrid electrolytes. *Adv. Mater.* **2010**, *22*, 3677-3680.

[351] Lu, Y.; Korf, K.; Kambe, Y.; Tu, Z.; Archer, L. A. Ionic-liquid–nanoparticle hybrid electrolytes: applications in lithium metal batteries. *Angew. Chem. Int. Ed.* **2014**, *53*, 488-492.

[352] Liu, H.-K.; Ren, L.-J.; Wu, H.; Ma, Y.-L.; Richter, S.; Godehardt, M.; Kübel, C.; Wang, W., Unraveling the Self-Assembly of Heterocluster Janus Dumbbells into Hybrid Cubosomes with Internal Double-Diamond Structure. *J. Am. Chem. Soc.* **2018,** *141*, 831-839.

[353] Tanaka, K.; Ishiguro, F.; Chujo, Y., POSS ionic liquid. *J. Am. Chem. Soc.* **2010**, *132*, 17649-17651.

[354] Chen, N.; Guan, Y.; Shen, J.; Guo, C.; Qu, W.; Li, Y.; Wu, F.; Chen, R., Heteroatom Si Substituent Imidazolium-Based Ionic Liquid Electrolyte Boosts the Performance of Dendrite-Free Lithium Batteries. *ACS Appl. Mater. Interfaces* **2019**, *11*, 12154-12160.

[355] Mallela, Y. L.; Jeong, S. Y.; Kumar, S.; Lee, J. S. Hyperbranched Poly (Glycidol)-Grafted Silica Nanoparticles for Enhancing Li-Ion Conductivity of Poly (Ethylene Oxide). *Macromol. Mater. Eng.* **2020**, 2000572.

[356] Nohara, T.; Koseki, K.; Tabata, K.; Shimada, R.; Suzuki, Y.; Umemoto, K.; Takeda, M.; Sato, R.; Rodbuntum, S.; Arita, T.; Masuhara, A. Core Size-Dependent Proton Conductivity of Silica Filler-Functionalized Polymer Electrolyte Membrane. *ACS Sustainable Chem. Eng.* **2020**, *8*, 14674-14678.

[357] Likos, C. N., Soft matter with soft particles. *Soft matter* **2006,** *2*, 478-498.

[358] Korolovych, V. F.; Erwin, A.; Stryutsky, A.; Lee, H.; Heller, W. T.; Shevchenko, V. V.; Bulavin, L. A.; Tsukruk, V. V., Thermally Responsive Hyperbranched Poly (ionic liquid) s: Assembly and Phase Transformations. *Macromolecules* **2018,** *51*, 4923-4937.

[359] van der Scheer, P.; van de Laar, T.; van der Gucht, J.; Vlassopoulos, D.; Sprakel, J., Fragility and strength in nanoparticle glasses. *ACS nano* **2017,** *11*, 6755-6763.

[360] Gury, L.; Gauthier, M.; Cloitre, M.; Vlassopoulos, D. Colloidal Jamming in Multiarm Star Polymer Melts. *Macromolecules* **2019**, DOI: 10.1021/acs.macromol.9b00674

[361] Chremos, A.; Douglas, J. F., Hidden Hyperuniformity in Soft Polymeric Materials. *Phys. Rev. Lett.* **2018**, *121*, 258002.

[362] Mogurampelly, S.; Keith, J. R.; Ganesan, V. Mechanisms underlying ion transport in polymerized ionic liquids. *J. Am. Chem. Soc.* **2017**, *139*, 9511-9514.

[363] Keith, J. R.; Mogurampelly, S.; Aldukhi, F.; Wheatle, B. K.; Ganesan, V. Influence of molecular weight on ion-transport properties of polymeric ionic liquids. *Phys. Chem. Chem. Phys.* **2017**, *19*, 29134-29145.

[364] Keith, J. R.; Rebello, N. J.; Cowen, B. J.; Ganesan, V. Influence of Counterion Structure on Conductivity of Polymerized Ionic Liquids. *ACS Macro. Lett.* **2019**, *8*, 387-392.

[365] Choi, U. H.; Mittal, A.; Price, T. L.; Lee, M.; Gibson, H. W.; Runt, J.; Colby, R. H., Molecular volume effects on the dynamics of polymerized ionic liquids and their monomers. *Electrochim. Acta* **2015,** *175*, 55-61

[366] Zhao, Q.; Shen, C.; Halloran, K. P.; Evans, C. M. Effect of Network Architecture and Linker Polarity on Ion Aggregation and Conductivity in Precise Polymerized Ionic Liquids. *ACS Macro Lett.* **2019**, *8*, 658-663.

[367] Schwab, E.; Mecking, S., Synthesis and properties of highly branched polycations with an aliphatic polyether scaffold. *J. Polym. Sci., Part A: Polym. Chem.* **2005,** *43*, 4609-4617.

[368] Zheng, T.; Ren, S.; Zhou, Q.; Li, Q.; Zhang, L.; Li, H.; Lin, Y., Synthesis and ionic conductivity of a novel ionic liquid polymer electrolyte. *J. Polym. Res.* **2014,** *21*, 361.

[369] Tamaki, M.; Taguchi, T.; Kitajyo, Y.; Takahashi, K.; Sakai, R.; Kakuchi, T.; Satoh, T., LCST-type liquid–liquid and liquid–solid phase transition behaviors of hyperbranched polyglycerol bearing imidazolium salt. *J. Polym. Sci., Part A: Polym. Chem.* **2009,** *47*, 7032-7042.

[370] Chen, C.; Fang, X., Synthesis and conductivity performance of hyperbranched polymer electrolytes with terminal ionic groups. *J. Appl. Polym. Sci.* **2010,** *117*, 3539-3544.

[371] Canilho, N.; Scholl, M.; Klok, H.-A.; Mezzenga, R., Thermotropic ionic liquid crystals via self-assembly of cationic hyperbranched polypeptides and anionic surfactants. *Macromolecules* **2007,** *40*, 8374-8383.

[372] Marcos, M.; Alcalá, R.; Barberá, J. n.; Romero, P.; Sánchez, C.; Serrano, J. L., Photosensitive ionic nematic liquid crystalline complexes based on dendrimers and hyperbranched polymers and a cyanoazobenzene carboxylic acid. *Chem. Mater.* **2008,** *20*, 5209-5217.

[373] Schüler, F.; Kerscher, B.; Beckert, F.; Thomann, R.; Mülhaupt, R., Hyperbranched Polymeric Ionic Liquids with Onion-like Topology as Transporters and Compartmentalized Systems. *Angew. Chem. Int. Ed.* **2013,** *52*, 455-458.

[374] Wang, A.; Xu, H.; Liu, X.; Gao, R.; Wang, S.; Zhou, Q.; Chen, J.; Liu, X.; Zhang, L., The synthesis of a hyperbranched star polymeric ionic liquid and its application in a polymer electrolyte. *Polym. Chem.* **2017,** *8*, 3177-3185.

[375] Korolovych, V.; Erwin, A.; Stryutsky, A.; Mikan, E.; Shevchenko, V.; Tsukruk, V., Self-Assembly of Hyperbranched Protic Poly (ionic liquid) s with Variable Peripheral Amphiphilicity. *Bull. Chem. Soc. Jpn.* **2017**, 90, 919-923.

[376] Baeza, G. P.; Dessi, C.; Costanzo, S.; Zhao, D.; Gong, S.; Alegria, A.; Colby, R. H.; Rubinstein, M.; Vlassopoulos, D.; Kumar, S. K., Network dynamics in nanofilled polymers. *Nat. Commun.* **2016**, *7*, 11368.

[377] Cheng, Y.; Yang, J.; Hung, J.-H.; Patra, T. K.; Simmons, D. S., Design rules for highly conductive polymeric ionic liquids from molecular dynamics simulations. *Macromolecules* **2018,** *51*, 6630-6644.

[378] Kremer, F.; Schönhals, A., Broadband dielectric spectroscopy. *Springer* **2003**.

[379] Nakamura, K.; Fukao, K., Dielectric relaxation behavior of polymerized ionic liquids with various charge densities. *Polymer* **2013**, *54*, 3306-3313.

[380] Choi, U. H.; Mittal, A.; Price Jr, T. L.; Gibson, H. W.; Runt, J.; Colby, R. H., Polymerized ionic liquids with enhanced static dielectric constants. *Macromolecules* **2013**, *46*, 1175-1186.

[381] Mapesa, E. U.; Chen, M.; Heres, M. F.; Harris, M. A.; Kinsey, T.; Wang, Y.; Long, T. E.; Lokitz, B. S.; Sangoro, J. R. Charge Transport in Imidazolium-Based Homo-and Triblock Poly (ionic liquid) s. *Macromolecules* **2019**, *52*, 620-628.

[382] Dyre, J. C., The random free-energy barrier model for ac conduction in disordered solids. *J. Appl. Phys.* **1988**, *64*, 2456-2468.

[383] Dyre, J. C.; Maass, P.; Roling, B.; Sidebottom, D. L., Fundamental questions relating to ion conduction in disordered solids. *Rep. Prog. Phys.* **2009**, *72*, 046501.

[384] Heres, M.; Cosby, T.; Mapesa, E. U.; Liu, H.; Berdzinski, S.; Strehmel, V.; Dadmun, M.; Paddison, S. J.; Sangoro, J., Ion Transport in Glassy Polymerized Ionic Liquids: Unraveling the Impact of the Molecular Structure. *Macromolecules* **2018**, *52*, 88-95.

[385] Ueno, K.; Tokuda, H.; Watanabe, M., Ionicity in ionic liquids: correlation with ionic structure and physicochemical properties. *Phys. Chem. Chem. Phys.* **2010**, *12*, 1649-1658.

[386] Liu, Y.; Chen, X.; Men, S.; Licence, P.; Xi, F.; Ren, Z.; Zhu, W., The impact of cation acidity and alkyl substituent on the cation-anion interactions of 1-alkyl-2, 3-dimethylimidazolium ionic liquids. *Phys. Chem. Chem. Phys.* **2019**, DOI: 10.1039/c9cp01381d

[387] Miran, M. S.; Kinoshita, H.; Yasuda, T.; Susan, M. A. B. H.; Watanabe, M. Hydrogen bonds in protic ionic liquids and their correlation with physicochemical properties. *Chem. Comm.* **2011**, *47*, 12676-12678.

[388] Hoque, M.; Thomas, M. L.; Miran, M. S.; Akiyama, M.; Marium, M.; Ueno, K.; Watanabe, M., Protic ionic liquids with primary alkylamine-derived cations: the dominance of hydrogen bonding on observed physicochemical properties. *RSC Adv.* **2018**, *8*, 9790-9794.

[389] Gilli, P.; Pretto, L.; Bertolasi, V.; Gilli, G., Predicting Hydrogen-Bond Strengths from Acid− Base Molecular Properties. The p K a Slide Rule: Toward the Solution of a Long-Lasting Problem. *Acc. Chem. Res.* **2008**, *42*, 33-44.

[390] Stoimenovski, J.; Izgorodina, E. I.; MacFarlane, D. R., Ionicity and proton transfer in protic ionic liquids. *Phys. Chem. Chem. Phys.* **2010**, *12*, 10341-10347.